NASA/CR–2012-217569

Dual-Pump CARS Development and Application to Supersonic Combustion

Gaetano Magnotti and Andrew D. Cutler
The George Washington University, Washington, D. C.

May 2012

NASA STI Program . . . in Profile

Since its founding, NASA has been dedicated to the advancement of aeronautics and space science. The NASA scientific and technical information (STI) program plays a key part in helping NASA maintain this important role.

The NASA STI program operates under the auspices of the Agency Chief Information Officer. It collects, organizes, provides for archiving, and disseminates NASA's STI. The NASA STI program provides access to the NASA Aeronautics and Space Database and its public interface, the NASA Technical Report Server, thus providing one of the largest collections of aeronautical and space science STI in the world. Results are published in both non-NASA channels and by NASA in the NASA STI Report Series, which includes the following report types:

- TECHNICAL PUBLICATION. Reports of completed research or a major significant phase of research that present the results of NASA Programs and include extensive data or theoretical analysis. Includes compilations of significant scientific and technical data and information deemed to be of continuing reference value. NASA counterpart of peer-reviewed formal professional papers, but having less stringent limitations on manuscript length and extent of graphic presentations.

- TECHNICAL MEMORANDUM. Scientific and technical findings that are preliminary or of specialized interest, e.g., quick release reports, working papers, and bibliographies that contain minimal annotation. Does not contain extensive analysis.

- CONTRACTOR REPORT. Scientific and technical findings by NASA-sponsored contractors and grantees.

- CONFERENCE PUBLICATION. Collected papers from scientific and technical conferences, symposia, seminars, or other meetings sponsored or co-sponsored by NASA.

- SPECIAL PUBLICATION. Scientific, technical, or historical information from NASA programs, projects, and missions, often concerned with subjects having substantial public interest.

- TECHNICAL TRANSLATION. English-language translations of foreign scientific and technical material pertinent to NASA's mission.

Specialized services also include organizing and publishing research results, distributing specialized research announcements and feeds, providing information desk and personal search support, and enabling data exchange services.

For more information about the NASA STI program, see the following:

- Access the NASA STI program home page at *http://www.sti.nasa.gov*

- E-mail your question to help@sti.nasa.gov

- Fax your question to the NASA STI Information Desk at 443-757-5803

- Phone the NASA STI Information Desk at 443-757-5802

- Write to:
  STI Information Desk
  NASA Center for AeroSpace Information
  7115 Standard Drive
  Hanover, MD 21076-1320

NASA/CR–2012-217567

Dual-Pump CARS Development and Application to Supersonic Combustion

Gaetano Magnotti and Andrew D. Cutler
The George Washington University, Washington, D. C.

National Aeronautics and
Space Administration

Langley Research Center
Hampton, Virginia 23681-2199

Prepared for Langley Research Center
under Cooperative Agreements NNX08AB31A, NNX07AC32A

May 2012

Acknowledgments

The authors would like to acknowledge the contributions of the many members of the research team that made this work possible. Deserving of credit are Paul Danehy, Sarah Tedder, Lloyd Wilson, Daniel Bivolaru, and Gregory Herring. Many other persons whose names are not mentioned here have contributed significantly, and the authors express their sincerest thanks.

Available from:

NASA Center for AeroSpace Information
7115 Standard Drive
Hanover, MD 21076-1320
443-757-5802

Abstract

Successful design of hypersonic air-breathing engines requires new computational fluid dynamics (CFD) models for turbulence and turbulence-chemistry interaction in supersonic combustion. Unfortunately, not enough data are available to the modelers to develop and validate their codes, due to difficulties in taking measurements in such a harsh environment.

Dual-pump coherent anti-Stokes Raman spectroscopy (CARS) is a non-intrusive, non-linear, laser-based technique that provides temporally and spatially resolved measurements of temperature and absolute mole fractions of N_2, O_2 and H_2 in H_2-air flames. A dual-pump CARS instrument has been developed to obtain measurements in supersonic combustion and generate databases for the CFD community. Issues that compromised previous attempts, such as beam steering and high irradiance perturbation effects, have been alleviated or avoided. Improvements in instrument precision and accuracy have been achieved.

An axis-symmetric supersonic combusting coaxial jet facility has been developed to provide a simple, yet suitable flow to CFD modelers. The facility provides a central jet of hot "vitiated air" simulating the hot air entering the engine of a hypersonic vehicle flying at Mach numbers between 5 and 7. Three different silicon carbide nozzles, with exit Mach number 1, 1.6 and 2, are used to provide flows with the effects of varying compressibility. H_2 co-flow is available in order to generate a supersonic combusting free jet. Dual-pump CARS measurements have been obtained for varying values of flight and exit Mach numbers at several locations.

Approximately one million Dual-pump CARS single shots have been collected in the supersonic jet for varying values of flight and exit Mach numbers at several locations. Data have been acquired with a H_2 co-flow (combustion case) or a N_2 co-flow (mixing case). Results are presented and the effects of the compressibility and of the heat release are discussed.

Table of Contents

List of Figures

List of Tables

List of Acronyms

CARS	= Coherent Anti-Stokes Raman Spectroscopy
CEA	= Chemical Equilibrium Analysis
CCD	= Charge Coupled Device
CFD	= Computational Fluid Dynamics
DNS	= Direct Numerical Simulation
DCSCTF	= Direct-Connect Supersonic Combustion Test Facility
FEM	= Finite Element Method
FWHM	= Full Width at Half Maximum
HW	= Herman Wallis
JK	= James-Klemperer
IR	= Infra-red
IRS	= Interferometric Rayleigh Scattering
LES	= Large Eddy Simulation
MTV	= Molecular Tagging Velocimetry
NASA	= National Aeronautics and Space Administration
PIV	= Particle Image Velocimetry
PLIF	= Planar Laser Induced Fluorescence
RANS	= Reynolds Averaged Navier-Stokes
RBCC	= Rocket Based Combined Cycle
SiC	= Silicon Carbide
SLPM	= Standard Liter Per Minute

SRP = Stimulated Raman Pumping

TB = Tipping Bouanich

TBCC = Turbine Based Combined Cycle

TDLAS = Tunable Diode Laser Absorption Spectroscopy

USED CARS = Unstable-resonator Spatially Enhanced CARS

UV = Ultra-violet

VULCAN = Viscous Upwind Algorithm for Complex Flow Analysis

WIDECARS = Width Increased Dual-Pump Enhanced CARS

List of Symbols

c	=	speed of light: 299,792,458 m/s
g	=	state degeneracy
h	=	convection heat transfer coefficient, W/(m^2 K)
h	=	Planck`s constant: 6.626 10^{-34} J s
$\hbar$	=	Planck`s constant/2π
k	=	Boltzmann's constant, 1.381 × 10^{-23} m^2 kg s^{-2} K^{-1}
$\vec{k}$	=	wave vector
Δk	=	phase mismatch
l	=	CARS probe volume length, mm
m	=	molecular mass
		magnetic (orientational) quantum number
r	=	narrowband dye laser FWHM at its focal plane, μm
p	=	pressure, atm
q	=	heat flux per unit area, W/m^2
u	=	velocity, m/s
v	=	vibrational quantum number
x_i	=	mole fraction of the ith species
z_R	=	Rayleigh range, mm
A	=	mole fraction of the gas coming from ambient air
B_v	=	rotational constant, cm^{-1}
BD	=	beam displacement

C	=	mole fraction of the gas coming from the co-flow
D	=	beam spreading coefficient
D_o	=	optical diffusion coefficient, m^2/s
D_v	=	centrifugal distortion constant, cm^{-1}
$\vec{E}$	=	electric field, $N\ C^{-1}$
E_e	=	electronic energy, J
E_r	=	rotational energy, J
E_v	=	vibrational energy, J
F	=	fractional strength of a sub-level
J	=	rotational quantum number
I	=	laser irradiance, GW/cm^2
I_{Total}	=	sum of the average irradiance of all laser beams, GW/cm^2
M_c	=	convective Mach number
M_e	=	exit Mach number
M_f	=	flight (enthalpy) Mach number
N	=	total number density, m^{-3}
P	=	laser power, W
$\vec{P}$	=	induced polarization A^2s^2/m
T	=	temperature, K
T_w	=	wall temperature, K
T_{aw}	=	adiabatic wall temperature, K
TKE	=	turbulent kinetic energy, m^2/s^2
V	=	mole fraction of the gas coming from the center-jet

α	=	crossing angle
α_e	=	vibration-rotation interaction coefficient, cm^{-1}
β	=	Galatry narrowing parameter, cm^{-1}/atm
δ_r	=	jet radius based on the temperature profile
δ_T	=	shear layer width based on the temperature profile
δ_V	=	shear layer width based on the center-jet mole fraction
ε_0	=	vacuum permittivity, 8.854 10^{-12} F m^{-1}
λ_ρ	=	density ratio
λ_p	=	pressure ratio
μ_0	=	vacuum permeability, 4π V s A^{-1} m^{-1}
ρ	=	density, kg/m^3
σ	=	½ of the e^{-2} beam diameter, μm
		standard deviation
$\tau_{\Delta N}$	=	stimulated Raman pumping characteristic time, s
υ_v	=	vibrational bandhead, cm^{-1}
$\chi^{(n)}$	=	n^{th} order susceptibility
χ_{CARS}	=	CARS susceptibility
χ_{NR}	=	non-resonant third order susceptibility
ω	=	circular frequency, cm^{-1}
ω_e	=	vibrational frequency, cm^{-1}
$\omega_e x_e$, $\omega_e y_e$, $\omega_e z_e$	=	anharmonic vibrational constants, cm^{-1}
ω_S	=	Stokes circular frequency, cm^{-1}
ω_p	=	pump circular frequency, cm^{-1}

ω_1	=	frequency of the Nd:YAG laser, cm^{-1}
ω_2	=	frequency of the narrowband dye laser, cm^{-1}
ω_3	=	frequency of the broadband dye laser, cm^{-1}
Δ_j	=	fractional population difference
Δk	=	phase mismatch
$\overline{\Delta \nu_{Stark}}$	=	Stark shift, cm^{-1}
Γ	=	linewidth, cm^{-1}
$\frac{\partial \sigma}{\partial \Omega}$	=	differential Raman cross section, m^2/sr
Π	=	compressibility parameter
Φ	=	equivalence ratio

CHAPTER 1 - Introduction

1.1 Hypersonic Air-Breathing Propulsion

Hypersonic air-breathing propulsion is extremely attractive for a wide range of applications including long range missiles, high speed military and commercial aircraft, and access to space. Research has been ongoing in USA and Europe for the last 50 years, yet several technological challenges need to be overcome to build a hypersonic airbreathing vehicle. [1-4]

The fastest manned aircraft propelled by an air-breathing engine is the SR-71 Blackbird with a top speed of Mach 3.2. Higher velocities cannot be reached with turbojet engines because the temperature would be too elevated for the turbine blades. This limitation is overcome by ramjet engine often used in missiles. At high flight speed, deceleration of the air through the inlet provides the required pressure rise, and there is no need of a compressor and therefore of a turbine. The main limitation is that a ramjet can only work at high speed; therefore it needs to be coupled to a different engine for the low speed portion of the flight. Although the flight Mach number is supersonic, the air entering the combustion chamber is subsonic. The elevated temperature reached in the combustor limits the speed of a ramjet engine to Mach 6. Missiles have used ramjet engines to fly up to Mach 5. At higher speed, rockets are currently the only option available.

In a supersonic combustion ramjet (scramjet) the inlet decelerates the air entering the combustor to a lower but still supersonic Mach number, reducing the thermal load and allowing greater flight speed. Since the air is decelerated less, for equal flight

Mach number the pressure rise is lower than in a ramjet, increasing the minimum operational flight speed to roughly Mach 5. The commonly reported range of operational speed for a scramjet engine is from Mach 5 to 15. Dual mode scramjet can operate as a ramjet at lower speed and transition to supersonic combustion at higher speed, extending the lower limit of the speed range down to Mach 3.

A hypersonic air-breathing aircraft that can fly to and from a runway must use a combined cycle engine, rocket based (RBCC) or turbojet based (TBCC) for the low speed portion of the flight envelope, operating as a ramjet between Mach 3 and 6, and transitioning to a scramjet for speed above Mach 6. For access to space applications, a final rocket stage would be necessary for insertion into orbit. Figure 1-1 shows the schematic of a TBCC vehicle during the high speed operation. Oblique shock waves departing from the vehicle forebody and from the inlet and the oblique shock train in the isolator decelerate the air entering the combustor to a lower supersonic speed and increase its pressure. The combustor is a variable area duct where the incoming air

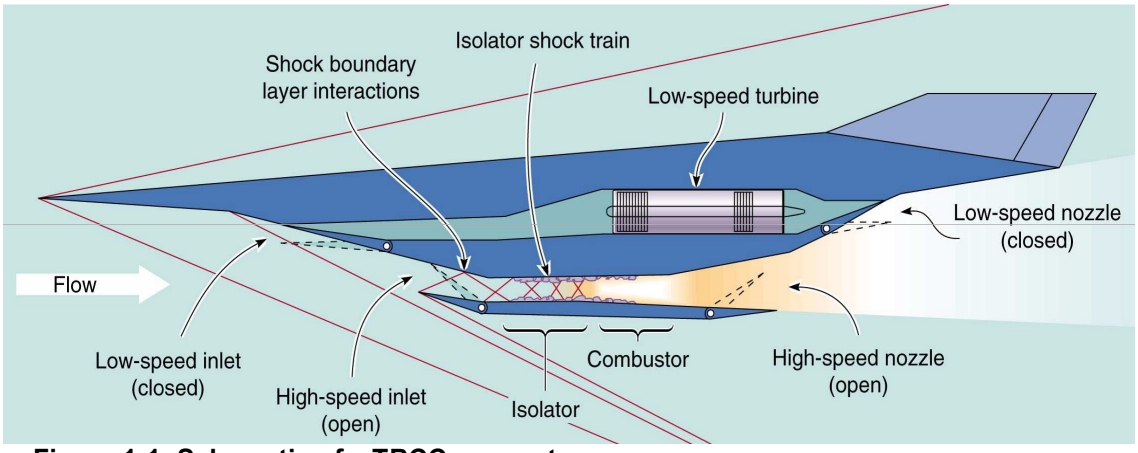

Figure 1-1: Schematic of a TBCC concept

J. C. McDaniel, H. Chelliah, C. P. Goyne, J. R. Edwards, P. Givi, and A. D. Cutler, "US National Center for Hypersonic Combined Cycle Propulsion: an Overview," in *16th AIAA/DLR/DGLR International Space Planes and Hypersonic Systems and Technologies Conference* 2009

reacts with the injected fuel. The area increase along the combustor is to offset the pressure rise and the Mach number reduction due to the heat release. The nozzle does not require a throat since the flow is already supersonic. During ramjet operation, a normal shock train is developed at the inlet, and the heat released from the combustion accelerates the combustion products to sonic speeds (thermal throat).

At NASA Langley Research Center, where the research for this dissertation was conducted, the focus is on access to space applications. For access to space an airbreathing vehicle offers several advantages when compared to a rocket based vehicle. The airbreather does not need to carry the oxidizer, therefore offering the potential of a reduced gross take-off weight, and larger payload. The use of a turbine based combined cycle vehicle would allow horizontal take off and landing, providing much greater flexibility than a conventional rocket. The ability of the vehicle to self ferry to any site would open several launching and landing options. Other advantages include an extended launch window, and the possibility to abort at any point during the mission, resulting in increases in safety.

On the other hand a hypersonic air-breathing vehicle is a much more complex system than a rocket. Aerodynamically efficient integration of the low speed engine to the dual mode scramjet is challenging and so is the transition from one operational regime to the other. A scramjet combustor can have a simple geometry, but the fluid dynamics involved is very complex. Achieving efficient supersonic combustion is not an easy task. Typical residence times of the air in a scramjet combustor are of the order of a millisecond. Therefore the injected fuel needs to mix with the ingested air, and react within tenths of milliseconds. Proper understanding and modeling of

supersonic combustion is critical to the design of a scramjet engine capable of operating efficiently over a wide range of flight Mach number.

1.2 Experimental Data for CFD Development and Validation

Flight tests of hypersonic air-breathers are costly, challenging and can provide only limited data. Only a few successful flight tests of scramjet engines have been accomplished to date. Ground testing cannot perfectly reproduce the test condition. Electrically (resistance heated or arc) heated or combustion heated facilities, that can operate for relatively long time, can only simulate the lowest flight Mach numbers (up to 7). Excess water in combustion heated facilities is known to affect the combustion.[5] Shock tubes can simulate the entire range of speed but the test duration is limited to milliseconds. In addition vibrational non-equilibrium and excess nitric oxide and atomic species can affect the combustion.

For these reasons design and analysis of scramjet engines relies on computational fluid dynamics (CFD) simulations. Both RANS (Reynolds Average Navier-Stokes) and LES (Large Eddy Simulation) codes employ models to describe the turbulent mixing and the turbulence-chemistry interactions. The models developed for subsonic combustion are not adequate in the compressible regime. New models need to be developed and validated in order to successfully simulate a scramjet engine, and large experimental databases are needed.

The primary role of ground testing in supersonic combustion is to provide data to the CFD community. Ground testing of an actual scramjet engine, not only is extremely challenging for the experimentalist, but the data may be difficult to

interpret by the modelers (i.e., it may be difficult to identify what aspect of the modeling or boundary conditions is at fault when there is a discrepancy with the data). Experiments for CFD validation typically address only a sub-set of physical phenomena, so that specific numerical models can be tested.

When the goal is to study mixing and combustion in supersonic flows, testing is limited to the combustor. An actual scramjet combustor would have a complex geometry with several injectors operating simultaneously. A scramjet combustor model for CFD development typically has a simple geometry (variable area duct) and a single injector. Examples of this approach are the combustor used for the SCHOLAR test program [6] or the Dual-Mode Scramjet experiment at UVA. [7]

When the focus is on supersonic mixing and combustion, many researchers choose to study chemically reacting compressible shear layers in a nozzle exit pressure-matched open-jet configuration. This class of flows maintains the fundamental physics related to the turbulent mixing and turbulence-chemistry interaction, but removes the complications due to the walls, shock waves, and streamwise pressure gradients. Furthermore such unducted flows simplify the application of spectroscopic measurement techniques. A supersonic-combusting coaxial free-jet is the flow of interest for this work, and is described in details in Chapter 7.

1.3 **Measurement Techniques**

Making measurements in a supersonic combusting flow is very challenging because of the elevated speed and temperature. Any probe directly inserted in the

flow would have to be designed to tolerate high temperatures and pressure loads, and can strongly perturb the flow. High levels of vibration and noise, limited or no access to the facility during a test run, high levels of turbulence and strong temperature variations further complicate data acquisition in supersonic combustion experiments.

The harsh test environment generally limits the applicability of conventional measurements techniques to the combustor walls. Static pressure taps and thermocouples along the combustor walls are commonly employed in supersonic combustion testing. [5, 6, 8] Skin friction gauges have been used to determine the drag and a thin film gauge has been used to measure the heat transfer on the wall of a supersonic combustor. [9] Ryan [10] used a thrust stand to measure the thrust produced by a supersonic combustor. Robinson [11] used a three-component stress-wave force balance for measurements of thrust, lift and pitching moment on a large scramjet model in a reflected shock tunnel.

Intrusive probes, properly outfitted to stand the harsh test environment, have been used in several experiments. Pitot probes or rakes are often used to measure total pressure in supersonic mixing experiments. [12-19] A thermocouple probe to measure stagnation temperature in supersonic combusting flows was developed at the ONERA. [20] Gas sampling probes have been used in supersonic flames to measure species concentrations. [21-23] These measurements are intrusive and strongly perturb the flow, but allow measuring useful quantities such as total pressure and total temperature.

Several imaging techniques have been used to visualize structures in the flow. Sometimes useful information can be obtained simply by direct video imagining. OH

chemiluminescence is visible; therefore videos and pictures with conventional cameras can provide useful information on the location of the combustion region and on the flame structure. [24, 25] Whitehurst used a high speed camera at 6 kHz to study ignition and flameholding in a supersonic combustor. [26] Infrared (IR) cameras operating in the mid-IR have also been used to visualize the flame structure. [24, 27] The Schlieren technique, which images the first derivative of the density, has been employed to visualize turbulent structures in compressible mixing layers, [14, 15, 28] and near the injector in scramjet combustors. [29-31]

Several laser-based imaging techniques have been implemented to study supersonic combustion. Laser-based techniques are particularly advantageous for measurements in supersonic combustion because they provide more information than direct imaging, while still being non-intrusive. OH planar laser induced fluorescence is often used to obtain 2D images of the OH concentration in supersonic combustors. [8, 31-37] In addition to qualitative images of the reaction zone, the PLIF technique can also provide quantitative information. Allen [35] extracted temperature distribution from NO PLIF in a shock tube scramjet experiment, in a non-reacting region of the flow. Quagliaroli [36, 38] measured the OH concentration from OH PLIF images with an uncertainty of ~21%. Gauba [37] used OH-PLIF to obtain planar velocity fields with a 200 μm resolution and a 6-8% uncertainty in a scramjet combustor.

Accurate velocity measurements are important for CFD validation. Hot wire probes can easily perturb the flow, causing large uncertainties in the measurements, and can only be used in mixing studies. [39] Particle-based velocimetry techniques

such as laser Doppler velocimetry (LDV) [40, 41] and particle imaging velocimetry (PIV) [42-44] have been applied to supersonic combustion experiments. Three-dimensional velocity field have been acquired with stereoscopic PIV in a dual mode scramjet combustor. [45] In particle based velocimetry laser radiation is scattered from tracer particles seeded in the flow. The particle lag (where the particle does not travel as the same speed as the flow) is a potential source of inaccuracies in presence of shocks or strong accelerations. [46] Furthermore, there are difficulties in seeding all parts of the flow with particles, as well as the windows of the facility becoming coated with particles.[45]

Laser-based molecular velocimetry measures directly the gas speed, rather than the speed of particles moving with the flow. In laser-induced fluorescence the velocity can be determined from the Doppler shift of the emission. PLIF velocity measurements have been performed using emissions from OH, [37, 47, 48] NO [49] and iodine. [50] Molecular tagging techniques mark a molecule with a laser (by excitation or photo-dissociation) and follow the motion of the tagged molecule to determine its velocity. Hydroxyl tagging velocimetry has been used to study cavity stabilized supersonic non-reacting and reacting flows. [52] In depth reviews of laser-based velocimetry techniques can be found in Ref. [52, 53]. Interferometric Rayleigh scattering has also been used to measure velocity in supersonic combustion open flames. [51]

Several laser-based techniques have been applied to measure species concentration in supersonic combustion experiments. Tunable diode laser absorption spectroscopy (TDLAS) is a line-of-sight technique that allows simultaneous

measurements of temperature and species concentrations, including water, [54-56] OH and water, [32] and O_2. [57] Two-dimensional, spatially (but not temporally) resolved measurements are possible using tunable diode laser tomography, which combines several TDLAS measurements with tomographic image reconstruction. [57, 58]

UV Raman has been used to measure temperature, CO, O_2, C_2H_4, H_2O and H_2 simultaneously in a scramjet combustor. Laser-induced fluorescence from combustion byproducts and from the windows, and the UV emission from the flame, partially obscure the Raman spectra in some region of the flow, diminishing the quality of the measurements. [59, 60]

Coherent anti-Stokes Raman spectroscopy (CARS) does not suffer from the same issues of UV-Raman thanks to the coherent nature of the signal. The signal-to-noise ratio is higher than in Raman, and it does not require large windows, making it particularly attractive for measurements in ducts, where optical access is limited. Compared to TDLAS the main advantage is that it is spatially and temporally resolved, allowing study of the turbulence fluctuations present in the flow. The feasibility of CARS in supersonic reacting flows was first demonstrated by Anderson. [61, 62] Waidmann [29] used N_2 vibrational CARS to measure temperature in a combustor chamber. Gong [25] obtained CARS temperature measurements along the centerline of a scramjet combustor and of a supersonic diffusion flame. Zhao [63] measured N_2 vibrational temperature at two points simultaneously in a scramjet combustor. Yang [64]obtained simultaneous measurements of O_2, and the S(5) and S(6) H_2 rotational lines. Magre [20, 65]

measured temperature in a supersonic combustor from the N_2 Q-branch and then the H_2 Q-branch. Previous CARS applications at NASA Langley are discussed in the next section. Details on the technique are found in Chapter 2.

From this short review of the available diagnostic techniques, it is clear that there is not a single instrument that can provide all the measurements needed to the CFD modelers. For this reason experiments are often repeated applying different measurements techniques. An on-going test on a dual-mode scramjet at the University of Virginia [7] includes stereoscopic PIV, TDLAS, OH PLIF and dual-pump CARS measurements (performed using the instrument developed for this work).

Replicating a flow-field and measuring a different parameter at a different time does not allow determining statistical correlations between different parameters that would be available if the quantities were measured simultaneously. However with a CARS instrument that measures simultaneous temperature and species mole fractions it is possible to obtain temperature-mole fraction co-variances. Simultaneous acquisition of multiple parameters combining different time resolved techniques can be very challenging, but it also provides very useful additional information. An example is the IRS-CARS instrument developed by Bivolaru and Tedder for simultaneous measurements of temperature, species, and 2 components of velocity. [66]

1.4 CARS in Supersonic Combustion Experiments for CFD Validation at NASA Langley Research Center

NASA Langley Research Center has a long history of applying CARS in scramjet combustors and supersonic flames. The first attempt was from Jarret in 1987. [67] He applied dual Stokes CARS for simultaneous measurements of temperature, N_2 and O_2 to a supersonic H_2-air open flame. He also applied LDV for velocity measurements in the same flame. The two measurements were not simultaneous. The flowfield was an axisymmetric jet of vitiated air, with a center jet of H_2, provided by a small burner. The nozzle exit diameter was 17 mm for the vitiated air, 1.5 mm for the H_2 center-flow. The size of the CARS measurement volume was 4 mm; therefore several features of the flow could not be resolved. Measurements were taken at several points along diameters at 5 axial locations. Only 100 shots were taken at each point and only average results were reported. Flow asymmetries were found and a diamond shock system at the exit of the nozzle dominated the flow, making comparisons between the experimental results and the numerical simulation challenging. [68]

Smith [69] successfully measured temperature using N_2 vibrational CARS in a scramjet combustor model, featuring a rearward facing step, and a single normal injector. The combustor was connected to the exit nozzle of the NASA Langley Direct Connect Supersonic Combustion Test facility (DCSCTF).This was the first set of CARS measurements in DCSCTF. The facility provided hot "vitiated" air at Mach 2, simulating the air entering a scramjet combustor flying at Mach 5.4. The test could run for only 10 seconds at a time, because of heating of the combustor model. The CARS instrument was operating at 10 Hz and the amount of data acquired was strongly limited by the short run duration. The heat load caused the model to deteriorate during the test.

A new scramjet combustor model, named SCHOLAR, was developed in 1999 and installed in DCSCTF. The new combustor featured a single H_2 injector with a Mach 2.5 nozzle inclined at 30 degrees with respect to the combustor wall. The model could operate for 20 seconds during each run. Springer [12] used N_2 vibrational CARS thermometry at 30 Hz to characterize the flow at the entrance of the SCHOLAR model when simulating flight Mach number equal to 7. The CARS signal-to-noise ratio was too low because of the low power and poor beam quality delivered by the higher repetition rate laser. Data were collected only at a single location on the centerline, 12 cm from the nozzle exit. Cutler performed N_2 CARS thermometry over 5 planes of the SCHOLAR model using a more powerful 10 Hz laser. [70] O'Byrne applied dual-pump CARS (DP-CARS) for simultaneous measurements of temperature, O_2, N_2 and H_2 concentration in the same model. Validation measurements in a flat flame burner showed that H_2 mole fractions were systematically low; therefore H_2 measurements in the combustor were not reported.[6] Accurate CFD modeling of the SCHOLAR experimental data proved to be very challenging. [71] In particular the numerical simulation had problems predicting the distance between the injector and the combustion-induced pressure rise. Calibration of the numerical models based on the experimental data was not possible because the flow was complex and several numerical models were involved in the simulation.

In 2005 an axisymmetric supersonic combusting coaxial jet flowfield was developed. [24] The flowfield consists of a center-jet of vitiated air, and a co-axial jet of N_2 for mixing studies, or H_2 or ethylene for combustion studies. The flow-field

allowed the study of mixing and combustion in a supersonic flow, removing all the complications encountered in SCHOLAR due to the presence of walls, pressure gradients and shock waves. The free-jet offers optical access on all sides downstream of the nozzle exit, simplifying the use of laser diagnostics. The flow field was developed in two sizes: a laboratory-scale supersonic burner, with center jet nozzle exit diameter of 10 mm described in details in Chapter 7, and a larger scale nozzle connected to DCSCTF [72], with center jet nozzle exit diameter of 63.5 mm. The laboratory-scale burner has three interchangeable silicon carbide nozzles, providing center jet exit Mach numbers of 1, 1.6 and 2 to study the effect of compressibility, and can provide center jet enthalpy that simulates flight speeds between 5 and 7. Only one nozzle with exit Mach number 1.6 was tested for the scaled up version.

CARS measurements in the large scale facility allow better resolution of some of the turbulence structures, compared to the laboratory-scale version. On the other hand it is much more costly to operate and requires a test engineer and several technicians, where the laboratory scale burner can be operated by one technician. Typical duration of a run in the DCSCTF was 50 seconds, whereas the small scale burner can operate continuously for hours at a time; therefore a much larger data-set could be acquired in the same time-frame.

The laboratory-scale jet was used in 2007 to test a modified version of O'Byrne's DP-CARS system, employing a modeless dye laser as Stokes beam to improve the instrument temperature precision. Data were collected only at a couple of locations, and have no relevance for CFD validation.[66] Measurements in a Hencken burner flame using this setup showed poor mole fraction accuracy, attributed to low signal-

to-noise ratio and a broadband dye laser that was too spectrally narrow, as well as to inaccuracy in the data processing. No improvements in the temperature precision were observed, and the modeless dye laser was replaced with a conventional dye laser in subsequent work.

An instrument combining interferometric Rayleigh scattering for single-point measurements of two velocity components and DP-CARS for measurements of temperature, N_2, O_2 and H_2 was developed by Bivolaru and Tedder. [66, 73] The instrument was mounted on a mobile cart, placed in the basement directly below DCSCTF, and tested in the scaled-up version of the free jet. The test proved to be very challenging and only limited data were analyzed. CARS temperature results for a mixing case (no co-flow) have been reported in Ref. [72, 74], but only 54% of the spectra that could be analyzed (data yield) mostly because of beam steering effects preventing CARS signal generation. Mole fraction measurements were not reported, because later analysis of experiments in a Hencken burner flame performed at same time showed poor accuracy in species mole fractions. Lack of linear polarization in one of the laser beams was suggested as a possible source of the error in mole fraction measurements, but this explanation could not be verified because the instrument had already been dismantled when the problem was found. [75] CARS measurements were attempted for a combustion case, but the laser failed before the test was completed and the data were never analyzed. The data yield was even lower than in the mixing case, and a significant amount of background light from the flame was overlapped with the CARS signal.

1.5 Development of a Dual-Pump CARS Instrument for Supersonic Combustion Experiments

Preliminary DP-CARS measurements in the laboratory scale burner and the test campaign with the scaled-up free-jet showed several issues with the instrument, which had to be resolved in order to obtain good quality CARS measurements in future supersonic combustion experiments. The research conducted for this dissertation had two main objectives. The first was to develop a DP CARS instrument capable of accurate temperature and mole fraction measurements in the harsh environment of supersonic combustion experiments in ducted or open jet configurations. The other goal of this work was to apply the DP-CARS instrument to generate a database of temperature and mole fraction measurements in the laboratory-scale supersonic combusting jet, for CFD validation.

The physics behind the CARS techniques is described in detail in Chapter 2. Chapter 3 provides a description of the DP-CARS instrument. Improvements to the instrument hardware, to the data acquisition software, and the data processing are discussed in detail.

DP-CARS measurements collected by Tedder [72] in the large scale supersonic free-jet presented low data yield (54.4% for a mixing case in the large supersonic free jet). Low data yield is a critically important problem because missing data can potentially bias averaged temperature measurements, as described in Chapter 6. A small fraction of the data (7.2 %) was rejected because the signal was too strong and it was saturating the camera detectors. A new approach was developed to reduce the number of spectra that saturate the camera (Chapter 3) and to obtain useful data from

saturated spectra (Chapter 5). Most of the data loss (38.2%) was a consequence of beam steering due to turbulence and vibrations. Chapter 4 describes a new technique developed to mitigate the effects of beam steering.

Chapter 5 describes a study of the high irradiance perturbation effect to determine thresholds for the laser irradiances. The study indicates that these perturbation effects were probably responsible for the poor accuracy in the H_2 mole fraction measurements of O'Byrne.[6]

In providing measurements for CFD validation it is important to characterize the instrument in terms of accuracy, precision and spatial resolution. Changes to the theoretical modeling of the CARS spectra, calibration of some molecular parameters, and the removal of high irradiance perturbation effects, allowed for better accuracy than obtained in previous experiments. Precision at low temperature was improved as a result of higher spectral resolution, and changes to the fitting algorithm. Measurements in a flat flame burner are used as benchmark to determine the accuracy and the precision. The instrument characterization study is described in details in Chapter 6.

Chapter 7 provides a detailed description of the laboratory-scale supersonic free jet, and CFD simulations of the flow inside the facility. About 800,000 single-shot CARS spectra have been acquired and analyzed for a variety of conditions in the laboratory-scale supersonic free-jet. Results of the measurements are discussed in Chapter 8. The conclusion summarizes the accomplishments of this work, and includes recommendations for future development of the instrument.

CHAPTER 2 -Coherent Anti-Stokes Raman Spectroscopy

2.1 **Introduction**

Coherent Anti-Stokes Raman Spectroscopy (CARS) is a non-intrusive, instantaneous and spatially resolved, laser-based measurement technique that has been implemented by several researchers to measure temperature and species concentration in scramjet combustors.[60-72] In CARS, three laser beams, conventionally named pump, probe and Stokes, are focused and crossed at their focal point, where a fourth laser-like beam is generated containing the Raman spectrum of the probed species. Laser frequencies are chosen so that the pump-Stokes frequency difference corresponds to the Raman shift associated with a molecular rotational-vibrational transition.

The technique was originally developed in 1965 by Maker [76] and applied in liquid benzene, but it was the work of Taran and the ONERA group [77, 78] in the mid seventies that demonstrated its potential as diagnostic tool in combustion. Since then, CARS has been adopted in a variety of combustors [79] and several variations of the original technique have been develop to extend the capability of the technique to multiple species (dual pump CARS, [80, 81] triple-pump CARS,[82] dual pump dual-broadband,[83, 84] WIDECARS[85]) and to detect minor species (electronic-resonant-enhanced CARS [86]).

This section includes a brief background of the fundamental physics behind molecular spectroscopy that is at the core of the CARS technique. Following is a

derivation of an expression for the CARS signal, largely based on the more detailed calculations found in Chapter 6 of Ref.[87]. The dependence of the CARS signal on the temperature and species concentration of the probed gas is shown. "Multi-color" CARS techniques that expand the capabilities of the original CARS technique to simultaneous measurements of multiple species are described.

2.2 Molecular Energy States and Population Distributions

The fundamentals of molecular spectroscopy are briefly illustrated in this section, to introduce concepts and definitions that will be often used in the rest of this work. The internal energy of a molecule is distributed between electronic, rotational and vibrational energy. Based on the Born-Oppenheimer approximation the three contributions can be decoupled and the total energy can be expressed as:

$$E = E_e + E_r + E_v \tag{2-1}$$

According to quantum mechanics, energy levels are discrete, and can be computed as solutions to the Schrödinger equation. CARS probes transitions between different ro-vibrational levels. Combustion phenomena generally do not alter the electronic state of a molecule, therefore for the application discussed in this dissertation E_e is constant.

Vibrating diatomic molecules (such as N_2, O_2 and H_2 probed by this CARS instrument) can be modeled as anharmonic oscillators. The vibrational energy E_v is obtained as a solution of the Schrödinger equation and can be expressed as:

$$E_v = hc\left[\omega_e\left(v+\frac{1}{2}\right)+\omega_e x_e\left(v+\frac{1}{2}\right)^2+\omega_e y_e\left(v+\frac{1}{2}\right)^3+\omega_e z_e\left(v+\frac{1}{2}\right)^4 .....\right] \tag{2-2}$$

where h is the Planck`s constant, c the speed of light, ω_e the vibrational frequency expressed in wavenumbers (cm^{-1}), $\omega_e x_e$, $\omega_e y_e$, $\omega_e z_e$ are additional vibrational constants that describe that anharmonicity. Values for ω_e, $\omega_e x_e$, $\omega_e y_e$ and $\omega_e z_e$ for several molecules can be found in Ref.[88]. The quantity v is the vibrational quantum number which takes positive integer values.

The rotational energy for diatomic molecule can be obtained as solution of the Schrödinger equation for a rigid rotator:

$$E_r = hc\left[B_v J(J+1) - D_v J^2 (J+1)^2 \right] \tag{2-3}$$

The rotational quantum number J is a positive integer B_v is the rotational constant and D_v is the centrifugal distortion constant. Since the molecule vibrates and rotates at the same time, its moment of inertia is not constant; therefore B_v and D_v are function of the vibrational quantum number v:

$$B_v = B_e - \alpha_e\left(v+\frac{1}{2}\right) + \gamma_e\left(v+\frac{1}{2}\right)^2 + \ldots \tag{2-4}$$

$$D_v = D_e + \beta_e\left(v+\frac{1}{2}\right) + \ldots \tag{2-5}$$

The energy separation between electronic states is ~ 10 times the separation between the different vibrational states and 100 times the separation between different rotational states.

For a gas at equilibrium the population distribution among the different energy states is governed by the Boltzmann distribution function:

$$N_i = N\frac{g_i e^{-\varepsilon_{i/kT}}}{\sum_i g_i e^{-\varepsilon_i/kT}} \tag{2-6}$$

where N_i is the number density of the molecules at the energy state e_i (uniquely determined by the vibrational and rotational quantum numbers); N is the total number density, k is the Boltzmann constant, T the temperature and g_i the degeneracy of the state. The denominator is the sum over all possible energy states, and is called the partition function. The population distribution is very sensitive to temperature; molecular spectroscopy can measure the population distribution, and therefore can determine the temperature. More specifically the population distribution over the vibrational levels within an electronic state is given by:

$$N_v = Ne^{-vhc\omega_e/kT}(1-e^{-hc\omega_e/kT}) \tag{2-7}$$

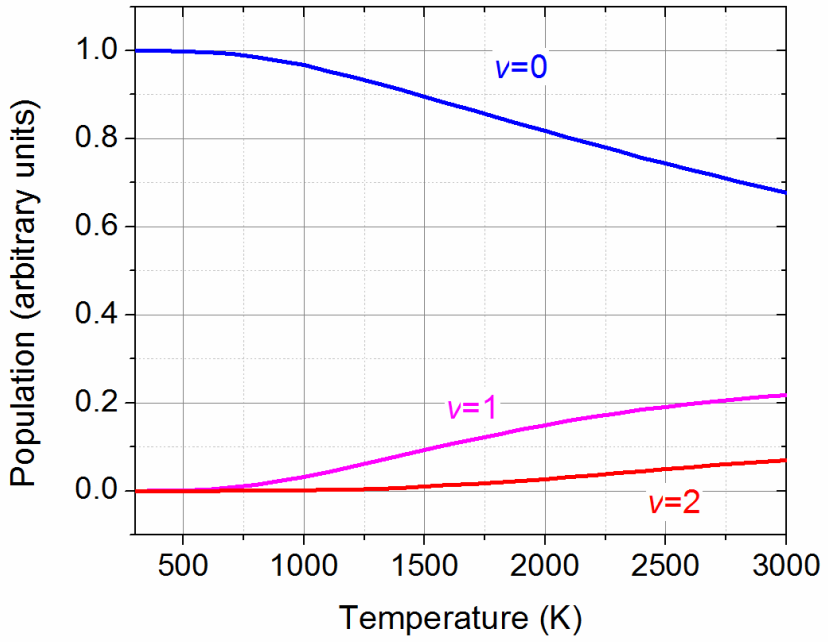

Figure 2-1: Vibrational population for N_2 as function of the temperature

The population distribution between the rotational energy states within a vibrational level is given by:

$$N_J = \frac{N g_J (2J+1) e^{-BJ(J+1)hc/kT}}{\sum_{J=0}^{\infty} (2J+1) e^{-BJ(J+1)hc/kT}} \tag{2-8}$$

Figure 2-1 shows the population distributions for the first three vibrational levels of N_2 as function of temperature. It is evident that even at high temperature, most molecules are at the ground vibrational states. The first vibrational band is populated (> 1%) for temperature above 700 K.

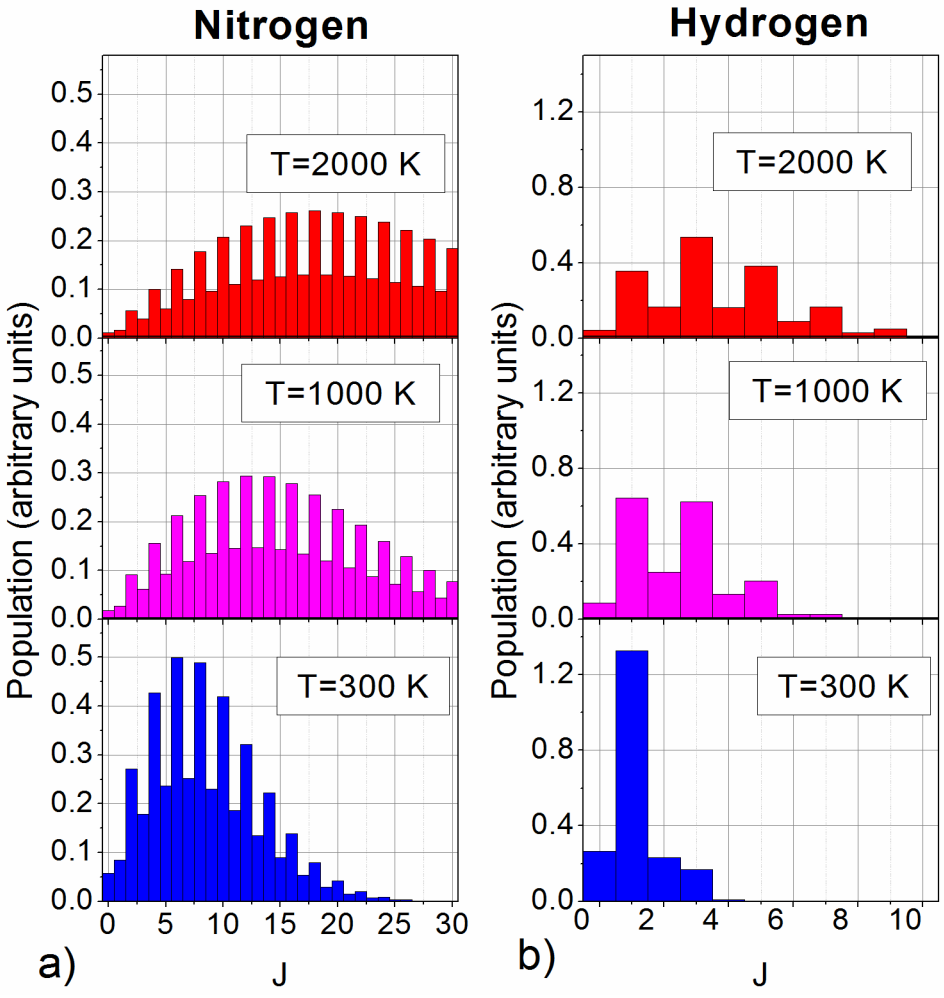

Figure 2-2: a) Rotational population for N_2 and b) H_2 for three values of temperature

Figure 2-2 shows the population distribution of the rotational levels for three values of temperature. It is evident that, especially at low temperatures the rotational population distribution is much more sensitive to temperature. Also notice that the population difference between two consecutive even or odd values of J drops rapidly with the temperature.

Molecular spectroscopy probes Raman transitions between different molecular energy states. Based on quantum mechanics only transitions that satisfy the selection rules are allowed. In particular the CARS system discussed here probes Q-branch and S-branch transition. A Q-branch transition is one for which $\Delta v = 1,2,3\ldots$ and $\Delta J = 0$. The transitions for $\Delta v = 1$ are the strongest. The frequency of the transition can be computed as:

$$\upsilon_Q = \frac{1}{hc}\left(E_v(v') - E_v(v'')\right) + \frac{1}{hc}\left(E_r(v', J) - E_r(v'', J)\right) = \upsilon_v + \alpha_e J(J+1) + \ldots \qquad (2\text{-}9)$$

where v' and v'' are the vibrational quantum numbers of the upper and lower states, and υ_v is the frequency of the transition for J=0, generally called the vibrational bandhead. Since the vibration-rotation interaction coefficient α_e is very small (0.0173 cm^{-1} for N_2), all the ro-vibrational transitions in the Q-branch are closely spaced. Notice in particular that the spacing is proportional to $J(J+1)$, hence the spacing is greater for higher rotational numbers. With the CARS system described here, the Q-branch of N_2 and O_2 are probed. The vibrational bandhead are 2330.7 cm^{-1} for N_2 and 1556 cm^{-1} for O_2. S-branch transitions are purely rotational transitions with Δv=0 and ΔJ=2. The transition frequency for a S-branch transition can be easily

obtained from Eq.(2-3). The CARS system described here probes the S(5), S(6) and S(9) transitions of H_2 , with frequencies at 1447.2, 1637 and 2130.1 cm^{-1}.

2.3 **Molecular Spectroscopy**

A photon, at a frequency that matches an electronic or a ro-vibrational transition frequency, can excite a molecule to a higher energy state. In the process the light is absorbed and the energy transferred to the molecule. This one photon process underlies absorption spectroscopy. Infra-red light is typically required to probe ro-vibrational transitions using absorption.

If the frequency of the incident light does not match any transitions, interaction is still possible in the form of elastic (Rayleigh) and inelastic (Raman) scattering. The incident photon drives the molecule to a virtual state that is not an allowable energy level (not a solution of the Schrödinger equation). The molecule cannot exist in this state, so it relaxes and either returns to its original state (Rayleigh scattering), or to a different, allowed energy state (Raman scattering). In both cases a photon is emitted, but in Rayleigh scattering no energy has been absorbed and the photon is at the same frequency of the incident light; in Raman scattering, the molecule has absorbed (or emitted) energy, therefore the frequency of the emitted photon is (Raman) shifted by the change in energy of the molecule (in frequency units).

Figure 2-3 shows the energy diagram for CARS. It is a four photon, non-linear optical process that is more complex than the linear, two-photon Raman process. The energy of the molecule is increased by the pump laser beam, at frequency ω_1 and decreased by the Stokes laser beam at frequency $\omega_3 < \omega_1$. The probe beam at

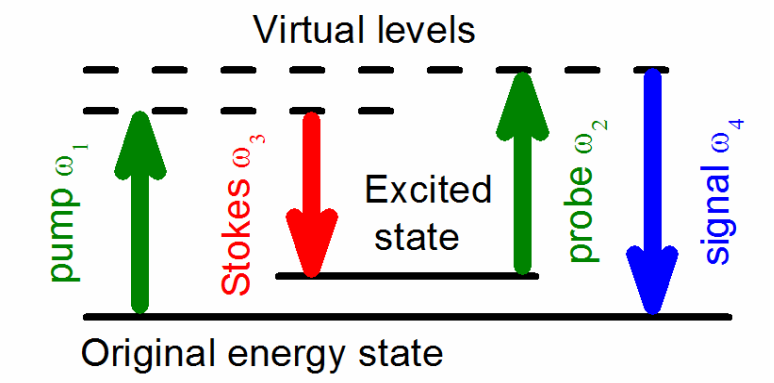

Figure 2-3: CARS energy level diagram

frequency ω_2 scatters the light from the molecule generating a laser-like CARS signal blue-shifted at frequency $\omega_4 = \omega_1 - \omega_3 + \omega_2$. When the pump-Stokes frequency difference (ω_1-ω_3) matches the energy of a vibrational-rotational transition, the combined effect of the two lasers is to induce a Raman coherence between the ground state and this excited state. Under this condition, the CARS signal is resonantly enhanced and the emitted signal contains information on the temperature and mole fraction of the species probed. Note that no energy is absorbed by the molecule in the process.

2.4 **Derivation of CARS Signal**

The CARS signal derivation presented here is based on more detailed calculations found in Chapter 6 of Ref.[87]. Interaction between light and any media is described by the Maxwell`s equation, which for gases with no free charge density, nor distributions of current simplifies to the wave equation:

$$\nabla^2 \vec{E} - \frac{1}{c^2}\frac{\partial^2 \vec{E}}{\partial t^2} = \mu_o \frac{\partial^2 \vec{P}}{\partial t^2} \qquad (2\text{-}10)$$

where $\vec{E}$ is the electric field , c the speed of light, μ_0 the permeability of the free space. $\vec{P}$, which appears as a source term in the wave equation, is the generalized induced polarization. E and P can be expanded in Fourier series, and the induced polarization can be expressed as power series of ω_i:

$$P_i(\omega_i) = \varepsilon_0 \chi^{(1)}(\pm\omega_i)E(\pm\omega_j) + \sum_{j,k} \varepsilon_0 \chi^{(2)}(\pm\omega_i, \pm\omega_j, \pm\omega_k)E(\pm\omega_j)E(\pm\omega_k) + \sum_{j,k,l} \varepsilon_0 \chi^{(3)}(\pm\omega_i, \pm\omega_j, \pm\omega_k, \pm\omega_l)E(\pm\omega_j)E(\pm\omega_k)E(\pm\omega_l) + ... \quad (2\text{-}11)$$

where ε_0 is the permittivity of the free space and $\chi^{(n)}$ the nth order susceptibility. The frequency of the induced polarization is determined by conservation of energy according to the relation:

$$\pm\omega_i \pm \omega_j \pm \omega_k \pm \omega_l = 0 \quad (2\text{-}12)$$

The first order term of the power series is what generates Rayleigh scattering and spontaneous Raman scattering, two linear techniques mentioned in the previous section. For isotropic media, such as gases, the second order susceptibility is zero because of inversion symmetry. The lowest order non-linear interaction that can occur in gases is therefore third order. Eq. (2-12) shows that there are several wave mixing combinations possible. Based on the energy diagram the third order polarization term, responsible for the CARS signal is

$$P_i^{(3)}(\omega_4, \vec{r}) = \varepsilon_0 \chi_{ijkl}^{(3)}(-\omega_4, \omega_1, \omega_2, -\omega_3)E_j(\omega_1)E_k(\omega_2)E_l(\omega_3) \quad (2\text{-}13)$$

The third order susceptibility is a third order tensor, but for a gas only 21 terms are not null, and only three are independent. If all three beams have the same polarization (as in the present work), Eq.(2-13) reduces to:

$$P^{(3)}(\omega_4,\vec{r}) = 3\varepsilon_0\chi_{xxxx}(-\omega_4,\omega_1,\omega_2,-\omega_3)E(\omega_1,\vec{r})E(\omega_2,\vec{r})E(\omega_3,\vec{r})$$
$$= \varepsilon_0\chi_{CARS}E(\omega_1,\vec{r})E(\omega_2,\vec{r})E(\omega_3,\vec{r}) \quad (2\text{-}14)$$

Substituting Eq.(2-14) into the wave equation, assuming a refraction index of 1, solving for the electric field of the CARS signal, and integrating over the length of the probe volume *l*, the time averaged irradiance of the CARS signal can be expressed as:

$$I_{CARS} = \frac{\omega_3^2}{c^4\varepsilon_0^2} I_1 I_2 I_3 \left|\chi_{CARS}^2\right| l^2 \left(\frac{\sin\frac{\Delta k l}{2}}{\frac{\Delta k l}{2}} \right)^2 \quad (2\text{-}15)$$

where I_1, I_2 and I_3 are the irradiances of the three laser beams, and Δk is the phase mismatch defined as:

$$\Delta k = \overrightarrow{k_4} - \overrightarrow{k_1} + \overrightarrow{k_3} - \overrightarrow{k_2} \quad (2\text{-}16)$$

where $\vec{k}$ are the wave vectors defined as:

$$\vec{k} = \frac{\omega}{c}\vec{r} \quad (2\text{-}17)$$

Eq. (2-15) shows that the CARS signal is proportional to the product of the irradiances of the three laser beams. High irradiance effects such as optical breakdown, Stark broadening, and stimulated Raman pumping limit the laser irradiances and the CARS signal. These phenomena will be discussed in details in Chapter 5.

The CARS signal also depends on the phase mismatch and the interaction length *l*, parameters related to the geometric arrangement of the laser beams. The CARS irradiance is maximized if the phase mismatch is zero.

$$\Delta k = 0 \Leftrightarrow \overrightarrow{k_4} = \overrightarrow{k_1} + \overrightarrow{k_2} - \overrightarrow{k_3} \quad (2\text{-}18)$$

Eq.(2-18) is known as the "phase matching" condition and is a statement of conservation of momentum. Physically this condition means that the CARS signal generated at any location is in phase with the signal generated anywhere else. There are several geometries that satisfy the phase matching condition; the most common are collinear, USED, planar and folded BOXCARS. The criteria for the selection of the phase matching geometry are discussed in Chapter 4.

Derivation of the CARS susceptibility χ_{CARS} from quantum mechanics is reported in detail in books [87] and review papers, [79] and it will not be repeated here. The CARS susceptibility is generally expressed as sum of a resonant and a non-resonant susceptibility. The resonant portion contains all those contributions for which combination of the frequencies coincide with a Raman resonance; all the other terms are lumped in the non-resonant contribution.

$$\chi_{CARS} = \sum_j \frac{K_j \Gamma_j}{2\Delta\omega_j - i\Gamma_j} + \chi_{NR} \tag{2-19}$$

where the summation is over all the Raman resonance transitions at frequencies ω_j. $\Delta\omega_j$ is the detuning defined as $\Delta\omega_j = \omega_j - \omega_1 + \omega_3$, Γ_j is the linewidth. K_j is defined as:

$$K_j = \frac{(4\pi)^2 \varepsilon_0 c^4 N \Delta_j}{\hbar \omega_2^4 \Gamma_j} \left(\frac{\partial\sigma}{\partial\Omega}\right)_j \tag{2-20}$$

where N is the number of molecules, Δ_j is the fractional population difference between the 2 energy levels involved in the wave mixing process, $\hbar$ is the Planck`s constant divided by 2π, $\frac{\partial\sigma}{\partial\Omega}$ the differential Raman cross section. This term (K_j) is where the potential of CARS as a diagnostic tool is. In fact the CARS susceptibility is

proportional to the number of molecules *N* and it depends on the temperature through the fractional population difference, as shown in Eq.(2-6).

The modulus of the CARS susceptibility appears squared in Eq. (2-15). For this reason CARS spectra are more complex than spontaneous Raman spectra, since constructive and destructive interference occurs. Additionally in typical diagnostics application the Stokes beam is spectrally broad and several Raman resonances are excited at once. Neighboring transitions can interfere further changing the spectral shape. Generally CARS spectra cannot be obtained analytically, but numerical routines are required to simulate the spectral shape and intensity.

2.5 **Lineshape Models**

Transitions between energy levels are not infinitely sharp but have a finite width (linewidth), generally indicated with the symbol Γ. Knowledge of this quantity is very important, since it appears in the expression of the CARS susceptibility (Eq.(2-19)). Based on the Heisenberg uncertainty principle, the energy of a molecule cannot be precisely known, causing a spread of the emission (or absorption) frequency that is the natural linewidth. The resulting line-shape is a Lorentzian. The natural linewidth can be expressed as:

$$\Gamma = \frac{1}{2\pi}\left(\frac{1}{\tau_1}+\frac{1}{\tau_2}\right) \tag{2-21}$$

where τ_1 and τ_2 are the lifetimes of the 2 states involved in the transition. In a gas other broadening mechanisms occur, changing the linewidth of the transition.

In a gas the lifetime of an energy level can be shortened if collisions between molecules occur, increasing the linewidth of the transition. This effect is known as pressure (or collisional) broadening. The lineshape is still a Lorentzian, but the linewidth is proportional to the pressure, and approximately proportional to the inverse of the square root of the temperature, depending on the cross section of the molecules colliding.

Radiation emitted by a molecule with a non-null velocity in the direction of propagation of the light will be shifted in frequency. This effect is the Doppler shift and is the principle behind several velocimetry techniques. In a gas, in addition to a macroscopic flow velocity, there is always a random motion of each molecule. The motion is function of temperature and the velocity distribution is given by the Maxwell-Boltzmann expression. As result of the velocity distribution the lineshape is a Gaussian, with a linewidth that is function of the temperature alone.

At low pressures and high temperatures, Doppler broadening is the dominant term, where at low temperatures, pressure broadening is dominant. In most practical applications both collision broadening and Doppler broadening are significant, and the resulting lineshape is a Voigt function. This is the lineshape model used for computing the theoretical N_2 and O_2 CARS spectra reported in this work.

Collisional (motional or Dicke) narrowing [89] is a mechanism that alters the linewidth of Doppler broadened lines. From the uncertainty principle the velocity obtained from the Doppler shift is averaged over a displacement of $\sim \lambda/2\pi$, where λ is the wavelength of the incident light. If there are many velocity-changing collisions in the time necessary to travel $\lambda/2\pi$ then the average velocity is reduced, and so is the

Doppler frequency shift. The effect is a reduction of the Doppler broadening, and a lineshape that differs from the Voigt. Two analytical models are available to model this process, the hard collision [90, 91] and the Galatry (soft) collision model. [92, 93] The first assumes that the velocity after the collision is completely uncorrelated to the velocity before the collision. In the Galatry model the change in velocity after each individual collision is negligible, and the velocities before and after a collision are strongly correlated. The hard collision model is more appropriate when the molecule that is interacting with the radiation is considerably less massive than the collider. In practice the numerical values of the two models are almost the same. The Galatry model requires the knowledge of an additional quantity, the motional narrowing parameter β, which is related to the optical diffusion coefficient D_o via the relation:

$$\beta = \frac{kT}{mD_o} \tag{2-22}$$

where k is the Boltzmann constant, m the molecular mass, and T the temperature. Units of β are cm^{-1}/atm. Physically it represents the effective frequency of velocity-changing collisions. Several studies show that the optical diffusion coefficient D_o differs from the conventional mass diffusion coefficient D_m, although they have the same order of magnitude.[90, 94, 95]

The motional narrowing is significant for transitions with large rotational spacing in which the Doppler broadening is dominant, and should not be neglected for H_2.[96] The Galatry model has been used to compute the H_2 rotational lines in the theoretical spectra, and a calibration of the optical diffusion coefficient is discussed in Chapter 6.

Eq.(2-9) shows that in Q-branch spectra the spacing between adjacent ro-vibrational line is proportional to $J(J+1)$. Since the rotation-vibration interaction

coefficient α_e is small, the ro-vibrational lines are overlapped for low values of *J*. For such conditions, computation of the lineshape as an isolated line undergoing pressure broadening is no longer adequate. Collisional narrowing, "which causes a coalescence or collapse of adjacent transitions toward a frequency center of gravity determined by the most populous rotational state" [97] becomes significant. This phenomenon is relevant at low temperature, where only the lower rotational states are populated. For higher values of *J*, the line splitting, proportional to *J(J+1)*, increases and collisional narrowing is no longer significant. In Chapter 6 the effect of the lineshape models on the measurement accuracy is discussed.

2.6 **Multi-Color CARS**

In early CARS experiments a narrowband tunable dye laser acted as Stokes beam, exciting a specific molecular transition. Spectra were constructed piecewise, by scanning the frequency of the laser. This approach offers the best spectral resolution, limited only by the linewidth of the laser, but it is not appropriate for turbulent combustion, where instantaneous single-shot measurements are desirable. In broadband CARS the Stokes beam is a broadband dye laser, so that an entire ro-vibrational band can be excited simultaneously.[98] Broadband CARS probing of the N_2 Q-branch is the most common approach to CARS thermometry, because N_2 is generally present in combustion environments while also having a spectrum from which temperature can be measured sensitively. Broadband CARS requires a spectrometer to disperse the CARS signal. The spectral resolution of a broadband CARS signal is often determined by the spectrometer, rather than by the laser

linewidth. Therefore broadband CARS spectra are less resolved than scanning CARS spectra. In a broadband dye laser several spectral modes are excited and are competing, causing shot-to-shot intensity fluctuations, known as mode noise. Loss of spectral resolution and mode competition within the broadband laser make the broadband vibrational CARS less precise than scanning CARS, but the advantage of the instantaneous measurements outweigh the loss of precision when studying turbulent flames.

Figure 2-1 and 2-2 show that the population distribution between vibrational levels is much less sensitive to temperature than between rotational levels. In addition the frequencies of the different ro-vibrational transitions within the Q-branch are closely spaced, especially for the lower J's. The spectrometer, needed to disperse the CARS signal, limits the spectral resolution and the ro-vibrational transitions are often overlapped for the lower values of J. In particular at lower temperatures, only the lower J's in the ground vibrational state are populated. This reduces the sensitivity of N_2 Q-branch broadband CARS at lower temperature, and therefore its accuracy and precision. Because of this limitation, for low temperature applications it is often preferred to probe the pure rotational transitions (rotational CARS) since they are more widely spaced than the rotational-vibrational transitions used in the current work. An approach often used for pure rotational CARS is the dual-Stokes CARS in which the pump and the Stokes are provided by the same broadband laser. Rotational CARS provides better precision and accuracy at low and moderate temperature. At higher temperature, the signal-to-noise ratio decreases rapidly, because the population differences are smaller as observed in Figure 2-2; for this reason vibrational CARS is

a better choice for measurements in high temperature flames flames, such as in the current work where temperatures up to ~2400 K are expected from H_2-air combustion.

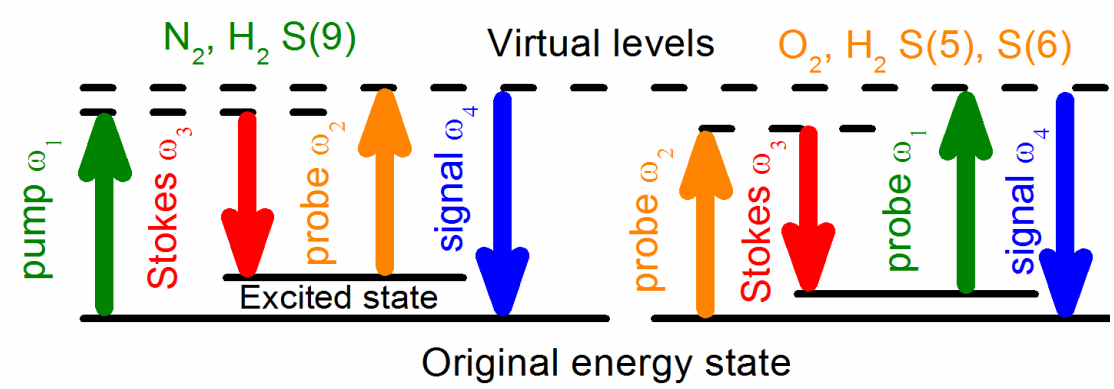

Figure 2-4: Dual-pump CARS energy level diagram

Since the rotational spectra of most species are close to each other, rotational CARS offers the potential for multiple species detection with the same detection system. In reality, the spectra from different species are overlapped and interfere with each other. Ultimately the major species dominate the spectra. Several CARS techniques other than rotational CARS have been developed to allow simultaneous detection of multiple species. One of the most popular is dual-pump CARS,[81] which is the technique used in this work. In DP-CARS the pump and probe laser beams have different wavelengths, and their role interchanges so that two different regions of the Raman shift are probed simultaneously. Figure 2-4 shows the energy level diagrams for DP-CARS. Opportune choice of the frequency difference between the pump and probe beams allows avoiding spectral overlap, while keeping the 2 regions close enough so that a single spectrometer and camera can be used. DP-

CARS has been used for simultaneous measurements of N_2-O_2,[81] N_2-CO_2,[99] N_2-CH_4, [100] N_2-H_2. [101] Recently Tedder [85] has demonstrated a variation of DP-CARS called WIDECARS in which a very broad Stokes beam is used to simultaneously probe the vibrational band of N_2, O_2, CO, C_2H_4 and CO_2 and two rotational H_2 lines (S(3) and (S4).

The version of DP-CARS used in this work was originally proposed by O'Byrne,[6] and allows simultaneous measurements of N_2, O_2 and three pure rotational H_2 lines S(5), S(6) and S(9) . If two or more species are resonant, CARS can measure the ratio of the mole fractions of the resonant species. Measurements of absolute mole fractions require knowledge of the CARS non-resonant susceptibility, which varies with composition. If all but one of the major species is resonant, and all non-resonant third-order susceptibilities are known, the composition can be fully determined. A dual-pump CARS instrument probing N_2, O_2, and H_2 allows absolute mole fractions to be determined in a H_2-air flame since the only other major species present is water (radicals, such the hydroxyl radical, OH, which can be present at a level of only a few tenth of a percent are neglected).

All the CARS systems mentioned above use pulses that are nanoseconds long and have repetition rates of tens of Hz. These ns pulses are short enough to freeze the flow but the repetition rate is too slow to resolve time fluctuations in the flow; instead, each spectrum is uncorrelated with prior or subsequent measurements. In recent years there has been a growing interest toward the use of femtosecond lasers for CARS diagnostics that allow repetition rates of kHz or more. CARS system based on pico-second lasers are also being developed. They offer the advantage of

suppressing the non-resonant background (particularly important in hydrocarbon flames) [102] and the possibility of using fiber optics to deliver the lasers. [103] These systems are still in development and have not been demonstrated in large scale facilities. Ref. [79] provides a much more detailed review of the CARS technique. For the case of supersonic combustion, a repetition rate on the order of many 100's of kHz would be required to time-resolve flow structures. Even the highest performance fs CARS systems in development today are 1-2 orders of magnitude too slow to meet this requirement. Still, acquiring non-time-resolved data at a higher rate (eg. 5 kHz vs 20 Hz) is an attractive feature for future CARS systems.

CHAPTER 3 -The Dual-Pump CARS Instrument

A dual-pump (DP) CARS system has been developed for this work. The instrument is based on the DP-CARS system of Ref.[72], but most components have been upgraded and several new features added. The instrument is designed to acquire data in supersonic combustion experiments for CFD validation. Mobility of the instrument was a requirement so that it could be transported to different test facilities. The instrument has a modular structure. The three lasers needed for the CARS process are located on a mobile laser cart. Mirrors relay the beams from the cart to the combining optics, which focus and cross the beams at the measurement volume. The receiving optics separate the CARS signal from the other beams, and direct it to a spectrometer. The combining and receiving optics are mounted on two aluminum plates for easy transportation.

Databases for CFD validation require a large number of measurements to acquire statistical variances and correlations. The data acquisition system has been heavily automated, to improve the data acquisition rate, especially in facilities that can operate continuously. Addittionally, there was a significant effort in reducing the time needed to analyze the CARS data.

3.1 Experimental Set-Up

3.1.1 The Laser Cart

Figure 3-1 shows a picture of the laser cart with all the lasers running. The laser cart consists of a lower and upper level, each housing an optical table. The lower level contains the Nd:YAG laser, optics to separate the visible 532 nm beam from the 1064 nm beam, and the dye circulators for the two dye lasers. The upper level contains the two dye lasers and several additional optis. The core of the instrument is an injection seeded Nd:YAG (Quanta-Ray Pro-350) laser operated at 20 Hz. It replaced the Quanta-Ray Pro-290 used in Ref.[72]. This laser provides one of the

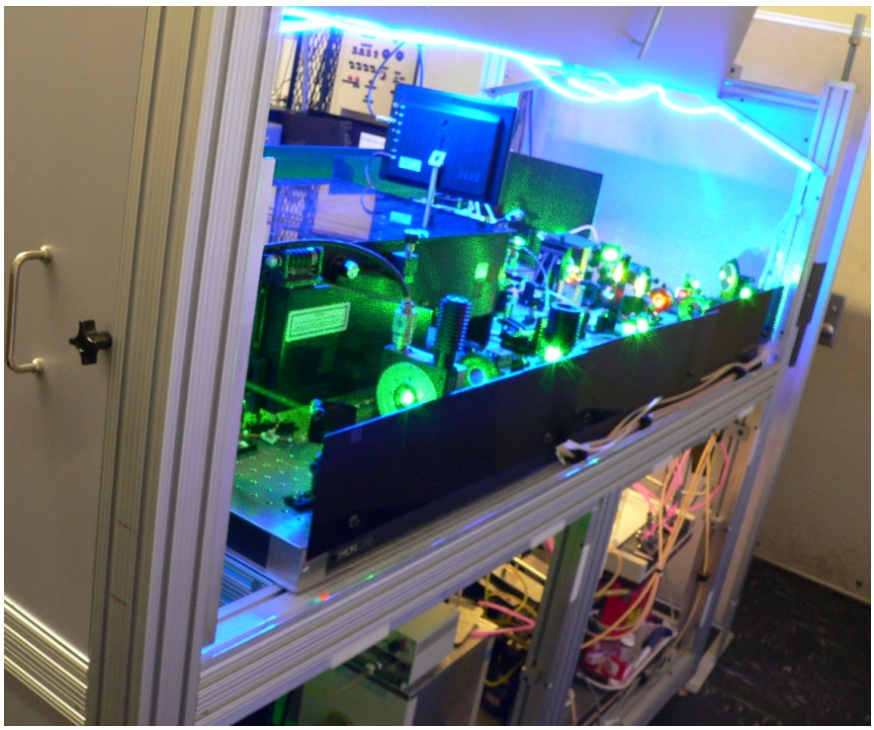

Figure 3-1: Picture of the laser cart

three laser beams generating the CARS signal, and acts as the energy source (pump) for the narrowband and the broadband dye lasers. The output of the Nd:YAG laser, at 1064 nm, is frequency-doubled to 532 nm. At the output of the doubling crystal the visible 532 nm beam is overlapped with unconverted 1064 nm light. Dichroic mirrors, that reflect the visible light and transmit the infrared (IR), separate the two wavelengths. The IR light transmitted through the first dichroic mirror passes through another doubling crystal generating a secondary 532 nm laser beam. The remaining IR light is separated from the visible and carefully blocked. Pellin-Broca prisms in the path of the primary 532 nm beam separate it from incoherent broadband blue light coming from the laser flashlamps. The two 532 nm beams have a pulse width of ~10 ns and a linewidth < 0.003 cm^{-1}. Mirrors relay the 532 nm laser beams from the lower to the upper level of the cart. The primary 532 nm beam, approximately 900 mJ per pulse, is divided three ways: 170 mJ to pump the amplifier of the broadband dye laser, 415 mJ for the narrowband dye laser, and 280 mJ for the green CARS pump beam. The secondary 532 nm beam, approximately 80 mJ per pulse, pumps the oscillator of the broadband dye laser.

Figure 3-2 is a schematic of the laser cart upper level. The drawing is not to scale, but provides a qualitative overview of the optical set-up. The narrowband dye laser chosen for this instrument is a Quanta Ray PDL 3. It is a more compact laser, easier to align and more efficient than the one used previously.[72] An adjustable grating in the oscillator cavity allows selecting the output wavelength of the laser beam. The estimated linewidth is ~0.5 cm^{-1}, based on fitting of experimental N_2 CARS spectra. An etalon can be added to the oscillator cavity to narrow the

linewidth, but was not used for this work. Typical energy of the output beam is 75 mJ. Wavelength selection is accomplished by changing the angle of the grating making up one end of the oscillation cavity, and the peak wavelength is set to 551 nm. A solution of Rhodamine 575 in methanol is the lasing medium in the oscillator and the amplifier. The dye concentrations for the oscillator (~ 80 mg of dye in 700 ml of methanol) and amplifier (~ 33 mg of dye in 700 ml of methanol) are optimized separately to maximize the power output of the laser at the desired wavelength.

The same home-made conventional broadband dye laser used in Ref.[72] is employed in this instrument. The laser peak is centered at 604 nm and has a FWHM of ~10 nm and output energies of 40 mJ per pulse. The peak frequency and the spectral width are determined by the choice of the dye, of the solvent and by the dye concentration in the oscillator. Adding dye increase the peak wavelength, adding methanol decreases it. The spectral width of the laser can be increased by using a

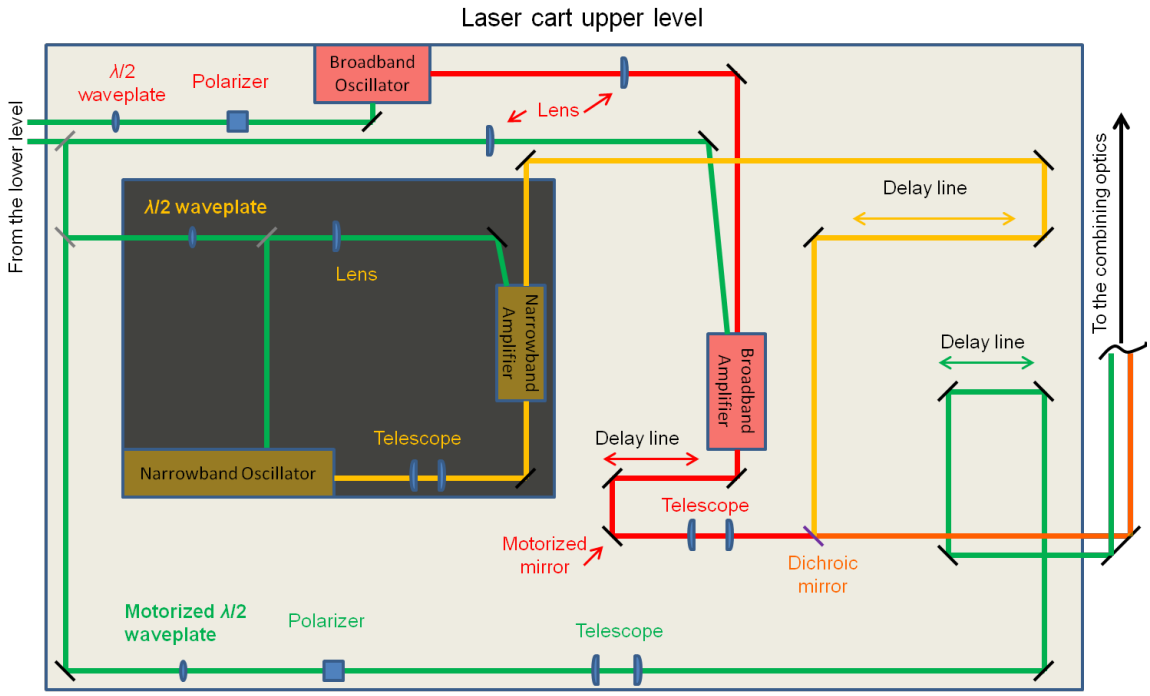

Figure 3-2: Schematic of the optical set-up on the upper level of the laser cart

mixture of two dyes. For the oscillator, a mixture of 8.4 mg of Rhodamine 610 and 1 mg of Rhodamine 640 in 500 ml of methanol was used. This solution provided a peak wavelength of 604 nm, a FWHM of ~ 10 nm, and 4.7% conversion efficiency, for an input power of 1.1 W. The concentration of dye in the amplifier is set to maximize the power output of the laser. A solution of 8.3 mg of Rhodamine 640 in methanol was used for the amplifier with a conversion efficiency of ~ 20%.

Delay lines are included on the path of each laser beam. They are used to match the total path-length of all the lasers, so that the beams arrive simultaneously at the measurement volume. Telescopes are present on the path of each beam to collimate the beam while avoiding local focusing or hot spots in the beam irradiance distribution. An adjustable telescope inside the narrowband dye laser expands the output of the oscillator cavity to match the amplifier. A lens was placed in the path of the Nd:YAG beam pumping the narrowband amplifier to slightly focus it, so that it would match better the size of the expanded oscillator output, thereby improving the laser efficiency. The telescope of the broadband dye laser was used to expand the beam size and set the beam divergence so that it would focus at the same location as the narrowband.

A combination of a half-wave plate and a polarizer is installed on the path of each beam. The half-wave plates are mounted on a rotation stage. By rotating the wave plate, it is possible to carefully control the beam energy without affecting its pointing and its focusing. The half-wave plate installed on the path of the Nd:YAG beam is on a motorized rotation mount that can be remotely controlled.

A planar BOXCARS phase-matching geometry, with the narrowband and the broadband dye lasers collinearly overlapped, and a crossing angle between the dye laser beams and the Nd:YAG beam of 4.5 degrees, was chosen for this set-up. This configuration mitigates the beam steering effects (Chapter 4) while maintaining a good spatial resolution. The narrowband and broadband dye lasers are overlapped using a dichroic mirror which lets the broadband beam through but reflects the narrowband.

3.1.2 Combining and Collecting Optics

The beams are relayed to the combining optics plate through four 3" diameter mirrors. Typical aser energies at the measurement volume are approximately 90, 30

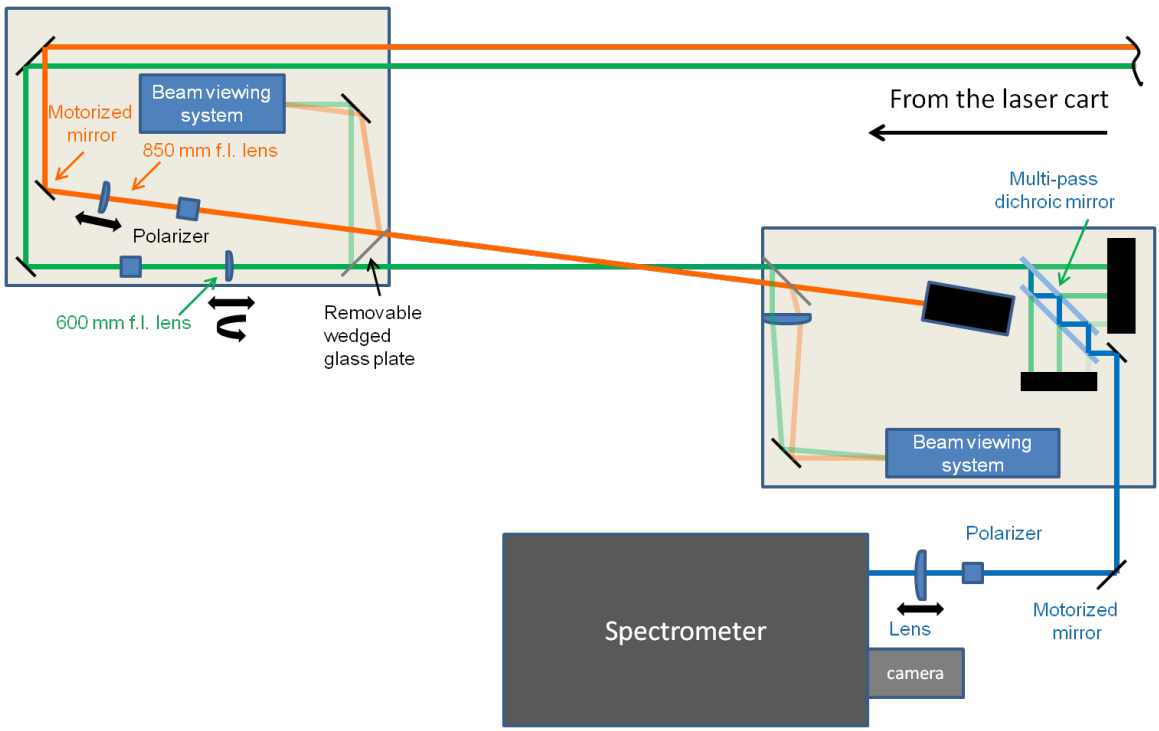

Figure 3-3: Schematic of the combining and collecting optics

and 20 mJ for the Nd:YAG, the narrowband and the broadband dye laser, respectively. Figure 3-3 shows the optical set-up used for the combining and receiving optics. The Nd:YAG beam coming from the laser cart is collected by a mirror, and sent through a polarizer and a 600 mm focal length spherical lens. The lens is mounted on a translation stage so that the location of the focal plane can be varied. The lens is rotated to add astigmatism and to generate an elliptical-shaped beam at the focal plane. This feature is used in the beam shaping technique to mitigate beam steering described in Chapter 4.The overlapped dye laser beams are collected by a mirror and sent through a polarizer and an 850 mm focal length spherical lens mounted on a translation stage. The polarizers ensure that the beams interacting at the measurement volume have the same linear polarization.

Commonly CARS systems use a single large lens to focus all three beams. The use of two separate lenses has several advantages. First of all it allows the crossing angle to be more easily set. The crossing angle, together with the focal spot size determines the spatial resolution. In order to obtain the same crossing angle, if a single 600 mm focal length lens were used, the beam separation would have been 2", therefore requiring a 3" or greater lens. The separation would be bigger for longer focal length. Three inches lenses are expensive and larger sizes are generally custom made. In addition, when using two lenses, the beams are centered on the lens, reducing spherical aberrations, which are worse near the edges of a lens. Another advantage is the possibility of using lenses of different focal lengths for the two beams, so that the beam sizes at the focal plane would be better matched, maximizing

the CARS signal. In our specific set-up it also offered the possibility of shaping one of the beams to an ellipse, while keeping the other beams circular.

Several factors need to be considered in choosing the focal length of the two lenses. Geometrical constraints, such as the width of the combustor model and of the region where the measurements are performed set a minimum focal length (since the lenses must not strike the model). High irradiance perturbation effects (Chapter 5) and the damage threshold of windows, if present, also limit the minimum focal length. Increasing the focal length excessively reduces the spatial resolution and decreases the signal. The focal length values selected are a compromise between these constraints.

Two beam viewing systems[104] are used to image a cross section of the three beams in the vicinity of the measurement volume. The first beam viewing system is placed before the measurement volume and consists of wedged glass plate (front surface is uncoated, back surface has an anti-reflection coating) placed in the path of the beams at 45 degrees which creates a secondary (low irradiance) beam crossing. A microscope objective lens, filters, and a CCD camera are used to detect an image of the crossing. This beam viewing system is used to accurately focus and cross the beams so that the CARS signal is maximized. The wedged glass plate is removed during data acquisition to maintain the crossing location. The second beam viewing system is placed after the measurement volume, and also contains a splitter, but differs from the first by an achromatic spherical lens that refocuses the three beams to form another secondary beam crossing that is imaged by another microscope objective and CCD camera. The system is used to monitor the position and the

focusing of the beams during a test, and to evaluate the effect of beam steering and temperature changes of the optics.

At the measurement volume the three beams interact and generate a coherent laser-like beam containing a broad CARS spectrum centered at 490 nm. As shown in the figure, the collecting optics separate the CARS signal from the overlapped 532 nm beam and direct it to the spectrometer. A multi-pass dichroic mirror separates the CARS signal from the overlapped 532 nm beam and two additional low pass filters remove the residual green light. The signal is then focused by a spherical lens on the input slit of a one-meter McPherson spectrometer equipped with a 2400 lines/mm grating. The CARS signal is dispersed by the spectrometer and recorded by a back illuminated CCD camera (Princeton Instruments PIXIS 100B). The camera detector has a 26.8 x 2.0 mm imaging area with 1340 x 100 imaging pixels. Each pixel is 20 x 20 μm and the dynamic range is 16 bits. The device is thermoelectrically cooled to −80°C providing a dark charge of 0.0014 e^-/pixel/s. The read noise is 12.61 e^- (rms), the gain is 1.05 (e^-/ADU), and the non-linearity is below 1%. Spectral rates, with a 2 MHz digitalization are up to 387 Hz, measured with all rows vertically binned.

3.1.3 Wavelength Selection

The selection of the wavelength of the dye lasers determines what species the instrument probes. The wavelengths reported here are selected for simultaneous detection of the Q-branch of N_2 and O_2, and of three H_2 rotational lines. The red curve in Figure 3-4 shows a theoretical dual-pump CARS spectrum containing all the transitions probed by this instrument. This DP-CARS instrument probes two regions

of the Raman shift; the first region is between 2050 cm^{-1} and 2350 cm^{-1} and contains the N_2 Q-branch and the H_2 S(9); the second is approximately between 1420 cm^{-1} and 1720 cm^{-1} and includes the O_2 Q-branch, and the S(5) and S(6) rotational transitions for H_2. One of the advantages of DP-CARS is that the two probed regions appear close to each other in the CARS spectra. Conventionally the horizontal axis in plots of DP-CARS spectra corresponds to the Raman shift for the CARS process in which the 532 nm laser is the pump laser (ω_1 in Figure (2-3)). Along this axis the Raman shift for the CARS process for which the narrow band dye laser is the pump laser is shifted by the frequency difference between the 532 nm and the narrowband dye laser. The wavelength of the narrowband dye laser can be tuned to minimize the spectral overlap between the species probed by the two Raman processes.

The CARS signal at any particular Raman shift frequency is proportional to the spectral irradiance of the broadband (Stokes) dye laser corresponding to that

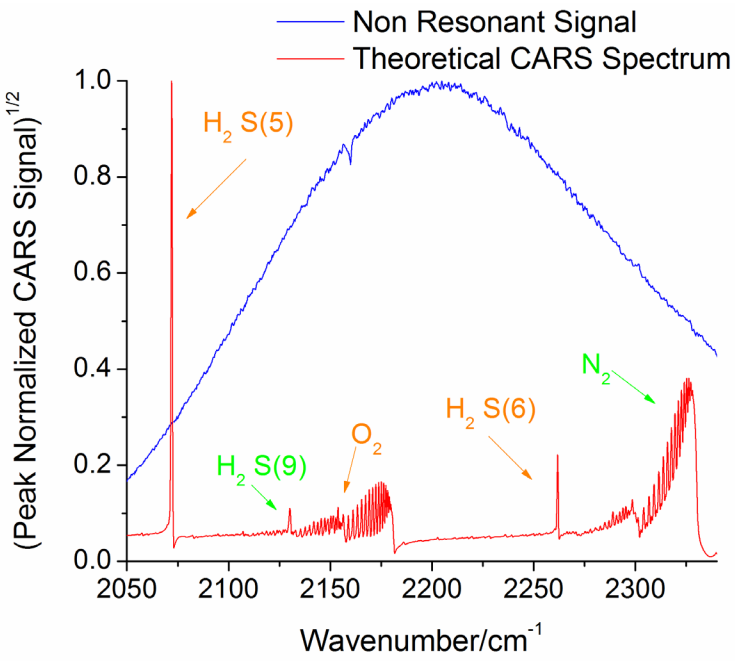

Figure 3-4: Theoretical dual-pump CARS spectrum (red) and experimental non-resonant signal spectrum (blue) collected in Argon

frequency. The blue curve in Figure 3-4 is an average CARS spectrum taken in argon. Argon has no resonances and signal is generated only by the constant CARS non-resonant susceptibility, so the spectrum of the non-resonant CARS signal is determined by the spectrum of the broadband dye laser. In the current work it is roughly Gaussian. The CARS susceptibility spectrum is recovered by dividing the CARS signal spectrum by the spectrum of the non-resonant gas. The wavelength of the broadband dye laser is chosen so the argon peak is between the O_2 bandhead and the H_2 S(6) lines. For typical test conditions in combustion environments, O_2 CARS signal is lower than N_2 because of the lower mole fraction, and the H_2 S(6) is weaker than S(5); centering the broadband between the O_2 and the H_2 (S6) increases the signal-to-noise ratio for these weaker spectral lines and helps avoiding exceeding the detector dynamic range for the stronger lines.

3.1.4 Laser Alignment

Working with pulsed dye lasers (class 4) requires safety eyewear to avoid permanent eye damage in case of accidental exposure to laser light. Protective eyewear that blocks all the wavelengths in the DP-CARS system (ranging from 532 to 620 nm and 1064 nm) is available, but also blocks most of the visible light. Blue led lights have been mounted on the cart to improve the visibility when wearing the protective eyewear. Fluorescent cards and cameras are used to visualize the beams.

Alignment of a DP CARS system can be a complex and time consuming task, especially when the beams have to travel several meters to reach the measurement volume. A procedure has been developed that simplifies this task and greatly

improves safety. The initial alignment of all the mirrors used in the optical set-up is performed using two low power green laser pointers, simulating the Nd:YAG and the narrowband dye laser, and a low power HeNe laser at 632 nm, replacing the broadband dye laser. Operation of these lasers does not require the use of protective eyewear. Mirrors, mounted on flip mounts, are used to insert the laser pointers beams into the path of the pulsed lasers. The low power lasers are used to set-up and adjust several mirrors on the laser cart, the relay mirrors, and all the optics on the combining and receiving plates. The low-power beams are crossed at the measurement volume with the help of the beam viewing system on the combining optics plate.

A beam from a blue laser pointer passes through the Nd:YAG mirror on the combining optic plate, and is overlapped to the beam from the green pointer. The blue beam is used to set-up the multi-pass dichroic mirror, and the optics relaying the signal to the spectrometer. The mirrors are adjusted so that the blue beam is centered on the spectrometer entrance slit, and on the CCD camera. Once the system is aligned, irises are added to the path to outline the position of the beams, and the mirrors that inserted the pointer beams into the path flipped down.

The next step is to turn on the high-power lasers, and simply align them to the irises. The power of the laser during this alignment procedure is reduced to a working minimum, by rotating the half-wave plates. This approach does not change the pointing or the focusing of the lasers. The beams will appear on the beam viewing system camera, but they will be out of focus if they were focused using the laser pointer beams because the divergence of the pointers does not match the divergence of the high-power beams. The lenses are mounted on translation stages with motion

aligned to the beam path and can be adjusted until the beams appear focused on the beam viewing system (imaging the beams at the crossing plane). This operation is performed to set the focus of the Nd:YAG and the narrowband dye lasers. The telescope on the path of the broadband dye laser is then adjusted so that also the broadband beam is also focused at the crossing plane.

At this point all the beams are crossed and focused at the same location and the optics are set-up so that the resulting CARS signal would be directed to the spectrometer. The mirror for the first beam viewing system is flipped down, the power of the laser increased, and a CARS signal is detected on the camera. The signal needs to be focused on the CCD camera, and this can be done by adjusting the distance between the spherical lens and the entrance slit of the spectrometer. Fine adjustments can be performed to maximize the CARS signal using the 2 mirrors on picomotor controlled mounts. These allow fine adjustments of the overlap of the dye lasers on the Nd:YAG beam, and of the overlap of the two dye laser on each other. The same two picomotor-controlled mirrors can be used to remotely adjust the position of the two dye lasers with respect to the Nd:YAG beam during a test. For example the picomotors can be used to counter the effect of temperature changes of the mirrors, as discussed in Chapter 8.

3.2 **The Data Acquisition System**

A graphical interface written in Labview controls a pulse generator, a translation stage, a rotation stage (for a half-wave plate), and the PIXIS CCD camera. The data acquisition software has been optimized for measurements in facilities that can run

continuously, like the laboratory scale supersonic jet of Chapter 7, or the dual mode scramjet combustor discussed in Ref.[105]. The data acquisition has been strongly automated, so that the overall data acquisition rate is improved.

For all the data presented in this work a three axis translation stage was used to move the burner, so that different locations in the flame could be probed. In large scale facilities the combining and collecting optics plate are mounted on the translation stage, allowing the movement of the CARS measurement volume within the flow of interest.

The camera has a detector of 1340 x 100 pixels. The Labview interface allows binning of the CCD camera. For all the data presented in this work the CCD is binned into three rows (1340 x 33 pixels) to reduce the read-out time and to allow data acquisition at 20 Hz. Binning also increases the signal-to-noise ratio. The CARS signal is only in the central bin (bin 2); the upper and lower bins are used for background subtraction as described in more details in the next section.

The dynamic range of the camera is 16 bits, limiting the maximum number of counts to 65535. CARS signal intensity is strongly dependent on the temperature ($\propto T^{-3.5}$), therefore a large variation of the signal intensity is expected in combustion studies. When the CARS signal exceeds this threshold, it can be lowered by reducing the energy of the Nd:YAG laser; this is accomplished by rotating a half-wave plate followed by a polarizer, placed on the path of the Nd:YAG beam on the laser cart. The half-wave plate is mounted on a motorized rotation stage controlled by the same Labview code that controls the camera acquisition and the translation stage. During acquisition of a typical dataset, the software moves the translation stage to the desired

location; once it has arrived, it collects typically 20 spectra and counts how many have peak intensity above a user-defined threshold (set to 50,000 counts for all the data presented in this work). If 10% of the spectra are above the threshold, it rotates the wave plate to a preset value, reducing the signal intensity, and samples the flow again. The process is iterated until fewer than 2 (10%) of the spectra are above the threshold. In previous works, [6, 66, 72] the dynamic range issue was solved by adding a neutral density filter in the path of the signal when the signal exceeded the saturation threshold. In those works the process was not automated, and the operator had to verify the threshold level and insert the appropriate neutral density filter. The process described here is completely automated (integrated in the Labview routine that controls the camera and the translation stage), greatly increasing the number of spectra per hour that can be acquired. The approach guarantees that a large percentage (~90%) of the shots at a given location does not saturate the camera. Preventing detector saturation in 100% of the shots, by signal reduction, can be counterproductive in a very turbulent region of the flow. In a location where the temperature range is very large, it is preferable to let the coldest 10% of spectra saturate the camera, rather than lowering the signal-to-noise ratio below acceptable levels at the highest temperature. It is not possible to analyze spectra with signal that is too low, but we can still extract information from spectra having saturation in some pixels, as it will be shown in Chapter 6.

3.3 **Data Analysis**

CARS data analysis consists of three steps. First, the pre-processing extracts the square root of the CARS signal from the raw data. The second step consists of generating a library of theoretical spectra to compare to the experimental spectra. The final step is the fitting of the preprocessed experimental spectra to the theoretical library to extract temperature and mole fractions. The procedure described in the next section is the one followed for the data analysis of the CARS spectra in the supersonic combusting free-jet, described in Chapter 8. Some of the steps were not necessary in analyzing the data from the laminar Hencken burner flame discussed in chapter 6.

3.3.1 Data Pre-Processing

The raw signal collected by the CCD camera contains not only the CARS signal but also contributions from other sources that have to be removed. A major contribution is the camera dark noise. This contribution is almost identical in all three bins (within 1 count); shot-to-shot variations of dark noise in each binned pixel have a standard deviation of 4.5 counts. The mean value typically changes 1-2 counts over a few hours (depending on the CCD temperature) as long as the camera has been warmed up for few hours before the test. Ambient light, primarily from the room illumination, can reach the camera. Barriers, built around the camera and the relay mirrors limit this contribution to 1-2 counts above the dark noise level, provided the room overhead lights are extinguished. With the current set-up some light from the Nd:YAG laser flashlamps reaches the camera. The light is collinear with the Nd:YAG

beam, and therefore partially overlapped to the CARS signal itself, because in the planar boxcars phase matching geometry the signal beam is collinear with the green pump beam. The portion of the light at the same wavelength as the CARS signal reaches the camera's central bin (bin 2) as shown in Figure 3-5. Contribution in the other two bins (bin 1 and 3) is negligible. The two set of spectra shown in figure were collected before (red lines) acquiring CARS data in a laboratory-scale supersonic jet (see Chapter 8), and 4 hours later, after the data acquisition was completed (blue lines). The figure shows the average signal obtained blocking the dye lasers so that no CARS signal could be generated, and subtracting the average camera dark noise in each bin. The contribution is not uniform over the CCD, but has a well-defined spectral distribution. Use of Pellin-Broca prisms on the cart reduces its peak amplitude to ~ 20 counts. This emission passes through and is altered by the half-wave plate and the polarizer used to reduce the signal intensity in the presence of detector saturation. To take into account this contribution 250 background spectra are taken for each value of the half-wave plate angle used during the test, by blocking the narrowband dye laser on the cart. For each test run, we subtract, bin by bin, from the raw signal the average of the background obtained with the same angle of the half-wave plate used for that specific run.

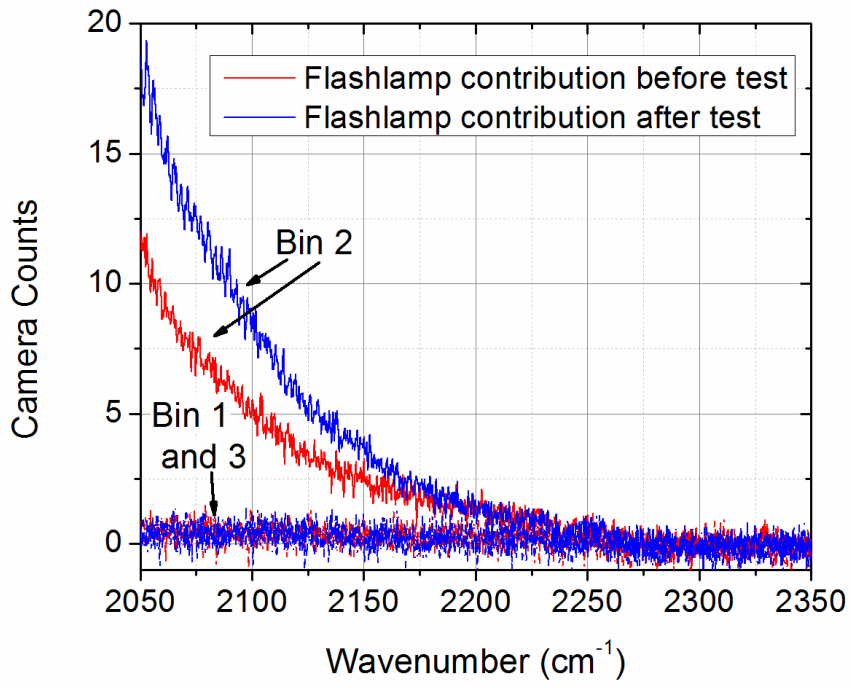

Figure 3-5: Contribution from the Nd:YAG flashlamps

The procedure described above does not remove the contribution from the flame emission. This contribution depends on the location of the flame, and therefore could not be taken into account by subtracting a reference spectrum. This contribution is present in all three bins, but it is higher in the central bin (the one containing also the CARS signal) as shown in Figure 3-6. In this work, significant contribution from the flame was observed for the combustion cases in the laboratory-scale supersonic free-jet, but not the mixing cases, discussed in Chapter 8. The ratio of the flame luminosity between bins is approximately constant (within 10%) with the flame location. This ratio (scaling factor) is determined once for each test case from spectra taken with all lasers blocked and the supersonic burner operating at test conditions. To take into account the flame luminosity contribution, the algorithm subtracts from the central

bin the average of the bin containing the least signal, multiplied by the scaling factor that takes into account the different light distribution in the three bins.

Data acquisition in the supersonic jet typically lasted as long as 4 hours. Small changes with time in the background spectra are taken into account by interpolating between spectra taken before and after the test. Tests in the Hencken burner (Chapter 6) were generally completed within an hour, and variations of the background spectra with time were neglected.

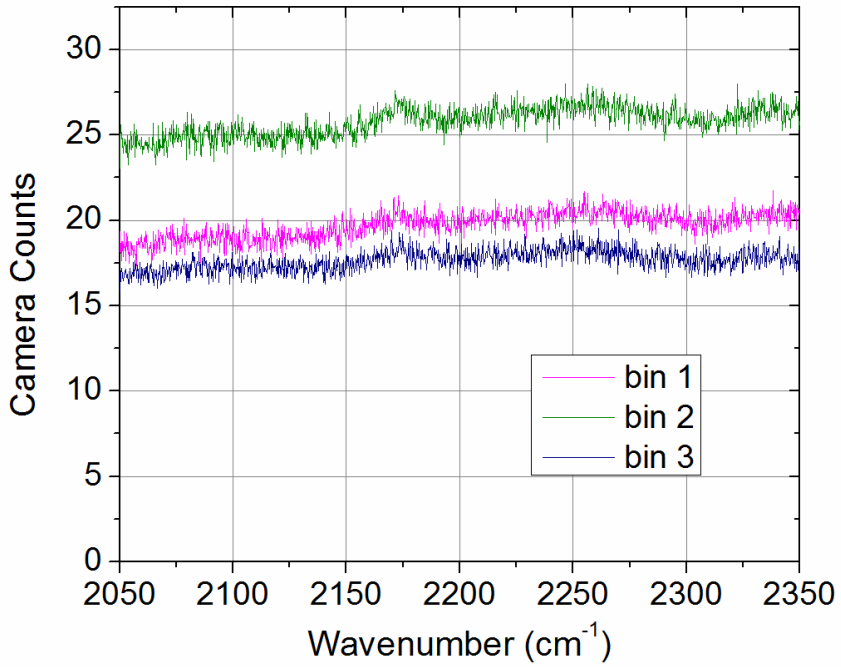

Figure 3-6: Contribution from the flame luminescence

CARS spectra have resonant and non-resonant parts. In DP-CARS absolute mole fraction measurements are determined by the ratio between the resonant and the non-resonant portion of the spectrum. The non-resonant baseline intensity ranges from 15 counts to a few hundred; therefore it is comparable to the contributions from the

flashlamps and the flame luminescence. Correct removal of spurious light from the non-resonant baseline is therefore critical for accurate measurements of absolute mole fractions.

The CARS signal, obtained by removing the background from the raw signal, needs to be normalized by the non-resonant spectrum. This spectrum is obtained by averaging 500 single-shots CARS spectra obtained in a flow of argon. Non-resonant spectra are collected at the beginning and at the end of the test day. During the several hours required for data acquisition, the measured non-resonant spectrum changes its peak wavelength and its shape as shown in Figure 3-7. The change is due to several factors, including changes in the temperature of the dye, solvent evaporation, laser misalignment and changes in the intensity of the Nd:YAG beams that pump the dye cells. The preprocessing algorithm determines the difference in the peak locations of

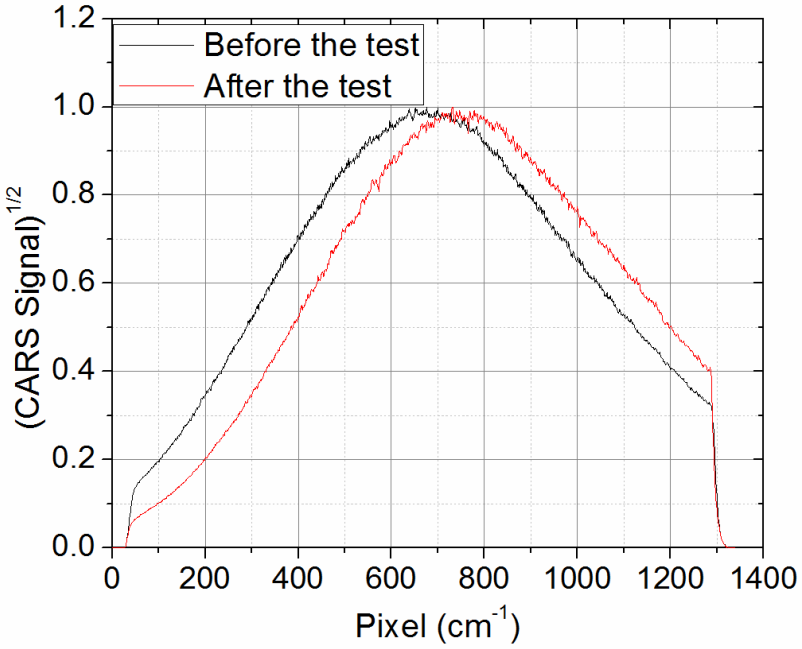

Figure 3-7: Average non-resonant spectrum in argon

the two non-resonant average spectra (before and after a test), shifts the non-resonant spectrum collected at the end of the test so that the peaks overlap, and computes the difference between the two spectra, to determine the change in shape. For each run, the time passed from the acquisition of the first non-resonant spectrum is computed and divided by the time between the acquisitions of the two non-resonant spectra. An interpolated spectrum is then obtained by adding to the first non-resonant spectrum the product of this ratio and the difference between the two non-resonant spectra. This accounts for the changes in shape. The result of this operation is then shifted by a number of pixels equal to the product of the time ratio defined above and the difference in the peak location of the two non resonant spectra. This approach assumes that the changes in the non-resonant spectrum are linear with time – an assumption that was shown to be sufficient for measurements in the Hencken burner. Over the four hours of a typical test in the supersonic jet, the change in the non-resonant spectrum peak wavelength is not monotonic; therefore the linear approximation can cause errors. Unfortunately this was not anticipated at the time of data acquisition, and only two non-resonant spectra are available, one before and one after the whole data set is acquired. Figure 3-8 a) shows the fit to the theory of an average spectrum obtained with the non-resonant referencing described above. The left side of the spectra is lower than the theory, the right side higher. This error is a typical consequence of an erroneous referencing (due to an incorrect shift in the Gaussian shape of the non-resonant spectrum) and can be corrected by shifting the non-resonant spectrum by an additional 35 pixels as shown in Figure 3-8 b). Visual

inspection of all data is impractical given the large amount of data collected in a typical test campaign.

In Ref. [6] O`Byrne faced a similar problem and determined the position of the non-resonant spectrum by fitting the middle one third of the spectra obtained in each run for three or more values of the center wavelength of the non-resonant spectrum, and determining the optimal values as the one minimizing the fitting residual. This approach is time consuming since it requires multiple fits of each dataset; given the large amount of data a less accurate but faster approach was chosen. Figure 3-8 a) shows that an incorrect non-resonant shift causes an erroneous slope in the non-resonant baseline. An algorithm was developed that evaluates the ratio of the average experimental spectra in the 2085-2090 cm^{-1} to the average in the 2240-2245 cm^{-1} region. This ratio is a function of temperature and composition, but does not change much in the range of temperature and concentration expected. For the combustion case, values of the ratio are ~1.04 for the nozzle exit composition and temperature, 0.84 for the pure H_2 or N_2 co-flow, and 0.95 for air, based on theoretical spectra obtained with CARSFT. The ratio is mostly sensitive to changes in the O_2 and H_2O mole fractions. The algorithm first determines if significant amounts of O_2 are present (peak of the O_2 spectrum greater than 10% of the total spectrum peak, before normalization by the non-resonant), to choose which value of the average ratio to use (0.84 if O_2 is negligible, 1.04 otherwise). Then it computes the ratio in the experimental average spectra that have been normalized by the interpolated non-resonant spectrum, and by the same spectrum shifted by ±60 pixels. Finally, it fits the computed average ratios with a quadratic function to determine the shift necessary so

that the ratio in the experimental data matches the desired value. The algorithm returns the shift in the non-resonant spectra up to 100 pixels, and change in the shift computed for two consecutive runs is within 30 pixels.

The main limitation of this approach is that the theoretical ratio is not known a priori and is approximated to one of two set values. For the range of temperature and concentrations expected in the test, the ratio can take values in the 0.84-1.1 range; for a given spectrum the difference in the non-resonant shift computed by the algorithm using the two limit values is 32 pixels, therefore an uncertainty of ±16 pixels is caused by not knowing the exact composition and temperature in the preprocessing. In terms of measured mole fraction, a 16 pixel shift corresponds to ~2% change in the measured absolute mole fraction, 5% in the relative mole fraction, and 1% in the temperature. Shot-to-shot referencing schemes as used in Ref. [106] might remove this source of uncertainty and greatly improve the instrument accuracy.

Errors in background subtraction can lead to bigger errors when this algorithm is used because they affect the baseline, and therefore the ratio used to determine the non-resonant shift. This is especially problematic for spectra taken in colder gases, where the laser irradiance has been strongly reduced to avoid detector saturation in the spectral peak. For this reason the algorithm uses the shift determined for the previous set of spectra for spectra having less than 25 counts on the non-resonant baseline.

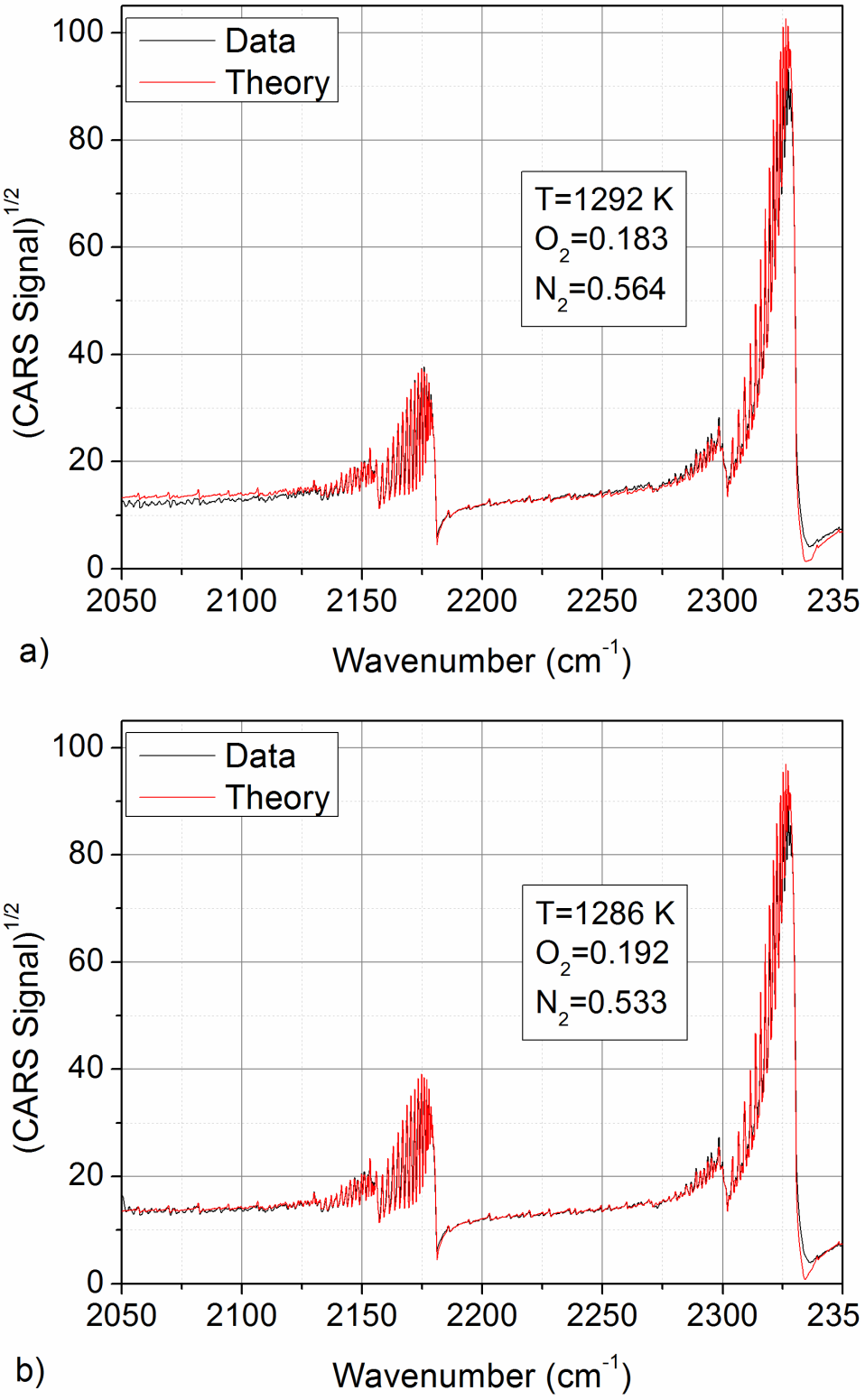

Figure 3-8: Experimental spectra and theoretical fit before (a) and after (b) shifting the excitation profile

The last step in pre-processing is the conversion from pixel to wavenumbers. In previous works, a linear conversion relation was used, but tests with calibrated spectral lamps show that the spectrometer is non linear. In this work the following quadratic relation is used:

$$\omega_e = \frac{10^7}{ap^2 + bp + c} - \frac{10^7}{d} \tag{3-1}$$

where p is the pixel number and ω_e the corresponding wavenumber. An algorithm has been developed to determine the mapping coefficients (a,b,c,d). The algorithm requires a high temperature experimental spectrum containing N_2 and either O_2 and H_2, and a theoretical spectrum generated from CARSFT containing the same species, and roughly at the same temperature (i.e. same peaks) is also required. A graphical user interface allows selecting any numbers of peaks for each species in the theoretical spectra, and the corresponding ones in the experimental spectra. The mapping coefficients are obtained as the values that minimize the function:

$$\left(\frac{1}{n^{(1)}} \sum_{i=1}^{n^{(1)}} \left(\omega_{e_i}^{(1)} - \omega_{t_i}^{(1)} \right)^2 + \frac{1}{n^{(2)}} \sum_{j=1}^{n^{(2)}} \left(\left(\omega_{e_j}^{(2)} - \omega_{e_1}^{(2)} \right) - \left(\omega_{t_j}^{(2)} - \omega_{t_1}^{(2)} \right) \right)^2 \right)^{\frac{1}{2}} = f(a,b,c,d) \tag{3-2}$$

The superscripts (1) and (2) indicate the peaks associated to the first (N_2, and H_2 S(5)) and to the second (O_2, H_2 S(6) and S(9)) CARS process, respectively (see Figure (2-3)). The sum goes from 1 to the number of peaks selected for each of the two CARS processes ($n^{(1)}$ and $n^{(2)}$). Equation (3-2) is a measure of the difference between the theoretical and the experimental location of the selected peaks, for a given set of the mapping parameters. The location of the peaks associated to the second process is a function of the frequency difference between the Nd:YAG and the

narrowband dye laser, that is not well known at this stage of the preprocessing . For this reason for the peaks associated to the second CARS process, the distance from the first peak selected appears in the equation, rather than the actual frequency. The parameters used to convert from pixel to wavenumber are the ones that minimize Eq. (3-2). The initial guess for the conversion parameters are a=0, b=0.006 (from spectral lamp measurements), c=center wavelength of the CARS signal and d=wavelength of the narrowband dye laser.

The parameters for the conversion from pixel to wavenumber are determined once for each day of testing. Beam steering and changes in temperature of the optics can move the location of the CARS signal on the camera. If the location (pixel number) of the ro-vibrational peaks changes from the value used to determine the mapping parameters, then the experimental spectra will appear shifted with respect to the theoretical. Small differences, below 1 cm^{-1} are taken care in the fitting algorithm, which has as a fit parameter a frequency shift. The fitting algorithm does not perform well in presence of larger frequency differences, and corrections in the pre-processing algorithm are needed. The pre-processing algorithm shifts the spectra so that the location where the N_2 band is 20% of its peak values is always at the same pixel location. For spectra where only H_2 is present the algorithm shifts it so that the S(5) peak is at a fixed pixel location. For this experiment, typical movements of the spectra on the CCD were limited to few pixels, but larger movements have been observed in previous work in the large scale jet.[72]

3.3.2 The Theoretical Library

The preprocessed spectra are analyzed using the fitting algorithm developed by Cutler.[107] The algorithm interpolates from a library of theoretical spectra generated with a version of CARSFT [108] modified by Hancock [109] and O'Byrne [110] for use with DP-CARS.

CARSFT requires several experimental parameters to generate the theoretical spectra. In addition to the molecular parameters, CARSFT requires the spectral line width of the pump laser (Nd:YAG), the instrument function (mainly owing to the focusing of the signal on the spectrometer entrance slit, on the camera pixel size, and on the spectrometer), the spectral line width of the probe laser (narrow band dye laser), and the offset in wavenumbers between the pump and probe beams. These parameters are determined by fitting experimental spectra to theoretical spectra, using the fitting routine included in CARSFT. The offset between the pump and probe is determined using CARSFT, so that the distance between the N_2 and O_2 spectra is the same in the theory and in the experiment. When the non-linearity of the spectrometer is properly taken into account, the position of the H_2 lines (S(5) and S(6)) are then also the same in theory and experiment. The Nd:YAG laser is injection seeded, and its width is considered infinitesimal in the spectral convolution. The instrument function is assumed to be a Gaussian and its width is determined as a result of a fitting over the O_2 portion of the spectrum. This region is chosen because the O_2 spectrum is not broadened by the finite width of the narrowband dye laser. The line width of the narrowband dye laser is determined by fitting this parameter in the N_2

region, using the width of the instrument function determined in the previous step. In this procedure all parameters are decoupled, and only one parameter at a time is determined by fitting.

Some changes have been made in the CARSFT code. The original code did not allow different spectral linewidth models to be selected for different molecules. The code has been modified to always use the Galatry linewidth model for the H_2 spectra and the linewidth model input to the code is applied to both N_2 and O_2. The impact of this change on the mole fraction accuracy is discussed in Chapter 6.

The differential Raman cross section $\left(\frac{\partial\sigma}{\partial\Omega}\right)$ appears in the expression of the CARS susceptibility (Eq.(2-20)). The effect of the interaction between the rotational and vibrational modes, on the differential Raman cross section is taken into account through the Herman-Wallis correction factor. [111] CARSFT originally uses the James Klemperer model [112] for the Herman Wallis factor, but recent studies[113, 114] showed improved CARS accuracy when using the Tipping Bouanich [115] model. I added to the CARSFT code the possibility of choosing between these two models or to neglect the Herman Wallis factor. [114]

3.3.3 Spectral Fitting

A new fitting algorithm has been developed by Cutler [107] and has been used for all the spectral fitting used in this code. The algorithm fits the experimental spectra to a sparse library of theoretical spectra. At each iteration of the code, theoretical spectra are interpolated from the library. Temperature, absolute mole fraction of the resonant

species, and a horizontal wavenumber shift are obtained as a result of a fitting algorithm that minimizes an appropriate residual between the experimental CARS signal intensity and the theoretical CARS spectra. Details on the criteria to generate the libraries and on the fitting algorithm can be found in Ref. [107].

The code is at least ten times faster than CARSFT since it uses a library of pre-generated spectra, rather than computing theoretical spectra at each iteration step. In addition, CARSFT tends not to converge to a global minimum, being very sensitive to the initial condition, when more than three parameters are fit simultaneously. The new method also offer advantages with respect to the library based algorithm used by O'Byrne, [6] since it uses sparse libraries rather than fully populated ones. The sparse libraries are smaller, and the increase in processing speed becomes increasingly significant as the number of the chemical species is increased (as for example in WIDECARS, [85] where 6 species are probed).

The algorithm offers the possibility of choosing between a weighted least square fitting to the CARS intensity (originally suggested by Snelling) [116], and least square fitting to the square root of the CARS intensity used in CARSFT. The first reduces the random error, and ultimately improves the instrument precision as shown in Chapter 6.

Another useful feature of the algorithm is the possibility of blocking selected regions from the fitting. A blocked region is not included in the computation of the residual. In this work the S(6) and S(9) H_2 lines are sometimes blocked, as well as regions of the spectra that saturate the detector, as it will be shown in Chapter 6.

CHAPTER 4 -Mitigation of Beam Steering Effects

4.1 **Introduction**

Laser beams travelling through a turbulent combustion environment are subject to small displacements in their path. Turbulence at the interface between combustion products and air, or between a supersonic jet and quiescent air, causes rapid spatial and temporal variations of density, which translate directly into refractive index gradients. Larger eddies with size comparable to the beam diameter randomly deflect the laser beam (beam *wandering*), and are responsible for phase shift fluctuations leading to the appearance of speckles in the beam profile. Smaller eddies scatter the light and cause a *spreading* and a defocusing of the beam [87, 117-119]. In CARS, three beams are focused and overlapped at the measurement volume, where they interact and generate a coherent signal containing the Raman spectrum of the probed species. Beam displacements of as little as a few tens of micrometers can prevent the beams from fully overlapping, causing a reduction in the CARS signal. The CARS signal is proportional to the product of the irradiance of the three laser beams; therefore beam defocusing also causes a reduction in the CARS signal. In addition to refractive index gradients, vibrations of the optics, either acoustically excited or transmitted through the optic's supporting structure, also affect the beam path. Beam steering is the motion of the beam at the focal plane of the measurement volume induced by both refractive index gradient induced wandering and by vibration of the optics.

Numerous studies have been conducted to evaluate the applicability of CARS in turbulent environments. Beam steering is tolerable for measurements in small combustors, but becomes an issue in supersonic free jets, or large flames. [87] Attal-Trétout [120] observed considerable CARS signal fluctuations and data yield (percent of acquired spectra that resulted in a good fit for temperature) below 50% when a turbulent hot air flow was interposed between the focusing lens and the measurement volume. Beam steering due to large density gradients was responsible for frequent loss of CARS signal in measurements performed by Klimenko [121] in a cryogenic LOX-H_2 rocket combustion chamber. Hemmerling [122] attempted single-shot folded BOXCARS temperature measurements in a high pressure combustor, but signal-to-noise ratio was too low because of severe beam steering. Beam steering is a potential problem for any laser based technique in which the laser beam coherence is critical and two or more laser beams needs to be overlapped. For example Herring [123] showed that beam steering is a serious obstacles to LITA measurements in high-density, compressible, and turbulent flows.

Recently, significant beam steering effects on CARS measurements were observed in a large, supersonic combusting, axisymmetric free jet, [66, 72] resulting in large variations of the signal to noise ratio, and data yield as low as 40%. [72] Such low data yields are undesirable because facility run times must be increased to acquire the necessary data and also because averaged temperatures can exhibit bias towards lower temperature, since spectra obtained at lower temperatures tend to have larger signal intensity and are therefore more often included in the average. [74, 120] Beam steering was less important for measurements in ducted combustor. [6, 105] In

a supersonic combusting free jet, the large density gradients at the turbulent interface between the hot reaction products and the atmospheric air are responsible for the severe beam steering effects.

The objective of this chapter is to investigate a new approach to reduce the sensitivity of CARS to beam steering. This new approach combines elliptical beam shaping and planar BOXCARS to achieve this goal, while leaving the length of measurement volume unaltered. The new technique is compared to previous methodologies used for measurements of large turbulent flows. Advantages and limits of this approach are investigated numerically and experimentally.

4.2 **Beam Steering Mitigation Technique**

In order to obtain a strong CARS signal, three incident beams have to be aligned so that the signal generated at some point will be in phase with the signal generated at subsequent points. Several strategies have been devised to satisfy the phase matching requirements while maintaining adequate spatial resolution. In the presence of beam steering some phase matching geometries are more robust than others. In USED (Unstable-resonator Spatially Enhanced Detection) CARS [124] the pump beam is donut shaped and the Stokes beam is concentric to the pump. Because of the concentric geometry and of the common propagation axis of the beams, beam steering has less effect on the beams overlap, but this approach greatly lengthens the probe volume and adds uncertainty to the location of the measurement volume. For example, Eckbreth [125] reported measurements in a jet engine exhaust using this approach, but the spatial resolution is 0.1 mm in diameter and 50 mm long, thirty

times longer than reported in Ref.[6, 70, 72]. Hemmerling [122] adopted the USED CARS phase-matching to obtain single shot temperature measurements in a high pressure combustor, with a spatial resolution of 11 mm. In most turbulent applications a higher spatial resolution is desirable, strongly limiting the applicability of USED CARS.

Folded BOXCARS [126] was used to collect the data in the large free jet described in Ref. [66, 72, 74]. This is a three-dimensional arrangement that allows good spatial resolution and signal strength. This phase matching strategy is prone to be affected by beam steering, since each beam travels along a different path, encountering different turbulence structures, and thus is refracted differently.

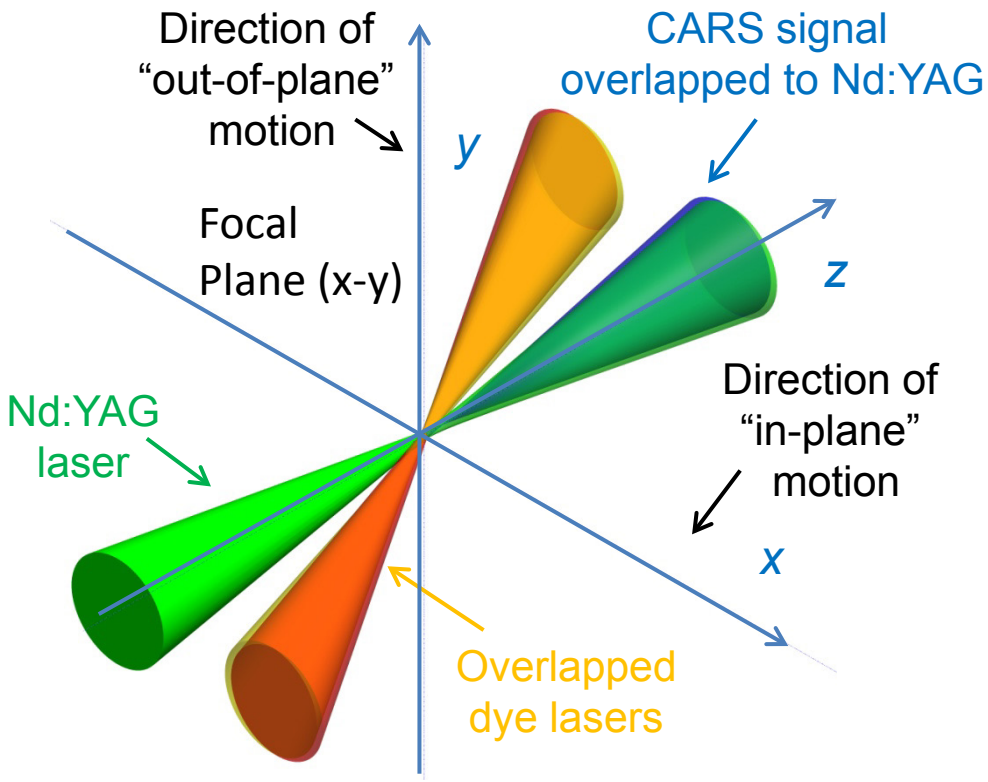

Figure 4-1: Planar BOXCARS

Planar BOXCARS (Figure 4-1) has all the beams travelling in the same plane. The reference system introduced in Figure 4-1 has its origin at the crossing point of the three beams before the effect of beam steering; the *z* axis is in the direction of the CARS signal beam, the *x* axis is in the plane of the beams and orthogonal to *z*, and the *y* axis is orthogonal to *x* and *z*. The planar BOXCARS phase matching condition requires that two of the three beams are almost superimposed as shown in Figure 4-1. In this instrument, the broadband Stokes dye laser (in red) and the narrowband pump dye laser (in yellow) are overlapped, and the CARS signal beam (in blue) is superimposed on the Nd:YAG pump beam (in green). Dichroic mirrors are used to combine the two dye laser beams and to separate the signal from the Nd:YAG beam. The beams are crossed at their respective waists (which are forced to be coincident), at the "focal plane". Signal is generated at the beam intersection, a region that resembles a very elongated ellipsoid with maximum cross section diameter determined by the smallest beam. The length of the probe volume is determined by the angle between the beams and by the beam diameters at the focal plane. [127] The main disadvantage with respect to "folded" BOXCARS is the weaker CARS signal [128] (40% lower for given probe volume length) and the need of dichroic mirrors to combine and separate beams. The advantage is that the superposition of two beams ensures that those beams remain overlapped at the focus, even in the presence of beam steering, whereas in folded BOXCARS all three beams can move independently.

Loss of signal will occur if the two superimposed beams do not overlap with the third beam. Any motion of the beams with respect to each other can be expressed as a

sum of two components, one "in-plane" (i.e. along the *x* axis), and the other "out-of-plane" (i.e. along the *y* axis). Figure 4-2 shows the effect of "in-plane" motion on the beam`s crossing. The "in-plane" motion does not prevent overlap, but moves the crossing location away from the common focal-plane (the *x*-*y* plane in figure), to a different *z* location. As a result the location of the probe volume is shifted and the beam irradiances at the crossing are lower causing a small reduction of the signal level.

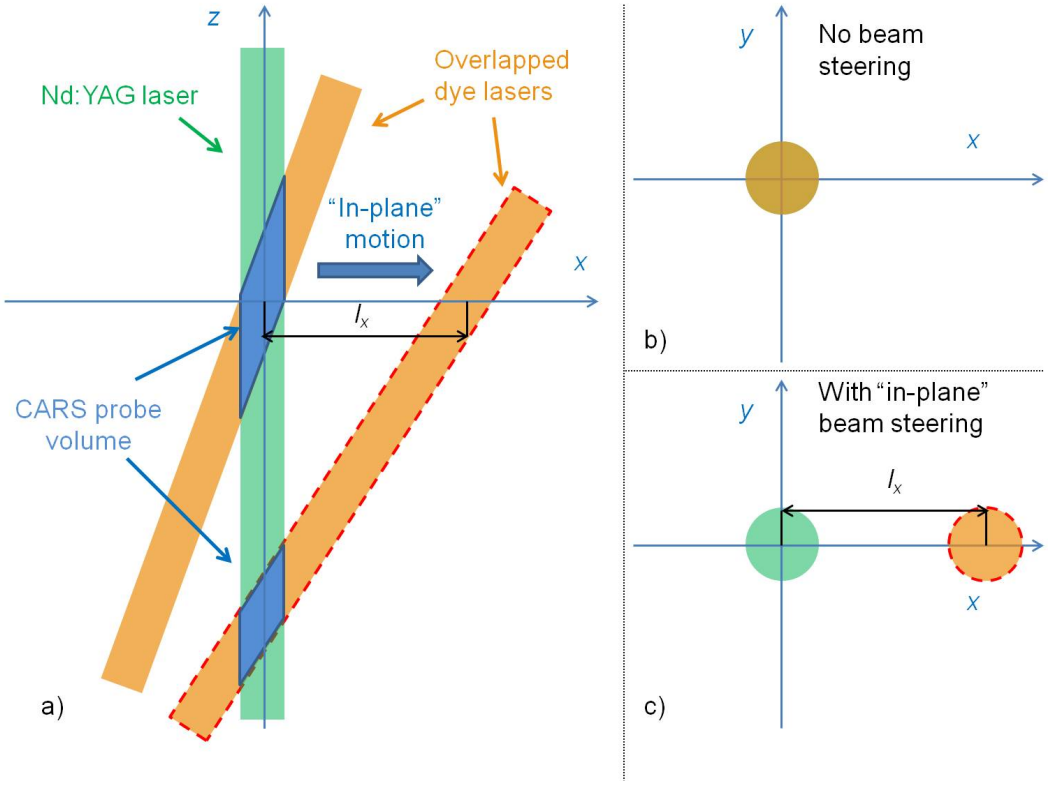

Figure 4-2: Effect of "in-plane" beam motion: a) beams sectioned by the *x*-*z* plane; the dashed red line around the overlapped dye lasers indicates the beam displaced by the beam steering; b) beams sectioned by the focal plane (*x*-*y*) without beam steering, and c) with "in-plane" beam steering

Figure 4-3 shows the effect of "out-of-plane" motion on the beam crossing. The figure show the 3 beams sectioned by the *x*-*y* plane that is the common focal plane. In absence of beam steering (Figure 4-3a) the beams overlap and generate the strongest

CARS signal. Just one beam diameter of displacement in the "out-of-plane" direction (i.e. along the *y* axis) is sufficient to prevent overlapping (Figure 4-3b) and CARS signal generation. An elliptically-shaped Nd:YAG beam, with the major axis in the direction orthogonal to the plane of the beams as shown in Figure 4-3c, would allow beams to overlap for larger displacement "out-of-plane" than a round beam. Thus an elliptical beam in the planar BOXCARS geometry will generate a signal less sensitive to beam steering, but weaker because of the decreased irradiance, since the same energy is now spread across a larger area.

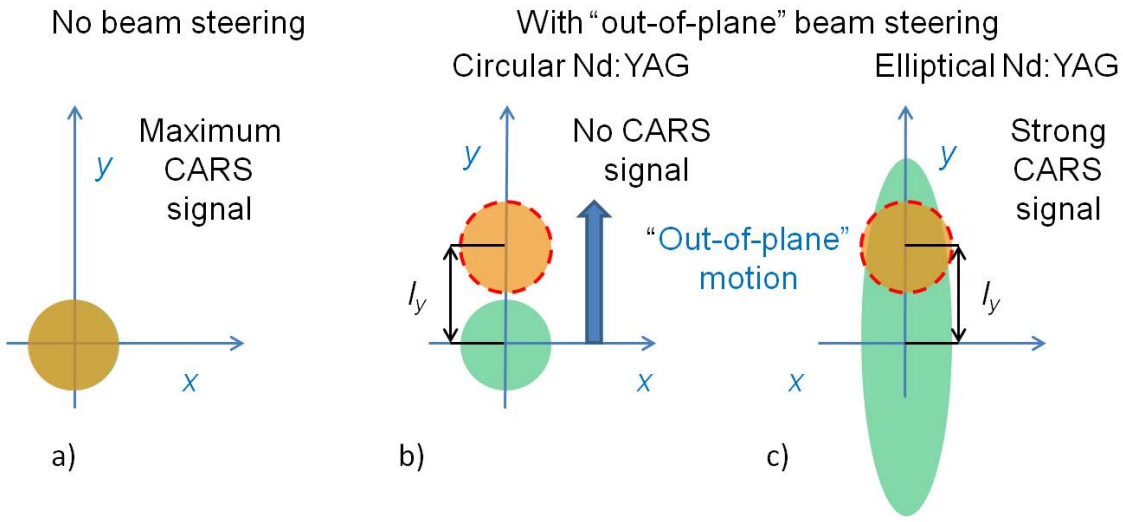

Figure 4-3: a) No beam steering, optimal beam overlap and maximum CARS signal; b) effect of "out-of-plane" beam motion when using a round Nd:YAG beam and c) an elliptical Nd:YAG beam

Often in CARS setups high irradiance perturbation effects such as optical breakdown, stimulated Raman pumping, and Stark broadening limit the laser irradiance at the measurement volume and excess laser energy is not used (see Chapter 5 for details). This extra energy allows beam shaping, i.e., increasing the major axis diameter of the Nd:YAG beam (leaving the minor and other beam diameters unchanged), while keeping the irradiance at the focus constant to prevent

any signal loss. From geometric considerations, [127] the length of the interaction region is determined by the minor axis beam diameters, and does not depend on the major axis diameter. The diameter of the interaction region is given by the diameter of the smallest beam. Although the length of the measurement volume is not affected by this approach, uncertainty is added to the location of the measurement volume.

4.3 **Numerical Results**

This section includes a numerical evaluation and comparison of the CARS signal strength and probe volume length for planar BOXCARS with and without beam shaping.

The total CARS signal P_{CARS} can be expressed as: [129]

$$P_{CARS} = \left(\frac{2\pi\omega_{CARS}}{c} \right)^4 \iint \left| \int \left(I_{p1} I_{p2} I_S \right)^{1/2} \chi^{(3)} dz \right|^2 dxdy \tag{4-1}$$

where ω_{CARS} is the signal frequency, I_{p1}, I_{p2} and I_S the two pump and the Stokes beam irradiances, $\chi^{(3)}$ the third order susceptibility. The coordinate system used for this calculation is the same of Figure 4-1. Some simplifying assumptions have been made: each beam's irradiance distribution is approximated to a bivariate normal with null covariance;

$$I(x,y,z) = \frac{P}{2\pi\sigma_x\sigma_y} \exp\left\{ -\frac{1}{2} \left[\frac{\left(x-\mu_x\right)^2}{\sigma_x^2} + \frac{\left(y-\mu_y\right)^2}{\sigma_y^2} \right] \right\} \tag{4-2}$$

P is the total beam power, σ_x and σ_y are ½ of the exp(-2) beam diameter along the x and y directions, μ_x and μ_y the coordinates of the beam centroid. The beam centroid locations are a function of z;

$$\mu_x = z \cdot \tan\alpha \tag{4-3}$$

where α is the angle between the direction of the beam and the z axis; $\mu_y = 0$ for all three beams because the beams are coplanar. The variation of the beam diameters with z are approximated by the Gaussian beam relation: [130]

$$\sigma = \sigma_0 \left(1 + z^2 / z_R^2 \right)^{1/2} \tag{4-4}$$

where σ_0 is ½ of the exp(-2) beam width at the focal plane and z_R is the Rayleigh range. The parameters P, σ_x, σ_y, and α, are different for each beam. The length of the measurement volume is defined as the distance along z over which the signal goes from 5% to 95%. The integral is computed numerically on a grid of 50 × 50 × 100 cells. (Doubling the number of grids points in each direction produces differences below 0.5% in the signal and measurement volume length.)

Figure 4-4 shows two sets of plots of the CARS signal as a function of the axis ratio of the Nd:YAG beam. The continuous lines are for a full width at half maximum (FWHM) diameter of 50 microns for all the beams (except that the major diameter of the elliptical Nd:YAG beam is larger). The dashed lines are representative of the setup used for the experimental portion of this work: the FWHM are 40, and 100 and 120 μm for the Nd:YAG, the narrowband and the broadband dye laser beams, respectively. For both cases, the angle α is 4.5, 4.3 and -0.18 degrees, for the broadband, the narrowband and the Nd:YAG beam respectively, conforming to phase matching requirements. The results are normalized by the CARS signal obtained for a round Nd:YAG beam, so that they are independent of the beam power. The CARS signal has been computed using two different assumptions: a fixed Nd:YAG laser

energy (and therefore its irradiance decreasing linearly with the axis ratio), or fixed irradiance (assuming unlimited Nd:YAG laser energy can be used). These are indicated by the red and blue curves in Figure 4-4. If the laser energy is kept constant the CARS signal drops when increasing the axis ratio, but less than linearly because of the Gaussian shape of the beams. If the laser irradiance is kept constant, then the signal increases by 19% for the 10:1 ratio. The results shown in Figure 4-4 are almost independent of the beam crossing angle and are only weakly dependent on the beam diameter if the diameter is equal for all the beams. The curves differ in the case of unequal beam diameters (dashed lines). As a consequence of the larger beam diameter for the two dye lasers, the signal strength decreases more slowly with increasing the axis ratio for the cases of constant energy. When keeping the peak irradiance constant the difference is even larger, with a signal for a 5:1 axis ratio that is 76% higher than the signal obtained for a round beam. The red dots in the figure are experimental results, and agree with the expected theory to within 2%. The length

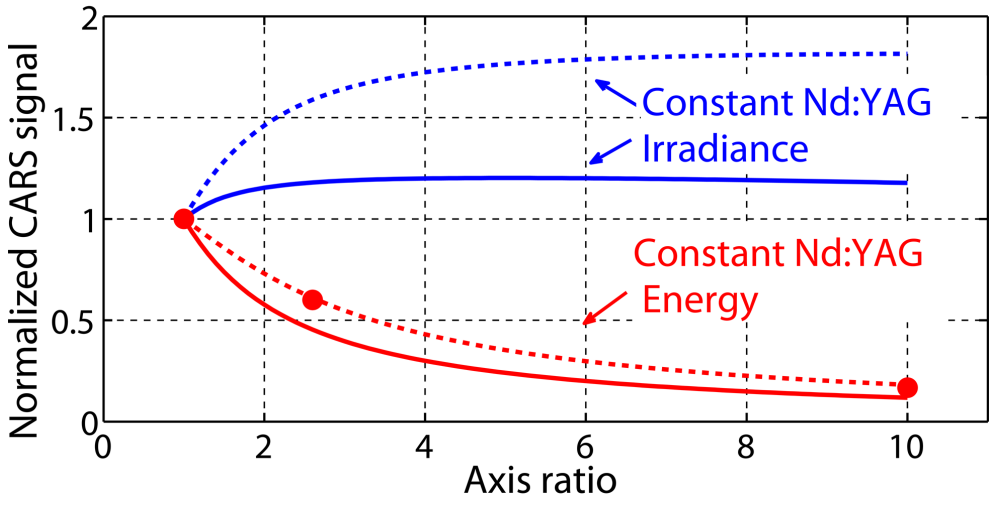

Figure 4-4: Normalized CARS signal as function of the axis ratio of the Nd:YAG beam. Results are normalized dividing by the values obtained for round beam. Red dots are experimental results

of the probe volume is independent of the axis ratio. Figure 4-4 shows that using the elliptical beam, in the case of available Nd:YAG laser energy, will cause an increase in signal compared to the conventional arrangement. This arrangement defends against beam steering and vibration while maintaining the same probe volume size as a conventional planar BOXCARS configuration.

The numerical results allowed characterizing the effect of the beam shaping on CARS signal for perfect beam overlap, providing a baseline for the behavior in the presence of beam steering that is investigated both experimentally and numerically in the next sections.

4.4 **Experimental Results**

4.4.1 Experimental Set-Up

The beam steering mitigation technique has been tested using the dual-pump CARS system described in Chapter 3. For the test described here, the beams are focused by two 25 mm diameter, 600 mm focal length spherical lenses, one for the superimposed dye laser beams, and the other for the Nd:YAG beam. The half-wave plate and polarizer on the path of the Nd:YAG beam (see Figure (3-2)) are here used to tune the power of the Nd:YAG beam. This feature is used to avoid optical breakdown when a round beam is used and to maintain constant beam peak irradiance when the axis diameter ratio is modified. With a round beam the Nd:YAG beam energy is limited by laser induced breakdown to 68 mJ, therefore up to a 4:1 ratio is possible with this system while keeping the peak irradiance constant. The energies of the broadband and narrowband laser beams at the measurement volume are

approximately 20 mJ and 50 mJ, respectively. The beam viewing system placed after the measurement volume (see Figure (3-3)) is used to image the beams at the focal plane, measure their size and their relative distance.

Elliptical beam shaping is easily achieved by rotating the focusing lens of the Nd:YAG beam. When the direction of the beam is not parallel to the lens axis, astigmatism occurs; therefore the "in-plane" (horizontal) and "out-of-plane" (vertical) foci occur at different locations along the path. Figure 4-5 shows pictures of a cross-section of the Nd:YAG beam taken at the "in-plane" focus for several rotation angles of the lens and Figure 4-6 shows the "in-plane" and "out-of-plane" FWHM diameter

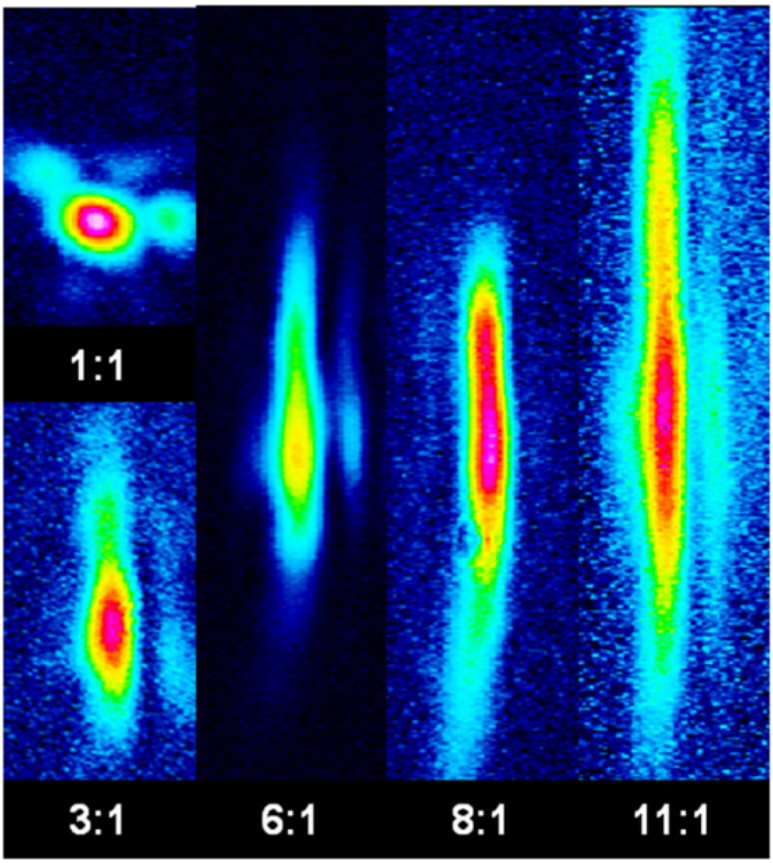

Figure 4-5: Images of the Nd:YAG pump beam at the "in-plane" focus, for different lens rotation angle. The numbers are the axis ratios

of the beam as function of the lens angle. Rotating the lens the “in-plane” beam diameter (minor axis of the ellipse) at the focus stays constant and the “out-of-plane” beam diameter at the “in-plane” focus (major axis) increases exponentially. Small angles are sufficient to obtain a large axis ratio.

In this set-up the spherical lens used to focus the Nd:YAG beam is mounted on a rotation stage with axis of rotation orthogonal to the plane of the beams. The lens is mounted in a translation stage to shift the “in-plane” focus of the Nd:YAG beam along the beam axis to the focus of the dye lasers, where all three beams are crossed.

With this setup, the axis ratio of the beam can be varied continuously and no additional lenses are required. Additional cylindrical lenses instead of a rotated spherical lens could have alternately been used to achieve a similar effect, but additional optics increase the complexity of the system and introduce beam energy losses.

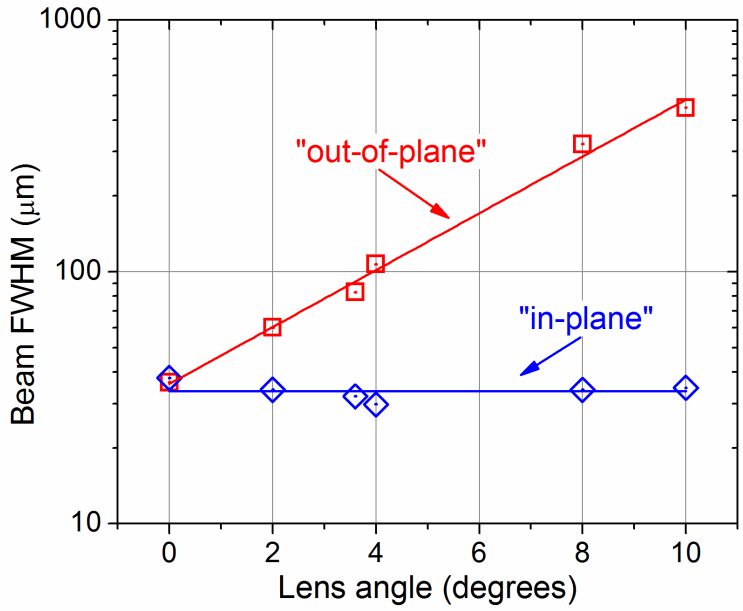

Figure 4-6: FWHM diameter of the Nd:YAG pump beam at the “in-plane” focus, as function of the lens rotation angle

4.4.2 Beam Displacement Experiment

Two experiments have been performed to characterize the efficacy of this approach. In the first experiment the two superimposed beams are intentionally misaligned using adjustments on the last mirror before the focusing lens. The displacement is monitored through the beam viewing system. The dimensionless coefficient (*BD*) quantifies the displacement of the beam. It is defined as:

$$BD = \left(BD_x, BD_y \right) = \left(\frac{l_x}{r}, \frac{l_y}{r} \right) \tag{4-5}$$

where *r* is the narrowband dye laser FWHM measured at its focal plane, *l* is the average distance between the centroids of the dye lasers and Nd:YAG beams at the focal plane, and the subscript *x* or *y* indicates displacement "in-plane" or "out-of-plane" , respectively. In the experiments presented in this work, the narrowband dye laser has an "in-plane" FWHM smaller than the broadband dye laser, but larger than the Nd:YAG. Since the two dye lasers are overlapped, the CARS signal strength is determined by the overlap between the Nd:YAG laser and the narrowband dye laser (i.e. the smallest of the two overlapped dye lasers). The choice of normalizing the beam displacement by the FWHM of the narrowband dye laser was arbitrary, and alternatively the FWHM of the Nd:YAG laser could have been used.

The goal is to design a system to provide a useful CARS signal even in flows with large *BD*. The *BD* is determined experimentally using the beam viewing system (see Chapter 3). Three axis ratios of the Nd:YAG beam at the "in-plane" focus have been considered for this experiment: 1:1, 2.6:1 and 10:1. Figure 4-7 shows images of all three beams obtained with the beam viewing system for these three axis ratios; note that the Nd:YAG and the overlapped dye lasers have been intentionally separated to make them distinguishable The "in-plane" FWHM are 40, and 100 and 120 microns, for the Nd:YAG, the narrowband, and the broadband laser, respectively.

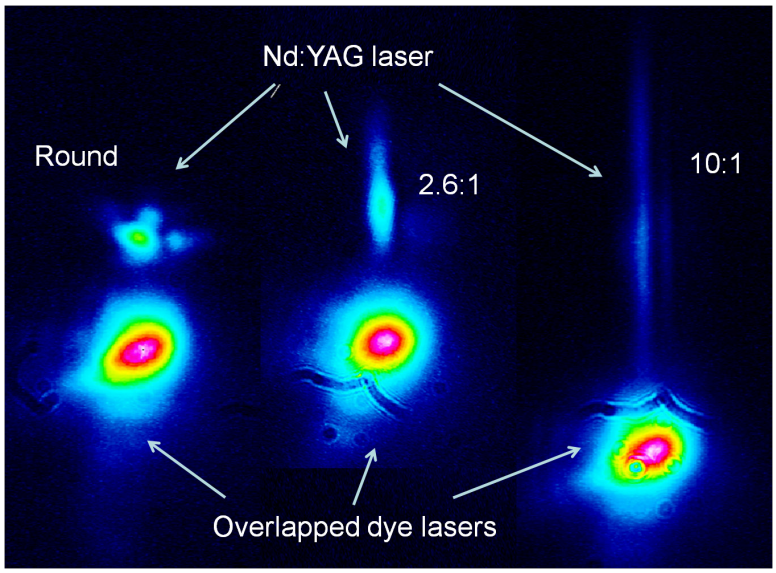

Figure 4-7: Three images of the beams at the focal plane, with circular and elliptical configurations of the Nd:YAG

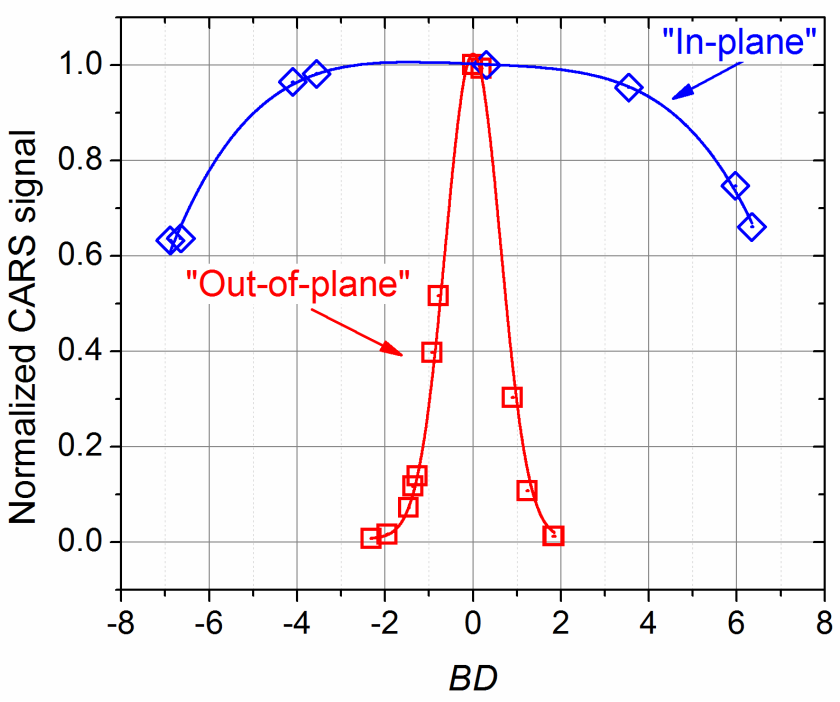

Figure 4-8: Sensitivity of the CARS signal to displacement of the overlapped dye lasers relative to the Nd:YAG beam; signal normalized by the peak signal, displacement expressed in narrowband dye laser diameters. Solid lines are a Gaussian fit

With the round Nd:YAG beam in a fixed location, the superimposed dye lasers were moved back and forth "in-plane" and then back and forth "out-of-plane" (see Figure 4-2 and Figure 4-3). Ambient air spectra were collected at each position. The area under each collected spectrum was integrated to obtain the signal. The normalized signal is the signal averaged over 1000 shots, divided by the peak average signal which occurs at $BD = 0$. The normalized signal plotted as a function of beam displacement, for the case of all round beams, is shown in Figure 4-8. Movement "in-plane" shifts the crossing point, so the beams are no longer crossing at the focal plane. The curve has a flat top because the beams stay focused for a distance and then the curve slowly drops as the beam diameters at the intersection increase and irradiances decrease. Movement "out-of-plane" causes a rapid drop in the signal level because the beams no longer overlap. Where a displacement of 4 *BD* "in-plane"

decreases the signal level by less than 10%, a displacement of 1 *BD* "out-of-plane" is sufficient to drop the energy to one third. The data follow a Gaussian curve with a FWHM of 1.3 *BD*.

The effects of "out-of-plane" displacement with elliptical Nd:YAG beams of three different axis ratios but the same power are shown in Figure 4-9. For beams crossing at the focal plane ($BD_y = 0$), the signal with the elliptical beam is 60% (2.6:1 ratio) and 17% (10:1 ratio) of the signal achieved with a round beam, because of the decreased irradiance at the focal plane. The values are in agreement with numerical calculations (61% and 18% as shown in Figure 4-4). The FWHM of the Gaussian fit to the data is 1.3 *BD* for the round beam, increases to 2.2 *BD* when using a 2.6 axis ratio, and to 3.8 *BD* for the 10:1 ratio. This is evidence of the effectiveness of this

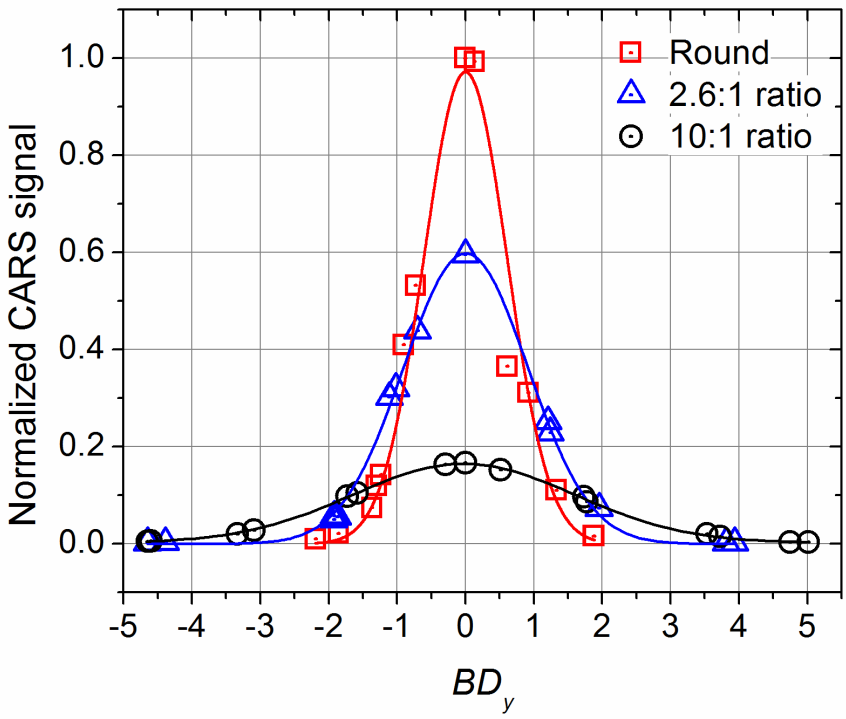

Figure 4-9: Sensitivity to "out-of-plane" beam displacement for round and elliptical Nd:YAG beam; signal normalized by dividing by the peak signal for round Nd:YAG beam. Solid lines are a Gaussian fit

strategy to defend against beam displacement. The plot suggests that in the presence of severe beam steering, an elliptical beam can produce a stronger signal than a round beam. For $|BD_y| > 0.7$, the 2.6 axis ratio beam produces a stronger signal than a round, where a 10:1 axis ratio becomes more efficient for $|BD_y| > 2$.

Figure 4-10 shows the same data points of Figure 4-9, normalized by the peak signal for that axis ratio. This applies to a situation where the power of the Nd:YAG beam is changed to keep the peak irradiance constant as the axis ratio is changed. With the current configuration the irradiance is limited by breakdown, and only 25% of the available Nd:YAG energy could be used when the beam is round.

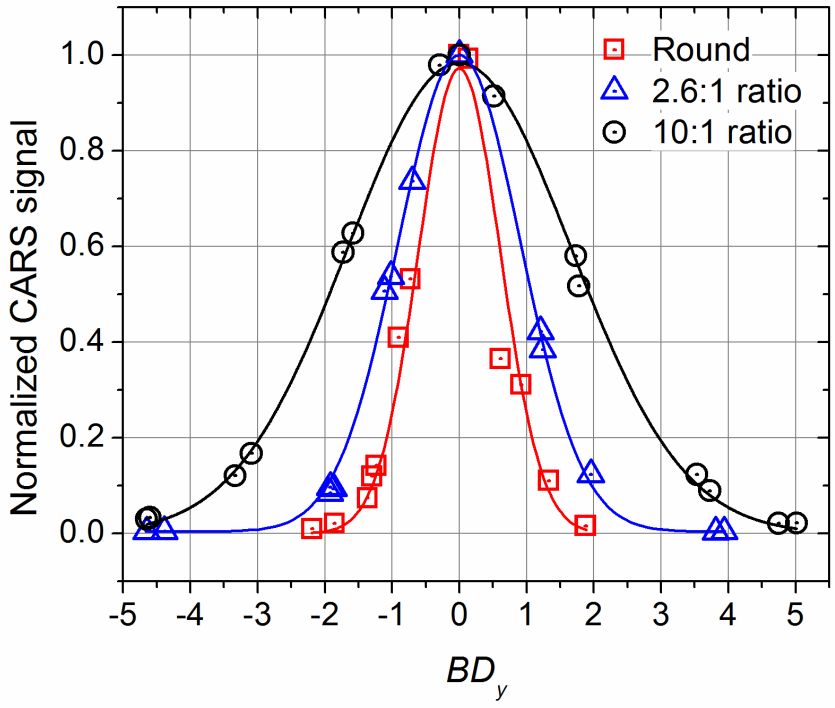

Figure 4-10: Sensitivity to "out-of-plane" displacement for round and elliptical Nd:YAG beam; signal normalized by the peak signal. Solid lines are a Gaussian fit

Figure 4-11 shows the CARS signal obtained with simultaneous "in-plane" and "out-of-plane" displacement, when using an elliptical Nd:YAG beam with a 5:1 axis

ratio. Each curve was obtained by varying the "out-of-plane" displacement BD_y for a fixed amount of "in-plane" displacement BD_x. The signal is normalized by the signal when the beams are crossed at the focal plane ($BD_x = BD_y = 0$). Figure 4-11 shows that, for $BD_x < 0$, the signal is weaker but less sensitive to "out-of-plane" displacements. Unexpectedly, for $BD_x > 0$ the signal is stronger but more sensitive to "out-of-plane" motion. Notably, this behavior is also predicted by the theory.

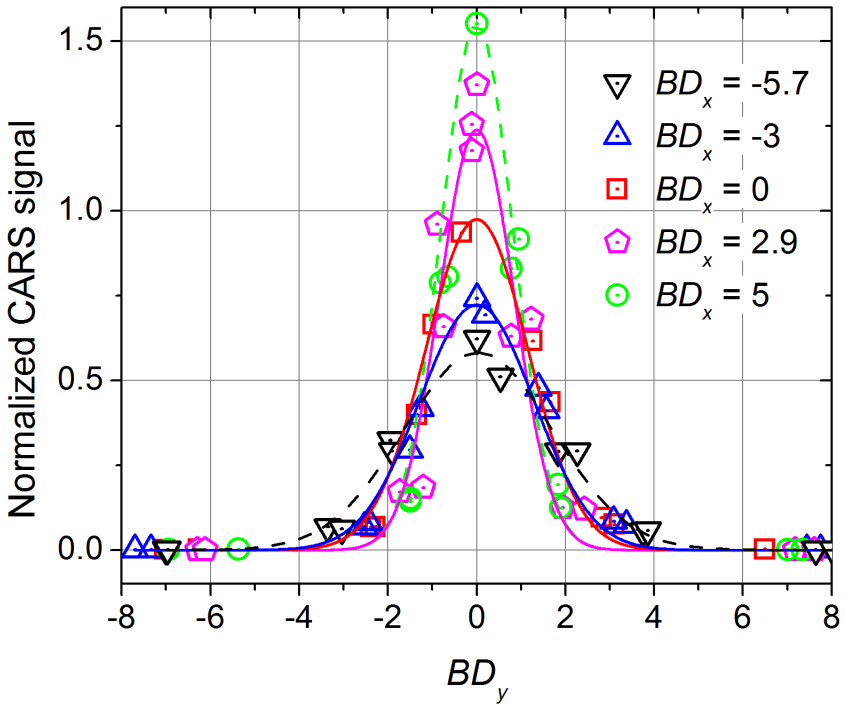

Figure 4-11: Sensitivity to combined "out-of-plane" and "in-plane" displacement for an elliptical Nd:YAG beam. Solid lines are a Gaussian fit

Figure 4-12 helps explain this behaviour. "In-plane" displacement shifts the crossing point away from the focal plane (the location of the narrowband, broadband and Nd:YAG laser "in-plane" foci). Figure 4-12 shows pictures of the Nd:YAG beam at the crossing plane, for the same values of "in-plane" displacement as plotted in Figure 4-11. Negative values of BD_x shift the crossing point toward the focusing lens,

therefore there is a small increase in the Nd:YAG beam major axis and an increase in the Nd:YAG minor axis and in the dye lasers diameters. Larger beam waists produce a weaker CARS signal that is less sensitive to "out-of-plane" beam displacement as shown in Figure 4-11. Positive "in-plane" displacement moves the crossing point toward the "out-of-plane" focus, therefore the major axis decreases and the minor axis increases. For $BD_x > 0$ the CARS signal is stronger, because of the increased irradiance of the Nd:YAG beam, but is more sensitive to "out-of-plane" displacement because of the reduced size of the Nd:YAG beam in the "out-of-plane" directions. These effects do not compromise the usefulness of beam shaping.

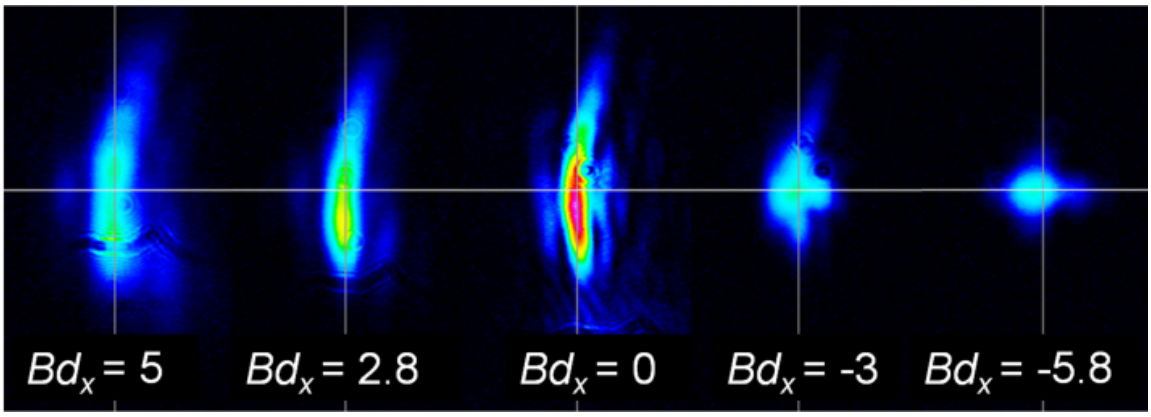

Figure 4-12: Nd:YAG beam at the location of the beam crossing where the crossing point is moved by "in-plane" displacement

The results presented above depend quantitatively on the diameters of the beams though the trends remain the same as diameters are changed. Figure 4-13 shows results obtained for the round beam and the 8:1 elliptical beam when the beam waist FWHM are 50, 60 and 120 microns for the Nd:YAG ("in-plane"), the narrowband and the broadband lasers, respectively. (Recall that in Figure 4-10, the beam diameters were 40, and 100 and 120 microns, respectively.) The FWHM of the

Gaussian fit to the data in Figure 4-13 is1.42 *BD* for the round beam and it is 8.1 *BD* for the elliptical beam. The increase in the width of the fit for the elliptical beam is associated with the smaller radius of the narrowband dye laser beam, *r*, used in the normalization to compute *BD*. Using small diameter Nd:YAG and narrowband dye laser beams without beam shaping make the conventional geometry very susceptible to beam steering, while using the elliptical beam makes the setup much more robust.

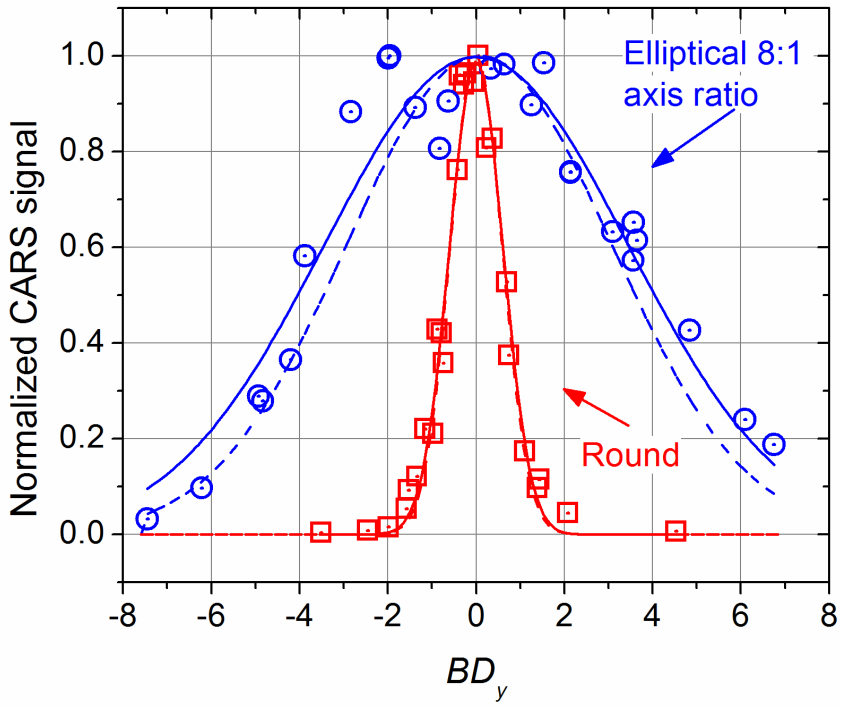

Figure 4-13: Sensitivity to "out-of-plane" displacement for round and elliptical Nd:YAG beam. The signal is normalized dividing by the peak signal. Continuous curves are Gaussian fits; dotted curves are obtained by numerical simulation

The dotted lines in Figure 4-13 are results obtained numerically using the algorithm introduced in the previous section, and assuming

$$\mu_y = BD_y r \tag{4-6}$$

for the dye lasers centroids. The numerical results predict a FWHM of 1.37 *BD* for the round beam (in agreement with the Gaussian fit to the experiment), and 7.1 *BD* for the elliptical beam (12% narrower). The validated numerical algorithm can be used to estimate the normalized CARS signal for any combination of "out-of-plane" beam displacement, beam diameters and Nd:YAG beam axis ratio.

The beam displacement experiment provides quantitative results which prove that the technique makes the CARS signal more insensitive to misalignment. The results can be used as guidelines to select an optimum axis ratio for the Nd:YAG beam in the presence of beam steering.

4.4.3 Turbulence Effects Experiment

Beam refraction caused by turbulence in variable density flows is a more complex problem than displacement due to vibrations. Two effects generally coexist: beam wandering and beam spreading. In these flows, density, and therefore index of refraction is not uniform either in space or time. Turbulent structures smaller than the beam refract some parts of the beam differently than others, increasing the beam diameter at the focus and making the beam irradiance profile more chaotic. Larger turbulent structures are responsible for the random wandering of the beam. Severe refraction effects are generally observed in large supersonic free jets [72] or the exhaust of jet engines [131], and high-pressure combustors [121, 122] because of long beam paths, large density gradients and high levels of turbulence. Replicating such flows in the laboratory was not feasible so only their effects on the beams are simulated. Variations in the index of refraction can be obtained through changes

either in pressure, temperature or gas composition. Helium has a very low refractive index in comparison to air; the difference in index of refraction between helium and air is roughly the same as the difference between air at 2300 K and room temperature air.

Turbulent effects were obtained through the device shown in Figure 4-14. A flow of 107 SLPM of helium enters a 25 mm internal diameter, "T" shaped pipe fitting, then bifurcates, generating two jets of helium. The two dye laser beams pass through the fitting. The Nd:YAG beam passes below the fitting and therefore it is only slightly affected by the flow. The device is placed 5 meters before the focusing lens. For this experiment the beam FWHM's at the measurement volume were 50, 60 and 120 μm for the Nd:YAG, narrowband and broadband lasers, respectively.

Figure 4-15 a) shows the narrowband dye laser centroid position normalized by its FWHM at the focal plane for 100 shots with and without the jet. The standard deviation of BD_y is 0.09 without the jet, 1.24 with the jet. Figure 4-15 b) shows single

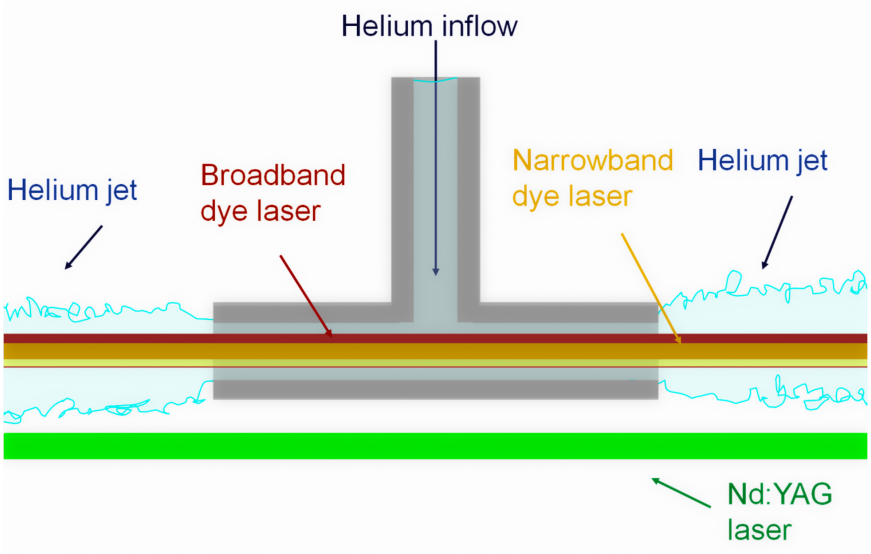

Figure 4-14: Schematic of the helium jet used to generate beam steering

shots images of the yellow beam at the focal plane. The image in the upper left corner was obtained without the jet, the others with the jet. The steering of the beam is clearly visible in this set of pictures, as well as the spreading effect due to turbulence. The beam is generally larger and the irradiance distribution is chaotic. The Nd:YAG beam does not pass through the pipe fitting and is only slightly affected by the helium jet; with no jet the standard deviation of BD_y is 0.2, and with the helium jet is 0.35 for the Nd:YAG beam. Displacements of the Nd:YAG beam cannot be neglected.

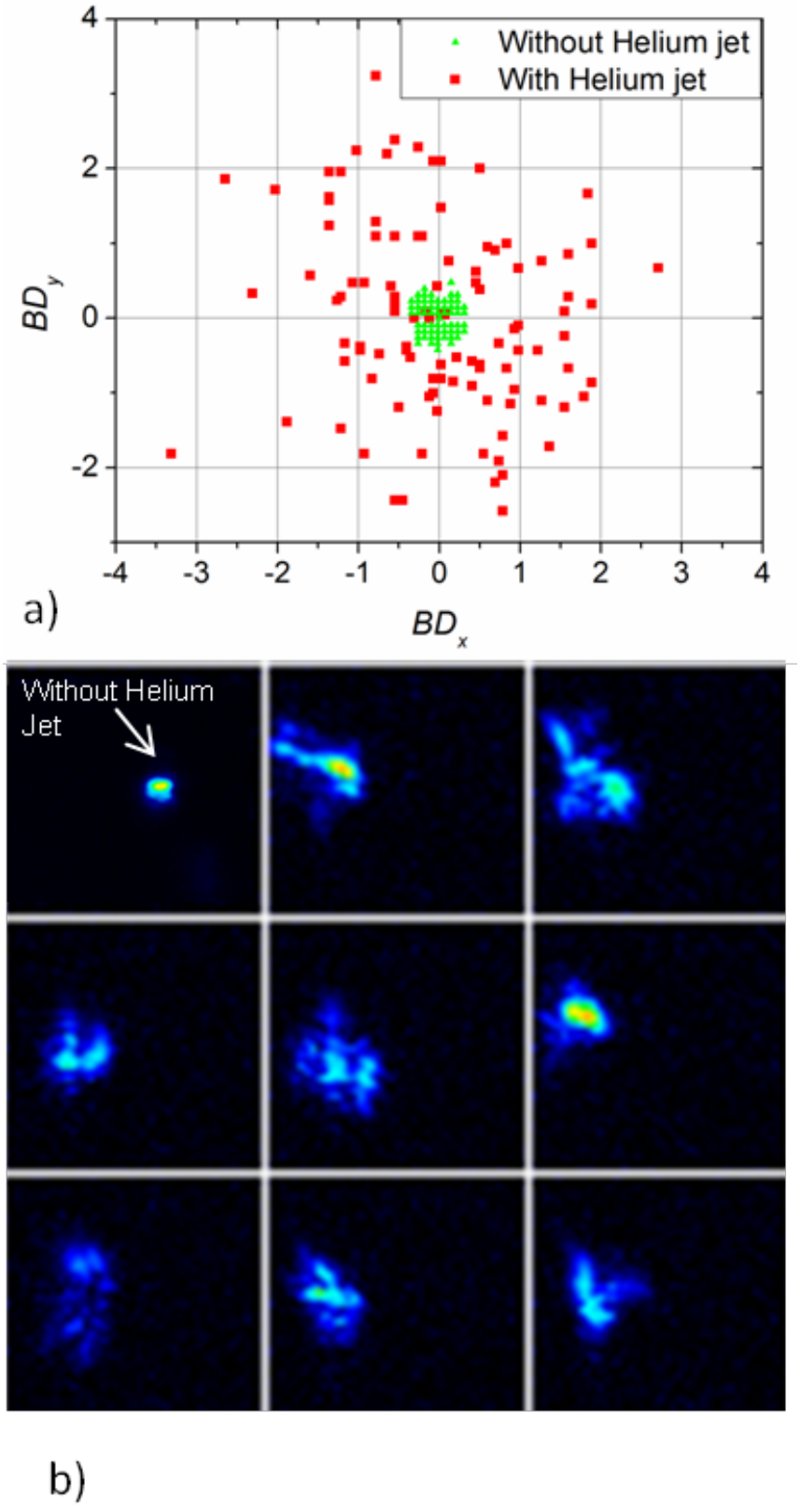

Figure 4-15: a) Centroid position of the narrowband dye laser with and without the turbulent helium jet; b) Images of the narrowband dye laser at the focal plane. The image on the left, upper corner is obtained without the helium jet

Five hundred ambient air spectra were collected with and without the helium jet for three axis ratios and the signal level evaluated as in the previous experiment. Figure 4-16 shows histograms of the signal level for the round and two elliptical beams without the helium jet. The irradiance of the Nd:YAG beam was tuned so that approximately the same signal level was obtained with the elliptical and the round beam. Signal levels are normalized by their average value. The use of the elliptical beam makes the CARS signal more stable even with the Helium jet turned off: The standard deviation of the signal level distribution is 11% of the average signal for the elliptical beam of axis ratio 8:1, is 15% for a 4.5:1 axis ratio and 24% for the round

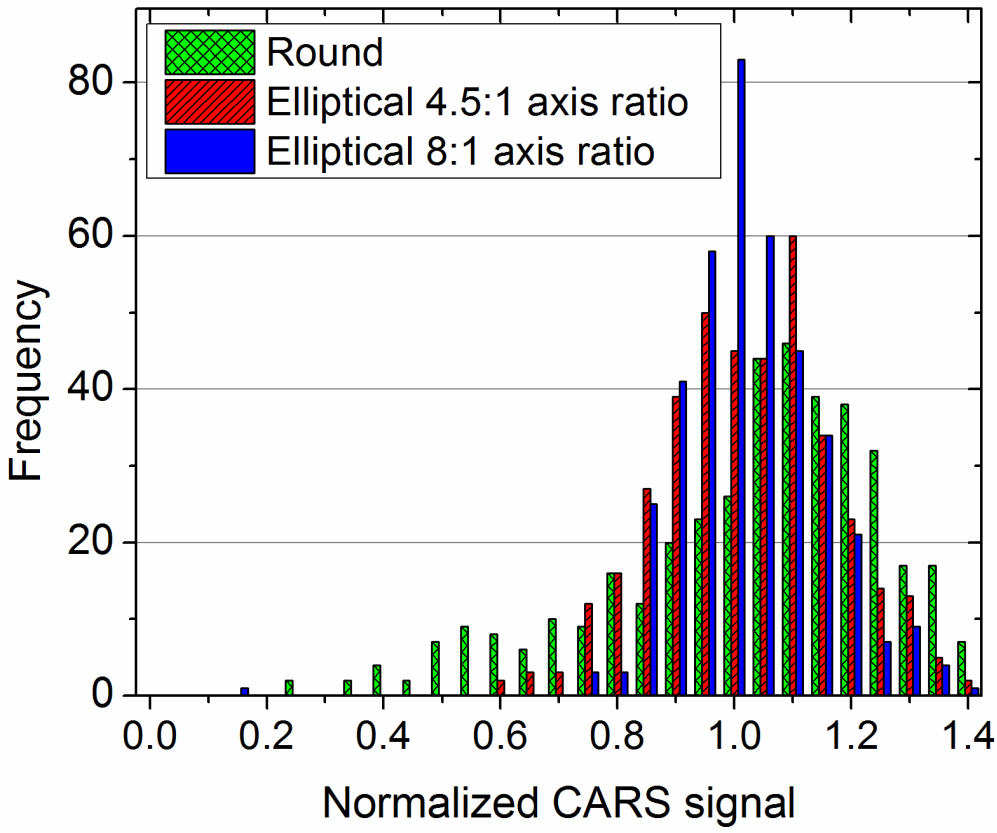

Figure 4-16: Histograms of the CARS signal for various axis ratios without the helium jet

beam, and for a round beam the histogram is no longer symmetric. The increase in the standard deviation is caused by beam steering. In fact the beams are aligned for optimum overlap, thus any beam steering can only lower the signal generating an asymmetry in the distribution.

CARS signal intensity is proportional to the product of the power of the three laser beams. Relative power fluctuations measurements for each laser were obtained by sending a small portion of the beam to a detector. Five hundred pulses for each beam were collected and analyzed. Measurements for each beam were not simultaneous. Since the Nd:YAG beam energy is a fixed fraction of the beams that pump the two dye lasers, some correlation in the power of the three beams is expected. To estimate the effect of the laser energy fluctuations on the CARS signal

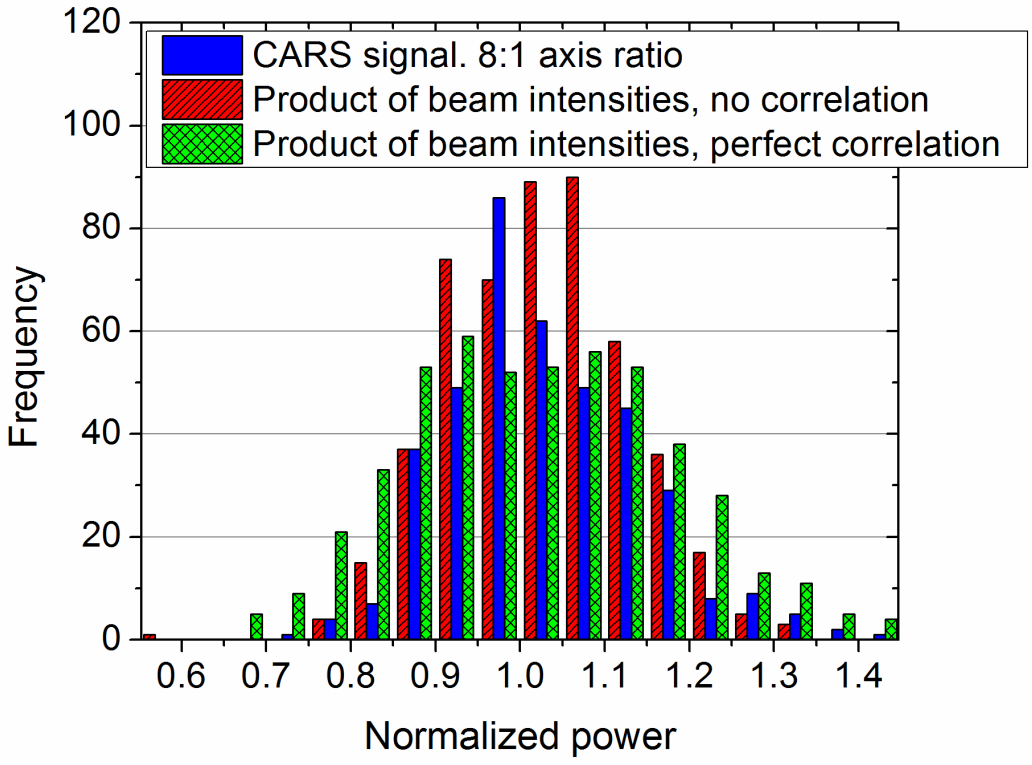

Figure 4-17: Comparison between the histograms of the CARS signal and the products of the laser intensities

the product of the three laser powers is evaluated in the two limit cases of full and no correlation. Physically full correlation implies that the fluctuation in the dye lasers are due exclusively to fluctuations in the pumping beam, no correlations assumes that factors other than the pump energy are predominant. The standard deviation of the product of the three laser powers is 11% of the average for no correlation and 18% for perfect correlation. Figure 4-17 compares the histogram of CARS signal obtained with an 8:1 axis ratio beam to the histograms of the product of laser intensities in the two limit cases. The CARS signal histogram lies within the two limit cases suggesting that for the 8:1 ratio the fluctuations are due mostly to power fluctuations, and not to beam steering. On the other hand, the round-beam results from Figure 4-16 show a much larger standard deviation (24% of the average) and cannot be attributed to pulse-to-pulse variations in laser intensity.

Figure 4-18 shows the results obtained with the helium jet flowing. CARS signal level is normalized dividing by the average signal level when the jet is off. The average signal increases with the increase in axis ratio, going from 8.2% for the round beam, to 20% for the 5:1 ratio, and 27% for the 8:1 ratio. The signal level distribution is broader for the elliptical beams; the standard deviations are 0.064, 0.126 and 0.129 for the round, 4.5:1 and 8:1 cases, respectively. More importantly, the signal standard deviations as a fraction of the mean decrease with elliptical beams, indicating a more steady and repeatable signal level. The change in the shape of the distributions as the ellipticity increases resembles the change in shape of a Poisson distribution as the number of samples is increased: for large ellipticity the distribution becomes more

Gaussian and the number of CARS spectra having very low counts becoming vanishingly small.

One of the major problems caused by beam steering is low data yield. [66, 120, 122] When the signal-to-noise ratio is too low, data have to be rejected. Assuming as 0.1 the threshold below which the data for this experiment are rejected, the data yield would be 30 % for the round beam, 76% for the 4.5:1, and 94% for the 8:1 ratio. The threshold chosen is completely arbitrary, but shows the effectiveness of the beam shaping technique in increasing the data yield.

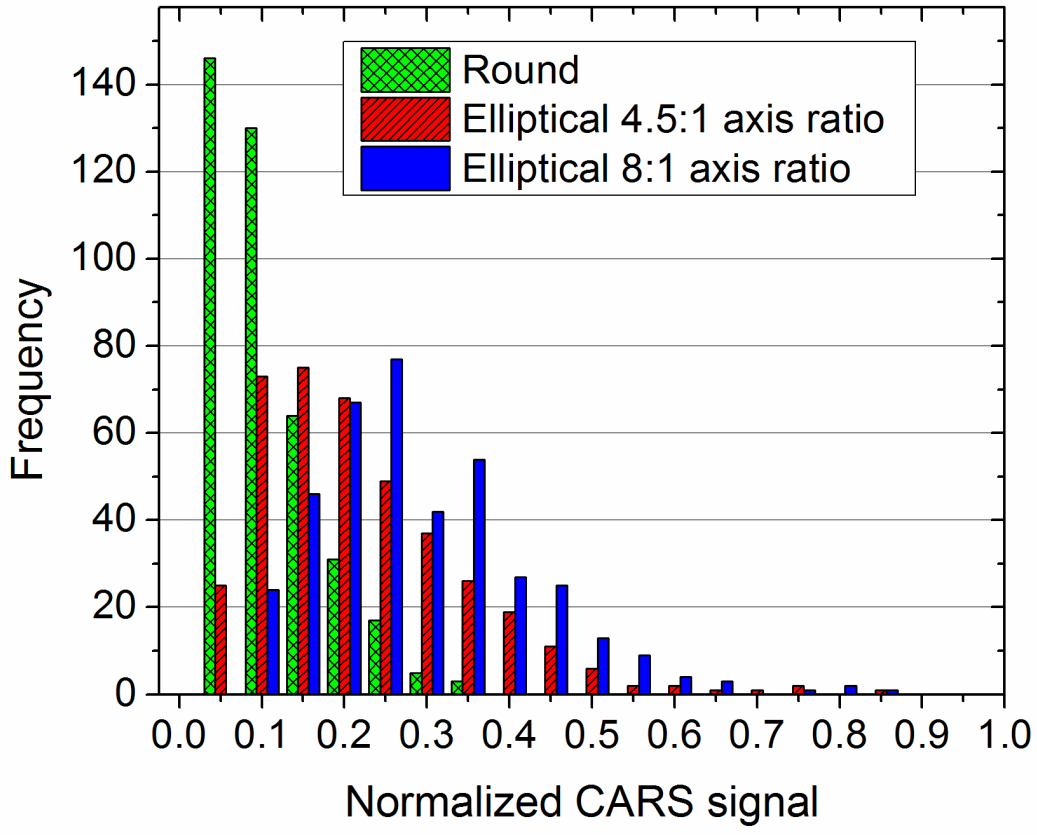

Figure 4-18: Histograms of the CARS signal for various axis ratios with the helium jet

4.5 **Modeling the Effects of Beam Spreading**

In the presence of the helium jet, laser power fluctuations, beam steering, and beam spreading affect the CARS signal level producing the histograms of Figure 4-18. Based on the experimental data collected, the effects on the CARS signal of the power fluctuations and of the beam wandering can be modeled, so that the effect of the beam spreading can be isolated. In an ideal case, where none of these perturbations are present, relative signal level would be constant and equal to 1. In the presence of power fluctuations, based on the results shown in Figure 4-16 and Figure 4-17, the CARS signal level has a Gaussian distribution with average 1 and standard deviation 0.11. According to the results of the beam displacement experiment (Figure 4-13), the relative signal level S_{CARS}, in the presence of the beam steering, can be expressed as a Gaussian function in BD_y with standard deviation σ_e, (equal to FWHM/2.35), of 0.6 for the round beam, 3.44 for the 8:1 axis ratio elliptical beam. When both beam steering and power fluctuations are present, the relative signal level can be expressed as:

$$S_{CARS} = F_{P3} \cdot \exp\left(-\frac{BD_y^2}{2\sigma_e^2} \right) \tag{4-7}$$

F_{P3} takes into account the effect of the random power fluctuation and BD_y, the beam displacement in the "out-of-plane" direction. F_{P3} and BD_y are normal random variables: $F_{P3} \sim N(1, 0.11)$, and $BD_y \sim N(0, 1.24)$. Means and standard deviations of the Gaussian distributions are obtained from experimental results discussed in the previous section. The function $N(\mu, \sigma)$ indicates a generic random variable with Gaussian distribution of mean μ and standard deviation σ. Beam displacement in the x

direction ("in-plane") is neglected. A numerical experiment has been performed giving as input to Eq. (4-7) five hundred values of P_3 and BD_y extracted randomly from their respective distributions. The results are representative of what would have been obtained experimentally if the beam spreading effect was negligible.

Figure 4-19 shows histograms of the numerical results. For the round beam the average normalized signal is 0.43, its standard deviation 0.38, and 32% of the values are below 0.1. For the elliptical beam the average is 0.93, standard deviation 0.14, and the signal is always above 0.1. However the average values are lower in the

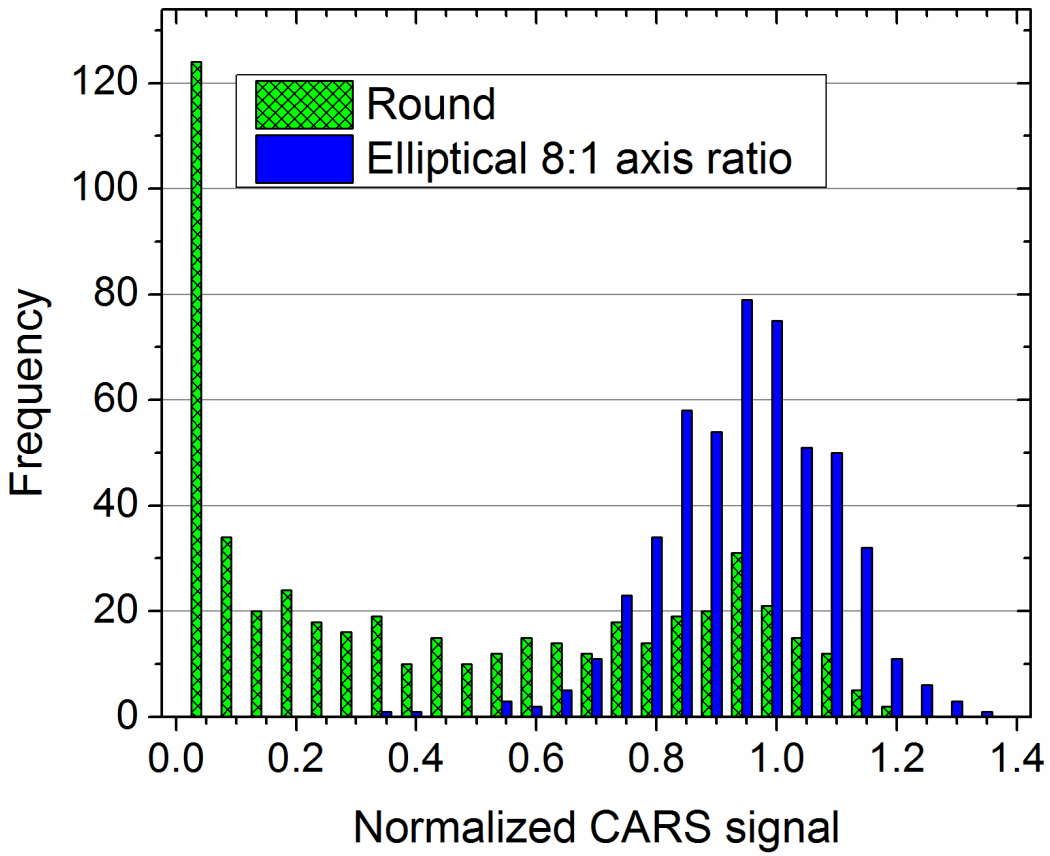

Figure 4-19: Histograms of the CARS signal computed with the helium jet, neglecting beam spreading

experimental results (Figure 4-18) because the spreading makes the beam diameter larger at the focal plane. The reduction of the irradiances of the beams causes a clustering of the data in the lower bins. However the increased size of the beams makes the signal less sensitive to the beam steering. When using a round beam, these two effects combined produce a lower standard deviation relative to the mean in the experimental data than in the computed values.

Beam spreading can be added to the numerical model to simulate the effect of the turbulent helium jet on CARS signal. For each beam a spreading coefficient is defined as the ratio of the beam diameters with and without the turbulent jet flowing

$$D = \left(D_x, D_y \right) = \left(\frac{\sigma_x^{(turbulent)}}{\sigma_x}, \frac{\sigma_y^{(turbulent)}}{\sigma_y} \right) \tag{4-8}$$

Average and standard deviation of the spreading coefficient were evaluated from focal plane images of fifty single shots of the yellow beam taken with the turbulent jet flowing (similar to what shown in Figure 4-15 b). From these measurements the D of the narrowband lasers have a normal distribution: $D_x \sim N(1.53, 0.27)$ and $D_y \sim N(2.86, 1.03)$. The same distribution is used for the broadband. In the presence of beam spreading, beam steering and power fluctuations the CARS signal level can be estimated as

$$S_{CARS} = F_{P3} \cdot P_{CARS} \tag{4-9}$$

P_{CARS} is evaluated from Eq.(4-1) using the algorithm previously described in this paper. The irradiance of the narrowband and broadband beam is given by Eq. (4-2) but the parameters μ and σ are modified by beam wandering and spreading respectively:

$$(\mu_x, \mu_y) = (\tan(\alpha) - BD_x \cdot r, BD_y \cdot r) \tag{4-10}$$

$$(\sigma_x^{(turbulent)}, \sigma_y^{(turbulent)}) = (D_x \cdot \sigma_x, D_y \cdot \sigma_y) \tag{4-11}$$

F_{P3}, BD_x, BD_y, D_x, and D_y are normal random variables with mean and standard deviations evaluated experimentally.

A numerical experiment has been performed, evaluating the CARS signal level for five hundred values of the random variables above. Figure 4-20 compares the numerical results to the experimental results. The numerical simulation predicts an average signal of 0.1 for the round beam, and 0.28 for the elliptical beam, only slightly higher than the measured 0.08 and 0.26. The standard deviations obtained

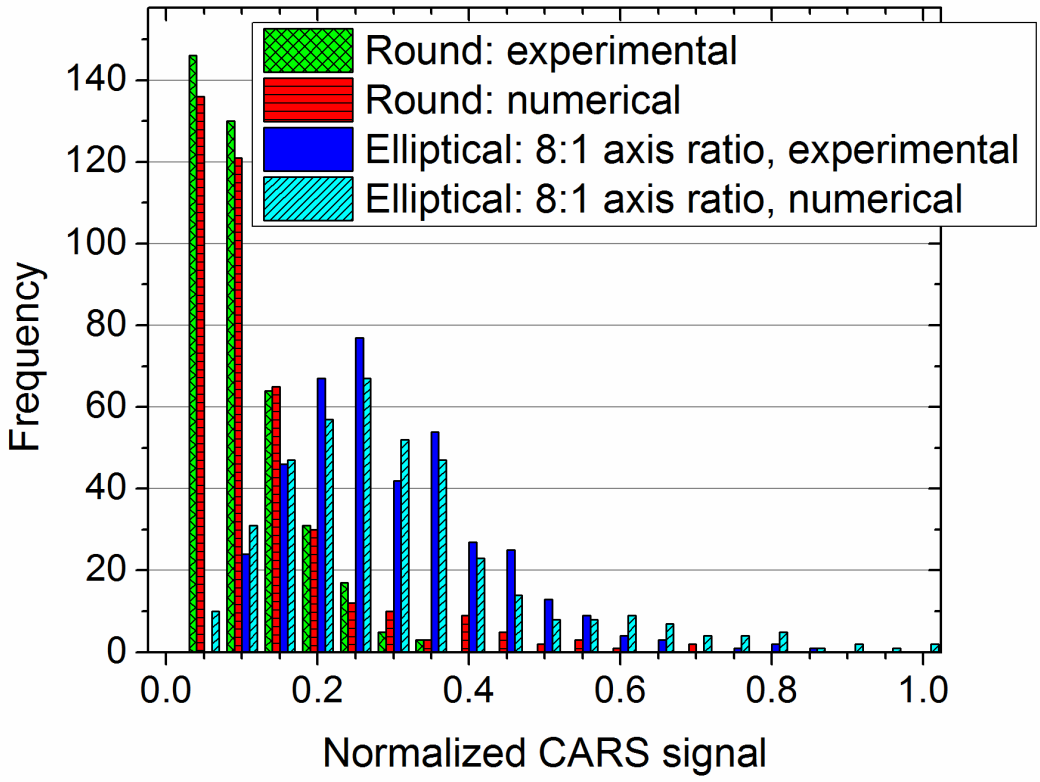

Figure 4-20: Histograms of the CARS signal with the helium jet from experiments and numerical simulations including beam spreading

numerically are 0.11 and 0.16, compared to 0.06 and 0.13 experimentally. The discrepancy between the numerical and experimental results is consequence of the simplifying assumptions in the modeling, but the agreement is surprisingly good given the complexity of the problem. The validated numerical model can be used to predict the CARS signal level distribution, for any given beam steering conditions and beam diameters, and therefore determine the optimal axis ratio for given experimental conditions.

CHAPTER 5 -High Irradiance Perturbation Effects

5.1 **Introduction**

The CARS signal amplitude is proportional to the product of the beam irradiances and to the square of the probe volume length. However it is highly desirable to reduce the length of the measurement volume so that smaller turbulence structures can be resolved. The measurement volume size can be reduced by using shorter focal length lenses to focus the beams to a smaller diameter and shorter crossing length, for example. Sensitivity of CARS spectra to Stark broadening and saturation is strictly intertwined with the spatial resolution. Generally, CARS spatial resolution for combustion measurements at atmospheric pressure is 1-2 mm long, typically insufficient to resolve the smallest turbulence structures. Focusing the beams more tightly, reduces the probe volume length, while maintaining a good signal-to-noise ratio. Unfortunately focusing more tightly may cause optical breakdown, saturation or Stark broadening because of the increased irradiance.[79, 120, 132, 133]

At low irradiances CARS is a non-intrusive technique and the collected spectral shapes are independent of the laser irradiance. At sufficiently large irradiances, the large electric field generated by the focused pulsed lasers induces a dipole moment in homonuclear molecules and causes a shift and a broadening of the transition line (Stark broadening). The magnitude of this effect is directly proportional to the electric field, and therefore to the sum of the irradiances of the three beams. Further increasing the electric field amplitude, the gas may “break down”, generating a spark and becoming ionized.

Large values of the product of the pump and Stokes irradiance can also cause stimulated Raman pumping (SRP), which is the process of changing the population distribution of the rotational and vibrational states being probed by the CARS process. This is a saturation mechanism and causes a reduction of the CARS signal in the ground vibrational band and an increase in higher vibrational bands. The effects of high irradiance perturbations on CARS measurements has been previously investigated, [132-135] but no systematic study of high irradiance perturbation effects in dual-pump CARS measurements of temperature and multiple species concentration was found in the literature.

The goal of the study described in this chapter is to provide guidelines to discern the presence of such perturbations in experimental spectra, estimate their effects on measurement accuracy, and validate criteria to determine the threshold below which these effects are negligible. A background section provides a short review of previous theoretical and experimental works on saturation and Stark broadening. Simple theoretical models, previously proposed by other authors, are applied to the specific conditions of our dual-pump CARS system. It provides a framework to correctly interpret the changes in spectral shapes observed in the experimental CARS spectra, discussed later in the chapter. It also provides simple criteria to determine perturbation thresholds. Then, a results and discussion section describes experimental results obtained for several levels of irradiances in ambient air, fuel-lean and fuel-rich flames. This is the first systematic, experimental study investigating, the effect of high irradiance spectral perturbations on dual-pump (DP) CARS measurements of temperature and absolute concentration. The role of temperature in changing CARS

signal sensitivity to high irradiance effects is experimentally observed. Saturation and Stark broadening thresholds are determined and compared to the theoretical criteria.

5.2 **Background**

Several research groups investigated the effects of Stark broadening and saturation on CARS spectral shape, both theoretically and experimentally. This section presents a brief review of the findings published in these works. The section is divided in two sub-sections, one dealing with Stark broadening, the other with saturation. In each subsection, first we describe the physics of the process, based on simple models introduced by other authors. Changes applied to the models specific to our dual-pump CARS instrument are discussed. Criteria to determine irradiance thresholds for a dual-pump CARS system are proposed. We also review some of the experimental work from previous authors, with emphasis on providing guidelines to identify the high irradiance effects in experimental spectra. The few available works dealing with the effects of Stark broadening and saturation on temperature and concentration measurements are reviewed.

Optical breakdown has not been investigated experimentally for this work. Clean air breakdown threshold are ~ 350 GW/cm^2, [136] and values up to 1000 GW/cm^2 are anticipated in clean flames. [137] These values are higher than the Stark broadening and stimulated Raman pumping thresholds, therefore optical break down is not the liming factor in setting the laser irradiances. Threshold values in practical applications are much lower because of the presence of dust or large particles in the gas. Occasional breakdowns, occurring when the lasers hit these large particles, are

allowed for, and are removed in pre-processing. In the presence of breakdown the CARS signal is completely destroyed; therefore the occasional breakdowns can be easily identified and removed during the data pre-processing. Less than 5% of the spectra collected in room temperature air present optical breakdown. This percentage is much lower in flames, and the overall percentage of breakdown spectra is less than 0.3 % of the total for the data set discussed in Chapter 8.

5.2.1 Stark Broadening

To generate the CARS signal, three pulsed laser beams are crossed at the common focal spot, generating a strong electric field. For molecules having no permanent dipole (such as N_2, O_2 and H_2), the electric field induces a small dipole moment, proportional to the electric field itself. [88] The electric field interacts with the induced dipole, changing the energy level of each state by an amount proportional to the irradiance (quadratic Stark effect). The dipole moment is a function of the rotational and the orientational (magnetic) quantum number; it also depends on the vibrational quantum number through the polarizability tensor. The change in the energy levels, induced by the Stark effect, causes a shift of the Raman transitions to lower frequencies. Because of the dependency of the dipole moment on the magnetic quantum number, the orientational degeneracy is lifted and line splitting occurs in the presence of a strong electric field. For S-branch transitions, the frequency Stark shift of each energy sublevel can be expressed as: [138], [139]

$$\Delta\nu_{v,j',m}^{v,j,m} = \frac{I_{Total}}{hc}\left[\frac{1}{3}\gamma_v^v\left(\frac{3m^2 - j'(j'+1)}{(2j'-1)(2j'+3)} - \frac{3m^2 - j(j+1)}{(2j-1)(2j+3)}\right)\right] \qquad (5\text{-}1)$$

where I_{Total} is the total irradiance defined as the sum of the average irradiances of all the beams present; γ is the anisotropic part of the polarizability tensor; v, j, and m are the vibrational, rotational and magnetic (orientational) quantum numbers of the lower state of the transition; v', j', m' are the quantum numbers of the upper state of the transition. S-branch transitions are characterized by $\Delta v = 0$ and $\Delta j = 2$. Equation (5-1) is valid when the polarizations of all lasers are parallel, for which only transitions with Δm=0 are allowed. The magnetic quantum number m can assume values between $-j$ and j, and appears squared in the equation above. The electric field splits a given transition into j+1 sub-lines which are double degenerate, except for the one with m=0. The fractional strength, F, of a sub-level is defined as the ratio of its intensity to the sum of the intensity of all sub-lines in a given transition. For S-branch transitions, it can be computed as:

$$F_{j+2,m}^{j,m} = \frac{15}{2}\frac{\left[(j+2)^2 - m^2\right]\left[(l+1)^2 - m^2\right]}{(j+1)(j+2)(2j+1)(2j+3)(2j+5)} \tag{5-2}$$

In broadband CARS the spectral resolution is not sufficient to resolve the splitting, thus the lifting of the orientational degeneracy causes a broadening of the line. For Q-branch transitions, expressions for the Stark shift and the fractional strength can be found in Ref. [138].

The Stark effect strongly perturbs the spectral shape of the Raman transitions, causing a shift and a broadening of the lines. Stark perturbations have been observed in Raman spectra of all the molecules of interest for this work (O_2, N_2, and H_2). Rahn [140] observed a shift of 0.12 cm^{-1} in the H_2 S(3) line when applying 200 mJ of infrared (IR) light focused to a 80 μm focal spot. Splitting of the S(2) and S(6) pure

rotational lines of N_2 were observed by Farrow. [139] Dyer [141] measured Stark shift and splitting for the Q(0) and Q(1) H_2 lines. Owyoung [142] reported Stark shift and splitting for the pure rotational transitions of O_2. In the Q-branch rotational-vibrational manifold the transitions are not isolated lines. Each line interacts with its neighboring lines through constructive interference, affecting the amplitude and the line shape of the transitions and reducing the peak-to-valley ratios. [140]

In all the works listed above, an intense IR laser beam superimposed on the Raman spectra generating beams provided the strong electric field that generated the Stark effect. The focal waist and the pulse length of the IR beam were twice or more the size of the other beams, so that the electric field producing the Stark shift was spatially and temporally uniform. In more typical CARS applications, where this extra laser beam is absent, the total irradiance is not constant in the region where the CARS signal is generated, either in space, or time, leading to asymmetrical broadening of the rotational-vibrational lines. Moosmuller [138] investigated Stark broadening of N_2 Q-branch CSRS spectra in a collinear phase matching configuration. [87] In a collinear geometry, a significant portion of the signal is generated in low irradiance regions where the Stark effect is negligible. Therefore the overall Stark broadening is smaller than in the more typical crossed beam geometry where the signal generation is confined to a relatively high irradiance region. Herring [143] observed that in a crossed beam geometry, with crossing angles above one degree, the Stark broadening is doubled as compared to a collinear geometry.

Detailed models that integrate the Stark broadening into the computation of the CARS susceptibility have been proposed [132, 143, 144] but are computationally

intensive and require a good knowledge of the distribution of the irradiance over the entire measurement volume. Fluctuations in the laser power, vibrations, and beam steering effects in real world environments prevent a good knowledge of the irradiance distribution over the entire CARS probe volume, limiting such models to very controlled environments.

CARS concentration and temperature measurements are typically obtained by fitting an experimental spectrum to a theoretical one. Since Stark effects are generally not included in the theoretical model, large electric fields can compromise the accuracy of the measurements. CARS fitting codes can generally fit experimental spectra containing Stark broadening to theoretical models that do not include these effects, [132, 135] but the fitted temperature and concentration may be inaccurate. Vibrational temperature measurements obtained this way are not very sensitive to Stark broadening since the mechanism acts on all the vibrational levels in a similar way, although errors of 20-30 K in temperature have been observed at sub-atmospheric pressure. [132] Rotational temperature obtained from isolated lines, such as the H_2 S transitions considered in this study, are affected because of the j dependence of the Stark shift.

Measurements of the ratio of mole fractions of O_2 to N_2 are not sensitive to Stark broadening because the broadening effects on the Q-branch of these species are similar. The effect of Stark broadening on the isolated H_2 lines is different than on the N_2 Q-branch manifold, making the measurements of the ratio of H_2 to N_2 sensitive to the total irradiance, as will be shown later in this chapter. Absolute mole fraction accuracy is compromised by Stark effects because the broadening reduces the

amplitude of the resonant lines, but leaves the non-resonant baseline unperturbed. [135] Since Stark broadening compromises the measurement accuracy, it is critical to maintain the total irradiance sufficiently low that its effects are negligible. A crude criterion to determine if Stark broadening is significant is to compare the average Stark shift to the Raman transition linewidth (full-width at half maximum, FWHM), Γ_R. For

$$\overline{\Delta\nu_{Stark}} < \Gamma_R \tag{5-3}$$

Stark broadening can be neglected. A similar approach was proposed by Péalat. [144-146] This criterion uses the average Stark shift, computed using a simple algebraic formula given in Eq. (5-4), as a rough index of the Stark broadening.

$$\overline{\Delta\nu_{Stark}} = \sum_{m=-j}^{j} F_{j',m}^{j,m} \Delta\nu_{v'j',m}^{v,j,m} \tag{5-4}$$

Figure 1a shows the variation of the Voigt linewidth (FWHM) of the N_2 Q(5) transition with temperature, computed using CARSFT [108] with negligible instrument linewidth. Figure 1b shows the average Stark shift (Eq. 5-4) for the N_2 Q(5) line against the total irradiance.

The values of the fractional strength and Stark shift for each sublevel of the N_2 Q(5) transition are taken from Ref. [138]. It turns out that the average Stark shift is only a weak function of the rotational quantum number, so the Q(5) line is representative of the whole first vibrational band. Through a simple graphical procedure, the plots in Figure 5-1 allow for the determination of the Stark broadening total irradiance threshold for a given temperature. The graphical procedure is as follows: locate on the horizontal axis in Figure 5-1 a) the given temperature and draw a vertical line to find the intersection with the linewidth curve; the ordinate of the intersection is the computed linewidth. From the intersection draw a horizontal line that intersects the estimated Stark shift line in the plot of Figure 5-1 b). The abscissa of the intersection is the total irradiance threshold below which Stark broadening is avoided, according

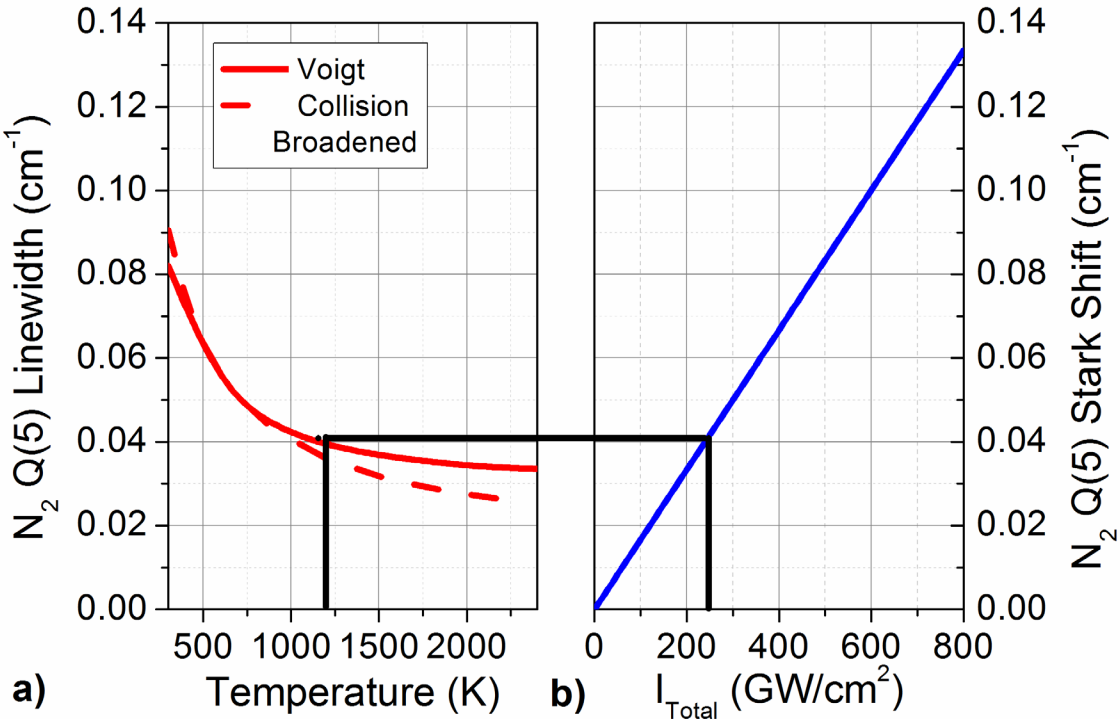

Figure 5-1: a) Voigt (continuous) and collision broadened (dashed) N_2 Q(5) linewidth (FWHM) as function of temperature; b) Estimated Stark shift as function of the total irradiance

to the criterion of Eq. (5-3). It may be concluded from Figure 5-1 that increasing temperature reduces the N_2 linewidth, and therefore Stark broadening is a more serious limitation for high-temperature environments. Experimental results, discussed later in this chapter, show that the simple criterion can correctly predict the presence of Stark broadening in N_2 spectra. N_2 and O_2 have similar molecular parameters; therefore it would be expected that the Stark broadening perturbs those molecules in a similar way.

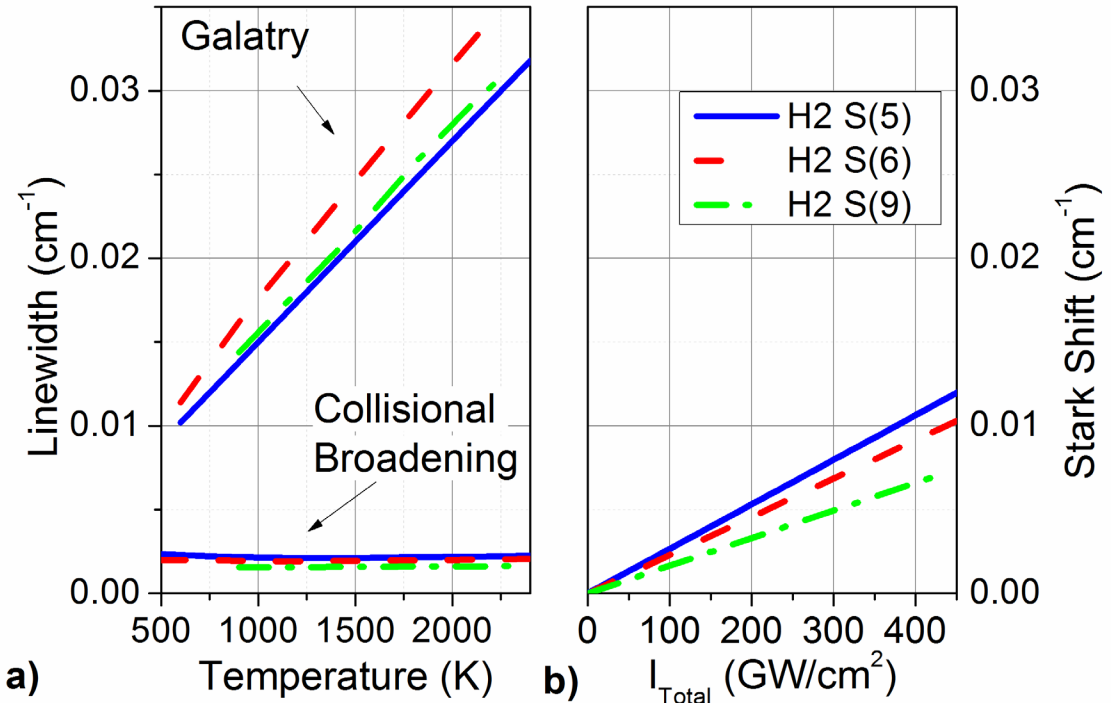

Figure 5-2:a) Collision-broadened and Galatry linewidth (FWHM) for three H_2 rotational lines as function of temperature; b) Estimated Stark shift as function of the total irradiance

Figure 5-2 a) shows the variation of the collision-broadened and the Galatry linewidth (FWHM) of the H_2 S(5), S(6) and S(9) transitions at atmospheric pressure with temperature. Figure 5-2 b) shows the estimated Stark Shift for the three lines with total irradiance. The estimated Stark shift is computed using Eq. (5-1) and Eq.

(5-2) using a polarizability anisotropy γ [147] of 7.1×10^{-25} cm^3. The same graphical procedure described for Figure 5-1 can be used to determine the Stark broadening threshold for the H_2 lines. For total irradiances between less than 450 GW/cm^2 the criterion predicts no Stark broadening, if the Galatry model is used to compute the Raman linewidth Γ_R. This is in contrast with the experimental observations as shown later in this chapter.

The criterion to estimate the Stark broadening, presented in this section, is obtained from crude approximations of the physical mechanism involved. Stark broadening is a consequence of the lifting of the orientational degeneracy and of spatial and temporal non-uniformity of the electric field. Obviously this cannot be accurately modeled through the Stark shift alone.

5.2.2 Stimulated Raman Pumping

When the product of pump and Stokes beams irradiance is sufficiently high, the number of transitions from the ground state to an excited state, by a process known as stimulated Raman pumping (SRP), becomes significant. [87] This process is a two photon process which occurs simultaneously with the CARS process and reduces the population difference between the ground and the excited state. The rate of change of population difference (slump rate) for monochromatic beams can be approximated by: [77, 148]

$$\frac{1}{\Delta N}\frac{\partial \Delta N}{\partial t} = 2\left(\frac{4\pi c}{\hbar \omega_S^2}\right)^2 \left(\frac{\partial \sigma}{\partial \Omega}\right) \frac{\Gamma_R}{4(\Delta\omega)^2 + \Gamma_R^2} I_p I_S = \tau_{\Delta N}^{-1} \tag{5-5}$$

ΔN is the unperturbed population difference, $\left(\frac{\partial\sigma}{\partial\Omega}\right)$ the Raman cross section, I_pI_S the product of the pump and Stokes beam irradiances, and Γ_R is the Raman linewidth; $\Delta\omega$ is a detuning factor given by $\omega-(\omega_p-\omega_s)$, where ω, ω_p and ω_s are the transition, the pump and the Stokes circular frequencies, respectively. The probe beam does not contribute to SRP. The CARS signal is proportional to the product of the three irradiances of the pump, probe and Stokes beams and to the square of the population difference. Stimulated Raman pumping is often referred to as saturation, because, when present, the CARS signal increases less than linearly with the irradiance. As the pump-Stokes irradiance product becomes large, the increase in signal caused by the higher irradiance and the decrease caused by SRP balance out and the CARS signal becomes a function of only the probe beam irradiance. The change in population is most intense at the resonance frequency ($\Delta\omega$=0) and rapidly decreases off resonance, causing the appearance of a dip at the centerline of saturated high resolution narrowband CARS spectra. This feature has been observed experimentally in both N_2 [149, 150] and H_2 [151, 152] lines, and several detailed models have been developed to accurately predict it. [144, 153-155] Stimulated Raman pumping perturbs broadband CARS spectra in a very different way than narrowband CARS. In broadband CARS the dip is no longer observed because of the low spectral resolution, but the spectra are modified due to the change in population distribution. Broadband CARS of a Q-branch manifold allows simultaneous probing of the SRP induced population changes. For room temperature air spectra, only the ground vibrational state is thermally populated and CARS probes v=0→1 transitions; SRP pumps molecules to higher vibrational states, and vibrational transitions between higher

states appear in the CARS spectra. For example, SRP-induced population of three vibrational bands of N_2 at room temperature was observed experimentally by Gierulsky. [134]

Changes in the spectral shape of N_2 and O_2 Q-branch due to SRP result in errors in fitted parameters, such as temperature, concentration and pressure. At high temperature, higher vibrational states are populated, according to a Boltzmann distribution, causing the appearance of "hot bands". SRP-induced population changes also cause the appearance of "hot bands". A CARS fitting code will fit the "hot bands" to higher temperatures. A fitted vibrational temperature of 2550 K was reported by Gierulsky [134] for highly saturated room-temperature spectra. Ground-state rotational temperature is unaltered because SRP is similar for all the rotational-vibrational transitions. [134], [149] Similar effects on N_2 vibrational temperature measurement were reported by Woodmansee [132] and by Kroll.[133]

Stimulated Raman pumping, by altering the observed CARS transition amplitudes, causes errors in fitted mole fractions. Broadband dye lasers used in CARS are spectrally non-uniform, therefore SRP will be more intense for transitions pumped near the peak of the Stokes laser spectrum (which occurs for the O_2 Q-branch in this set-up) and weaker for transitions pumped by the tails of the Stokes laser (N_2 Q-branch and H_2 S(5) in this set-up). Different species also have different Raman cross sections and linewidths, therefore effects on population may differ. In DP-CARS, when the two pump beams have different irradiances, SRP will be different in molecules pumped by one or the other pump beam. Non-uniform SRP across the spectral range of Raman shift probed causes variations in the ratio of N_2 and O_2 mole

fraction, since the Stokes beam irradiance can differ by a factor or two or more for one molecule than the other.

In broadband CARS, Eq. (5-5) is still valid as a crude estimate of the rate of change of population difference, but only a small portion of the Stokes irradiance contributes to the SRP process. Integrating Eq. (5-5) over the Raman linewidth $\Gamma_{R,}$ the rate of change in population difference can be expressed as:

$$\frac{1}{\Delta N}\frac{\partial \Delta N}{\partial t} = \pi\left(\frac{4\pi c}{\hbar\omega_S^2}\right)^2\left(\frac{\partial\sigma}{\partial\Omega}\right)I_p\frac{\beta I_S}{\Delta\omega_S} = \tau_{\Delta N}^{-1} \tag{5-6}$$

The group $\frac{\beta I_S}{\Delta\omega_S}$ approximates the spectral irradiance of the Stokes beam at the transition frequency ω_s. $\Delta\omega_s$ is the FWHM of the broadband dye laser. This approach, by Woodmansee [132], is modified by the coefficient β which is the ratio between the Stokes spectral irradiance at ω_S and the peak Stokes spectral irradiance, which takes into account the spectral dependence of the Stokes beam. To prevent the loss of measurement accuracy caused by SRP, it is necessary to limit the product of the pump and Stokes beam irradiances. A simple criterion to determine the threshold can be derived from the simple theoretical model discussed above. Equation (5-6) is integrated to obtain the population difference as function of time:

$$\Delta N(t) = \Delta N(0)e^{(-t/\tau_{\Delta N})} \tag{5-7}$$

If the SRP characteristic time $\tau_{\Delta N}$ is much longer than the laser pulse length τ, then the change in the population difference is negligible.

$$\tau_{\Delta N} >> \tau \tag{5-8}$$

Woodmansee estimated a threshold of 3600 GW^2/cm^4 to prevent significant SRP in broadband N_2 CARS for a 1900 GHz width of the Stokes laser and 10 ns pulses. The criterion was validated for ambient air temperature measurements, but no data were presented for concentration measurements.

Wilson-Gordon [153] showed that Eq. (5-5) is mathematically accurate only for conditions where SRP is negligible, and is only a rough estimate otherwise. Pressure and molecular motion effects are neglected in the SRP model considered. By increasing pressure, collisional transfer out of the laser-pumped upper rotational levels becomes significant and reduces SRP effects. [155] Molecular motion may move the saturated molecules out of the measurement volume replacing them with unsaturated ones. This becomes significant when the transit time through the measurement volume is comparable to the pulse length, which is true for light molecules at high temperatures. [144]

Because of these simplifications intrinsic to the Stark broadening and SRP threshold criteria, they need to be validated for dual-pump CARS for specific methods and test conditions. Experimental data are especially needed to validate the above criteria for concentration measurements since little information is available in the literature. The work described in this chapter attempts to fill this gap through a systematic, experimental study of the effect of varying irradiances on temperature, mole fractions, and the ratios of mole fractions of different species. This present validation is limited to dual-pump CARS measurements of temperature, N_2, O_2 and H_2 mole fractions in quiescent air and H_2-air flames at ambient pressure.

5.3 **Experimental Set-up**

Details of the DP-CARS instrument used for the experimental portion of this work are in Chapter 3. Planar BOXCARS, having the narrowband and the broadband dye lasers overlapped, is the phase-matching geometry chosen for this instrument. Two distinct lenses focus the beams at the measurement volume. A 500 mm focal length lens focuses the Nd:YAG beam; the lens is tilted so that, it shapes the focal spot at the beam crossing to a roughly 4:1 axis ratio ellipse with the major axis orthogonal to the plane formed by the three laser beams (Chapter 4). Three interchangeable lenses of focal lengths 300, 500, and 850 mm are available to focus the two, overlapped dye lasers; this allows control of the energy density at the measurement volume. The beam viewing system (see Chapter 3) is used to image a cross section of the three beams in the vicinity of the measurement volume, and to measure the dimensions of the beams at their focus, needed to compute the irradiances.

The maximum energy per pulse at the measurement volume for the Nd:YAG, the narrowband laser, and the broadband laser, are respectively: 90, 30, and 20 mJ. The beam irradiances at the measurement volume can be controlled by reducing beam energies and by selection of lens focal length. A larger spot size at the focus decreases the irradiance, but also increases the size of the measurement volume, allowing an increased signal at lower irradiances. Using a combination of these two mechanisms the total irradiances is varied in the 80-800 GW/cm^2 range and the pump-Stokes products in the 10^2-10^5 GW^2/cm^4 range, while keeping sufficient signal-to-noise ratio

at flame temperatures. The irradiance reported in this work is the average irradiance computed as:

$$I = \frac{E}{\pi r^2 \tau} \tag{5-9}$$

where E is the laser energy per pulse, r is the e^{-2} radius at the focus and τ the pulse length. The pulse length (FWHM) of the Nd:YAG, narrowband and broadband dye laser are 10, 6.5, and 5 ns respectively. They have been measured using a fast (<1 ns time response) photodiode connected to a 1 GHz oscilloscope. The focal spot dimensions are determined from images collected on the beam viewing system camera.

The other variables considered in this test are the temperature and composition of the flow probed. In addition to ambient air, a Hencken burner, producing a laminar, roughly homogeneous, nearly adiabatic H_2-air flame, provides the test medium for this work (Chapter 6). Two equivalence ratios are considered: φ=0.3 to study effects on N_2 and O_2 and φ=2 to study effects on H_2. For the fuel-lean case the adiabatic chemical equilibrium temperature is 1180 K. It would have been desirable to go to higher temperature where the perturbation effects may have been stronger, but the signal-to-noise ratio of the O_2 signal would have been too low at irradiance levels low enough for this study. Results from three separate tests, differing in the focal length of the dye laser focusing lens, are presented. During each test, data were collected varying the energy of one beam while keeping the energy of the other two beams at their maximum value. The order of the acquisition was fully randomized. All spectra presented here are averaged over 250 single shots to reduce effects of the broadband dye laser noise. Measurements in the Hencken burner were always taken in the same

location, 40 mm from the base and on the center line, to avoid errors from non-uniformities in the flow. Air flow rates are 58.6 SLPM and 28 SLPM for the fuel-lean and fuel-rich cases, respectively. H_2 flow rates are 7.4 and 23.5 SLPM, respectively. Accuracy of the flowmeters is 0.3 SLPM.

5.4 **Results and Discussion**

The non-resonant background susceptibility is not perturbed by high irradiance effects. Spectra are normalized to the signal baseline level (in the non-resonant portions of the spectrum) to remove the direct dependence of the signal on the three laser irradiances, leaving only the Stark and SRP effects. By fitting the experimental spectra to a theoretical library, temperature and absolute concentration measurements are obtained. Sensitivity of the measurements to the high irradiance effects is discussed. Finally, experimental SRP and Stark broadening thresholds are obtained and compared to those predicted by the simple theoretical models presented in the previous section.

Figure 5-3 a) shows spectra collected in ambient air for narrowband dye laser (pump-2) irradiances of 100 and 400 GW/cm^2 while Nd:YAG (pump-1) and Stokes laser irradiances are 153 and 240 GW/cm^2 respectively. The Stokes irradiance is multiplied by the coefficient β introduced in Eq. (5-6) to take into account the spectral non-uniformity of the broadband laser. SRP for N_2 is proportional to the irradiance of pump-1 (the Nd:YAG laser), and independent of pump-2 (the narrowband dye laser). Vice-versa SRP for O_2 is proportional to the irradiance of pump-2 and independent of pump-1. Stark broadening is proportional to the total irradiance (that includes both

pumps). The first vibrational bands of both N_2 and O_2 are excited, revealing the presence of SRP (hot bands for neither molecule should be populated at room temperature). The O_2 hot band is more pronounced than the N_2. Reducing the narrowband dye laser irradiance (pump 2) will decrease SRP in O_2, and leave it unaltered for N_2. Stimulated Raman pumping from the ground to the first vibrational levels causes the appearance of the first vibrational band and an amplitude reduction in the ground band. When the irradiance of the pump-2 laser is reduced by a factor of four the O_2 hot band is still present, but its normalized peak is reduced by 10% and the ground band peak is increased by 15%, consistent with a reduction in SRP. When the pump-2 irradiance is reduced by a factor of 4 the total irradiance goes from 793 GW/cm^2 down to 493 GW/cm^2. The 5% amplitude increase in the N_2 peak can be attributed to a reduction in the Stark broadening. Since the Stark broadening is similar for both N_2 and O_2 Q-branches, we can infer that it is present also in O_2. When the pump-2 and Stokes irradiances are fixed and pump-1 is halved (not shown in the figure), we observe a 2.5% increase in the N_2 ground peak, a 1.5% reduction in the first vibrational band and a 0.8% increase in the O_2 peak. The small variation obtained when halving the product of pump-1 and Stokes, suggests that the irradiance product is close to the SRP threshold.

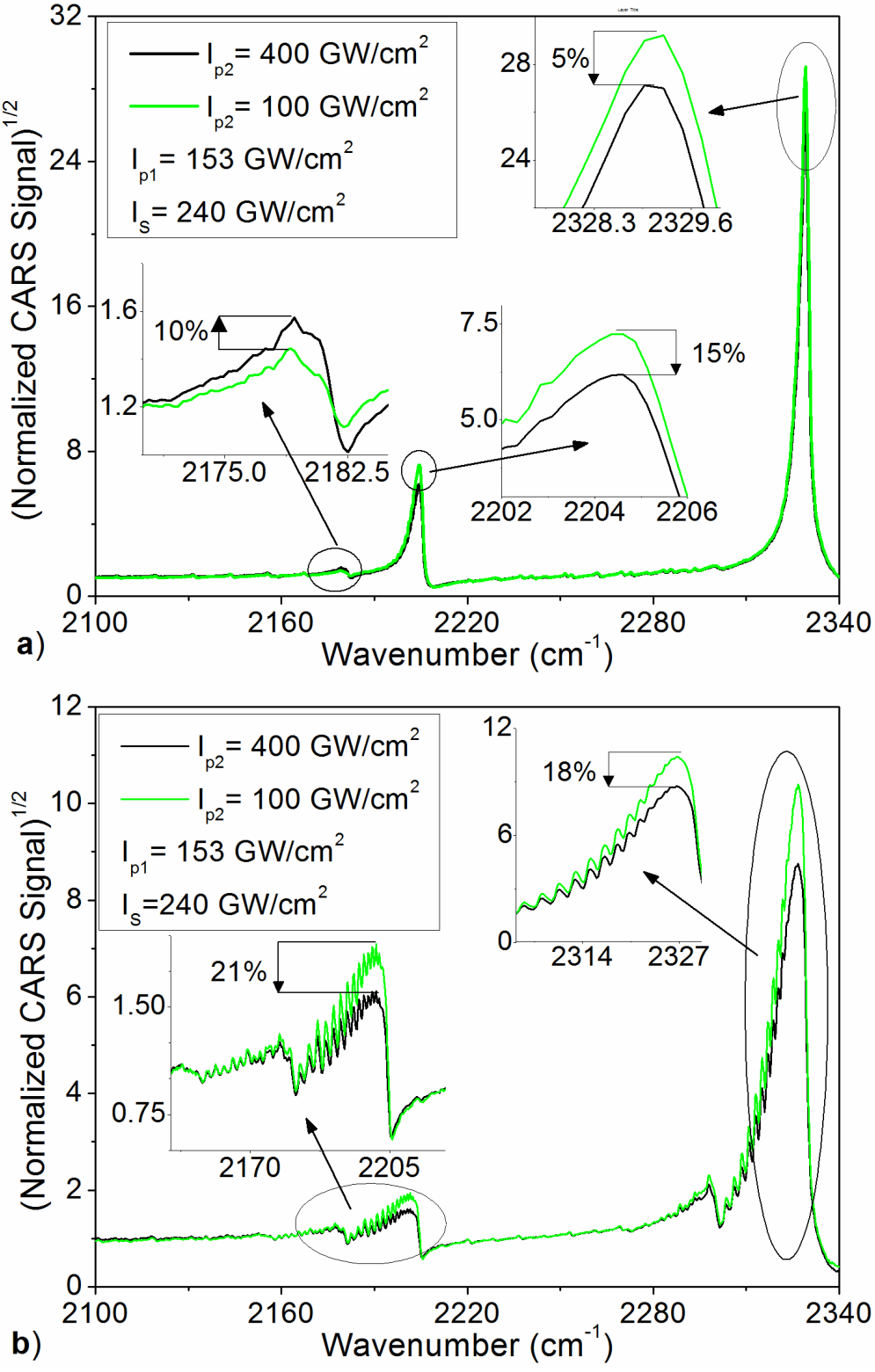

Figure 5-3: a) CARS spectra in ambient air and b) in a Hencken burner flame at Φ =0.3, narrowband dye laser irradiance varied

The experimental spectra in air are consistent with predictions from the threshold criteria of Eq. (5-3) and Eq. (5-8). In the range of irradiances considered in Figure 5-3, the SRP characteristic time for O_2 varies between 1.5 and 6 ns (as compared to the laser pulse lengths of ~10 ns). When halving pump-1 irradiance, the N_2 SRP characteristic time goes from 13 to 26 ns. The criterion of Eq. (5-8) is not satisfied for both molecules in agreement with the experimental observation of the "hot bands". The shorter SRP characteristic time for O_2 than N_2 is consistent with the more pronounced first vibrational band observed experimentally in the O_2 spectra. Based on Eq. (5-4) the Stark shift for a total irradiance of 800 GW/cm^2 for the N_2 Q(5) line is 0.13 cm^{-1}, 40% larger than the 0.08 cm^{-1} Raman linewidth. According to Eq. (5-3), a small spectral perturbation due to Stark broadening is expected, and this is consistent with the 5% reduction observed in the N_2 peak.

Figure 5-3 b) shows spectra collected in a Hencken burner flame for equivalence ratio of 0.3, using the same irradiance levels as the spectra in Figure 5-3 a). Increasing the pump-2 irradiance by a factor of 4 decreases peak amplitudes for the O_2 ground and hot bands by 21% and 4.5%, respectively. It also decreases peak amplitudes for the N_2 ground and "hot" bands by 18% and 9%, respectively. Note that at high temperature both the ground and the first vibrational bands decrease when increasing the irradiance. Based on Eq. (5-6), the change in population difference with SRP is proportional to the original population, thus for the first vibrational band the amplitude increase caused by stimulated v=0→1 transitions is larger than the reduction due to stimulated transitions from v=1 to higher vibrational levels. Also, there is no evidence of a second vibrational band in the collected O_2 spectra. Stark

broadening is thus probably responsible for the reduction in the first vibrational band of O_2. Evidence of a stronger Stark broadening in N_2 than was observed in air is provided by the reduction of the N_2 ground peak that is more than three times what was observed in ambient air. Stark broadening acts in a similar way for both O_2 and N_2 molecules, and therefore the amplitude reduction in O_2 spectra is also expected to be stronger in the flame than in room temperature air. In particular the reduction of the first vibrational band caused by the Stark effect is larger than the increase caused by SRP. The experimental results are consistent with the theoretical model discussed in the previous section. From Figure 5-1, the N_2 collision-broadened linewidth at 1180 K is ~0.04 cm^{-1}, three times smaller than the estimated Stark shift of 0.013 cm^{-1} expected at 800 GW/cm^2. The theory correctly predicts that the Stark broadening at higher temperature is much more significant.

Figure 5-4 summarizes the results of the tests in the fuel-lean flame for the whole range of irradiances considered. The ratio of the peak signal to the baseline signal (i.e., without SRP or Stark effects, computed at chemical equilibrium conditions), normalized to the theoretical ratio of peak to baseline (from CARSFT calculations), is plotted for the strongest line in the ground (filled symbols) and first vibrational bands

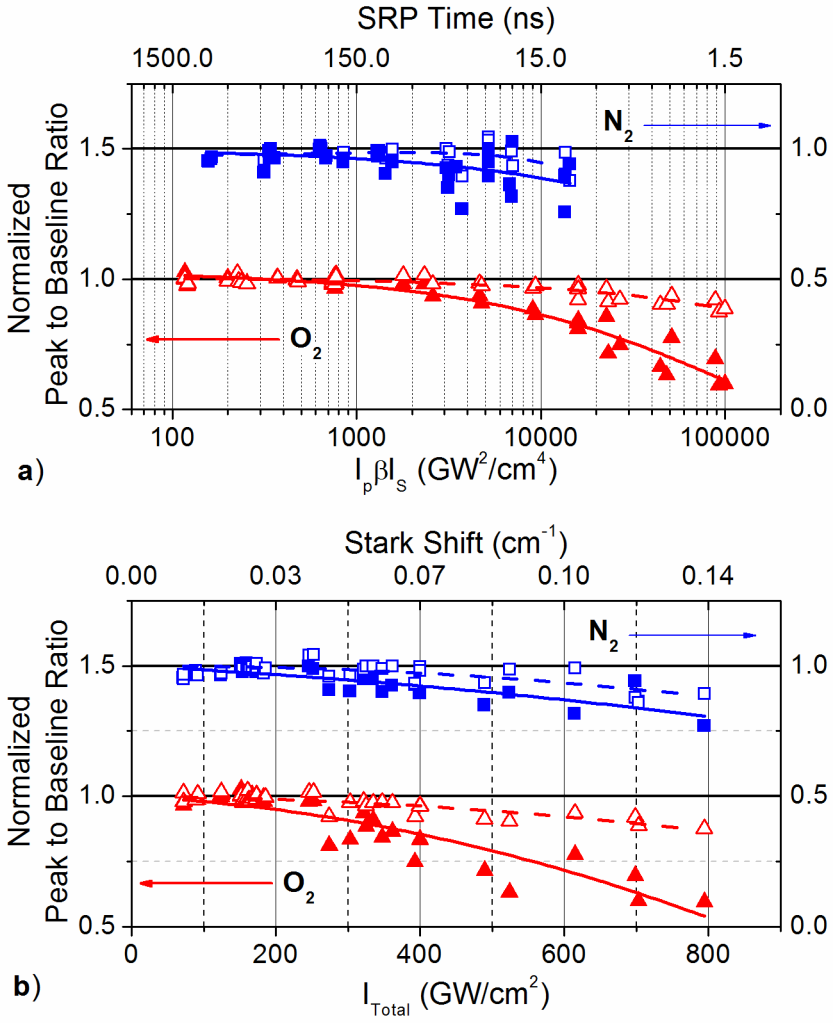

Figure 5-4: Normalized peak to baseline ratio for N_2 and O_2 measured in a Φ=0.3 Hencken burner flame (a) as function of the pump-Stokes irradiance product and (b) total irradiance. Top horizontal scale provides the calculated SRP characteristic time (a) and Stark shift (b). Closed symbols are for the ground vibrational band, open symbols for the first vibrational band

(open symbols) of O_2 and N_2 against the pump-Stokes irradiance product (a) and the total irradiance (b). The top axes are the characteristic SRP time (a) and the expected Stark shift (b) as computed for the N_2 Q(5) line from Eq. (5-6) and Eq.(5-4). The continuous lines are best fit second order polynomials. Figure 5-4 a) shows that the O_2 signal strongly depends on the pump-Stokes irradiance product, suggesting that SRP is the dominant effect on O_2. The spread around the fitted line visible for $\beta I_p I_S > 2 \times 10^4$ GW^2/cm^4, suggests that at these high irradiances, Stark broadening is also significant. For irradiances below 2 x 10^3 GW^2/cm^4 the effects of SRP on the O_2 spectral shape are negligible. The experimentally determined threshold of 2 x 10^3 GW^2/cm^4 correspond to a SRP characteristic time $\tau_{\Delta N} \sim 75$ ns; this is one order of magnitude longer than the pulse length, therefore the experimental results are consistent with the criterion of Eq. (5-8).The N_2 data do not show such a significant trend with the pump-Stokes irradiance product, suggesting that Stark broadening is the dominant effect. Figure 5-4 b) is a plot of the same set of data as function of the total irradiance. The O_2 data varies with the total irradiance for I_{Total}>350 GW/cm^2, but the curve fit is poor because SRP effects are also significant, as shown in Figure 5-4 a). Data correlate poorly with the total irradiance in the 250-350 GW/cm^2 range, since SRP is the dominant effect in this region. Below 250 GW/cm^2 the peak to baseline ratio has converged to the theoretical value, and stays constant. The N_2 data collapse on the fit line, therefore Stark broadening is the dominant effect. For values below 250 GW/cm^2 convergence is achieved. The Raman linewidth of the N_2 transition is ~0.04 cm^{-1}, the computed Stark shift is 0.037 cm^{-1}, and therefore the experimental results are consistent with the criterion of Eq. (5-3).

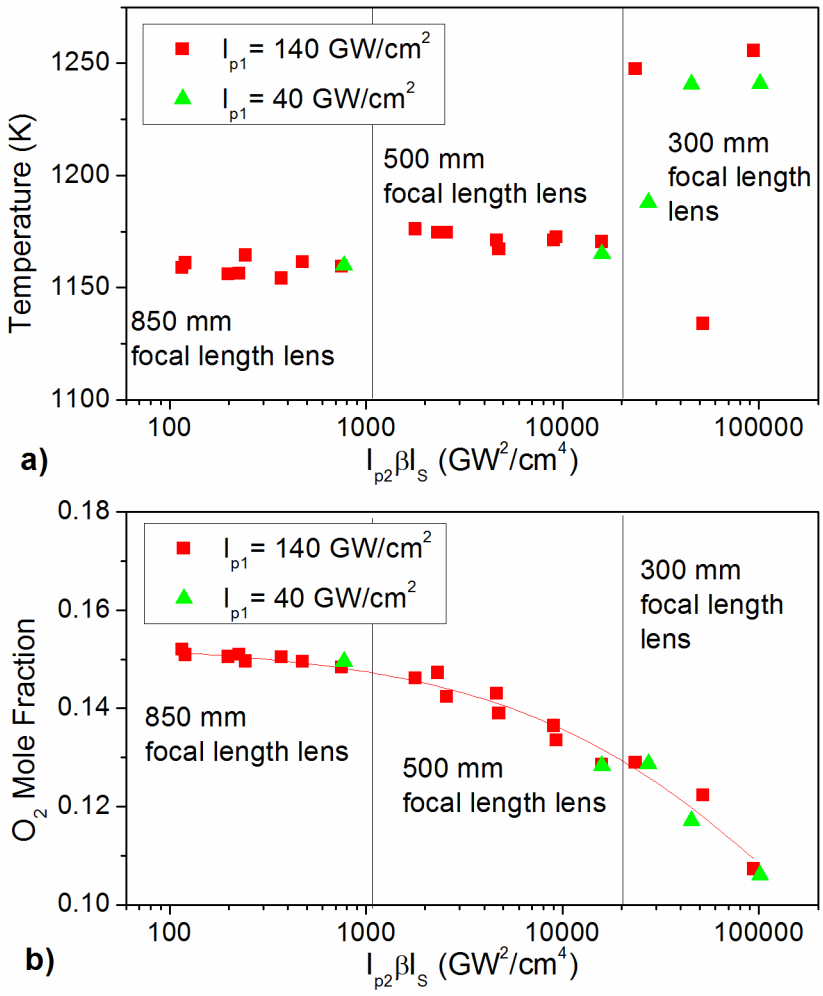

Figure 5-5: Fit (a) temperature and (b) O_2 mole fraction as function of the pump-Stokes irradiance product

High irradiance perturbations affect both concentration and temperature measurements obtained by fitting the spectra (Chapter 3). The fitting code is usually able to provide a good fit (to incorrect temperature and concentrations) in the presence of Stark or SRP perturbation effects. Results are shown in Figure 5-5 for temperature (a) and O_2 concentration (b) plotted as a function of pump-Stokes irradiance product (appropriate to SRP effects). Temperature is not affected significantly by perturbation effects other than at high irradiance ($I_p\beta I_s$>2x10^4

GW^2/cm^4), corresponding to a characteristic SRP time shorter than 8 ns. Perturbation effects do not significantly change the rotational temperature, but do change the vibrational temperature; the fitting method does not distinguish between these temperatures, but fits to a single temperature. The large temperature measurement spread at the highest irradiance is caused by a poor fitting of the spectra which occurs because the rotational and vibrational temperatures are not equal. Oxygen concentration is strongly perturbed, with errors up to 50% at the highest irradiances. Stimulated Raman pumping also affects the O_2/N_2 mole fraction ratio with errors up to 30%. These results differ from Péalat`s, [135] where Stark broadening was dominant and relative concentrations were not affected. Keeping the total irradiance and the pump-Stokes product below the thresholds described in the previous paragraph, temperature and concentration measurements with errors smaller than 3% are obtained. Note that Woodmansee [7] suggested as threshold a characteristic SRP time equal to the pulse length, but these researchers were interested in obtaining accurate temperature only. This is consistent with our results of Figure 5-5 a), where a SRP characteristic time lower than 8 ns was necessary to observe variations in the temperature. Accurate concentration measurements are much more likely to be limited by SRP than are temperature measurements.

Figure 5-6 shows perturbation effects on the rotational H_2 lines. Data were acquired only with the 500 and 850 mm focal length lenses, with the product of the pump and Stokes irradiances up to 10^4 GW^2/cm^4 and total irradiances up to 450 GW/cm^2. In the N_2 and O_2 spectra the SRP-induced population change was revealed by the appearance of "hot bands", but for the H_2 rotational lines both Stark and SRP produces only an amplitude reduction. Figure 5-6 shows that when the total irradiance is increased the amplitude of all the lines decreases. Stimulated Raman pumping is proportional to the product of the pump and Stokes irradiances. If the Stokes irradiance is changed by a factor of 2 with minor changes to the total irradiance (Test D vs Test E), the lines are not significantly affected, and therefore SRP is negligible and Stark broadening dominant.

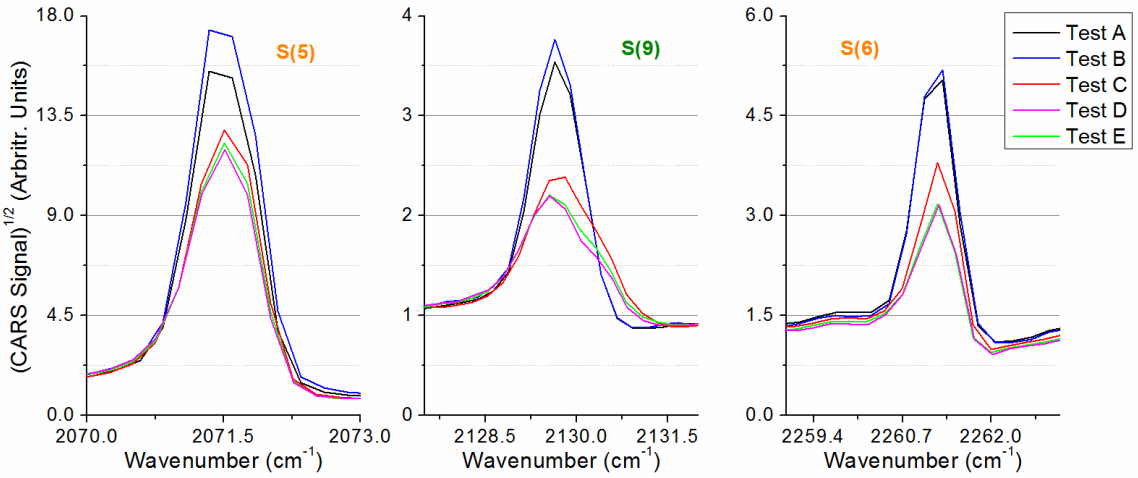

Figure 5-6: CARS spectra collected in a Φ=2 Hencken burner flame with different irradiances for the S(5), S(6) and S(9) lines; A) I_{Total}=187, $I_{p1}I_S$=3250, $I_{p2}I_S$=800; B) I_{Total}=174, $I_{p1}I_S$=1560, $I_{p2}I_S$=384; C) I_{Total}=324, $I_{p1}I_S$=4050, $I_{p2}I_S$=3969; D) I_{Total}=429, $I_{p1}I_S$=1950, $I_{p2}I_S$=3458; E) I_{Total}=443, $I_{p1}I_S$=4050, $I_{p2}I_S$=7182. Products are in GW^2/cm^4, I_{Total} in GW/cm^2

The ratio of the line peak to the baseline for the rotational H_2 lines, normalized by the theoretical value of this ratio, for a larger number of tests similar to those in

Figure 5-6, is plotted in Figure 5-7. In Figure 5-7 a) it is plotted as a function of the product of the pump and Stokes irradiances, and in Figure 5-7 b) as a function of the total irradiance. The peak to baseline ratio correlates well with the total irradiance, decreasing monotonically with it, but correlates poorly with the pump Stokes irradiance product. This again suggests that the Stark effect is dominant. In this experiment total irradiance may not have been lowered enough to reach the unperturbed condition. Figure 5-7 shows that at 170 GW/cm^2, that is the lowest irradiance tested, the peak amplitudes differ from the theoretical values by less than

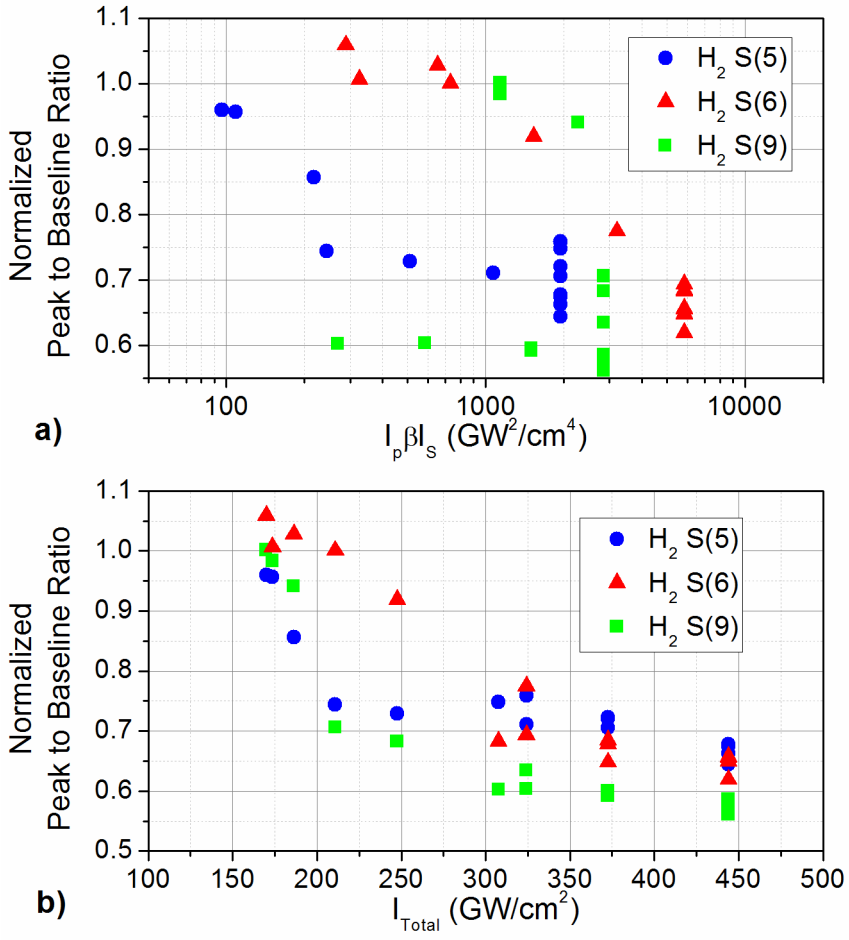

Figure 5-7: Normalized peak to baseline ratio for H_2 rotational lines measured in a Φ=2 Hencken burner flame as function of the pump-Stokes irradiance product (a) and total irradiance (b)

5%. Figure 5-7 b) shows that the amplitude reduction is not the same for the three rotational H_2 lines. Temperature sensitivity in H_2 rotational spectra is given by the ratio between the amplitudes of the different lines, therefore the Stark broadening compromises temperature obtained by fitting these H_2 lines. The fitted concentration of H_2 is strongly affected by Stark broadening for total irradiances above 170 GW/cm^2. This is probably one of the reason why in previous measurements [6, 66, 72] the H_2 mole fraction was systematically low (see Chapter 6). The Figure 5-2 b) shows that the expected Stark shift is much smaller than the Galatry linewidth (Figure 5-2 a) for the whole range of irradiance considered (150-450 GW/cm^2) so the simple model does not predict the observed Stark broadening. Note that, if the collisional broadened linewidth is used as Γ_R, the criterion of Eq. (5-3) correctly predicts the presence of Stark broadening in the range of total irradiances tested.

CHAPTER 6 -Characterization of the Dual-Pump CARS Instrument

6.1 **Introduction**

In providing measurements for CFD validation it is important to include estimates of the measurement uncertainties, so that the difference between the experiment and the simulation can be correctly quantified. In this chapter, measurements in a Hencken burner flame, to determine the accuracy and the precision of the dual-pump (DP) CARS instrument, are described. Changes to the modeling, and calibrations of some molecular parameters to remove systematic errors are described. Finally the spatial resolution of the instrument is measured and the effects of the spatial averaging on the measurements are discussed.

6.2 **The Hencken Burner Flame**

The Hencken burner (Research Technologies RD1X1) produces a steady, nearly adiabatic, non-premixed flat flame, often used for calibration and validation of non-intrusive optical diagnostics techniques. [156] Similar measurements, obtained at NASA Langley with earlier versions of the DP-CARS instrument are reported in Ref. [6, 66, 72]. Figure 6-1 shows a top view of the burner used for this test.

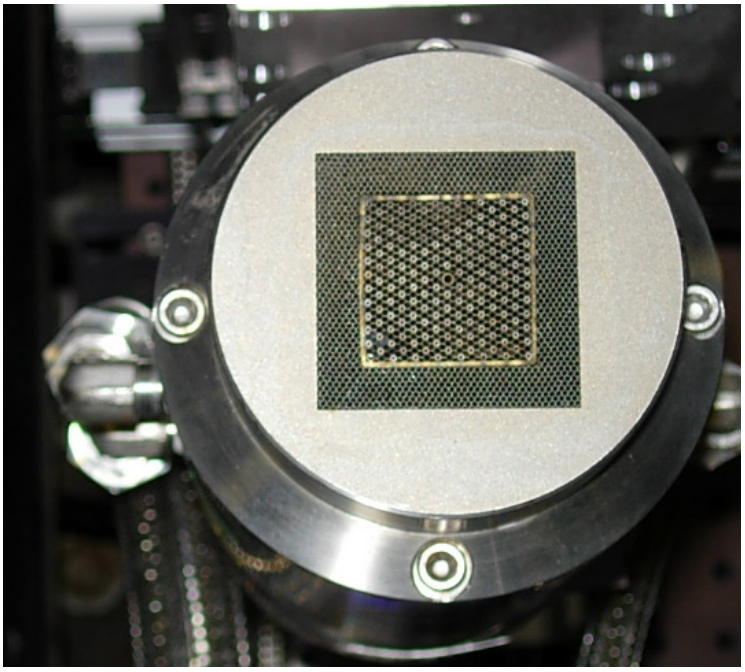

Figure 6-1: Hencken burner, top view

The figure shows the 1.5 in^2 hastalloy honeycomb which supports the stainless steel fuel tubes, which are in one cell out of every four. Oxidizer flows around the fuel tubes and through the honeycomb so that mixing occurs only above the surface. The center hole is available for seeding particles for measurements with other laser diagnostic technique. The center hole was plugged for the tests described here. The 1 in^2 burner surface is surrounded by a co-flow of inert gas. The co-flow improves the flame stability and prevents entraining of ambient air. A N_2 co-flow of 28 SLPM was used for all the measurements here reported. Four Tylan (model FC-280) mass flow controller were available to regulate the flow rate of H_2, air and O_2 to the burner. Each flow controller can provide flow rates up to 30 SLPM with an accuracy of 0.3 SLPM (1% of full scale). One flow-controller is used to regulate the H_2, one is dedicated to the O_2 flow rate, and the remaining two provide control over the air flow. The flow-meters are set to produce mixtures of air and H_2 with equivalence ratios in

the 0 to 3.5 range. Air flow-rates are varied between 17 and 60 SLPM, and only one flow controller is needed when the flow rate is below 30 SLPM, that is for $\Phi>2$. H_2 flow rates are in the 2.5 to 25 SLPM range. Total flow rates are in the 40 to75 SLPM range. The flow rates are doubled with respect to what was used in Ref. [6] and [72]; the higher flow-rates ensure that the flame is slightly lifted from the burner surface so that heat losses are reduced and the flame is near-adiabatic; in addition it allows for operation of the H_2 flow controller closer to full scale, reducing the effects of inaccuracies of the flow-meter. In addition to air-H_2 mixtures, mixtures enriched with O_2 have also been considered, with flow rates chosen so that the products of combustion have 21% O_2 by mole fraction. Such test cases provide additional validation points in conditions more similar to the vitiated air mixture often used to simulate hot-air in supersonic combustion experiments. The enriched mixtures are limited to equivalence ratio of 0.26, corresponding to a temperature of 1400 K. The additional oxygen moves the flame closer to the burner surface, and for higher equivalence ratios the larger heat transfer can damage the honeycomb structure of the burner.

6.3 **Non-Uniformities in the Hencken Burner Flame**

Previous measurements I performed, but not reported here, showed some spatial non-uniformity in the flame produced by the Hencken burner available at NASA Langley. For the current work, a more detailed survey of the flame produced from the burner has been performed. Two equivalence ratios (Φ) have been considered, one fuel lean ($\Phi=0.3$), and the other fuel rich ($\Phi=2$). For each equivalence ratio, data have been

collected in a vertical plane, orthogonal to both the burner surface and the direction of the Nd:YAG laser, and in a horizontal plane, parallel to and 40 mm above the burner surface. The test matrix for the vertical plane has 7 locations along the vertical centerline (axis) of the burner and 11 in the horizontal direction. The first axial location is 5 mm from the burner surface, the last 80 mm. The test matrix for the horizontal plane covered a 20x20 mm square region, with 11 data points in each direction, for a total of 121 distinct points. The dots in Figure 6-2Figure 6-3 represent the CARS measurements locations. Each point is visited twice, and 250 single-shot spectra have been acquired each time. The two replications allow verification of steady operation. The 250 repetitions are used to determine average and standard deviation at each location. The order of the test matrix for each plane and equivalence ratio was randomized. Figure 6-2 a) shows contour plots of average temperature in the vertical plane for the fuel lean case. The average is computed over the 250 repetitions and the two replications. Data collected 5 mm from the burner surface shows a very hot region (~1400 K) 1 mm from the center of the burner, coupled with a much colder region (~1000 K) on its right. This is evidence of an inhomogeneous distribution of the local equivalence ratio caused by the obstruction of some fuel tubes. Moving downstream, mixing makes the temperature more uniform, but 80 mm from the surface there is still evidence of the initial non-uniformity. Figure 6-3 shows the average temperature in the horizontal plane 40 mm from the burner. The temperature distribution is even more inhomogeneous than shown in the vertical plane. The hot region is coupled with a much colder one (less than 900 K) that is not visible in the vertical plane image.

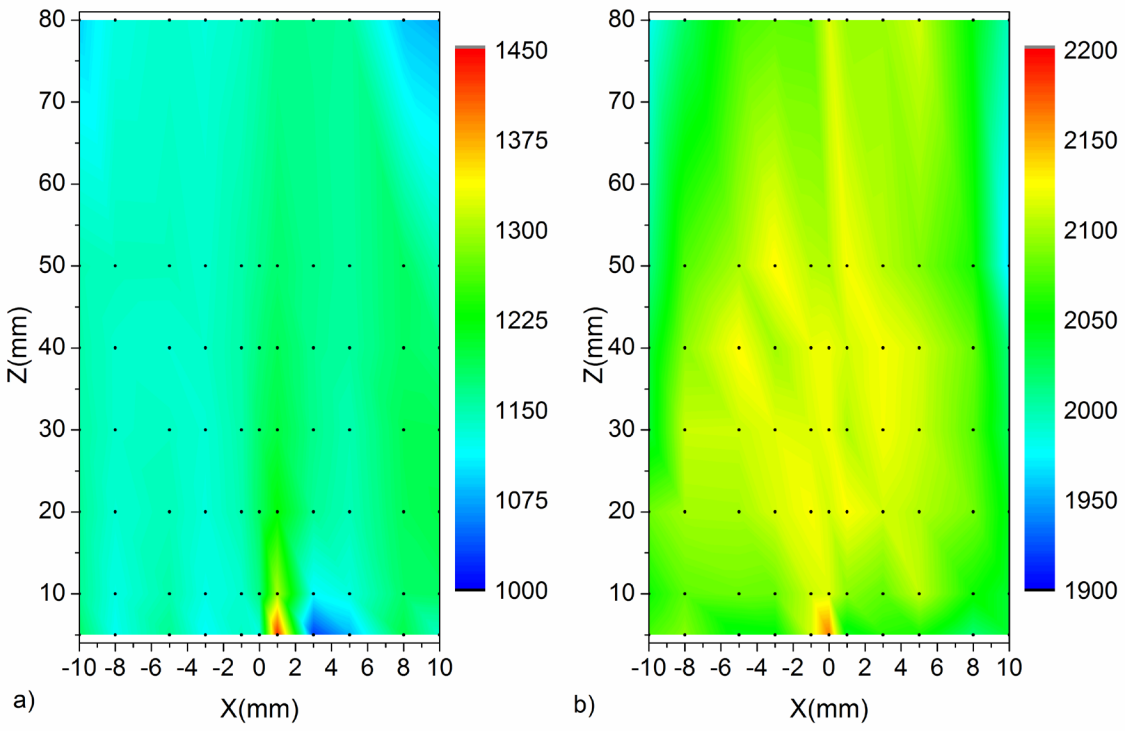

Figure 6-2: Temperature contour plot in the vertical plane (y=0) for a) Φ=0.3 and b) Φ=2

Figure 6-2 b and Figure 6-3 b are obtained for an equivalence ratio of 2. Again there is a strong non-uniformity 5 mm from the burner surface, with variations in the equivalence ratio that are consistent with what was observed in the fuel lean case. Notice that for equivalence ratios closer to 2, reducing the equivalence ratio increases the temperature. For given change in the equivalence ratio, the resulting temperature variation is larger for fuel lean mixtures than fuel rich. This explains the smaller temperature range observed for Φ=2 than for Φ=0.3. Mole fraction measurements of H_2 are consistent with the temperature measurements, and the range observed is comparable to the range of O_2 observed for the fuel lean case. Although there are very large variations 5 mm from the surface, the flame becomes much more uniform

further downstream. The survey of the horizontal plane shows significantly less variations than the fuel lean case.

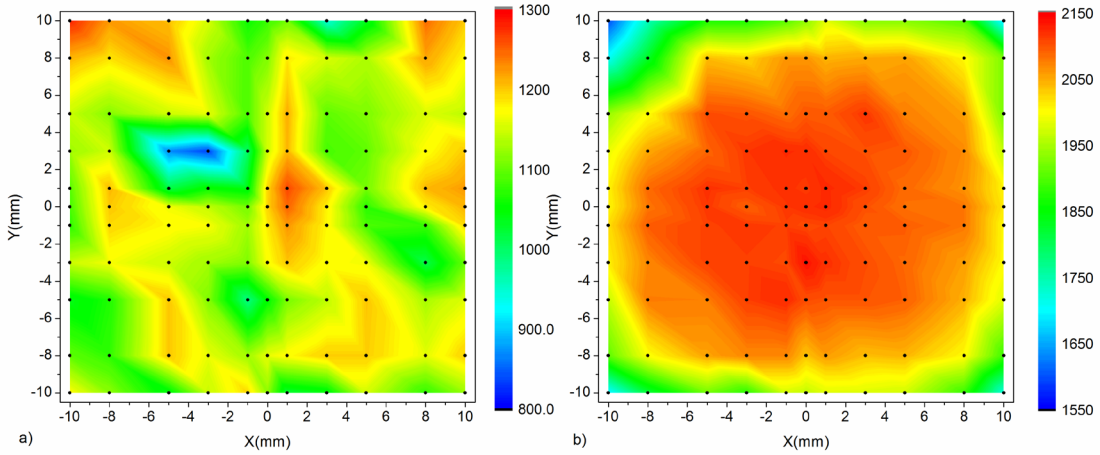

Figure 6-3: Temperature contour plot in the horizontal plane (z=40 mm) for a) Φ=0.3 and b) Φ=2

Based on these plots it appears that it would be best to take validation measurements as far downstream as possible. However, moving the probe volume downstream weakens the hypothesis of adiabatic flame, because of the cooling effects of radiation. In addition, N_2 from the co-flow increasingly penetrates the flame further downstream, reducing the temperature, affecting the mole fractions, and causing an increase in the standard deviation. The study does not show a region that is both uniform and for which the assumption of adiabatic, laminar flame is satisfied. Lacking a better test-medium, the validation study was performed in the Hencken burner flame, but these non-uniformities are taken into account when interpreting the results. The data presented in the next section were collected 50 mm above the burner surface at the center of the burner.

6.4 **Instrument Accuracy**

The instrument accuracy is determined by comparing CARS measurements in the Hencken burner to theoretical calculations for several values of the equivalence ratio. The calculations, which assume chemical equilibrium, have been performed using the Chemical Equilibrium Analysis code (CEA) from NASA Glenn Research Center. [108] Figure 6-4 and Figure 6-5compare temperature and mole fraction measured in the Hencken burner flame with this instrument (red symbols), to theoretical values computed using CEA (continuous black lines) and to measurements in the same burner performed by O'Byrne (green triangles) [6] and Tedder (blue squares) [72] with previous versions of the instrument. The fitted temperature and mole fractions shown here are obtained using the same models and spectral parameters employed in the fitting of the data of Ref. [6, 72]. In particular the James-Kemplerer model is used

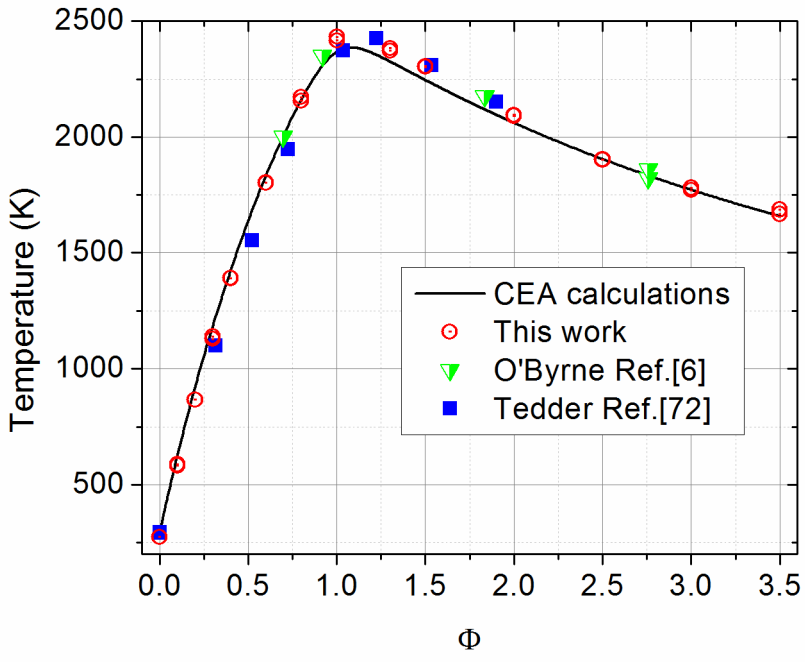

Figure 6-4: Measured (symbols) and computed (continuous black line) temperature as function of the equivalence ratio Φ

for the Herman-Wallis correction factor, the Voigt model used to model the lineshape for all species, and the values of the third order non-resonant susceptibility are based on measurements by Lundeen. [157]

Measured temperature profiles are within 3% of the computed values. The overall measured temperature profiles appear slightly shifted toward the right, suggesting an error in the mass-flow rates, rather than in the DP-CARS instrument. No significant differences are noticeable between the three datasets.

The fitted mole fractions in Figure 6-5 show a poorer agreement with the theory (errors up to 10%) than the temperature, for all three datasets. For fuel lean flames all datasets show similar behavior, with N_2 and O_2 being systematically higher, and the O_2/N_2 ratio being smaller than the theory at lower equivalence ratios (and lower temperature). The results are significantly different for fuel rich mixtures. In

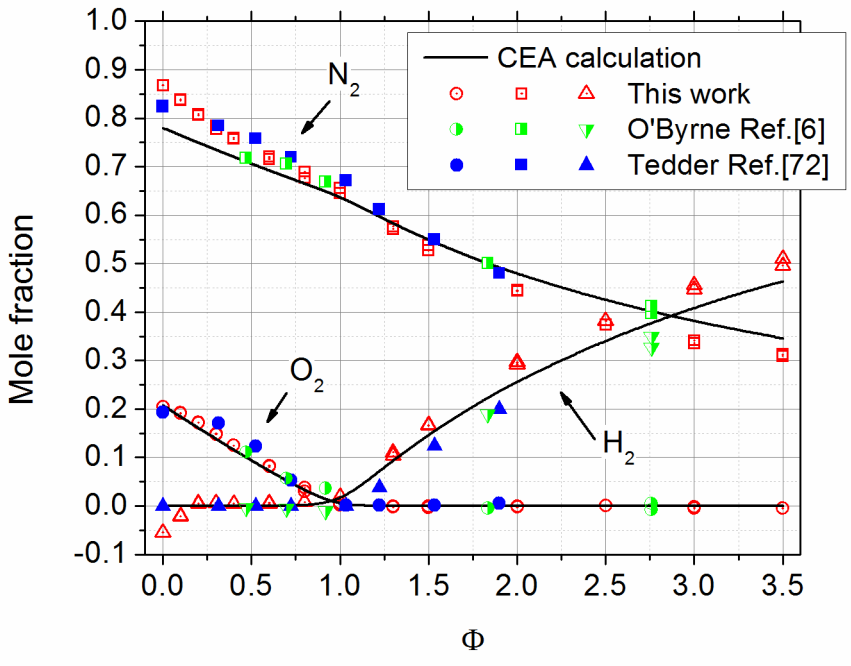

Figure 6-5: Measured (symbols) and computed (continuous black line) mole fraction as function of the equivalence ratio Φ

particular in the older datasets the ratio of H_2/N_2 is lower than the computed, where in the dataset collected for this work is higher. In Chapter 5 it was shown that Stark broadening reduces the H_2 line amplitude, causing lower measurements of the H_2/N_2 ratio. The results shown in Figure 6-5suggest the presence of Stark broadening in the data shown in Ref. [6, 72].

Systematic errors could be caused by inaccuracies in the theoretical modeling. In the following sections we examine some of the modeling choices of Ref. [6, 66]. In particular we will discuss the choice of the model for the Herman-Wallis correction factor, the lineshape model selected for each molecule, and the values of the third-order non resonant susceptibilities. A calibration of some molecular parameters for which there is large uncertainty in the measurements is proposed.

6.5 **Herman Wallis Correction Factor**

Based on chemical equilibrium calculation, the max temperature achievable in an air-H_2 flame is 2396 K. In this work the peak mean temperature measured is 2423 K, and Tedder [72] measured a max temperature of 2426 K. The higher measured temperature cannot be attributed to errors in the equivalence ratio, but it is a systematic error of the instrument.

In recent years there was a renewed attention on the modeling of the Herman Wallis factor, [111] and its effects on CARS temperature measurements. [113, 158-160] The Herman-Wallis (HW) factor models the effect of centrifugal force on the ro-vibrational line intensities. The CARSFT code use the James-Kemplerer (JK) model

[112] for the HW factor, but a more accurate model was proposed in 2001 by Tipping and Buoanich (TB-model). [115]

The discrepancy between the two Herman Wallis factors for N_2 and O_2, increases as function of the J number as shown in Figure 6-6. For this reason larger effects on measurements will occur at higher temperature.

For this work I modified the CARSFT code to include the option of using the TB model for the HW correction. Details can be found in Ref. [114]. Figure 6-7 a) shows the percentage difference between the measured temperature and mole fractions obtained using the two models, for the Hencken burner data. The difference is computed with respect to the TB model, and the horizontal axis shows the temperature as measured with the TB model. The top panel shows that the

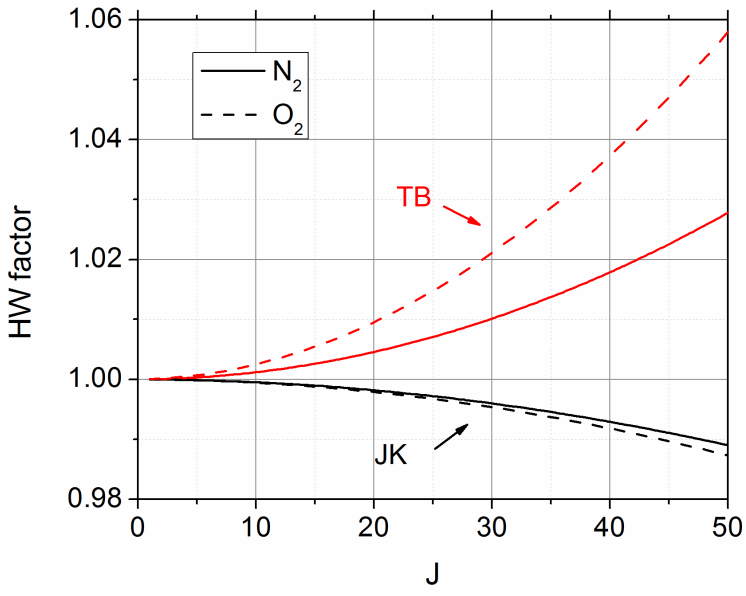

Figure 6-6: Herman-Wallis (HW) factor for N_2 and O_2 as function of the rotational quantum number J, according to the JK and TB models

temperature measured with the less accurate JK model is systematically higher (~0.6%, for T≥600K) than the temperature measured with the TB model. This result is consistent with what reported in previous works. [160] The closed symbols are for air-H_2 cases, where the open are for the enriched O_2 cases. There is a larger discrepancy between the two models for the enriched O_2 case as consequence of the larger difference in the HW factors for O_2 than for N_2. For this specific dataset the max temperature measured using the JK model was 2425 K, where using the TB model is 2409 K, closer to the theoretical limit. Note that the fit included the whole spectrum, where N_2 is dominant (because of the higher concentration). If the fit was limited only to the O_2 portion of the spectrum the difference would have been greater.

Figure 6-7 b shows the same plots for mole fractions. Mole fractions obtained with the JK model are systematically higher than the ones obtained with the TB

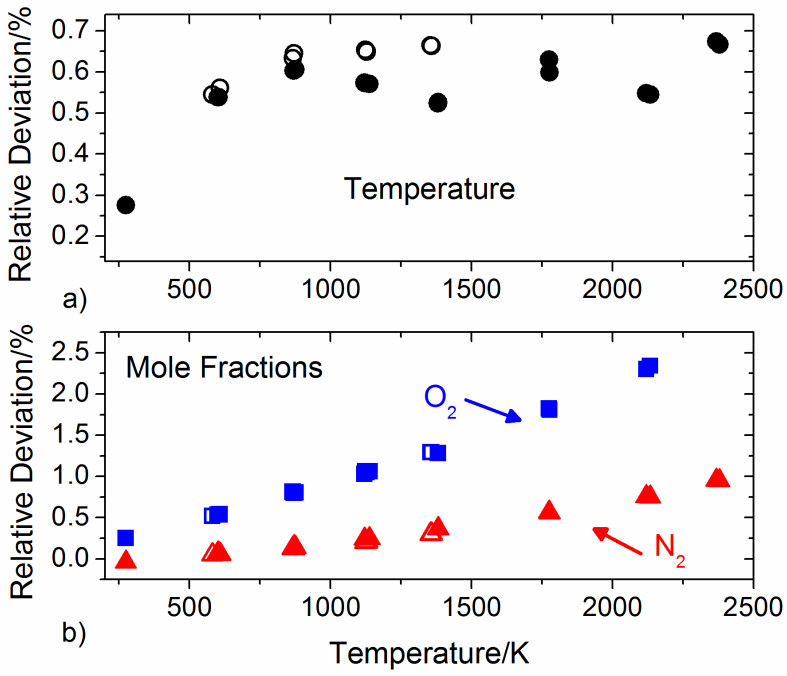

Figure 6-7: Difference in % between a) temperature and b) mole fractions obtained using the JK and the TB models for the HW factor

model. In particular the discrepancy increases with equivalence ratio, as expected since at higher temperature higher *J* lines appear and they`re more sensitive to the choice of the model. In comparison O_2 is more sensitive than N_2, as expected from Figure 6-6. The discrepancy is function only of temperature and independent of concentration; in fact the open symbols, representative of the O_2 enriched cases overlap to the closed symbols representing the air-H_2 flame. Notice that N_2 and O_2 were systematically higher, hence the use of the more accurate HW factor also improves (slightly) the mole fraction accuracy. This is the first study showing the effect of different HW factors on simultaneous mole fraction measurements of O_2 and N_2.

6.5.1 Temperature Accuracy

Figure 6-8 shows the CARS measured temperature (red circles) obtained using the TB model for the HW factor, as function of the equivalence ratio. Theoretical calculations (CEA) have been conducted for nominal flow-rates (continuous line) and for two limiting cases that bound the inaccuracies due to mass flow meters. One limit case is obtained by subtracting 0.3 SLPM from the flow-rate of H_2 and adding 0.3 SLPM to the flow-rate provided by each of the air flow-meters. It is denoted as "leaner" limit case (blue dashed line) since it produces a leaner mixture than the nominal case. Vice-versa, the "richer" limit case (red dashed line) is obtained by subtracting 0.3 SLPM from each oxidizer flow rate, and adding 0.3 to the H_2 flow rate.

Fitted temperatures are within 60 K of the expected nominal temperature over the entire range, and within 20 K for Φ>2. Measured temperatures are systematically low for fuel lean mixtures, and high for rich mixtures with Φ<2. This is evidence of a systematic difference between the local equivalence ratio and the global (average) which we attribute to non-uniformity described previously. Hancock [156] pointed out that the overall shape of the CARS fitted temperature provides a more accurate estimate of the equivalence ratio than one computed based on the mass flow-rates. For the remainder of this section, we use the composition corresponding to the measured temperature for a H_2-air flame in chemical equilibrium (except for the highest temperature, where a Φ=1.07 corresponding to T=2396 K is used instead). By

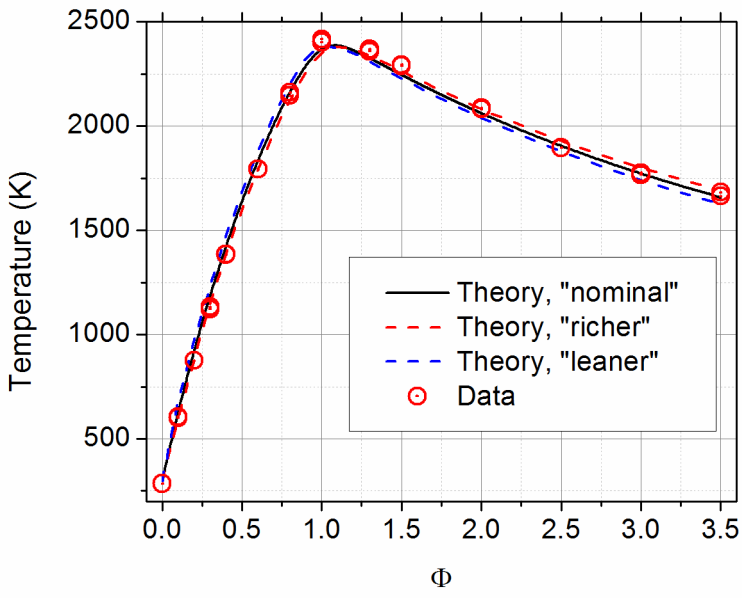

Figure 6-8: Measured (red circles) and computed (lines) temperature as function of the equivalence ratio Φ

doing so, we remove the uncertainty of the equivalence ratio, but we make a potential error by assuming the temperature measurement to be exact.

6.5.2 Lineshape Models

Correct choice of the lineshape models is essential to obtain accurate CARS measurements, since it affects both absolute mole fractions and the mole fractions of one species relative to another. The relative mole fractions measurements are independent of the third-order non-resonant susceptibilities, but systematic errors can be caused by inadequate line shape models. Different lineshape models have been described in Chapter 2-6. Here their effect on the relative mole fraction measurements is discussed.

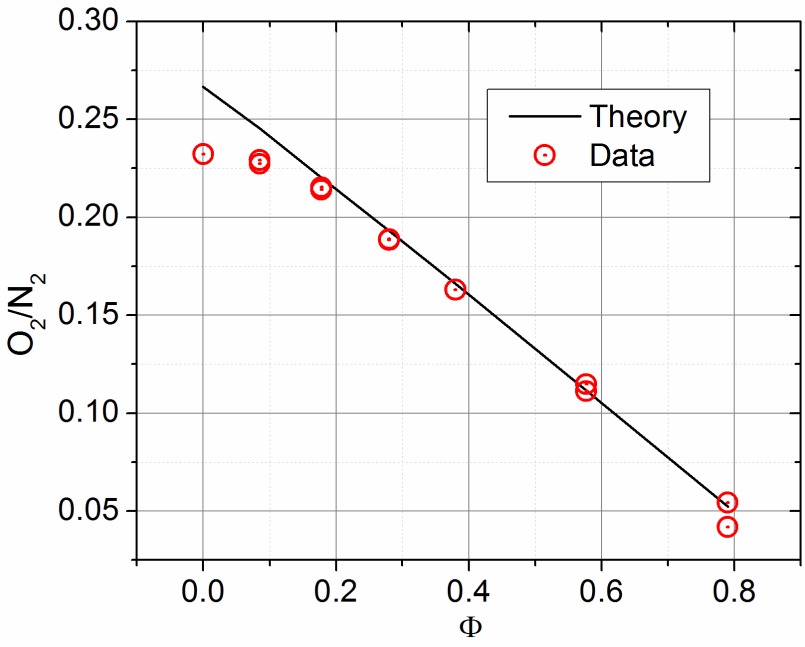

Figure 6-9: O_2/N_2 ratio as function of the equivalence ratio Φ

Figure 6-9 shows the ratio of O_2/N_2 measured for fuel lean mixtures using the Voigt model for both N_2 and O_2. The error in the mole fraction ratio is below 4% for $\Phi \geq 0.2$, corresponding to temperatures greater than 900 K. At lower temperatures the error is significantly larger, 8% at 600 K and 13% at 300 K. The results suggest that the line shape model might be inadequate at lower temperatures.

In Q-branch spectra for low values of the rotational quantum number *J* the ro-vibrational lines undergo collisional narrowing causing a coalescence of these lines. [97] The Voigt model includes the pressure and the Doppler broadening, but not the collisional narrowing. Figure 6-10 shows the fit of the average of 500 spectra collected in room air, to a theoretical spectrum computed using the Voigt model for

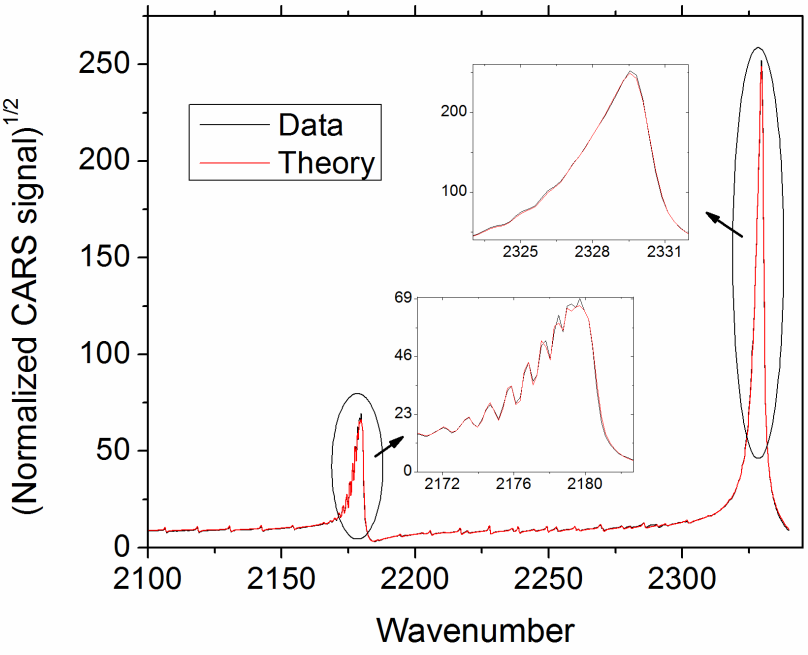

Figure 6-10: Fit of an average of 500 single shot spectra collected in ambient air to a theoretical spectrum computed using the Voigt model

the line shape of O_2 and N_2. The fit is good, except in proximity of the N_2 and O_2 band-head, hence confirming that the issue is limited to the lowest *J* numbers. There is the possibility of improving the accuracy at low temperatures by implementing line shape models that include the collisional narrowing effect such as the modified exponential gap model. [161] At the current time the model is not fully implemented in CARSFT, therefore we used the Voigt model for the line shape of O_2 and N_2.

When using the Voigt line shape model for all species, as in Ref. [6, 66, 72] the measured ratio of H_2/N_2 is systematically high (in the absence of Stark and SRP effects). For H_2 at atmospheric pressure, motional (Dicke) narrowing is significant and the Galatry model, rather than the Voigt, is recommended. [96] As observed in Chapter 2-6 the Galatry model requires the knowledge of an additional quantity, the motional narrowing parameter β, which is related to the optical diffusion coefficient D_o (see Eq.2-22). D_o, although of the same order of magnitude, differs from the

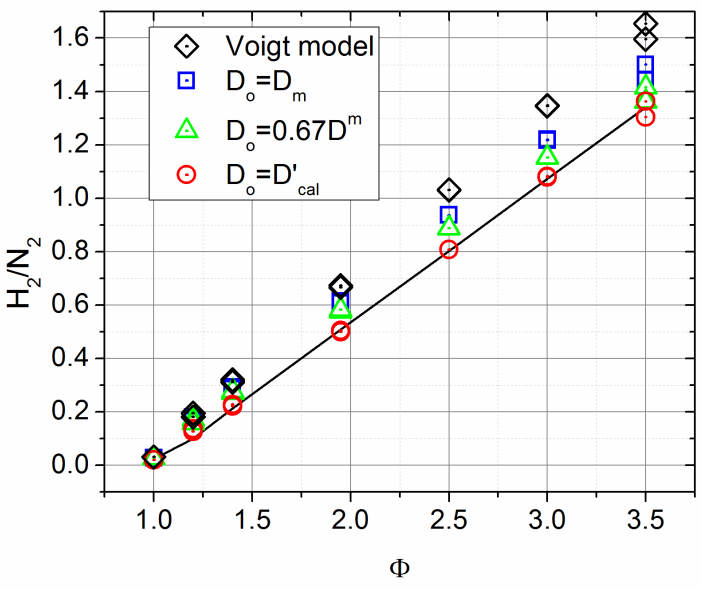

Figure 6-11: H_2/N_2 ratio as function of the equivalence ratio

conventional mass diffusion coefficient D_m. [90, 94, 95] Unfortunately the optical diffusion coefficient has been measured for only a few molecules and temperatures. Recently Kulatilaka [162] measured optical diffusion coefficient for the H_2Q-branch at room temperature, but not for the S branch.

The optical diffusion coefficient determines the ratio of the measured H_2 and N_2. The ratio does not depend on the non-resonant third order susceptibility. Given the uncertainty on this parameter, I calibrated it to minimize systematic errors in the measurements. Figure 6-11 shows the ratio H_2/N_2 obtained using the Voigt model, and narrowing parameters computed for $D_0=D_m$ and $D_0=0.67D_m$. Increasing the narrowing parameter reduces the ratio and provides better agreement with the theory. The measurements obtained for the two optical diffusion coefficients have been used to extrapolate the optical diffusion coefficient D_{cal} that would return the theoretical H_2/N_2 ratio for each Φ. The values so determined are fitted to an exponential function of the temperature ($D_{cal} = 0.0059e^{0.0011T}$) and input to CARSFT while generating the theoretical library. The red circles in Figure 6-11show the results obtained using this calibrated optical diffusion coefficient.

The calibration ensures that the instrument returns an accurate H_2 to N_2 ratio for the temperature and mole fraction combinations tested with the Hencken burner, but problems may arise when conditions vary significantly from those produced by the Hencken burner. The calibration is a function only of temperature and if the composition in the supersonic burner, for given temperature, differs significantly from what is observed in the Hencken burner, the calibration may be in error, affecting the accuracy of the composition measurement. Also the calibration assumes

that the N_2 line shape model is correct. This was based on the observation of good accuracy in terms of the N_2/O_2 ratio for fuel lean mixtures at high temperature. Note that errors in the ratio of the H_2/N_2 for the data presented in Ref. [6, 72] cannot be explained by the choice of line-shape model (or optical diffusion coefficient). Stark broadening [163] of the H_2 lines, was likely responsible of the erroneous measurements of the H_2/N_2 ratio reported in those previous works.

6.5.3 Non-Resonant Susceptibility

DP-CARS is capable of obtaining absolute mole fractions of all major species in an air-H_2 flame, provided a knowledge of the third order non-resonant susceptibility of all the major species, both resonant and non-resonant. Accuracy of the mole fraction measurement is obviously limited by the degree to which the non-resonant background is known. Unfortunately these parameters are not well known, and

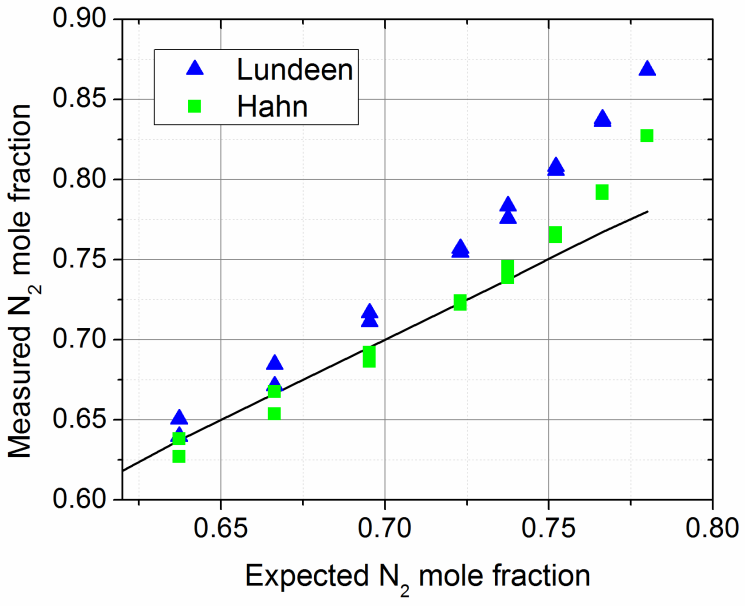

Figure 6-12: Measured N_2 mole fraction in Hencken burner, using Lundeen and Hahn values for the non-resonant susceptibilities

although several measurements have been reported, [157, 164-169] they are not consistent, and have large uncertainties (10%). Figure 6-12 and Figure 6-13 show the changes in the measured N_2 and O_2 mole fractions when using the non-resonant susceptibilities values measured by Lundeen [157] and Hahn. [168] The values from Lundeen are the ones used in previous experiments at NASA Langley. [6, 66]

For this work a calibration of the third order non-resonant susceptibilities of all major species was performed to optimize the accuracy of the absolute mole fraction measurements. The calibration assumes all other aspects of the modeling are correct (such as the line shape modeling), except for the non-resonant susceptibilities. The calibration was done in two steps: first the third order non-resonant susceptibilities for N_2, O_2 and H_2O were calibrated based on the fuel lean data (excluding test conditions for which the error on the O_2/N_2 ratio is above 10%, that is Φ=0 and Φ=0.1); then the H_2 third order non-resonant susceptibility was determined from the fuel rich data.

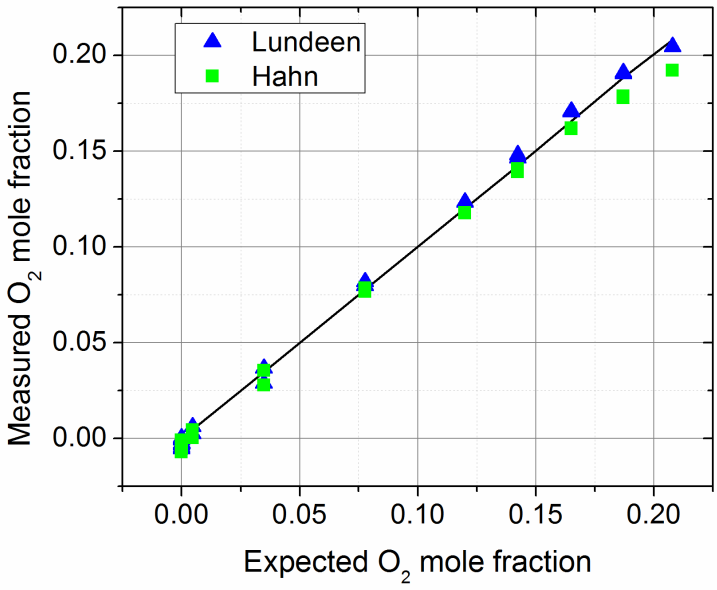

Figure 6-13: Measured O_2 mole fraction in Hencken burner, using Lundeen and Hahn values for the non-resonant susceptibilities

Following are details of the calibration procedure. Let`s denote x_i the mole fractions computed using the Hahn set of non resonant susceptibilities $\chi^{(3)}_{NR_i}$, *NR* the total non-resonant contribution fitted and *Ns* the number of major species.

$$NR = \sum_{i=1}^{Ns} \chi^{(3)}_{NR_i} x_i \tag{6-1}$$

When fitting for species, the code returns the correct ratio of mole fraction to non-resonant baseline $\frac{x_i}{NR}$, but not the correct mole fraction (due to errors in non-resonant susceptibilities) Let`s denote y_i the correct mole fractions (expected from the theory based on effective Φ), and c_i calibration factors for each non resonant susceptibility. The following relations are then satisfied for the resonant species:

$$\frac{x_i}{NR} = \frac{y_i}{CNR} \rightarrow \frac{y_i}{x_i} = \frac{CNR}{NR} \tag{6-2}$$

with

$$CNR = \sum_{i=1}^{Ns} c_i \chi^{(3)}_{NR_i} y_i \tag{6-3}$$

Since we can write as many equations as the test cases we acquired, then the calibration factors can be determined as solution of an optimization problem. The "residual" function we want to minimize is given by:

$$G(c) = \sum_{j=1}^{n} \sum_{i=1}^{N-1} \left(\frac{CNR^j}{NR^j} - \frac{y_i^j}{x_i^j} \right)^2 \tag{6-4}$$

The apex *j*, indicates the jth test case considered, and n is the total number of test cases available for the calibration. For the fuel lean case 10 test cases have been considered, with equivalence ratios between 0.2 and 0.6. Data collected at room temperature air,

Φ=0.1 and for Φ=0.8 have been excluded from the calibration, because showing inaccuracies in the O_2/N_2 ratios above 5%. The O_2 enriched test cases were not used for the calibration, because there is no unique relation between the temperature and the composition, thus no way to correct for flame non-uniformities or errors in the flow-meters. The procedure is then repeated for H_2 using the fuel-rich test case, and all the previously calibrated values of the non-resonant susceptibilities.

Calibrated values of the third order non-resonant susceptibilities are 7.85, 7.79, 19.74 and 10.02 (in units of 10^{-18} cm^3/(erg amagat)) for N_2, O_2, H_2O and H_2, respectively. Except for H_2, the calibrated values are within the uncertainty range (10%) provided with the measurements from Hahn. [168] The value determined for H_2 is 70% larger than what was measured by Hahn, [168] and 16% larger than the highest measurement we found in literature. [169] This suggests that there might be additional modeling issues for the fuel-rich mixtures that are being corrected by this selection of the third order non-resonant susceptibility of H_2. Without this correction, errors up to 3% were observed for N_2 and H_2.

These calibrations are not direct measurements of the optical diffusion coefficient or the third-order non-resonant susceptibilities, but values that are optimized for this instrument and may compensate for possible other deficiencies in the modeling, and so they can only be applied with confidence in the neighborhood of the conditions for which they have been determined.

Figure 6-14 shows the measured mole fractions of O_2, N_2 and H_2 as a function of the equivalence ratio. Continuous lines are the computed values based on an equivalence ratio corresponding to the measured temperature. The calibration

provides an overall reduction of the systematic error. The largest errors are at low temperature (below 800 K) and could be caused by not including the collisional narrowing in the lineshape model. The measured O_2 mole fraction is 1.2% lower than expected at 300 K and 0.7% lower at 600 K; N_2 mole fractions are 3.5% and 2% higher at room temperature and at 600 K, respectively. Errors are reported as a percentage of the total composition, not of the measured value. At higher temperatures, the accuracy significantly improves, with errors in the O_2 concentration that are below 0.5% (systematically low) and errors in N_2 below 1.5% (systematically high). H_2 mole fractions are within 1% of the total composition. The accuracy is significantly improved with respect to what is reported in Ref. [6] (errors in N_2, O_2 and H_2 below 2.6, 2.4 and 5% of total composition) and in Ref. [66] (errors in N_2, O_2 and H_2 below 8, 3.1 and 7% of total composition). Removal of some of the

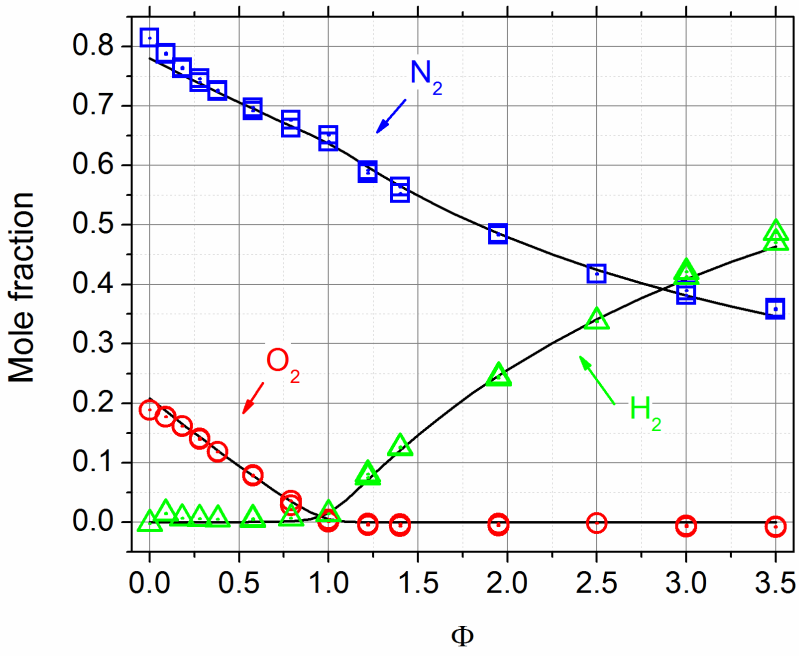

Figure 6-14: Measured (symbols) and computed (continuous line) mole fraction as function of the equivalence ratio Φ

experimental errors that may have affected previous measurements such as high irradiance effects, and improvements in the modeling (more accurate Herman-Wallis factors, better line shape model selection, and calibration of the non resonant susceptibilities) are responsible for the improved accuracy.

6.6 **Instrument Precision**

In the study of turbulent flows, a high precision is desirable since it determines the lowest amplitude of fluctuations that can be detected. Instrument precision also affects the amount of data that needs to be obtained to meet measurement uncertainty criteria. The instrument precision needs to be carefully characterized, so that fluctuations in the flow can be distinguished by those caused by the instrument. Standard deviation, computed from several single-shot measurements in an oven or a calibration flame, is often used as a metric for the instrument precision. [64, 106, 116, 133, 156, 170-174] Commonly reported single-shot temperature standard deviations for N_2 ro-vibrational CARS are 25-30 K at 300 K. [116, 133, 170, 172] The relative standard deviation, defined as the ratio of the standard deviation to the mean measured temperature, is ~8-10% at ambient temperature. CARS temperature precision improves at higher temperatures, with standard deviation of 60 K (3%) at flame temperatures > 2000 K. Spectral features in vibrational CARS spectra strongly depend on temperature; in particular, as temperature increases, N_2 and O_2 ro-vibrational structures becomes more marked, and higher order vibrational bands appear above 1000 K, improving the precision at higher temperatures. Still further increasing the temperature, this effect is offset by a reduction of the signal-to-noise

ratio. Improved spectral resolution increases the number of structures in low temperature spectra and is therefore helpful in improving the precision at lower temperatures.

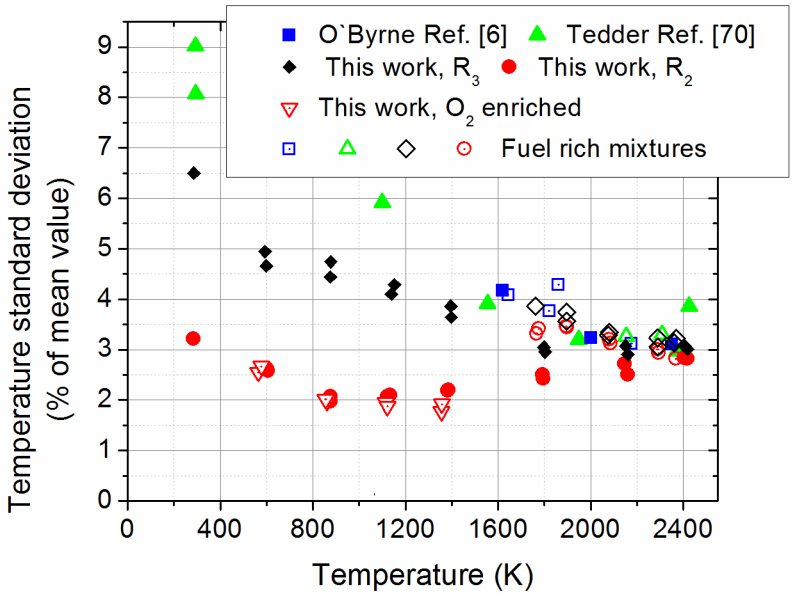

Figure 6-15: Temperature standard deviation as a function of the measured average temperature

Vibrational CARS systems with improved precision (10-15 K) at ambient temperature have been developed. [106, 173, 175] Such systems are characterized by high spectral resolution, and the use of a single mode pump laser and modeless Stokes laser. A modeless dye laser has smaller mode amplitude fluctuations than a conventional one, therefore reducing the main source of noise in ro-vibrational CARS. Kuehner [173] reports a standard deviation of 10-15 K in the 90-295 K range. Further improvements were obtained by van Veen [106] thanks to a simultaneous referencing that takes into account the shot-to-shot fluctuations in the modeless dye

laser. Use of a modeless dye laser was considered for this instrument, and attempted in the first preliminary measurements taken in the laboratory-scale free jet, [66] but results were unsatisfactory.

Figure 6-15 shows the relative standard deviation computed from 500 single shots measurements in the Hencken burner, and compares it to the results presented in Ref.[6, 72]. Data from Ref. [6, 66] were analyzed using the algorithm described in Ref. [6], which minimizes the mean square error of the square root of the signal intensity, the residual function R_3, based on the notation of Ref. [107]. This is the same residual minimized by the fitting routine in CARSFT. [108] The black diamonds are relative standard deviations obtained from the Hencken burner data discussed here, using the fitting algorithm developed by Cutler, [107] and using R_3. Figure 6-15 shows a 2% reduction of the relative standard deviation in the 300-1200 K range caused by the improved spectral resolution achieved with this instrument. At higher temperature, higher order vibrational bands appear and ro-vibrational structures become more marked with the more resolved instrument, but no improvement in precision is observed.

Snelling [116] observed that CARS temperature precision is improved by fitting to the intensity weighted on a pixel by pixel basis by an estimate of the uncertainty in the intensity. This approach is implemented in the fitting algorithm developed by Cutler [107] where this so-called reduced χ^2 statistic (R_2) residual can be selected in place of R_3. Red circles are relative standard deviations obtained minimizing the reduced χ^2 statistic. As already observed in Ref. [107] a significant precision improvement is achieved through the whole temperature range. In particular at 300 K

a temperature standard deviation of only 10 K (3.3%) is obtained. Such a low precision error is comparable to the one reported by van Veen using a modeless dye laser, and simultaneous referencing. [106] The relative standard deviation decreases further by increasing the temperature up to 1200 K, reaching a minimum of 2%. Precision in the 300 -1200 K range is comparable to what has been reported for pure rotational CARS. Further increasing the temperature, the effect of the reduced signal-to-noise ratio becomes dominant and the relative standard deviation increases, peaking at 3% at stoichiometric temperature (~2400 K). Note also that at the highest temperature the choice of the residual has small effect.

For the equivalence ratios above stoichiometric (empty circles), O_2 is no longer present, and two or more H_2 rotational lines appear. These are isolated lines, and are very sensitive to dye laser mode fluctuations. In particular if two or more H_2 rotational lines are present their relative ratio is a function of temperature. The ratio of the two isolated lines strongly depends on the mode noise in the broad-band dye laser and a deleterious effect on temperature precision is expected. To avoid such effects the S(9) line is omitted from the fitting and the S(5) and S(6) lines are "lumped" together; i.e., in both the theory and the data the two H_2 lines are replaced with a region of constant amplitude equal to the mean value over the 2 lines. This lumping removes any influence on the fitted temperature from the H_2 spectra and decreases the temperature standard deviation, but the H_2 mole fraction standard deviation is slightly increased (for example the temperature and H_2 mole fraction standard deviation at Φ=3.5 are 81 K and 0.03 when the two H_2 lines are kept separate, 60 K and 0.04 when lumped together).

The red open triangles are relative standard deviations obtained for the enriched O_2 case. In this case increasing the temperature past 1200 K further decreases the relative standard deviation with the lowest relative standard deviation (1.8%) observed at 1350 K. The reason for the improved precision is the higher concentration of O_2 (~21 %) in the enriched case, and therefore the larger signal-to-noise ratio of the O_2 spectrum. In the supersonic burner, for the mixing case the center jet is of vitiated air and therefore it has a mole fraction of O_2 close to 20% as in these data. As shown in the insets of Figure 6-10, O_2 spectra have better spectral resolution than the N_2 because the probe beam, which is the injection seeded Nd:YAG laser, has negligible line width. In addition, the Stokes laser center wavelength is chosen to excite the O_2 Q-branch, therefore the mode noise on O_2 spectra is lower than on N_2. For these reasons measurements in O_2 rich mixtures are more precise than in O_2 free environments.

The temperature standard deviations reported above also include temporal fluctuations of the flow in the Hencken burner. If the flow had no fluctuations, then the average of the measured fitted single-shot temperatures should coincide with the temperature extracted from the fit of the average of the spectra. This is verified for measurements in ambient air, but not in the flame, where the temperatures from the average spectra are systematically lower than the average of the single shots temperatures. The largest discrepancy is 15 K and it is observed at stoichiometric conditions. In averaging the spectra, the colder (higher signal) spectra weight more, biasing the temperature to lower values.

Figure 6-16 shows the standard deviation of the measured mole fractions. The O_2 standard deviation stays below 0.6% of the total mole fraction up to Φ=0.5, then increases up to 1.7% because of low signal-to-noise ratio. For Φ>1 no O_2 is detected, and the single-shot measurements are scattered around a null average value. The N_2 mole fraction standard deviation increases from 1.5% at room temperature to 3.4% at stoichiometric, and then decreases to 2.5% at the highest equivalence ratio. The N_2 standard deviation as a fraction of the average increases monotonically with the equivalence ratio from 1.7% to 7% over this range. The H_2 standard deviation increases monotonically with the equivalence ratio, where the standard deviation as fraction of the mean is constant and equal to 10%. The greater precision error in the H_2 measurements is largely due to mode noise in the broadband dye laser spectrum, which affects H_2 more than N_2 or O_2 since only two H_2 lines are probed, rather than the manifolds of lines for N_2 and O_2. Mole fraction precision for this instrument is

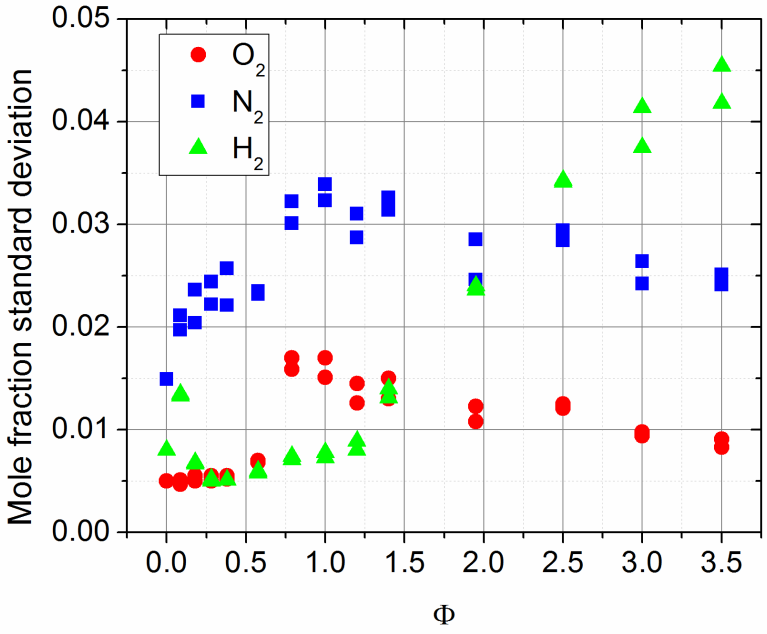

Figure 6-16: Mole fraction standard deviation as a function of the equivalence ratio Φ

similar to what is reported in Ref. [6, 66] except for H_2, which shows a larger standard deviation as a fraction of the mean (~10% for this work, 8% in Ref. [6]). This is a consequence of moving the S(5) line toward the tail of the non-resonant spectrum, where the fluctuation (as fraction of the mean) are larger, and of "lumping together" the S(5) and S(6) lines.

6.7 **Instrument Dynamic Range**

Study of the axisymmetric supersonic combusting jet requires an instrument capable of operating in the 300 K-2400 K temperature range. Peak CARS signal dependence on temperature is approximated by the relation: [176]

$$I_{CARS} \propto T^{-3.5} \tag{6-5}$$

The proportionality constant depends on several parameters, including laser irradiances, crossing angle, focusing at the entrance slit, properties of the spectrometer and the camera, and many other factors.

The Pixis 100B camera used for this test has a 16 bit dynamic range, therefore a limit of 65535 counts in each pixel of the three bins. The signal is only in the center bin; the upper and lower bins contain only the background. For the Hencken burner dataset here discussed, the N_2 peak signal at the highest temperature (~2400 K) is ~700 counts above the camera noise level.

Figure 6-17 plots the peak CARS signal photon counts as a function of temperature; the red circles are observed experimental values, the black curve is obtained from Eq. (6-5). The figure shows that for temperature below 700 K the pixels in the proximity of the N_2 peak would be saturated. Notice that the scale is

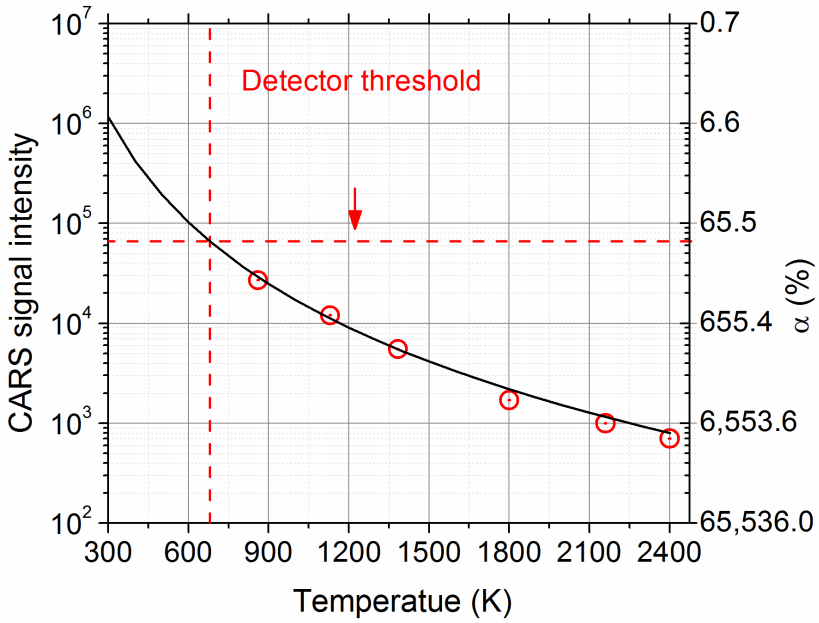

Figure 6-17: Measured (symbols) and predicted (continuous line) CARS signal intensity in camera counts as a function of the temperature

logarithmic and for room temperature spectra the number is above one million counts. As described in Chapter 3, we use a half-wave plate and a polarizer to reduce the Nd:YAG energy to prevent detector saturation when the detected signal is too large. The approach guarantees that a large percentage (~90%) of the shots at a given location does not saturate the camera. Avoiding detector saturation for all spectra in a location would have reduced the signal-to-noise ratio excessively for the higher temperature spectra in a turbulent region.

In previous data sets collected at NASA Langley, spectra with any detector saturation were simply thrown away; since colder spectra have larger signal, this approach biases the average measurements toward higher temperature, and artificially reduces the measured range and standard deviation. To avoid the bias, we process the spectra that saturate the detector, but the fitting algorithm is instructed to omit (block)

the “saturated” pixels when computing the residual function. A numerical test has been performed to evaluate the instrument accuracy when portions of the spectra are not available for fitting. In the numerical the detector saturation threshold expressed as a percentage of the peak value of the CARS signal for each test case and indicated as α is varied. In the numerical test, every pixel for which the CARS signal is above the threshold, is considered saturated, and is blocked in the residual computation. Figure 6-18 shows a non-saturated spectra (blue line), compared to a numerically saturated spectra with α=5% (red line). For visual purposes only, the code fits a cubic spline in the saturated region. The filled region indicates the area blocked from the fitting. Although most of the N_2 spectrum is lost, only few O_2 peaks are blocked.

Figure 6-19 a shows the percentage difference in the temperature measurements obtained for the unsaturated spectra and for spectra obtained setting the threshold to α. Note that decreasing the value of α, the portion of spectra blocked from the fitting becomes larger, is equivalent to a higher degree of saturation. In a real experiment the threshold value is set (65535 counts), but the CARS peak intensity varies as a function of temperature, composition and beams’ alignment. The right axis of Figure 6-16 can be used to estimate values of α for given temperatures in the Hencken burner flame. Above 1200 K, the N_2 peak is unlikely to be saturated, even when accounting for laser power fluctuations. At 500 K we expect the threshold to be ~ 30% of the peak signal, and only 6% at room temperature. Based on these considerations, α is varied in the 2%-75% range for this test. For temperature above 1000 K the error in temperature is below 3% for any value of α considered. The error is within 1% when we consider more likely values of α expected in our experiment, such as 2-10% for

room temperature, 10-50% at 500 K, and 50-100% above 800 K. Thus, accurate temperatures can be determined from detector saturated spectra taken in fuel-lean mixtures.

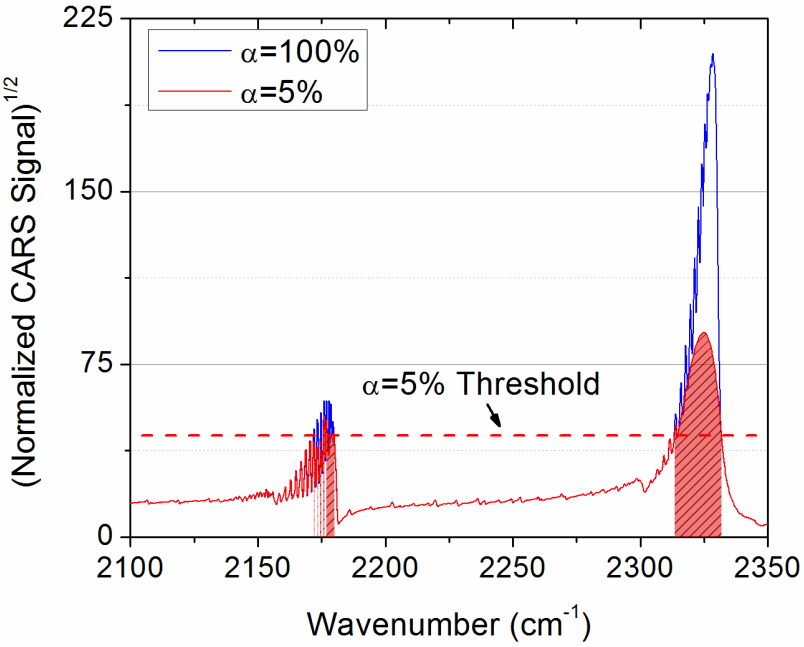

Figure 6-18: CARS spectra for Φ=0.2, acquired (blue line), and numerically saturated (red line)

Figure 6-19 b and c show errors on the O_2 and N_2 mole fractions as function of temperature for several values of α. In spectra collected with our DP-CARS instrument, in a fuel lean air-H_2 flame the N_2 signal is always stronger than O_2 and therefore more prone to detector saturation. In the presence of detector saturation of the N_2 spectra, the measured N_2 mole fraction is higher and the measured O_2 mole fraction lower. The error rapidly increases with decreasing α and with temperature, up to 6% for the most extreme cases. When considering more likely values of α at each temperature, the error in both mole fractions is within 1%. The test showed that for

fuel-lean mixtures, spectra with detector saturation can still produce accurate results, and no significant bias is introduced.

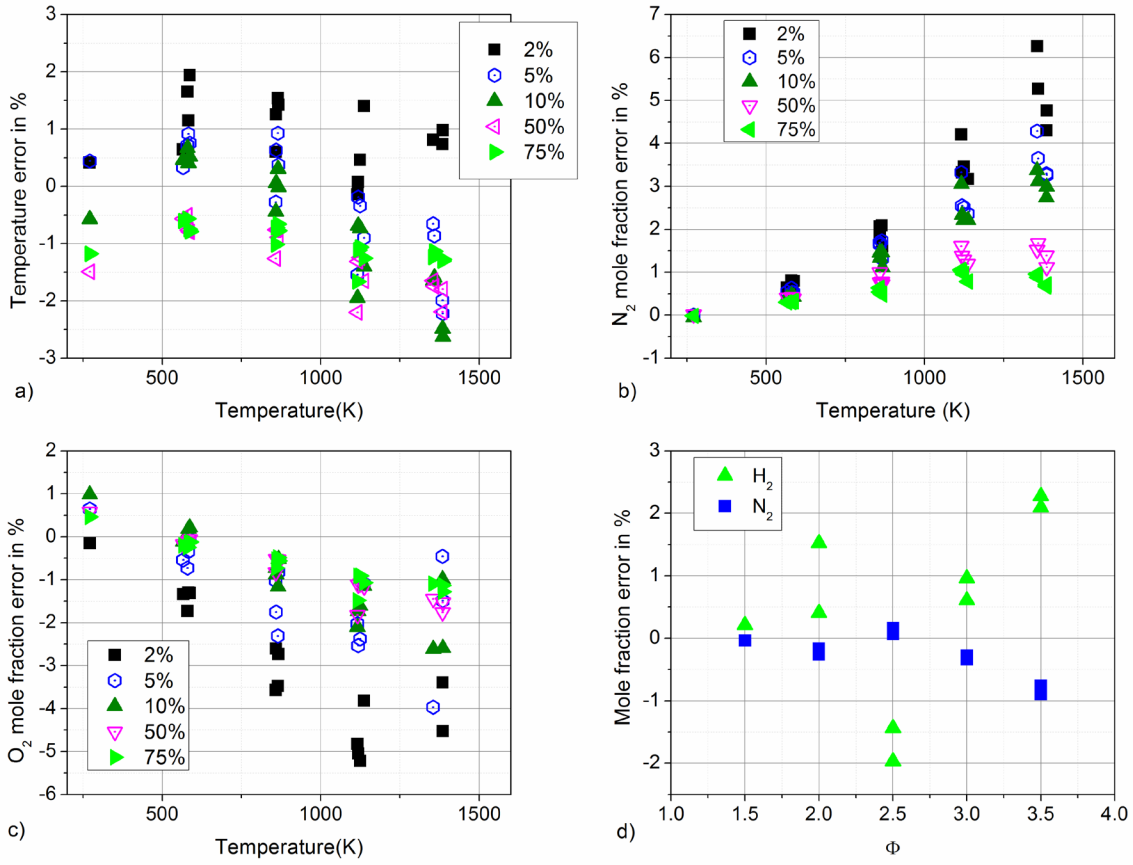

Figure 6-19: Error in temperature (a), N_2 (b), O_2 (c) for fuel lean cases as function of the temperature and of the ratio between the detector saturation threshold and the CARS signal intensity (α); d) error in N_2 and H_2 for fuel rich cases as function of the equivalence ratio when S(5) saturates the detector

For fuel rich mixtures at high temperatures, the H_2 S(5) line can potentially saturate the detector. Since the H_2 lines are not involved in the temperature measurement, there is no significant effect on temperature measurements. In the previous section we have shown that the S(5) and S(6) lines are lumped together in the fitting algorithm. In the presence of an S(5) line saturating the detector, any information on the line intensity is lost. For these spectra the fitting algorithm

automatically excludes the line from the fitting and obtain the mole fraction from the S(6) line alone. Figure 6-19 d shows that the resulting error is below 1% in N_2 mole fraction, and within ~2% in the H_2.

6.8 **Spatial Resolution**

In turbulent combusting flows, steep gradients are present and the spatial resolution affects the measurements. In principle, by changing the crossing angle, or reducing the beam focal spot, it is possible to adapt the CARS spatial resolution to resolve any flame thickness or turbulence micro-scale. In practice this is not possible because of the quadratic dependence of the signal intensity on the length of the measurement volume (Eq. 2-15) and of high perturbation effect occurring at high irradiance levels (Chapter 5). For this reason, in practical combustion application, the probe volume length is between 1 and 2 mm.

Spatial averaging has several consequences. The flame front appears thicker and displaced from its true positions. The fluctuations in turbulent flames are reduced, because spatial averaging within the probe volume. In CARS measurements there are additional issues related to the strong temperature dependence of the signal. This causes a bias toward lower temperature, since colder gas molecules produce a stronger signal. When comparing the experimental CARS measurements to the CFD results, the spatial averaging effects need to be taken into account. To this purpose is necessary to experimentally measure the length of the CARS measurement volume

The CARS measurement volume resembles an elongated cylinder, tapered at each end. The diameter of this cylinder is given by the minimum diameter of the laser beams at their crossing location and it is roughly 100 µm, much less than the length. Therefore averaging effects are negligible in direction orthogonal to the CARS signal propagation. The probe volume length for this experimental set-up has been determined by scanning a 200 µm microscope slide cover along the CARS measurement volume. The energies of all the beams were reduced so that the total peak irradiance was below the damage threshold of the cover material. CARS signal scales with the square of the density, therefore the signal in solids is orders of magnitude higher than in gases, and very low energies and integration volumes are sufficient. The CARS signal in glass is non-resonant. The microscope slide cover was scanned along the CARS measurement volume, ± 3mm from the location where the signal was maximum. 500 non-resonant spectra have been acquired at intervals of

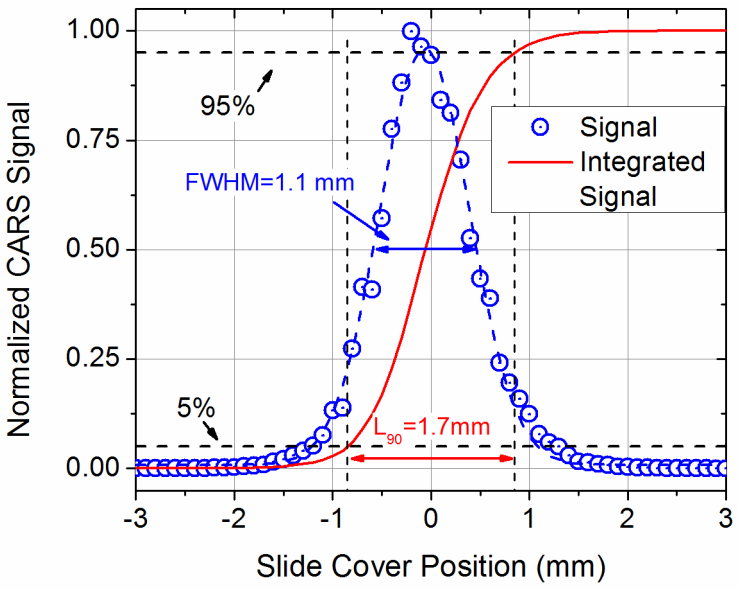

Figure 6-20: CARS spatial resolution

100 μm, and then background subtracted, averaged, and integrated. Figure 6-20 shows in blue the CARS signal (normalized to the peak), as function of the position of the microscope cover. The dotted blue curve is a Gaussian fit of the data, with a FWHM of 1.1 mm. Acquiring data in a gas, the CARS signal recorded is the integrated signal over the whole measurement volume. The CARS measurement volume is often defined as the distance over which the CARS signal goes from 5% to 95% of its total values. The red curve is obtained as piecewise integration of the CARS signal along the measurement volume. Based on the experimental data the L_{90} probe volume length is 1.7 mm.

CHAPTER 7 -Laboratory-Scale Supersonic Combusting Jet

The DP-CARS system described in the previous chapters was designed to collect relevant data in supersonic combusting flow for computational fluid dynamics (CFD) validation and development. Experimental facilities have been designed to provide flow-fields relevant to CFD modelers and that can also be studied with the DP-CARS technique. [14, 27, 177]

An axisymmetric supersonic-combusting, coaxial jet was chosen for this experiment. The facility provides a center jet of "vitiated" air, reproducing the sensible enthalpy of air entering the engine of a hypersonic vehicle flying at Mach numbers (M_f) between 5 and 7. The vitiated air is the product of combustion of O_2-enriched air with H_2 that has the same O_2 mass fraction of air, but high temperature and water. Nozzles with exit Mach number (M_e) 1, 1.6, and 2 are available to provide flows with different effects of compressibility. Hydrogen or ethylene co-flow is available in order to generate a supersonic combusting free jet. As an alternative, N_2 can be used as co-flow for non-reacting (mixing) studies.

This flow-field addresses the issue of mixing and combustion in a supersonic flow, but without all the complications of an actual scramjet combustor, such as walls, mean-flow three-dimensionality, flow curvature and strong shocks. The symmetry reduces the number of points necessary to characterize the flow, and simplifies the numerical simulation. A free jet offers excellent optical access which is a highly desirable feature for laser diagnostics. The possibility of changing the Mach number at the nozzle exit, the enthalpy, and the fuel, allows for a large number of

possible test cases, as described in details in Ref.[14]. In this work the study is includes the effects of the compressibility (by varying M_e), of the enthalpy (by varying M_f), and of the heat release (mixing versus combustion studies). The co-flow is either H_2 or N_2, and, when a H2 co-flow is used, the co-flow flame is always attached as shown in Figure 7-1. Visible and infra-red images of test-cases with ethylene co-flow and marginally attached or detached co-flow flames are shown in Ref.[14], but no CARS measurements were obtained at those conditions.

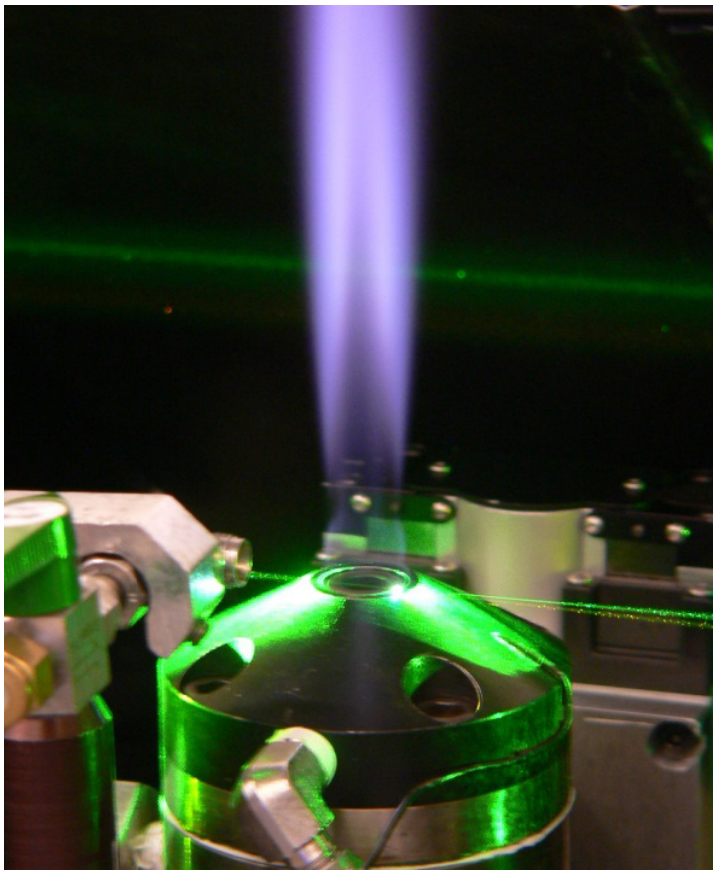

Figure 7-1: Visible image of the laboratory-scale supersonic combusting free jet

Two different sizes of experimental hardware were developed; the *laboratory-scale burner* has a 1 cm center-jet nozzle exit diameter, and flow rates compatible

with a combustion diagnostic laboratory; a second *large-scale burner* was scaled up by a factor of 6.35 from the smaller device and tested in NASA Langley's Direct Connect Supersonic Combustion Test Facility (DCSCTF).

Previous works describe the large-scale supersonic burner, and both numerical [178] and experimental [72, 74] data have been published. The experimental data were obtained with a previous version of the DP-CARS instrument, and are limited to temperature measurements in a non-reacting case. This chapter and the next focus on the laboratory-scale burner. This chapter describes the experimental hardware, illustrates results of some numerical simulations of the flow-field, and discusses some experimental results (pressure measurements and IR images). The next chapter will illustrate the DP-CARS measurements.

7.1 **Description of the Facility**

Figure 7-2 shows the burner and the nozzle sectioned along the symmetry plane and without bolts, tubes, spark plugs and other fittings. The hardware consists of an injection system, a premixing chamber, a water-cooled burner, and a ceramic nozzle surrounded by a co-flow nozzle. The H_2 injection system consists of a stainless steel tube with an external diameter of $1/8^{th}$ of an inch (3.175 mm) and a 0.084 inch (2.133 mm) internal diameter. The tube terminates with the external wall inclined at 30 degrees. The O_2 enriched air flows in the annular passage created by the water-cooled injector (internal diameter 4.76 mm) and the H_2 tube. The relative position of the H_2 tube and the combustion chamber determines the length of the mixing chamber. This length is fixed to 40 mm in order to ensure adequate mixing before the gases enter the

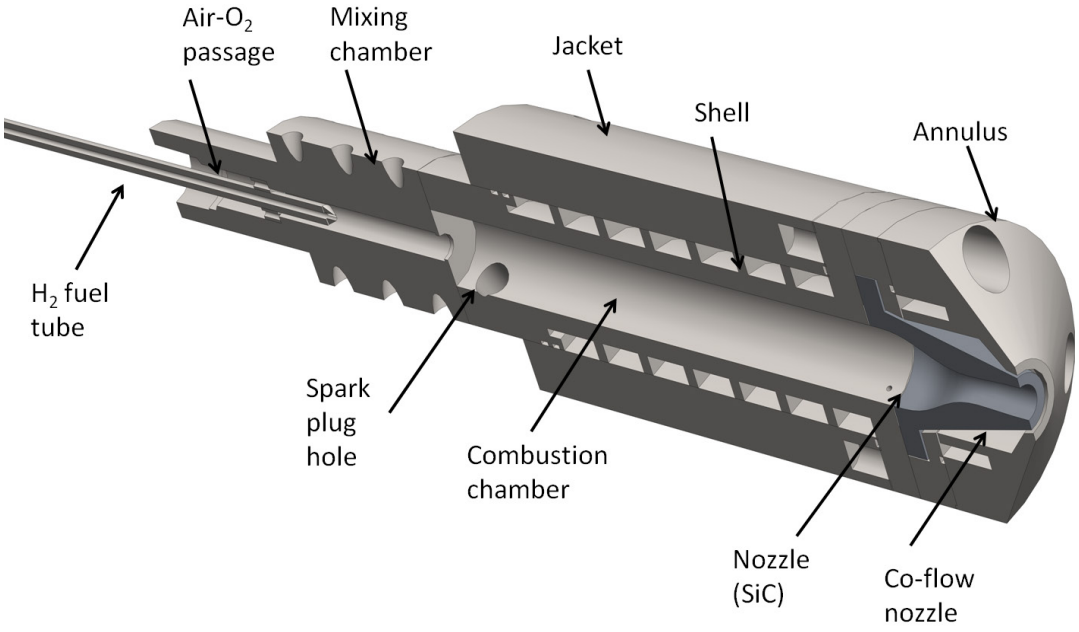

Figure 7-2: Schematic drawing of the laboratory-scale burner. Flow is left to right

combustion chamber, based on previous experiments and preliminary CFD calculations. In previous tests, a fully premixed flow entering the combustion chamber was attempted, but the flame propagated back to the injection system during combustion ignition, resulting in an unsafe operating regime. The injector is water cooled, although in the normal operation regime, the heat fluxes on its surface are small. The premixing chamber terminates with a sudden expansion where the reactants reach the combustion chamber. A spark plug placed at the entrance of the combustion chamber ignites the partially premixed gases. The combustion chamber consists of an exterior "jacket" and an interior "shell" between which water flows for cooling. The "shell" has an internal diameter of 25.4 mm and is 152 mm long. One of three interchangeable silicon carbide ceramic nozzles (one sonic, and two supersonic with M_e=1.6 and 2 respectively) is mounted at the exit of the combustion chamber. The nozzles have a 10 mm exit diameter. The nozzle contours were designed using

the method of the characteristics, assuming a ratio of specific heat capacities equal to 1.3.

An "annulus" surrounds the nozzle, holding it in place, and with the exterior wall of the nozzle it creates an annular, convergent "co-flow" nozzle. The co-flow gas is injected into a pre-chamber, which distributes the flow in the circumferential direction, and enters the co-flow nozzle through a narrow passage (0.5 mm wide). The internal diameter of the co-flow nozzle exit is 8 mm, the external 9 mm. The co-flow and center jets are concentric and separated by the 3 mm wide, annular base region of the nozzle, orthogonal to the center jet. The co-flow jet is inclined by 15 degrees towards the burner axis of symmetry. The "annulus" external walls are inclined at 60 degrees to improve the optical access.

The injector, the burner (shell and jacket) and the annulus are made of AISI 310 stainless steel. The three nozzles are made of Hexoloy grade SA silicon carbide. This ceramic material was selected because of its elevated maximum operation temperature in air (2170 K), its high thermal conductivity (60 to 120 W/mK, which varies as a function of temperature) and its low thermal expansion coefficient (5.32 x 10^{-6} mm/(mm K)). A high maximum operation temperature was essential in order to avoid an active cooling system for the nozzle. Ceramic materials can work at very high temperatures and can be shaped into complex forms, but are generally weak in tension and lack ductility; hence they are very sensitive to failure due to thermal tensile stresses. A large thermal conductivity, allowing a more uniform temperature across the component, combined with low thermal expansion, strongly reduces thermal stresses.

Thermal insulating gaskets inserted between the nozzle and the steel components are a simple and efficient way to minimize thermal gradients in the structure. Thanks to a low thermal conductivity, they assure a more uniform thermal profile in the ceramic nozzle, minimizing thermal stresses although producing an overall higher temperature. Cotronics ceramic paper 3000F, offering a thermal conductivity of 0.19 W/(m K) and a thickness of $1/16^{th}$ of an inch, was selected for this set of experiments. Grafoil gaskets are placed on both sides of the ceramic paper layer, to provide better sealing and to absorb thermal deformations.

7.2 **Numerical Analysis**

Numerical simulations were critical in the design of this facility. Results from a preliminary parametric study conducted by Gaffney [177] were used to determine the injection angle of the co-flow, and the size of the rearward surface between the co-flow and the center jet. Detailed numerical simulations of the internal flow-field were performed by me in order to determine whether the combustion would stabilize in the combustion chamber, whether the flow at the exit of the nozzle was uniform and free of shock waves, and to verify that material temperature and thermal stresses did not exceed the limit of the materials. [14, 27] The numerical analysis drove some critical changes to the design of the ceramic nozzle, and its integration in the burner.

Detailed numerical simulations also provide profiles of the flow properties at the nozzle exit and temperature distribution of the nozzle and annulus exit surfaces. These data constitute boundary conditions for numerical simulation of the external jet

and a benchmark for validation of non-intrusive laser diagnostics (such as dual-pump CARS), and other instrumentation.

Accurate simulation of the internal flow-field requires knowledge of the wall temperature profile. In particular, the enthalpy of the gas mixture at the exit of the jet is affected by the heat loss through the burner and the nozzle. Heat transfer from the nozzle to the co-flow determines the temperature of the fuel.

Two types of calculations were performed: calculations of the internal flow of the burner using the CFD code VULCAN, [179] and finite element (FEM) thermal and stress analysis using Cosmoworks, a commercial code. The two calculations were coupled. A tentative wall temperature profile was assigned to the burner and nozzle internal walls as boundary conditions for the CFD calculation. As a result, heat fluxes distribution and bulk temperature profiles were obtained. These data were given as boundary conditions for the finite element thermal analysis that returned an updated wall temperature profile. The process was then iterated until convergence on the wall temperature was achieved.

Numerical simulations were performed for the three nozzles (M_e=1, 1.6 and 2) and values of M_f=5, 5.5, 6, 6.5 and 7. H_2 is used as co-flow in all the simulation. Only selected results are presented in this work. Additional results and details can be found in Ref.[27].

7.2.1 Thermal Analysis

The temperature distribution in the burner assembly was computed using Cosmoworks, a commercial finite element analysis code. Several heat transfer

mechanisms compete in determining the temperature distribution in the structure. There is convection from the hot gas to the combustion chamber and nozzle, from the combustion chamber walls to the cooling water, and from the nozzle exterior walls to the H_2 co-flow. There is conduction between the different components of the assembly, and there is radiation between the nozzle and the annulus wall, and to the ambient. The complexity of this thermal analysis goes far beyond the capabilities of the computational fluid dynamic code chosen. The finite element analysis software takes into account all the heat transfer mechanisms, except for radiation from the gas.

A temperature dependent model was generated for the Hexoloy grade SA silicon carbide based on the specifications provided by the manufacturer. Finite elements analysis of the Cotronics ceramic paper used as gasket would have required an excessively fine mesh; hence, only its insulating effect is modeled by introducing a "thermal resistance". In analogy with electrical resistance, the thermal resistance per unit of area is defined as d / k where d is the thickness of the gasket and k is the thermal conductivity. Radiation from the solid surface to the ambient and to other surrounding surfaces is computed. The emissivity of stainless steel is assumed constant and equal to 0.7, where a constant value of 0.92 is used for the ceramic. Temperature of the surrounding environment is assumed constant and equal to 300 K. The radiative contribution from the hot gas is neglected. Water-cooled surfaces are assumed at a constant temperature of 390 K, which is the approximate boiling temperature at the pressure of the water in the cooling passages. The heat convection is not modeled directly by the software, but a heat transfer coefficient and an adiabatic wall temperature, obtained from the CFD computations are required as

input. Heat fluxes from the gas to the burner and nozzle surfaces are obtained as output of the VULCAN code. Convection heat-transfer coefficient is computed as

$$h = \frac{q}{T_{aw} - T_w} \tag{7-1}$$

where q is the heat flux per unit area, T_{aw} the adiabatic wall temperature, and T_w is the wall temperature. The adiabatic wall temperature is approximated to the total temperature of the gas outside the thermal boundary layer. It is a function of the axial distance and is an output of the CFD code. For the wall temperature, the profile obtained as output of the thermal analysis in the previous iteration is used. For the first iteration, a tentative constant temperature is assumed for the burner and a larger, constant temperature for the nozzle. The convection heat transfer coefficient is chosen over the heat flux as input for the FEM code because it decouples the fluid dynamics

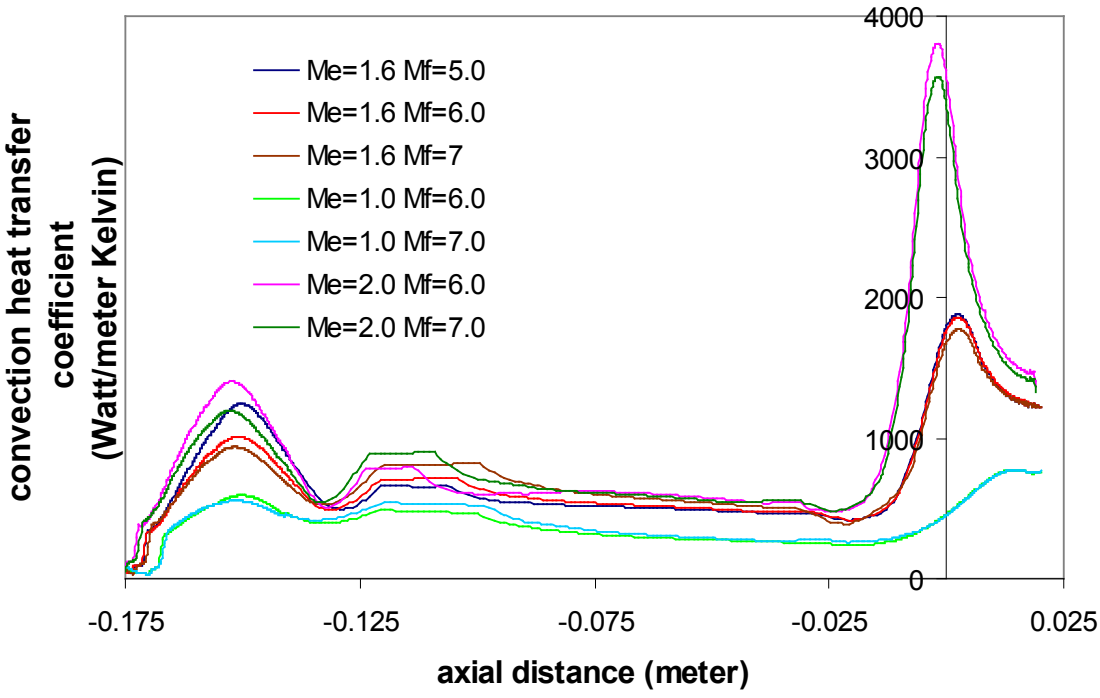

Figure 7-3: Convective heat transfer coefficient on the combustion chamber and nozzle internal wall for several values of exit and flight Mach number

of the flow from the wall temperature. Figure 7-3 shows the CFD computed convective heat transfer coefficient applied as a boundary condition to the FEM analysis on the internal walls for several cases of interest. The coefficient depends strongly on the exit Mach number (since the pressure, which strongly effects heat transfer, depends on exit Mach number) and only slightly on the enthalpy of the gas. Heat transfer coefficient profiles are also evaluated for the surfaces cooled from the co-flow.

The axisymmetric nature of the problem allowed limiting the analysis to a quarter of the structure. Only the combustion chamber, the nozzle and the co-flow-chamber are modeled. The analysis is further simplified by eliminating bolts, spark plugs and other small features that have a negligible effect on the temperature distribution. A non-structured grid of 87175 nodes defining 56426 tetrahedical elements is used for all of the calculations. The average element size is 3.0 mm but smaller elements are used to describe areas of greater interest or larger temperature gradients such as the nozzle, the contact surfaces between the ceramic and the metal, and the region where the co-flow impinges on the exterior wall of the nozzle. A grid made of 193092 nodes is used to test for grid convergence. The temperature distribution obtained with this grid differs less than 1% from the one obtained with the original grid.

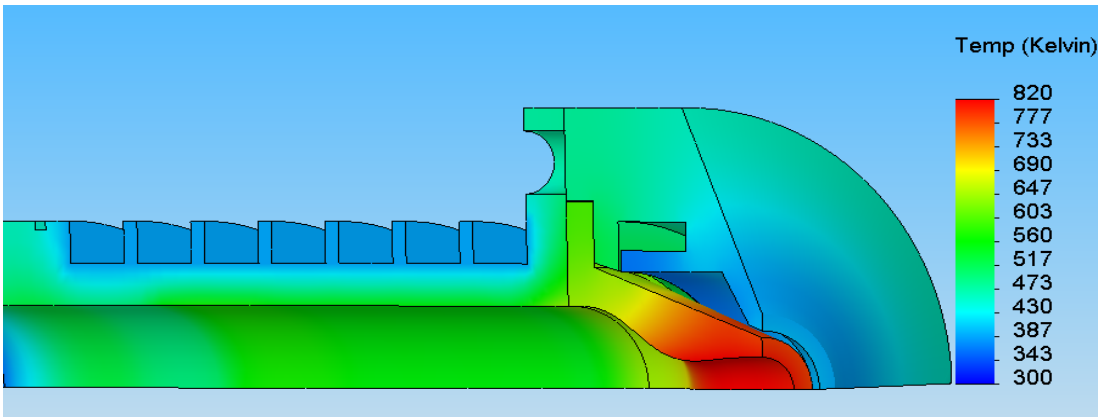

Figure 7-4: Temperature distribution for M_e=1.6 and M_f=6. Flow is left to right

Figure 7-4 shows a typical temperature distribution obtained from the numerical analysis. The temperature in the combustion chamber is almost uniform in the axial direction, but presents large thermal gradient in the radial direction. The sudden change in temperature between the nozzle and the burner is due to the insulating material. Thanks to the large thermal conductivity of the silicon carbide, the nozzle temperature profile in the radial direction appears to be uniform, although the interior is subject to a large heat flux from the accelerating gas, and the exterior is cooled by the H_2 co-flow. A larger thermal temperature difference can be seen in the axial direction, partially mitigated by the insulating gaskets. The "annulus" is heated by radiation from the nozzle and conduction from the combustion burner flange.

Updated wall temperature profiles are obtained as output of the thermal analysis and are given as input to the CFD code. The FEM calculations are repeated and the process is iterated until the peak difference between wall temperatures at the same location, as evaluated in two successive iterations, is below 1%. Typically 3 iterations were sufficient to satisfy this criterion.

Thermal analysis results show that all elements are at a temperature below their allowed threshold. For the nozzle thermal stresses were a concern because of the low tensile strength of the SiC. The thermal profile was used as input for a thermal stress analysis. In the original design, no insulation was interposed between the nozzle and the steel surfaces. Under these conditions the analysis predicted large thermal stress that would have caused nozzle failure. Ceramic paper gaskets, acting as a thermal barrier, and soft Grafoil gaskets absorbing some of the thermal expansion, were added to the design to reduce the thermal stresses well below the material threshold. Transient thermal stress analysis has been performed as well, showing that peak stress was reached after 15 seconds, and their amplitude was mitigated in presence of a co-flow. For this reason the non-reacting tests have also been conducted with a co-flow, in this case with a N_2 co-flow. In addition to provide critical information for the facility design, the thermal analysis also provides the temperature of the nozzle exit surface, which is a boundary condition for simulations of the external flow-field.

7.2.2 CFD Analysis

All of the computational fluid dynamics results shown in this work were obtained by me using NASA Langley`s VULCAN, a CFD code that solves the Favre-averaged Navier-Stokes equations using a finite volume method on a structured grid. [179]

The flow is assumed axisymmetric, and only a plane containing the axis is modeled. The structured grid, generated with a separate commercial code (Gridgen), has a total of 47225 points subdivided into air injection (61 × 29), H_2 injection (49 × 17), mixing chamber (113 × 45), combustion chamber (313 × 85) and nozzle (145 ×

85). Grid points are clustered at the entrance of the combustion chamber, in the throat and expanding region of the nozzle. In the entire domain, the grid spacing near wall is such that the dimensionless wall distance (y^+) is < 50 well within the domain of validity of wall matching functions (y^+<100). [180] The grid is further subdivided into 15 blocks to take advantage of the VULCAN block level parallelization. A grid convergence study was performed and can be found in Ref.[27].

A 2-interval, 7-coefficient curve fit created by McBride from NASA Lewis is used to model the mixture of thermally perfect gases. There are seven species (O_2, N_2, H_2, H_2O, OH, O, and H) and the Langley 7-species 7-reaction model, included with the VULCAN distribution, was chosen to model the chemistry. Molecular viscosity is computed using the Sutherland's law, whereas Wassiljewa's law evaluates molecular conductivity. Inviscid fluxes are modeled using the Edwards low dissipation flux split scheme with second order, kappa=1/3rd MUSCL interpolation and a "smooth" limiter. The flow is assumed fully turbulent and the Wilcox k-ω turbulence model is used. The turbulent Prandtl number is set to 0.89, and the turbulent Schmidt number is set to 0.5.

Time integration is performed using a diagonalized approximate factorization scheme. Each domain is solved elliptically. A 3-level coarse-to-fine grid sequencing is implemented to accelerate convergence. The local Courant- Friedrichs-Lewy (CFL) number is set to 4 for most of the calculations, and the time step is determined independently at each cell, based on its dimension and local flow properties.

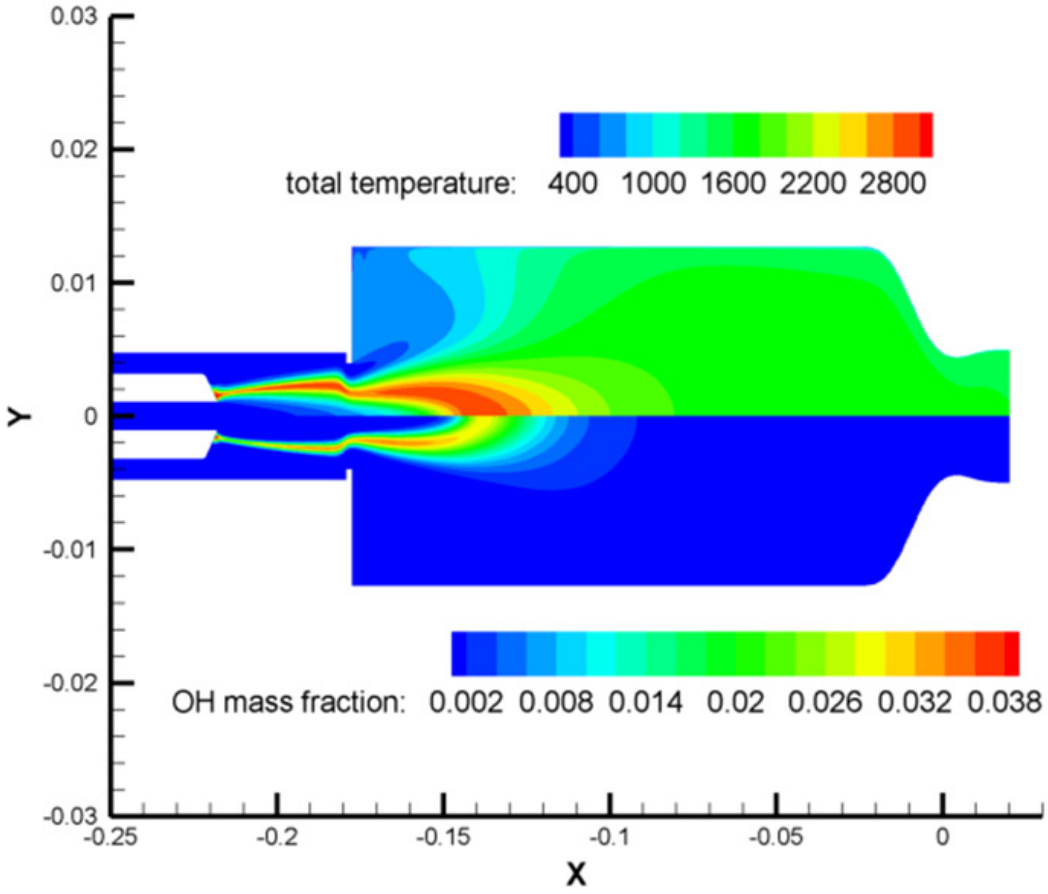

Figure 7-5: Total temperature (top) and OH mass fraction (bottom) distribution for M_e=1.6 and M_f=7

A quasi 1D analysis provides the inflow conditions for all the entries in the test matrix in terms of mass flow rate of H_2, O_2 and air. The CFD software requires mass fractions, total temperature (set to 300 K), velocity, static density, the turbulence intensity and the turbulent to molecular viscosity ratio. The product of the inflow velocity and static density is used to compute the mass flux and the mass flux is held constant. A supersonic outflow boundary with second order extrapolation of all variables is used for the simulation of the convergent-divergent nozzles. A subsonic outflow boundary condition with atmospheric backpressure is used for the sonic case.

For all the walls, a temperature profile is assigned from the FEM calculation and the no slip condition imposed.

Figure 7-5 shows the total temperature and the OH profile in the burner obtained from the CFD simulation for M_e=1.6 and M_f=6. Flame-holding occurs at the tip of the H_2 injection tube, and not at the entrance of the combustion chamber as originally expected. This was also verified experimentally. A thermocouple was inserted right after the exit of the H_2 tube, paying special attention to minimizing the perturbation to the flow. The measured temperature immediately increased above the limit of the thermocouple showing that a flame was present in this region.

A database of computed nozzle exit profiles was generated for several cases, providing boundary conditions for the simulation of the coaxial free-jet and a

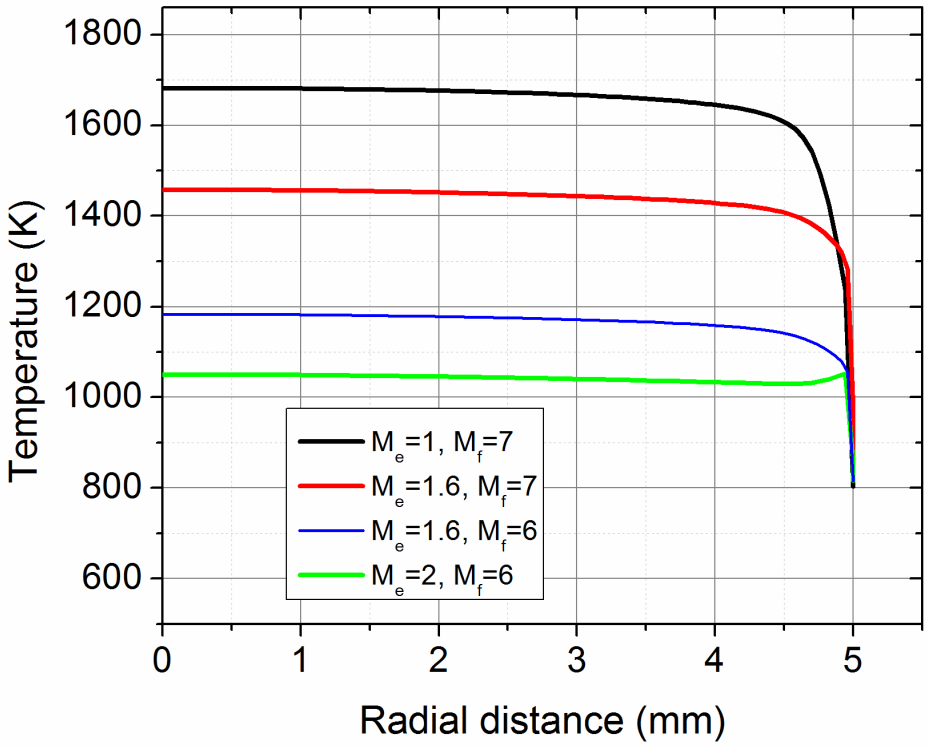

Figure 7-6: Static temperature profiles at the nozzle exit

benchmark for validation of non-intrusive laser diagnostics (such as dual-pump CARS), and other instrumentation. All species mass fraction are uniform at the exit. Figure 7-6 shows temperature profiles obtained for the values of M_e and M_f for which CARS data have been acquired.

Table 7-1summarizes the numerical results obtained at the nozzle exit on the centerline for several parameters of interest, for the conditions in which CARS measurements have been taken. For the supersonic cases the exit pressure is slightly above atmospheric, therefore the jet is under-expanded; expansion waves will depart from the nozzle exit and a system of expansion and compression waves will be generated.

Table 7-1: Centerline values at the nozzle exit

M_e	M_f	ρ(kg/m^3)	u(m/s)	M	TKE(m^2/s^2)	P(atm)	T(K)	O_2	N_2
1	**7**	0.188	787	0.952	8236	1.003	1681	0.230	0.569
1.6	**6**	0.283	1068	1.542	13708	1.030	1183	0.231	0.625
1.6	**7**	0.221	1189	1.538	17070	1.022	1458	0.231	0.569
2	**6**	0.345	1263	1.929	18816	1.063	1050	0.231	0.625

7.3 **Experimental Set-Up**

The laboratory-scale supersonic burner has been installed in the CARS laboratory at NASA Langley Research Center. Four Hastings flow-meters are used to measure the mass flow-rates. A 2500 standard liter per minute (SLPM) flow-meter measures the air-flow, two 1000 SLPM flow-meters measure the H_2 central jet flow, and the co-flow, and a 300 SLPM flow-meter measures the O_2 flow. The nominal accuracy of the flow-meters is 1% of the full scale, which is 25 SLPM for the air flow, 10 SLPM for H_2 and 3 SLPM for O_2. A set of experiments was performed to verify the factory flow-meter calibration. In each experiment 2 flow-meters were connected in series so

that the same amount of flow was passing through them, and the measured flow rates were compared. Observed discrepancies in between the two readings were within 1% of the full scale. The flow-meters are calibrated for atmospheric pressure at the outlet, but during a facility run the pressure at the exit of the flow-meters is much higher (up to 140 psi). To verify the effect of the outlet pressure on the mass flow rates accuracy, two flow-meters were connected in series, with a valve in between so that the desired pressure at the exit of the upstream flow-meter is obtained, where the downstream was discharging to atmospheric pressure. Increasing the outlet pressure, the reading decreases, but the error is below 1% of the full scale. The flow-rates were not adjusted to correct for this effect.

Pressure measurements are taken by means of wall static taps in the combustion chamber (reported in Table 7-2) and of the co-flow nozzle. A FLIR Model SC4000-MWIR infra-red (IR) camera, with sensitivity in the 3-5 μm range and an electronic exposure time set nominally to 12 μs was used to obtain IR images of the jet.

The laboratory-scale burner is mounted on a three-axis translation stage, remotely controlled through Labview. The capability of moving the flow field, rather than the optical set-up as in Ref.[72], simplifies the CARS instrument.

Table 7-2: Mass flow-rates, computed and measured pressure for the combination of M_e and M_f tested

		Mass Flow Rates (SLPM)					Total pressure (atm)		
M_e	**M_f**	Air	O_2	H_2	H_2 co-flow	Φ	Computed	This work	Ref.[27]
0.75	**7**	310.8	115.4	135.0	120.0	0.5	N/A	1.35	N/A
1.00	**7**	426.1	123.9	185.1	120.5	0.5	1.745	1.68	1.75
1.60	**6**	939.8	182.8	266.6	483.0	1	4.015	4.0	4.06
1.60	**7**	741.9	221.0	322.3	419.1	1	3.915	3.88	3.93
2.00	**6**	1273.0	242.0	361.0	666.0	1	7.809	7.12	7.36

The enthalpy of the vitiated air center-jet (expressed in terms of a nominal M_f) can be varied between 5 and 7 by changing the flow-rates of air, O_2 and N_2. For the sonic and subsonic case only for the M_f=7 case combustion is complete inside the burner.[27] Table 7-2 shows the flow rates required for the conditions tested for this work. The column labeled Φ indicates the equivalence ratio of a homogeneous mixture of only the H_2 co-flow and the vitiated air center-jet. For the mixing case, 120 SLPM of N_2 replaces the H_2 in the co-flow. The last three columns offer a comparison between the computed total pressure and measurements in the burner obtained during the test described in this work (during which CARS spectra were collected), and a previous set of tests described in Ref.[27]. The reduced total pressure could be caused by a reduced total mass flow rate, or reduced temperature

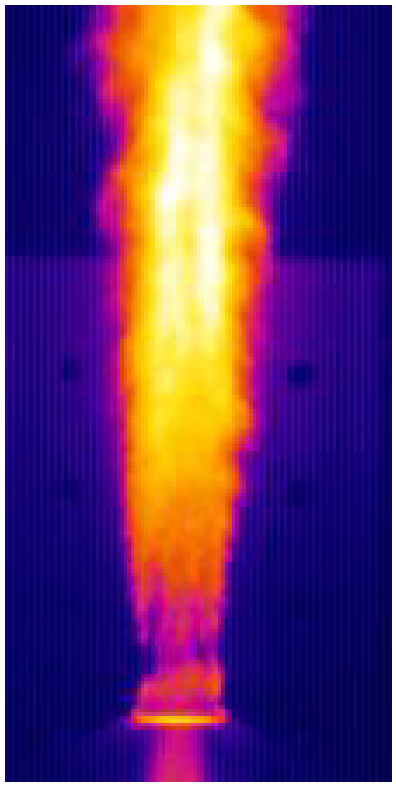

Figure 7-7: Infra-red image of the supersonic combusting jet

rise in the burner. Both could be consequences of inaccuracies in the mass flow rates. Measurements of the nozzle throat diameter using calibrated pin gauges, revealed that the M_e=2 nozzle throat is between 1.9% and 2.2% larger than the design value, explaining the large discrepancy in the total pressure for that case. Throat erosion was considered a possible cause for the total pressure reduction, but measurements performed after this test showed no difference from what was reported in Ref.[27]

IR-images of the free combusting jet for various combination of M_e and M_f were collected. Figure 7-7 shows an IR image of the supersonic-combusting free jet. The flame is attached to the burner at the interface between the co-flow and the ambient air, and this is the case for all the test conditions of Table 7-2. For the case with M_e=1.6 and M_f=7 auto-ignition occurred; in the other cases the flame was ignited with an electric spark lighter. Once ignited, the flame propagated upstream in the co-flow-ambient-air mixing layer, attaching to the co-flow nozzle exit. Local extinction is visible less than two nozzle diameters from the exit. The image shows asymmetry with respect to the centerline. As it will be shown in Chapter 8, the co-flow rate is not uniform through the co-flow nozzle. The asymmetry could be caused by small errors in centering the nozzle with respect to the annulus, thereby increasing the co-flow nozzle exit area on one side, and reducing it on the other. Efforts were made in centering the nozzle correctly, and visual inspection did not show significant asymmetry, yet the IR image and the DP-CARS measurements still show asymmetric co-flow. Another possible explanation for the asymmetry is that the center jet nozzle exterior surface, which forms the interior surface of the co-flow nozzle, is slightly asymmetric.

CHAPTER 8 - DP-CARS Measurements in the Laboratory-Scale Supersonic Combusting Jet

8.1 Introduction

The dual-pump CARS (DP-CARS) instrument has been applied to obtain measurements in the flow-field provided by the laboratory-scale supersonic burner described in the previous chapter. The goal of the test was to demonstrate the capability of the DP-CARS instrument in a flow relevant to the study of supersonic combustion, and to provide a database for the validation of computational fluid dynamics (CFD) models applied in the simulation of compressible mixing layers.

DP-CARS provides instantaneous, spatially resolved, simultaneous measurements of temperature and mole fractions. Mean, variances, co-variances and histograms are obtained from the single shots measurements, providing the CFD modelers with quantities never measured before in similar flows. Several test cases have been considered, both reacting and not, to isolate the effects of the compressibility, of the enthalpy, and of the heat release, on mixing in a compressible shear layer.

This chapter begins with a brief review of published works on compressible mixing layer to provide the necessary background to correctly interpret the DP-CARS measurements. The test matrix is described, and the challenges encountered during the data acquisition discussed. Measured nozzle exit profiles are compared to the results of the numerical simulations presented in Chapter 7. DP-CARS measurements for the mixing case are illustrated and when possible compared to previously

published results. Finally, DP-CARS data for the combustion cases are presented, and the role of the heat release on mixing discussed.

8.2 **The Compressible Shear Layer**

The flow provided by the facility described in chapter 7, was developed to provide further insight in the physics of compressible mixing layer. This is a key issue in designing a scramjet engine, and adequate CFD models needs to be developed to compute these flows and validated. Published experimental studies of compressible shear layers involve several techniques, including Pitot pressure measurements, [13-19] gas sampling, [22] laser Doppler velocimetry, [15, 181] Schlieren imaging [14, 15, 28], planar laser-induced fluorescence (PLIF) and planar laser Mie scattering (PLMS). [182] To my knowledge, this is the first successful application of the DP-CARS technique to measurements in a compressible shear layer. In this section, the discussion is limited to key aspects of the flow physics, to provide a framework for the interpretation of the DP-CARS results. In depth reviews of works on compressible shear layers can be found in Ref. [183] and [184].

Early experimental studies of supersonic jets expanding in a quiescent medium are summarized in a review work by Birch. [185] All those experiments show a decreasing spreading-rate of the shear layer with increasing Mach number. The spreading-rate reduction was attributed to the lower density ratio associated with the higher Mach number. Brown [186] investigated the effect of the density ratio on low-speed planar shear layers by using different combinations of gases to simulate density ratios similar to what observed in supersonic shear layers. The study showed that the effect of a decrease in the density ratio on the spreading-rate is much smaller than

measured in compressible shear layers. Brown showed that compressibility effects, and not changes in the density ratios were responsible for the reduced spreading-rate reported in Ref. [185].

Ortwerth [187] and Oertel [188] observed large coherent structures in supersonic shear layers and suggested that instabilities of these large scale structures govern the growth of the shear layer. Experimental studies [15, 181, 182] show that for increasing compressibility, these coherent structures become more three-dimensional, less coherent and the turbulent fluctuations are reduced. Since these large structures are critical for the mixing, compressibility needs to be defined in a reference system moving with these coherent eddies. This concept was first introduced by Bogdanoff [189] and Papamoschou [19] with the definition of a compressibility parameter, the convective Mach number (M_c), that is the Mach number of the jet in a reference system moving with the large eddies. The definition of this quantity, introduced for planar shear layers between two flows at different speeds, can be extended to an axisymmetric jet spreading in a quiescent gas. Under the assumption of null total drag force on the eddies, the convective Mach number can be expressed as:

$$M_c = \frac{M_j(1-\lambda_u)}{(1+\lambda_\rho^{-1/2})\lambda_\gamma^{1/4}} \tag{8-1}$$

where M_j is the center jet Mach number, $\lambda_{u,}$ $\lambda_{\rho,}$ λ_γ are the ratios of velocity, density and specific heat ratio between the freestream (numerator) and the center jet (denominator).

Papamoschou [19] observed that the rate of growth of the shear layer thickness (based on Pitot measurements), normalized by its incompressible value, drops

drastically as the convective Mach number is increased up to 0.8, and then it stays roughly constant. This also implies that at higher convective Mach numbers, mixing is reduced.

Slessor [190] plotted the results of several experimental studies [15, 16, 19, 28, 181] as function of the convective Mach number, and showed that the data do not collapse well. In particular, larger discrepancies between the expected behavior and the experimental values were found in presence of large density ratios and when one of the two streams is subsonic. Based on the observation that the compressibility is an energy transfer mechanism (kinetic and thermal), Slessor proposed an alternative compressibility parameter Π defined as:

$$\Pi = \max\left[\frac{\sqrt{\gamma_i - 1}}{a_i}\right]\Delta u \tag{8-2}$$

where a is the speed of sound, γ the ratio of specific heat, and Δu the speed difference between the two gases. The quantity in brackets is evaluated for both streams, and the greater of the two values is selected in computing Π. The parameter coincides with the convective Mach number for density ratios close to 1, but differs largely (3 times larger than M_c for λ_s=0.1 or 10) otherwise. Much better collapse of the data is achieved when using this parameter as shown in Figure 4 of Ref.[190] . The flow-fields examined in this chapter have velocity ratio close to zero (supersonic jet in quiescent air), and density ratio between 4 and 7; therefore, the compressibility parameter Π is a better choice than the convective Mach number to evaluate the compressibility effects.

All the experimental works agree that increasing the compressibility reduces the spreading-rate, makes the coherent structure increasingly three-dimensional, and reduces the turbulent fluctuations. Insight on the fundamental mechanism driving the observed phenomena has been provided in recent years by direct numerical simulations (DNS) as the one performed by Pantano [191]. In this work, the authors show that a reduction in turbulent production is responsible for the decrease in the spreading-rate. The reduction in turbulent production is ultimately caused by the finite speed of sounds in compressible flows, which limits the propagation of pressure fluctuations across the shear layer, and disrupts the agglomeration of the turbulent eddies.[191]

The flow-field complexity increases in presence of chemical reaction and heat release. In the incompressible case, the dominant effect is displacement caused by the heat release. The heat release slows the development of the large-scale structures and the resulting entrainment of the reactants. The spreading-rate and the turbulent shear stresses decrease with increasing heat release for both incompressible and compressible flows. These effects have been observed experimentally[192] and in DNS simulations.[193, 194]

Publicly available experimental data for reacting compressible shear layers are scarce, and more data are desirable to improve RANS and LES models. Accurate quantitative measurements of multiple parameters, capable of providing converged statistics (mean, variances, and co-variances) are needed. The data set collected with the DP-CARS instrument described in the previous chapters is the first containing

simultaneous measurements of temperature and all major species mole fraction in a compressible turbulent shear layer.

8.3 **DP-CARS Data Acquisition and Test Matrix**

DP-CARS data have been acquired for 5 combinations of exit Mach number (M_e) and flight Mach number (M_f), for both mixing and combustion cases as illustrated in Table 8-1.

Table 8-1: Test cases for DP-CARS measurements. *M* indicates a mixing test case, *C* a combustion test case.

$M_f\downarrow \backslash M_e\rightarrow$	0.75	1	1.6	2
6			*M/C*	*M*
7	*M*	*M/C*	*M/C*	

M_f is varied by changing the mass flow-rates of air, O_2 and H_2 in the burner, M_e, by selecting the appropriate SiC nozzle, and mass flow-rates. The three nozzles differ by throat area, but have the same exit diameter (10 mm). The co-flow was either H_2 (combustion case) or N_2 (mixing case). For the combustion case, the H_2 co-flow was set to be in stoichiometric ratio with the O_2 from the center jet. The N_2 co-flow was constant and equal to 120 SLPM in all the mixing test cases.

The test cases were selected so that the effect of each variable (compressibility, enthalpy, and heat release) could be isolated. For the lower exit Mach numbers (M_e=0.75 and 1) combustion in the burner was not complete for M_f<7 as observed in Ref.[27]. A combustion test case for M_e=2 and M_f=6 was attempted but the large amount of heat released prevented successful data acquisition. (Warm combustion

products mixed with air recirculating within the laboratory caused excessive beam steering, preventing acceptable CARS data quality, and radiant heating of the optical system caused problems with maintaining optical alignments. See discussion Section 8.4.)

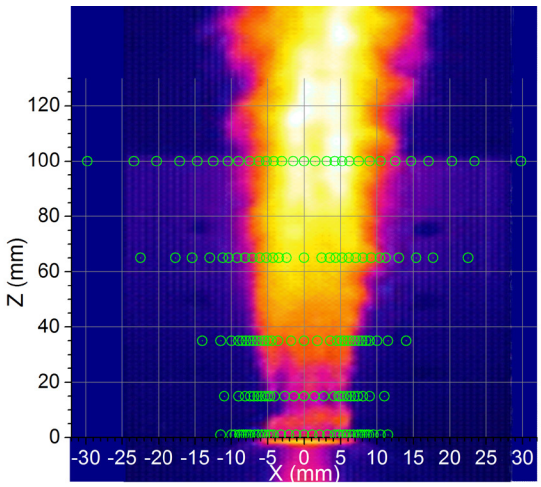

Figure 8-1: Infra-red image of the supersonic combusting jet. Green circles are the measurement locations

The laboratory-scale supersonic burner is mounted on a three-axis translation stage, which allows changing the position of the measurement volume with respect to the flame. As shown in Figure 8-1, measurement locations reported here are in a reference system having the origin at the center of the nozzle, at its exit plane. The z axis is orthogonal to the nozzle exit plane, the y direction parallel to the Nd:YAG laser beam. Data have been acquired along five lines parallel to the x-axis and at z = 1, 15, 35, 65 and 100 mm downstream of the nozzle exit, as shown in Figure 8-1. This orients the CARS probe volume orthogonal to the direction of the maximum temperature gradient, reducing spatial averaging effects (see Chapter 6 and 8). In addition, data have been collected along two lines parallel to the y-axis and 1 mm and

100 mm downstream of the nozzle exit. Data along this direction are obtained to evaluate the effect of the probe volume length on the measurements, and to evaluate the symmetry of the flame. The number of points varies for each line between 27 and 39. Each location along the z = 65 and 100 mm lines and along the centerline (x=0) is visited 4 times (replications), where points along the z = 1, 15 and 35 mm lines were visited only once. For each replication, 250 single shot spectra were acquired. For each condition, ~ 100,000 spectra were collected. Closer to the nozzle exit, the accuracy of the means, variances and co-variances computed from the CARS measurements is limited by the steep gradients, rather than by the sample size (error associated to the spatial averaging larger than sampling error), therefore a single replication was deemed sufficient. Further downstream the gradients are smoother, CARS measurements more accurate, and therefore increasing the sample size was helpful in obtaining better statistics. For given test conditions (M_e, M_f, mixing or combustion) the test matrix is fully randomized. All the test cases using the same nozzle were done sequentially to avoid disassembling and reassembling the burner several times.

Data acquisition is controlled through a Labview graphical interface, which drives the translation stage and the CARS instrument (laser, camera, pulse generator, rotation stage for the wave-plate). Before starting the supersonic jet, background spectra were collected in ambient air and in argon, providing the spectra for the background subtraction and non-resonant normalization described in Chapter 3. The origin of the reference system is determined experimentally immediately before the data acquisition. The distance between the nozzle exit and the measurement volume

was determined by placing a piece of black-painted aluminum on the nozzle and marking it with the laser. A micrometer was then used to determine the distance between the nozzle exit and the laser mark. With the supersonic burner running at the test conditions, CARS signal intensity in the O_2 spectrum was recorded at several locations along the *x* and *y*-axis, 1 mm from the nozzle exit. Since O_2 is not present in the co-flow, this allows determining the location of the nozzle centerline, with respect to the CARS measurement volume. The process was automated, and was performed daily before starting the data acquisition. The accuracy of this approach is within 1 mm. Once the origin had been determined, the DP-CARS data acquisition started. The Labview software reads a position from a text file containing all the randomized locations, moves the translation stage to that location, reduces the energy of the Nd:YAG laser to avoid detector saturation if necessary, acquires 250 single shots and then moves to the next location. No further input from the operator is needed once the acquisition has begun. The automation of the data acquisition process was critical in increasing the amount of data that could be collected in a single test day. Once the test matrix was completed, background spectra and CARS spectra in argon were acquired again to take into account shift in the broadband dye laser spectrum (details and limitation of this approach are illustrated in Chapter 3). A typical test lasts 4-5 hours during which the burner operates continuously. The test was monitored from a control room across a hallway from the laboratory. Here the operator could monitor the peak CARS signal intensity and the advancement of the test along the test matrix (through the Labview interface), the crossing and focusing of the beams through the

beam-viewing system placed after the measurement volume, the correct operation of the burner and the translation stage through the IR camera.

The collected data were analyzed as described in Chapter 3, and returned instantaneous measurements of temperature, and N_2, O_2 and H_2 mole fractions. A post-processing algorithm written in Matlab rejects spectra having a poor fit, based on a quality-of-fit parameter obtained in output from the fitting code. The post-processing algorithm merges all the data collected at a single location, and computes mean, standard deviation, covariance and skewness for all the measured quantities. A single text file containing the measurement locations and all the computed statistics is obtained in output for each test case.

8.4 **Additional Challenges in DP-CARS Data Acquisition in the Laboratory-Scale Supersonic Free Jet**

Data acquisition in the supersonic jet presented some additional challenges compared to acquisition in the steady, laminar Hencken burner flame. Beam steering effects due to turbulence and vibrations were expected, and the beam shaping technique demonstrated in Chapter 3 was implemented to mitigate this issue. Figure 8-2 is a video of typical motion of the laser beams traversing the supersonic jet. The camera is imaging the three beams, slightly before their intersection, so that the Nd:YAG (the elliptical beam on the right) is separated from the overlapped broadband (in red) and the narrowband (blue-white color in the image). The video shows movements of the overlapped beams with respect to the Nd:YAG that would have prevented the beam from crossing and generate the CARS signal if the Nd:YAG

Figure 8-2: Beam steering caused by turbulence in the laboratory-scale supersonic free jet.
Click on the figure to start the video

beam was not elliptical. The axis ratio used for the Nd:YAG beam for this test is ~4:1 and the data yield (percentage of the shots that produces acceptable measurements) is 97% for the mixing case, and 95% for the combustion case. The test is a successful application of the beam shaping technique in an actual test environment.

In addition to the random motion, a drift of the laser beams' alignment with time was observed. The large amount of heat released by the supersonic jet caused an increase of the room temperature and of all optical elements in the proximity of the jet. Changes in temperature of the mirrors cause steering of the beams, degradation of the beam overlap, and consequent signal reduction. (Note that the signal reduction does not change the results, since it is the relative intensity of the CARS spectrum that matters, not the absolute.) Such drift was monitored using the beam viewing system placed after the measurement volume, while the Labview interface was monitoring the CARS signal level. Periodically the test had to be interrupted, so that the relative position between the lasers could be restored. Using the Nd:YAG beam as

reference, the dye lasers position was restored with respect to this beam by remotely controlling two mirrors (mounted on New-Focus pico-motors mounts); one is placed on the laser cart and adjusts the broadband dye laser, the other which adjusts the superimposed dye lasers is placed immediately before the focusing lens. Note that a sideways drift of the location of the measurement volume with time was not corrected by this system, though the error induced by this drift is estimated to be a fraction of the length of the probe volume.

Analysis of the CARS data was the same as described in Chapter 3. The long test duration, the increase in the room temperature, and in the dye temperature, were responsible for changes in the dye lasers spectral output. Chapter 3 includes a detailed discussion on the consequences of the spectral changes in the broadband dye laser profile, how it affects the measurements accuracy, and how to minimize its effects.

The frequency of the narrowband dye laser changed in time during the data acquisition because of the temperature increase in the room. The shift was monotonic, and changes up to 0.8 wavenumbers were observed for the combustion cases. The frequency difference between the two pump beams (the Nd:YAG and the narrow band dye laser) is not a fitting parameter, but an input required for the theoretical library. For this reason for each test day, four libraries of theoretical spectra were generated, with different values of the offset between the two pumps, one for each hour of testing.

8.5 **Measurements at the Nozzle Exit**

In this section the results of measurements taken at the most upstream location (z = 1 mm) for $|x| < 5$ mm are described. Measurements at the centerline are relatively steady and are used to evaluate the repeatability of the measurements, which is useful for determining their capability to resolve turbulent fluctuations. Experimental measurements along x are compared to their numerical counterparts. Experimental profiles along y are shown to illustrate the effect of the CARS probe volume length on the measurement accuracy. A strategy that uses the nozzle exit profile to obtain a better estimate of the measurement locations is described.

Table 8-2: Measurements and confidence intervals at the nozzle exit on the centerline for M_e=1.6, and M_f=7, and H_2 co-flow. The values in brackets are the 1% confidence interval

Run	T_{av}(K)	T_{sd}(K)	N_{2av}(%)	N_{2sd}(%)	O_{2av}(%)	O_{2sd}(%)
A	1392±11	63 [57,72]	49.9±0.3	2.0 [1.8, 2.3]	20.2±0.2	1.2 [1.1, 1.4]
B	1394±10	62 [56, 70]	50.1±0.4	2.9 [2.6, 3.2]	20.0±0.2	1.3 [1.2, 1.5]
C	1387±10	63 [56,71]	50.6±0.4	2.8 [2.5, 3.1]	20.0±0.2	1.1 [1.0, 1.3]
D	1407±10	60 [53, 68]	50.3±0.5	3.0 [2.7, 3.4]	20.1±0.2	1.3 [1.1, 1.4]
Pooled	1395±25	62 [59, 67]	50.2±0.8	2.7 [2.6, 2.9]	20.2±0.3	1.2 [1.2, 1.3]

For each test condition, the location on the centerline, 1 mm downstream of the nozzle exit is visited 4 times (4 replications) and 250 single shot spectra are acquired at each passage. The length of the CARS probe volume is not a significant issue since numerical simulations indicated that the temperature at the nozzle exit is uniform. Table 8-2 shows the average and the standard deviation of temperature, N_2 and O_2

mole fraction computed for each replication (250 single shots) for the combustion case with M_e=1.6 and M_f=7. The data span an acquisition time of approximately 4 hours. The values following the means in Table 8-2 are the 99% confidence intervals defined for the mean as:[195]

$$\pm t_{1-\alpha/2} s / \sqrt{n} \tag{8-3}$$

where n is the number of shots, s the estimated standard deviation, $t_{1-\alpha/2}$ is the 99.5th percentile of a t distribution with n-1 degrees of freedom. Similarly for the standard deviation the confidence interval is given by:[195]

$$[(n-1)s^2 / \chi^2_{1-\alpha/2}, (n-1)s^2 / \chi^2_{\alpha/2}] \tag{8-4}$$

where χ^2 is the chi-square distribution with n-1 degrees of freedom. Analysis of variance (ANOVA) shows that the temperature between runs is significantly different (for a significance level α=1%) but there is no significant difference between the mole fraction measurements. Although there is a statistically significant difference between the temperatures measured in each run, there is no trend with time. Small changes in the mass flow-rates probably cause the run-to-run variations. The measured standard deviations instead are independent of the time. The row labeled "pooled" contains the average over all the measurements taken at a single location. Since there is a significant difference between the runs, then it would be incorrect to compute the interval of confidence as in Eq. (8-3) using as n the total number of acquisition. Instead the 1% interval of confidence is based on the 4 averages over each run, and is larger (2.5 times) than that computed over a single run, as expected since it includes the variation between runs. For the rest of this work, unless specified, "pooled" averages will be shown.

The variance of the pooled results can be expressed as sum of the variance due to variations between runs ($\sigma^2_{Between}$) and within a single run σ^2_{Within}. The variance within a single run can be further decomposed in the contribution due to the turbulence in the flow and the contribution due to instrument error.

$$\sigma^2_{Total} = \sigma^2_{Between} + \sigma^2_{Within} = \sigma^2_{Between} + (\sigma^2_{Turbulence} + \sigma^2_{\mathrm{Pr}ecision}) \tag{8-5}$$

For the data of Table 8-2 $\sigma^2_{Between} \sim 1.5\% \sigma^2_{Total}$. Based on measurements in the Hencken burner, for a temperature of 1355 K and an O_2 mole fraction of 21%, the temperature standard deviation due to the instrument precision is 25 K. At the centerline, the instrument precision is responsible for ~ 15% of the total variance. The estimated temperature standard deviation due to the turbulence alone is 57 K. For the N_2 mole fraction the total standard deviation is 2.7 % of the total mole fraction, where in the Hencken burner for similar conditions it was 2.1%. Turbulence contributes to 45% of the total variance and the estimated standard deviation of N_2 due to the turbulence is 1.8%. Similarly for O_2 the turbulence contribution to the variance is 76% of the total and the standard deviation is 1.1%. These results show that the DP-CARS instrument is capable of resolving the temperature fluctuations due to the turbulence at this location, but it performs worse for the mole fraction fluctuations.

Table 8-3: Measurements and confidence intervals at the nozzle exit on the centerline for M_e=1.6, and M_f=7, and N_2 co-flow. The values in parenthesis are the 1% confidence interval

Run	T_{av} (K)	T_{sd} (K)	N_{2av}(%)	N_{2sd}(%)	O_{2av}(%)	O_{2sd}(%)
A	1382±11	64 [57,72]	49.2±0.4	2.7 [2.4, 3.0]	19.9±0.2	1.2 [1.1, 1.4]
B	1372±10	62 [55, 70]	50.4±0.4	2.9 [2.6, 3.3]	20.0±0.2	1.3 [1.1, 1.4]
C	1373±10	60 [56,71]	50.4±0.5	3.1 [2.8, 3.5]	20.1±0.2	1.1 [1.3, 1.6]
D	1365±10	62 [54, 68]	49.9±0.4	2.7 [2.4, 3.0]	20.3±0.2	1.3 [1.2, 1.5]
Pooled	1373±20	62 [55, 70]	50.2±0.8	2.9 [2.7, 3.1]	20.1±0.4	1.3 [1.2, 1.4]

Table 8-3 is analogous to Table 8-2 but obtained for the mixing case. The two data sets were collected on different days. The average temperature is ~22 K lower and the temperature standard deviation is the same. Mole fraction of N_2 and O_2 are within the 1 % interval of confidence determined for the combustion case. This shows that there is no significant difference in the pooled statistics between data taken in different days.

Figure 8-3 shows the temperature profiles of the center jet measured 1 mm from the nozzle exit and compare it to the CFD results presented in the previous chapter. The experimental results are systematically lower (~5%) than the prediction and the curvature is greater. The lower exit temperature could indicate that the numerical solution underestimated the heat transfer, or that the actual equivalence ratio in the burner differs from its nominal value. The higher curvature is likely a consequence of the CARS probe volume length; 90% of the CARS signal is generated over a length of 1.5 mm, which is longer than the shear layer between the center-jet and the co-

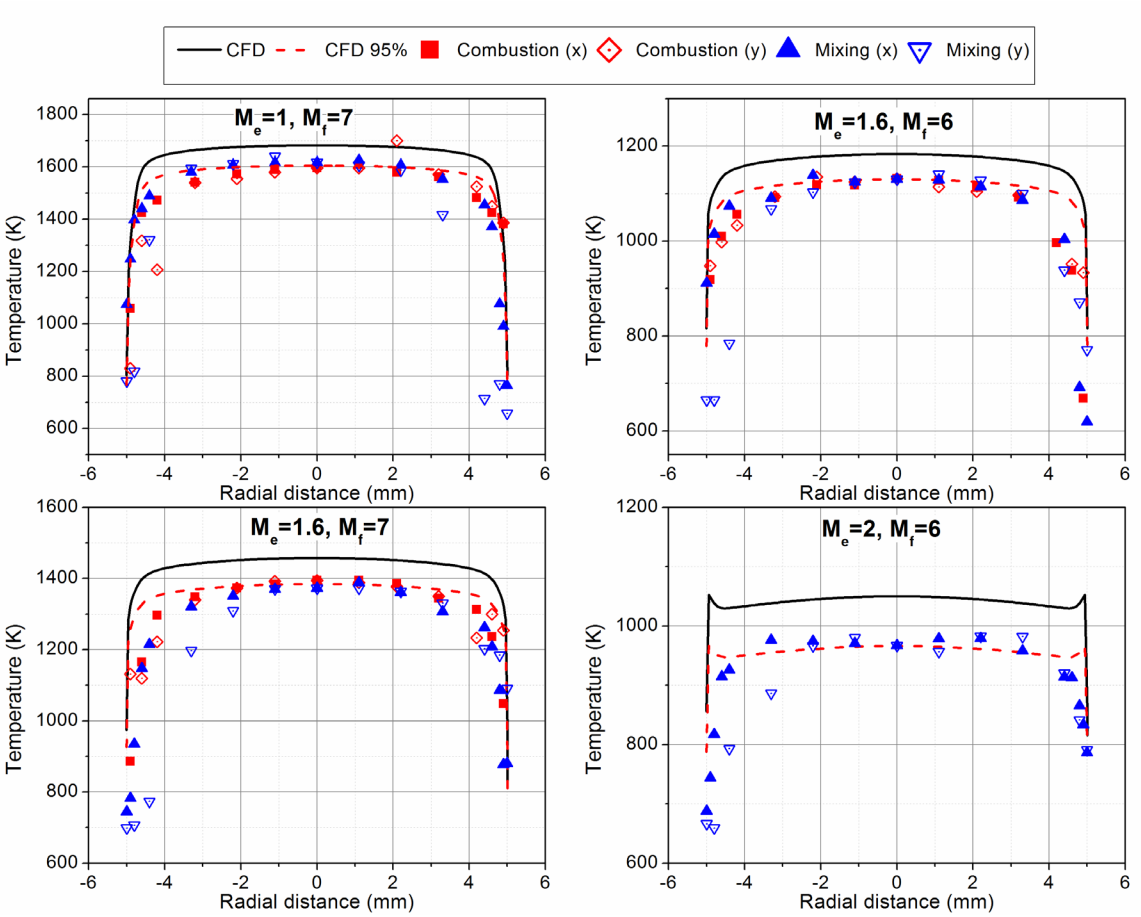

Figure 8-3: Comparison of numerical and experimental temperature profiles at the nozzle exit for 4 combinations of M_e and M_f

flow. CARS signal is a strong function of temperature, with much stronger signal generated in the colder co-flow and quiescent air region.

The measured temperature is not an average along this distance, but it is biased toward lower values of temperature. As consequence of the CARS probe volume length and of the signal temperature dependence, the instrument artificially decreases the steepness of the flame front. The closed symbols in Figure 8-3 are measurements for variable *x*, having the probe volume oriented in direction orthogonal to the temperature gradient. Open symbols are measurements along *y*, with the probe volume oriented in the direction of the maximum gradient, therefore more subject to

the averaging effect. The measurements are overlapped in proximity of the centerline, but moving toward the edge of the jet, temperatures taken along *y* (open symbols) drop more quickly because the probe volume includes larger portions of the co-flow. Figure 8-3shows that the DP-CARS measurements are inaccurate in presence of steep gradients, tend to overestimate the thickness of the shear layer, and not predict correctly its location. Orienting the probe volume in direction orthogonal to the temperature gradient mitigates this deleterious effect, thus most of the CARS data were taken in lines along *x*.

In turbulent flows, the measurement fluctuations are indicative of the turbulence level. Since the probe volume cannot resolve the smallest turbulence scales, the CARS signal will integrate over these finer structures; colder regions produce stronger signal, therefore the measured temperature is biased toward lower values. Furthermore, the spatial averaging reduces the intensity of the measured fluctuations. [196] Also mole fractions are biased toward the mole fractions associated to the lower temperature.

Figure 8-4 shows the nozzle exit profiles for the mole fraction measurements. In terms of total mole fraction the measured N_2 is systematically lower, (up to 1%), where O_2 is systematically higher (up to 1.5%). Measurements in the Hencken burner showed accuracy within 0.5% for O_2 and within 1% for N_2. Errors in the division by the non-resonant spectrum can potentially cause inaccuracies up to 1% on O_2 and 2.5% on N_2, but no evidence of incorrect normalization was found in the fitted spectra. The lower burner pressure (see Table 7-2) and exit static temperature, and the increased O_2 mole fraction suggest that less O_2 burned in the burner. Errors in the mass flow-rates are the most likely cause for the discrepancy.

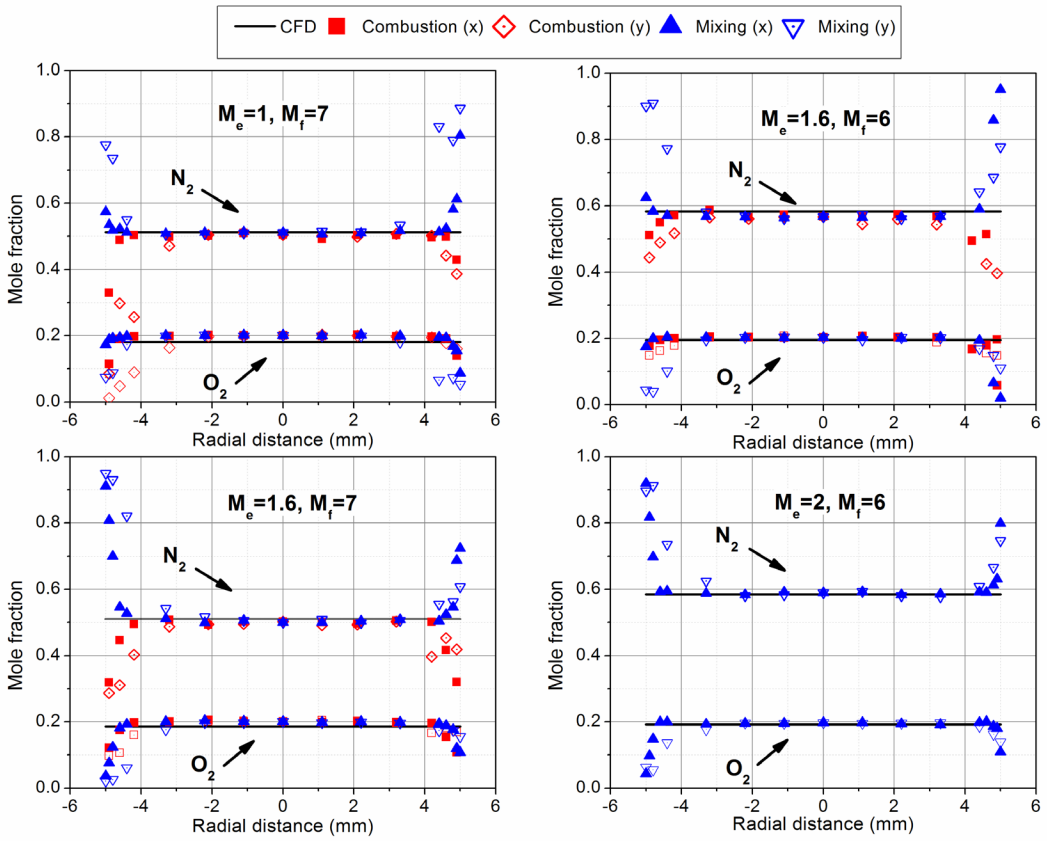

Figure 8-4: Comparison of numerical and experimental mole fraction profiles at the nozzle exit for 4 combinations of M_e and M_f

In order to compare experimental and computational results, it is necessary to know the exact location at which the data have been collected. In section 8-3 the procedure to determine the location of the nozzle center in the reference frame of the translation stage is described. The algorithm relies on quickly analyzing just a few samples of unprocessed spectra. This can potentially lead to errors of 1 mm or more. The profiles of temperature and mole fractions obtained near the nozzle exit, combined with the assumption of symmetry of the center jet allow for a more precise determination of the nozzle center. An improved estimate of the origin (x=0, y=0) location with respect to the actual centerline can be obtained by fitting temperature profiles in the core of the jet (over a region of ±3.3 mm for the mixing case, ±4.6 mm for the combustion case) with a quadratic function; the vertex of the fitted parabola provides the actual location of the centerline. As an example, for M_e=1.6 and M_f=7 the values determined along x are -0.016 mm for the mixing, and -0.05 for the combustion, therefore they are negligible. On the other hand, along y the centerline is 0.55 mm from the origin of the reference system for the mixing data, and 0.06 mm for the combustion data. This approach allows accurate determination of the location of the measurement points, for a more faithful comparison to CFD simulations. Based on the results of this approach, the data presented in this work have been shifted so that the centerline coincides with the z axis of the reference system.

8.6 **Mixing Study**

This section discusses the measurements acquired for the mixing case, that is for a constant flow of 120 SLPM of N_2, and variable M_f and M_e. Since the co-flow has low

speed, and small total mass flow rates, the flow can be treated as jet in quiescent air. Four exit Mach numbers are considered (0.75, 1, 1.6 and 2) and for M_e=1.6, flight Mach number (M_f) of 6 and 7 are compared. Parameters that characterize the flow are the velocity ratio λ_u, the density ratio λ_ρ, the convective Mach number (M_c) and the Slessor compressibility parameter Π. Table 8-4 shows the values of these parameters for the test cases considered. The velocity ratio is 0, assuming that the supersonic jet is mixing with quiescent air. The mean values obtained from the DP-CARS measurements are shown, and compared to what it was expected, based on the published results discussed in section 8-2. The spreading-rates are estimated, and the effect of compressibility and of the density ratio is identified. Standard deviations and co-variances plots are presented and discussed.

Table 8-4: Values of the velocity ratio (λ_u), density ratio(λ_ρ), convective Mach number M_c, and Slessor`s compressibility parameter Π for the conditions tested

M_e	M_f	λ_u	$\lambda\rho$	M_c	Π
0.75	7	0	6.5	0.52	1.33
1	7	0	6.2	0.7	1.73
1.6	6	0	4.0	1.04	2.25
1.6	7	0	5.2	1.08	2.53
2	6	0	3.7	1.28	2.63

8.6.1 Mean Values

Figure 8-5 shows the DP-CARS average measurements of temperature and mole fractions, as a function of the radial distance x at different heights, z, for the two

mixing cases with M_e=1.6. The black triangles are for M_f=6 (M_c=1.05), the red circles for M_f=7 (M_c=1.08). The average at each location is computed over the total number of replications and repetitions (pooled average). The error bars represent ± one standard deviation, and include fluctuations due to the instrument precision, the turbulence in the flow, and the small contribution due to the run-to-run variations, as discussed in the previous section. The exit temperature of the center jet is higher for M_f=7 because of the higher total enthalpy and so is the density ratio (λ_ρ=5.2 for M_f=7, 4.0 for M_f=6). For M_f=7 the heat transfer from the flow inside the burner to the SiC nozzle and to the co-flow (acting as coolant) is larger than for M_f=6; therefore the N_2 co-flow is hotter for the higher enthalpy case. There is no significant difference in the O_2 mole fraction between the two cases. The N_2 mole fraction in the center jet is lower and H_2O higher for M_f=7 because more H_2 had to be burned to achieve the desired enthalpy. No H_2 lines were visible in the spectra, indicating that the combustion is complete at the nozzle exit, as predicted from the CFD simulation. The co-flow is pure N_2, but the CARS system measures mole fraction of ~97%, and O_2 mole fraction of ~1%. This is a systematic error of the DP-CARS system. A likely cause of this error is that the fitting algorithm does not allow for mole fraction greater than 1, and uses lower order interpolation in proximity of 1, biasing the error toward lower mole fraction. Also small errors in the background subtraction can contribute. At 1 mm from the exit, the boundaries between the co-flow jet and the center jet and between the co-flow and the ambient air are well defined. Notice that the temperature of the co-flow jet is not exactly symmetric, but it is lower for positive x. The co-flow is asymmetric with higher mass flow rates for positive values of x.

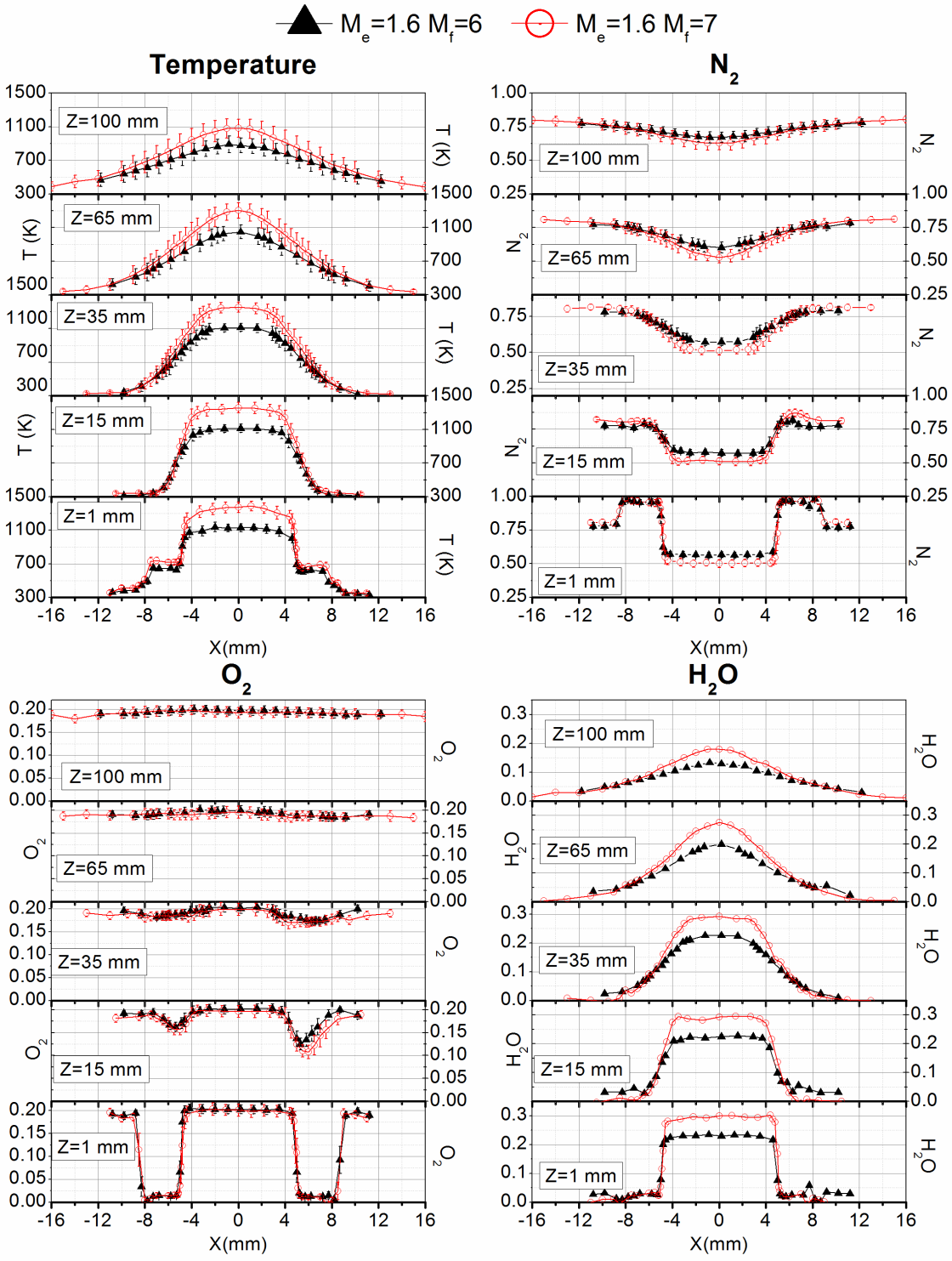

Figure 8-5: Average temperature and mole fractions at different heights for M_e=1.6 and M_f=6 and 7. Error bars indicate ± one standard deviation

At 15 mm downstream of the nozzle exit, the center of the supersonic jet is largely unaltered, although a growth of the shear layer is detectable. The low speed N_2 co-flow, as expected, mixes more efficiently with the ambient air, as can be observed in the N_2 and O_2 mean profiles. O_2 mole fractions up to 15% are recorded because of the entrained air in the co-flow jet. The asymmetry in the co-flow volumetric flow rates is evident from the N_2 and O_2 profiles. Water, present only in the center jet, is a good indicator of jet spreading and mixing. The DP-CARS instrument is unable to measure water vapor directly, but the water mole fraction is computed by subtracting the measurements of N_2 and O_2 from one, assuming that all other species are negligible. The instrument accuracy in measuring mole fractions is lower at low temperature, where the O_2/N_2 ratio is measured incorrectly (see Chapter 6) and the sensitivity to background subtraction is higher. This problem is more evident for the M_e=1.6, M_f=6 case. It was the first data set acquired, and not enough background spectra were collected.

Further downstream, 35 mm from the nozzle exit, the co-flow is no longer distinguishable from the entrained air. The shear layer is growing, but the mixing is limited to the outer region of the supersonic jet. The asymmetry is no longer evident, suggesting that the co-flow constitutes only a small portion of the entrained mixture.

For z > 65 mm the entrained mixture has reached the centerline, causing a reduction in temperature, and water mole fraction, and an increase in N_2 mole fraction. The O_2 mole fraction is uniform, where the N_2 maintains a wake profile. The

water mole fraction is spreading outward, indicating the spreading of the supersonic center jet.

The mean values plots show no major differences in the behavior of the jet for the two flight Mach numbers. This was expected because the convective Mach number is approximately the same for both cases (M_c=1.05 and 1.08 for M_f=6 and M_f=7, respectively). The results confirm that the density ratio plays only a small role in the mixing of a supersonic jet, as it had already been observed by Brown. [186]

Figure 8-6 compares mean measurements collected for constant M_f=6, and M_e=1.6 (black symbols), and M_e=2 (magenta symbols), corresponding to M_c=1.05 and 1.28, respectively. The overall behavior of the flow is the same as described above. The change in convective Mach number produces some significant differences in the mixing. The mean profiles show that the N_2-air mixture penetrates sooner in the supersonic jet for lower values of M_c. Up to 65 mm from the nozzle exit the profiles obtained for the lower convective Mach number are wider both in temperature and H_2O mole fraction. Curiously the temperature profiles at 100 mm match almost perfectly, but the same is not observed for the water mole fraction that maintains a wider profile at lower M_c. Increasing the convective Mach number reduces the mixing and the spreading-rate in the upstream region (see section 8-6-3 for details on the spreading rate) .

Figure 8-7 shows the results obtained for constant M_f=7 and M_e=0.75, 1 and 1.6 corresponding to values of M_c=0.53, 0.69, and 1.08. For the M_f=0.75 case data were collected only along three lines (z=1, 65 and 100 mm) and replications were limited to the centerline and to a subset of radial locations.

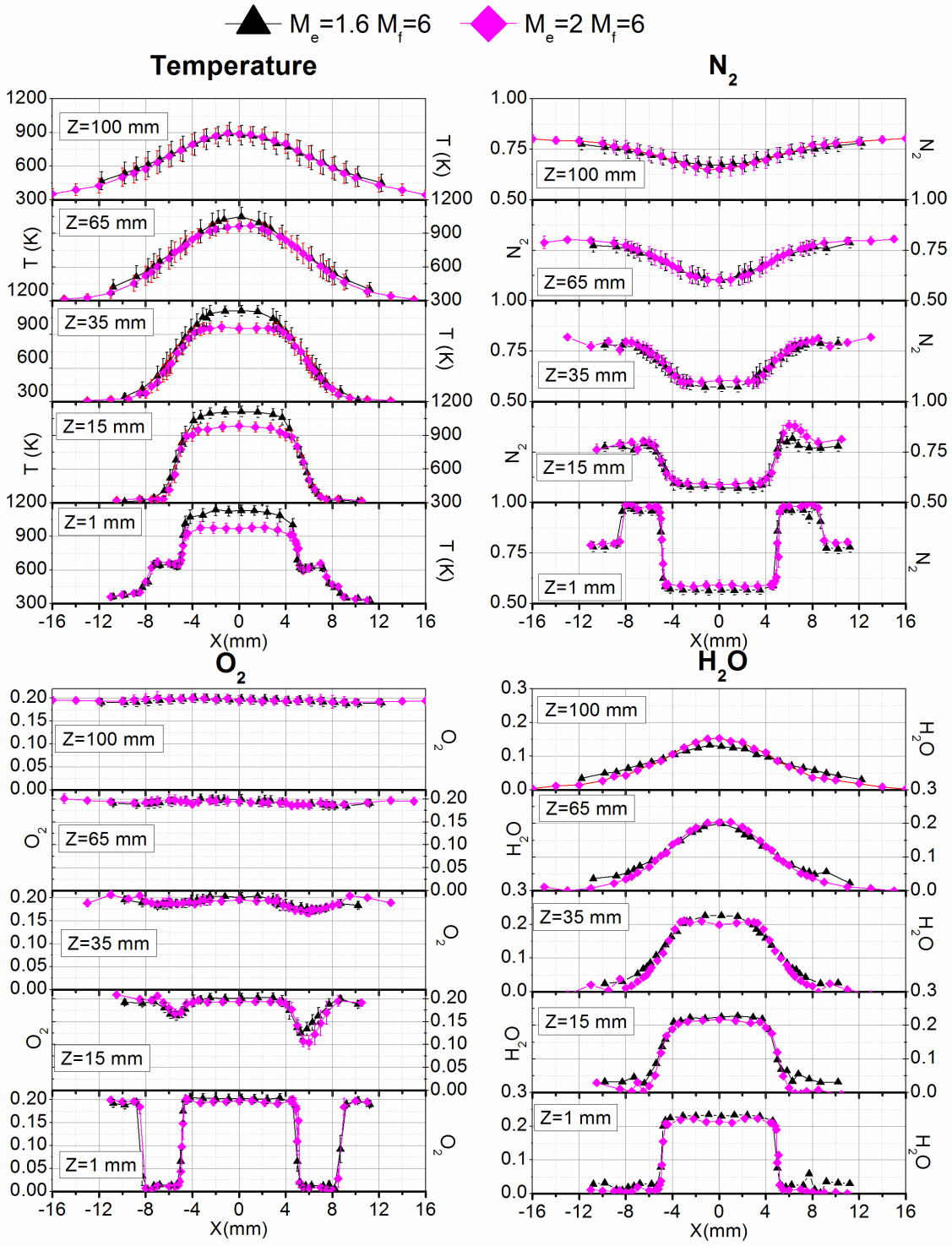

Figure 8-6: Average temperature and mole fractions at different heights for M_f=6 and M_e=1.6 and 2.Error bars indicate ± one standard deviation

During preliminary tests performed with the mass flow rates that provide M_f=7 for M_e=0.75, a high pitch whistle was heard, pressure changes observed in the burner and severe fluctuations of the flame were visible in the IR image. This was likely a symptom of combustion instabilities. To remove the high pitch whistle the air flow rate was reduced to 285.8 SLPM (from the nominal 310.8) and the O_2 flow rate increased to 115.4 (from 90.4). The high pitch noise was effectively removed during most of the test, but occasionally was still heard. This explains the different O_2 mole fraction values measured for this test case with respect to the other M_f=7 cases. The temperature and H_2O profiles show some distortions near the center jet 65 mm and 100 mm from the nozzle exit. This has been observed only for the M_e=0.75 case and it is probably consequence of combustion instabilities.

The temperature and H_2O plots in Figure 8-7clearly show the compressibility effect in reducing the shear layer spreading-rate and the mixing. In particular, for the sonic and subsonic cases the air has penetrated the jet up to the centerline already at 35 mm from the nozzle exit.

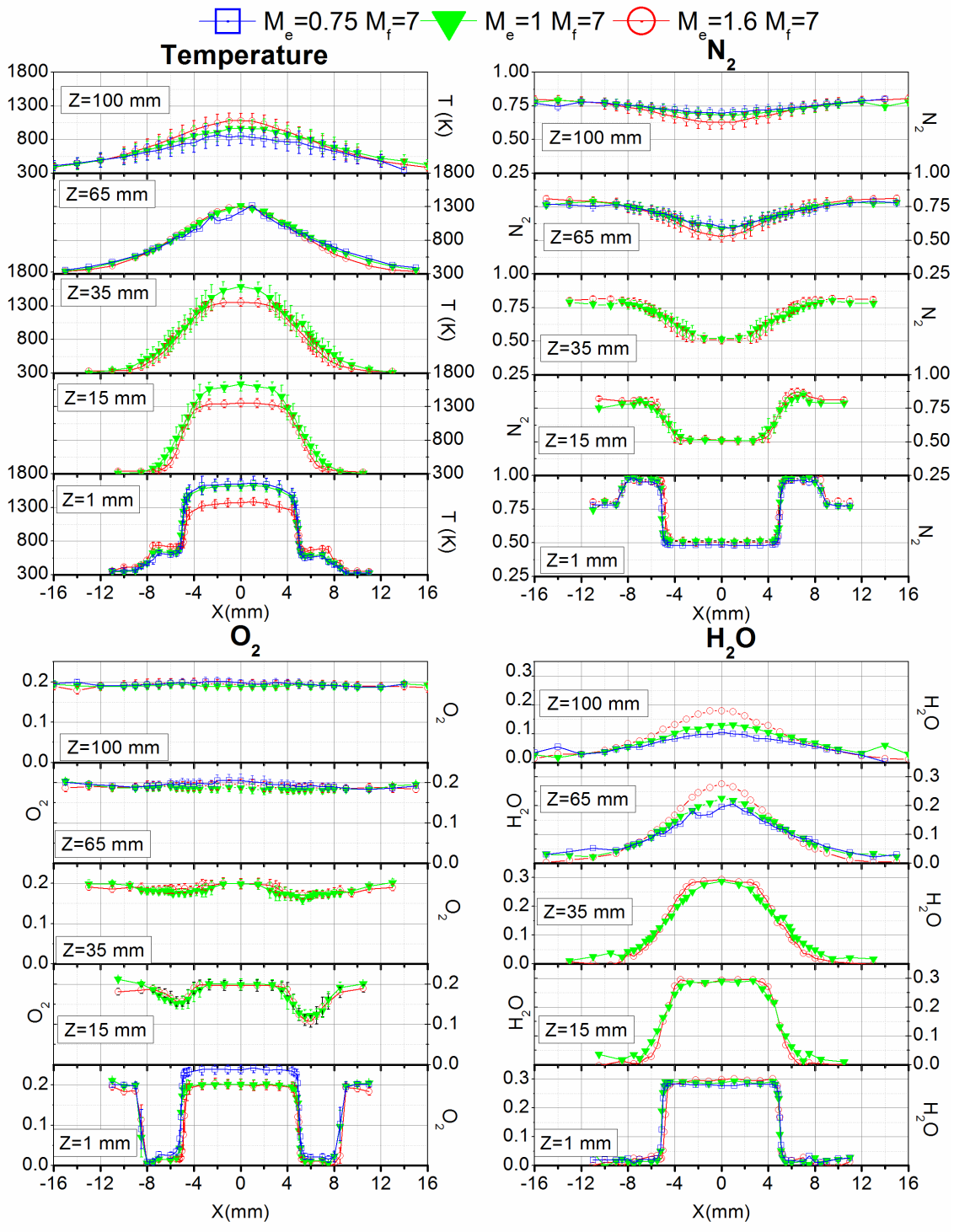

Figure 8-7: Average temperature and mole fractions at different heights for fixed M_f=7 and, M_e=0.75, 1 and 1.6. Error bars indicate ± one standard deviation

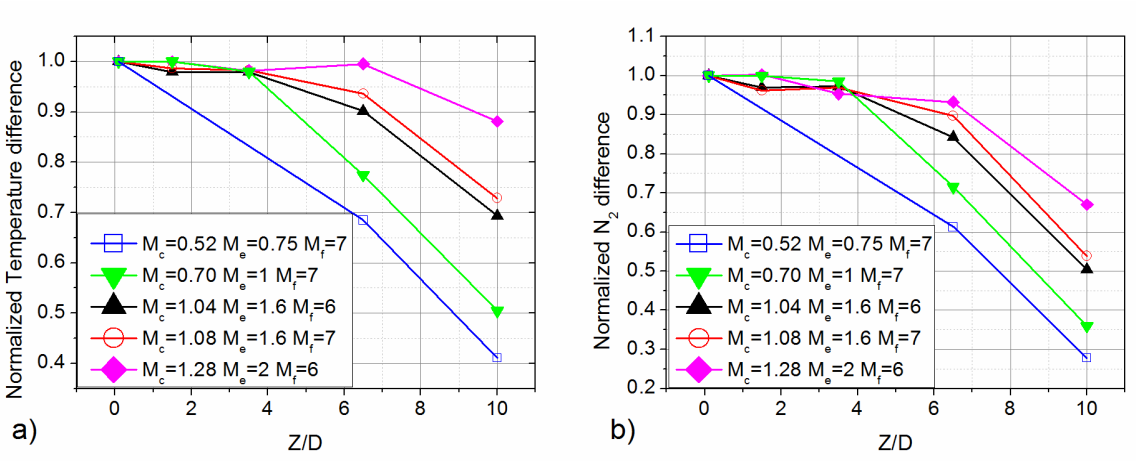

Figure 8-8: Normalized temperature (a) and N_2 mole fraction (b) difference as function of the normalized *z* coordinate

Figure 8-8 a) plots the difference between the centerline and the freestream temperature as function of the downstream distance (expressed in nozzle diameters). The difference is normalized by its value measured 1 mm from the nozzle exit. Figure 8-8 b) shows the same quantity except computed for N_2. Increasing the convective Mach number the penetration of the entrained air is delayed to locations further downstream, consistent with what has been reported in the literature and discussed in Section 8-2.

All sonic and supersonic flow curves show a relatively flat region (up to 3.5 diameters), followed by a drop in the normalized difference indicating that the entrained surrounding air has reached the centerline. The figure also shows that the variation in this normalized quantity is not linear with the *z* coordinate, and its slope increases with the distance from the exit. Notice a small reduction of the temperature and N_2 difference for $z/D = 1.5$, and then a subsequent increase to its original value for $z/D = 3.5$. Previous computational analysis shows that the nozzle is not pressure matched, but slightly under-expanded, and a system of expansion and compression

waves is generated. The pressure along the centerline is therefore not uniform, but this is neglected in the DP-CARS data analysis which assumes in the calculation of theoretical spectra that the pressure is constant (pressure changes the spectra; for example using a pressure of 1 atm instead of 1.03 atm at the nozzle exit for M_e=1.6 and M_f=6 causes an error of 9 K in temperature, and ~ 0.17% (of the total composition) in O_2 and N_2).

8.6.2 Mole Fraction of Gases Based on their Provenance

For a better understanding of the flow physics, it is helpful to know at each location the mole fraction of gases originating from the center-jet, the co-flow, and the freestream. *V, C,* and *A* are the mole fractions of these contributions.

$$\begin{aligned} V &= aN_2 + bO_2 + cH_2O \\ C &= N_2 \\ A &= dN_2 + eO_2 \end{aligned} \tag{8-6}$$

where the coefficients *a, b, c* are measured at the centerline, 1mm from the nozzle exit, *d*=0.78, *e* =0.208. By definition

$$V + C + A = 1 \tag{8-7}$$

The atomic mole fractions of N, O and H in a generic mixture (*V, C, A*) can be expressed as

$$\begin{aligned} x_N &= \frac{2aV + 2C + 2dA}{(2a+2b+3c)V + 2C + 2(d+e)A} \\ x_O &= \frac{(2b+c)V + 2eA}{(2a+2b+3c)V + 2C + 2(d+e)A} \\ x_H &= \frac{2cV}{(2a+2b+3c)V + 2C + 2(d+e)A} \end{aligned} \tag{8-8}$$

At each location x_N, x_O and x_H can be computed from the measured molecular mole fractions (H_2O is computed by difference).

$$x_N = \frac{2x_{N_2}}{2x_{N_2} + 2x_{O_2} + 3x_{H_2O}}$$
$$x_O = \frac{2x_{O_2} + x_{H_2O}}{2x_{N_2} + 2x_{O_2} + 3x_{H_2O}} \qquad (8\text{-}9)$$
$$x_H = \frac{2x_{H_2O}}{2x_{N_2} + 2x_{O_2} + 3x_{H_2O}}$$

Equating Eq. (8-8) to Eq. (8-9) a system of 3 equations in 3 unknowns is obtained, but only 2 of the three equations are linearly independent. Replacing one of the linearly dependent equations with Eq. (8-7), a system of three independent equations in three unknowns is obtained. The system of equations is solved for (V,C,A) at each location. Results obtained using this procedure are displayed in Figure 8-9.

The algorithm seems to correctly identify the center-jet, the co-flow and the ambient air at the nozzle exit. The lack of accuracy in the DP-CARS measurement when only one species is present, and for cold air spectra was previously discussed. In these cases the water mole fraction is systematically high, and since molecules containing H atoms are present only in the center jet, this error causes a systematically higher value of the center jet mole fraction, where it should be 0. This effect is evident 1 mm from the nozzle exit in the co-flow region. Figure 8-9a) shows a comparison between data collected for M_e=1.6 and M_f=6 (full symbols), and M_f=7(open symbols). The two plots are almost identical, with the lower enthalpy case spreading slightly faster than the higher enthalpy one. The results confirm that changes in density ratio are relatively unimportant. The plot shows the fast mixing of

the co-flow with the ambient air 15 mm from the base, where the N_2 co-flow is less than 50% of the total composition. Above 15 mm the co-flow becomes only a minor constituent of the total composition in any location, as increasing amounts of air are entrained. Notice that most of the co-flow gas stays confined outside the original diameter of the central jet ($|x|> 5$ mm). For z=65 mm and above the air has penetrated up to the centerline, consistently with observations in the previous section. The figure clearly shows that the incompressible shear layer between the co-flow and the freestream grows much faster than the compressible shear layer between the supersonic center-jet and the co-flow.

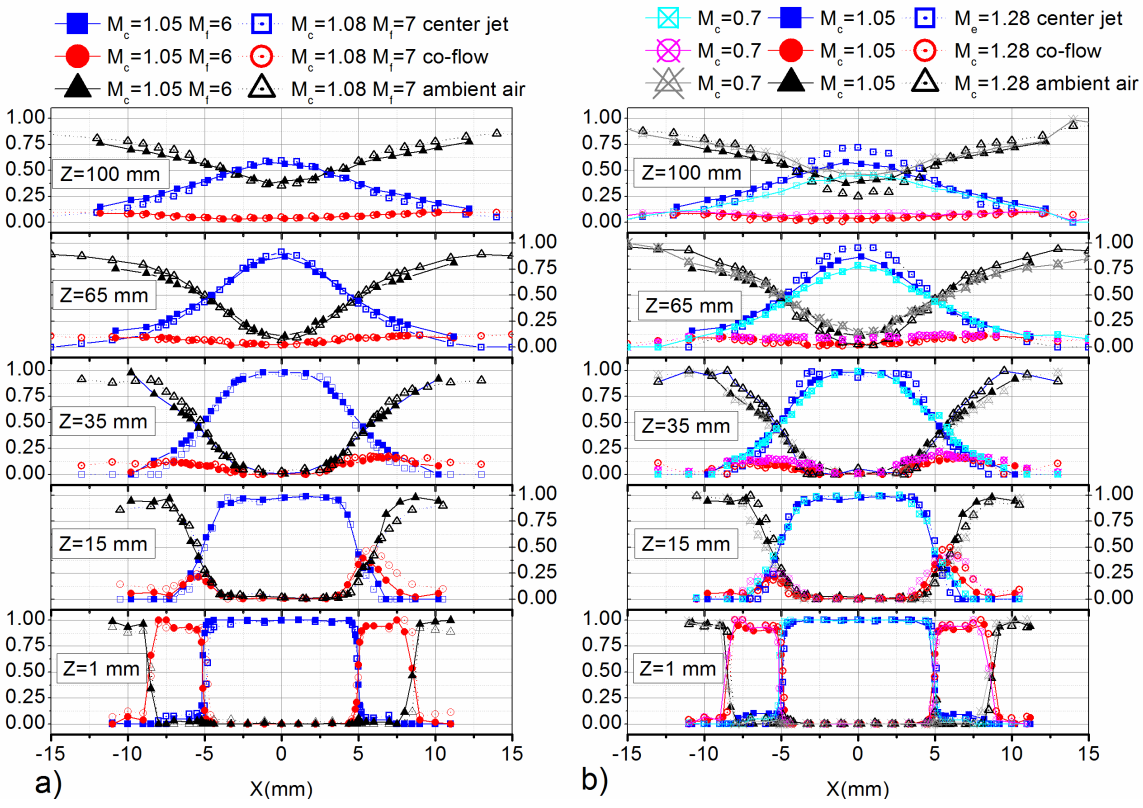

Figure 8-9: Mole fractions of gases based of their provenance

Figure 8-9 b) shows the same quantities measured for varying convective Mach number. The plot clearly shows that compressibility, through the convective Mach number, plays the key role in determining the mixing between the center-jet and the co-flow. Air penetrates the center jet sooner at lower convective Mach numbers and the jet spreading-rate decreases with increasing Mach number, as previously observed.

8.6.3 Spreading Rate

From the average temperature and mixture fraction profiles shown in the previous sections it is possible to determine the jet diameter and the width of the shear layer as a function of the downstream distance z. Temperature and mixture fraction radial profiles are normalized as follows:

$$T_{norm}(x,z) = \frac{T(x,z) - T_{freestream}}{T(0,z) - T_{freestream}} \tag{8-10}$$

$$V_{norm}(x,z) = \frac{V(x,z)}{V(0,z)} \tag{8-11}$$

$T_{freestream}$ is the temperature in the core of the co-flow jet for z = 1 mm, and the freestream air temperature (300 K) everywhere else. V indicates the mole fraction of the gas originated in the center jet (vitiated air). The jet diameter δ_R is defined as the distance between the two locations where the normalized temperature drops to 0.1. The shear layer width δ_T is defined as the distance between the radial locations where the normalized temperature is 0.9 and 0.1. Two values of δ_T are obtained, one for positive and one for negative values of x, and the shear layer width is defined as the average of these two values. Similarly, another shear layer width δ_V can be defined

based on the 20% and 90% thresholds in the center-jet mole fraction profile. The choice of the thresholds to define the shear layer width and the jet radius is arbitrary, and other choices are possible. The x locations of the thresholds have been determined based on a quadratic interpolation.

Figure 8-10 shows the width of the jet and of the shear layer according to the definitions given, as function of the distance z from the nozzle exit. As a general trend, increasing the convective Mach number, the computed width decreases, consistently with previous works. Notice that the slope of the curves changes after the turbulent shear layer has reached the centerline of the jet. The spreading-rate is here defined as the slope of the curves of Figure 8-10 for $15 \leq z \leq 65$ mm. Values of the shear layer width measured 1mm from the exit are unreliable, because the length of

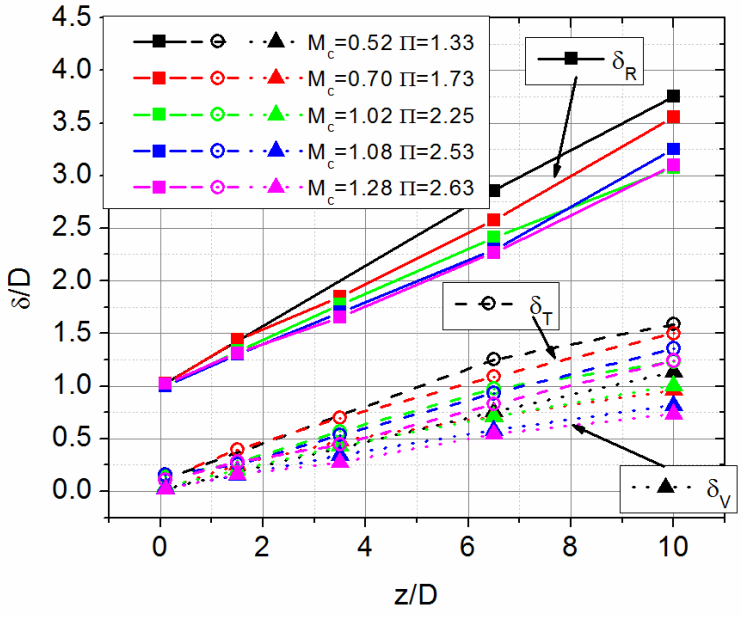

Figure 8-10: Jet diameter (δ_R), shear layer width based on the normalized temperature (δ_T) and on the center-jet mole fraction (δ_f) as function of the distance from the nozzle exit, expressed in nozzle diameters

the probe volume cause a reduction of the steepness of the measured profile, and therefore larger shear layers widths. Past 65 mm the shear layer has reached the centerline, and the physics of the process is different. The spreading-rate contains both the effects of the density ratio, and of compressibility. The two effects can be decoupled by normalizing the spreading-rate by its incompressible value, that can be estimated based on a spatial growth model, as in Ref.[197].

$$\delta_0^{'} = C_\delta \frac{(1-\lambda_u)(1+\sqrt{\lambda_\rho})}{2(1+\lambda_u\sqrt{\lambda_\rho})}\left[1-\frac{(1-\sqrt{\lambda_\rho})/(1+\sqrt{\lambda_\rho})}{1+2.9(1+\lambda_u)/(1-\lambda_u)}\right] \tag{8-12}$$

where λ_u and λ_ρ are the velocity and density ratio, respectively and C_δ a constant, which depends on the definition of the width, on the facility, the inflow conditions and other details. Figure 8-11 compares the measured normalized growth rate to the value predicted using a fitting curve proposed by of Slessor [190]:

$$\frac{\delta'}{\delta_0'} = (1+4\Pi^2)^{-0.5} \tag{8-13}$$

The curve is a best fit of several experimental results, expressed as function of the compressibility parameter Π. The value of C_δ is set so that the spreading-rate for Π=2.53 matches the value obtained from the fitted curve. This is arbitrary, but it forces the agreement at Π=2.53, and then agreement over the other values of Π indicates consistency with the theory. The range over which Π is varied is small (1.33 to 2.63) but this is the best that can be done with the present data. Figure 8-11 shows that Eq.(8-13) correctly predicts (within 10%) the relation between the compressibility parameter and the spreading rate. The agreement is surprisingly good, considering the CARS smoothing effect on gradients. Notice that at the lower values

of the compressibility parameter Π, the width based on the center-jet mole fraction is higher than that computed based on temperature.

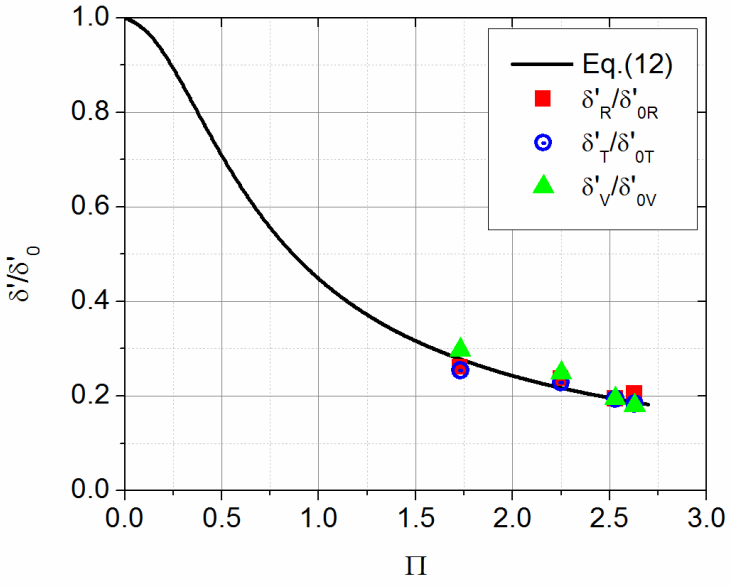

Figure 8-11: Normalized growth rates as function of the compressibility parameter Π, compared to Slessor`s fitting curve

8.6.4 Standard Deviation and Co-Variances

The DP-CARS system allows for instantaneous measurements at a 20 Hz rate, therefore higher order statistics (variances, and co-variances) can be obtained from repeated measurements at each location. 1000 single shots acquisitions are available along the centerline, and for lines at z = 65 and 100 mm, 250 shots elsewhere. The standard deviations reported in this section contain contributions from the flow turbulence, the instrument precision, and the flow repeatability, as illustrated in section 8-5. In general, large values of standard deviations are encountered in the shear layer, where entrained gases from the hot center-jet and the quiescent air are

mixing. Temperature-N_2 co-variance (<T, N_2>) is also shown. Large negative values of the co-variance indicate that the high temperature measurements are correlated to low measurement of mole fractions. Peaks in the standard deviation profile, coupled to negative peaks in <T, N_2> indicate where mixing of the co-flow-air mixture (colder and with more N_2) with the center jet occurs.

Figure 8-12 shows the effect of the enthalpy Mach number on the standard deviations. The plots show small fluctuations at the outer edge, corresponding to the relatively quiescent freestream ambient air, and relatively low fluctuations in the center core of the jet. The temperature standard deviation (σ_T) of the center jet depends on the enthalpy content. Removing the contribution from the instrument precision and the flow repeatability, the component due to the turbulence on the centerline is 42 K for M_f= 6, and 57 K for M_f= 7 (3.7% and 4.1% of the centerline temperatures). Local maxima in the standard deviations can be found at the interface between the co-flow and the center jet, and the co-flow and the quiescent air, indicating some degree of entrainment in the co-flow. Moving downstream the region of higher standard deviation becomes broader and of higher intensity. Up to 35 mm, the temperature standard deviation profiles in the shear layer are approximately the same for the 2 cases, except for higher fluctuations at higher M_f. At 65 mm the standard deviation for x = 0 is increased signaling that the mixing layer has reached the centerline. For z = 65 mm the effect of the flight Mach number is significant and the two profiles are very different. For M_f= 6 the standard deviation profile is more flat and has lower amplitude than for M_f= 7. The standard deviation presents a valley at the centerline much more pronounced for the higher enthalpy case.

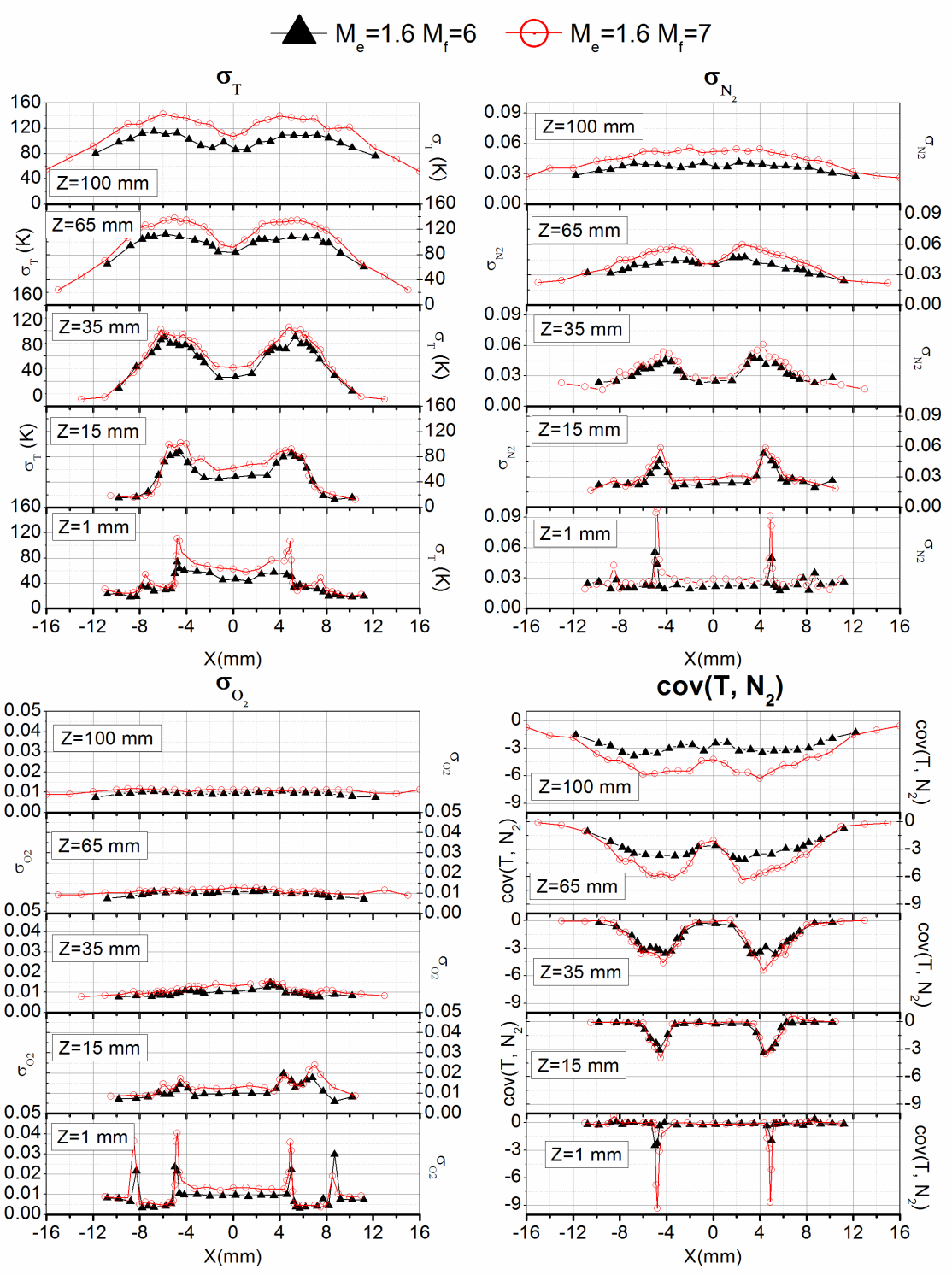

Figure 8-12: Temperature and mole fractions standard deviation, and temperature, N_2 co-variance (<T, N_2>) at different heights for M_e=1.6 and M_f=6 and 7

Similar considerations apply to the N_2 standard deviation, with the only difference that the valley at the centerline has disappeared for both cases at z = 100 mm. The O_2 standard deviation profile at 1 and 15 mm from the nozzle exit is an indicator of the mixing of the co-flow with the jet and the ambient air. Past 15 mm from the nozzle exit, the co-flow has approximately the same O_2 content of the center jet; therefore, the σ_{O2} profile flattens. The large negative values of the <T, N_2> co-variance indicate intense mixing. Again, profiles are identical up to 35 mm, then they differentiate, with larger (negative) values and more pronounced valleys and peaks for the higher enthalpy case.

Figure 8-13 and Figure 8-14 show the effect of compressibility on the standard deviations and on <T, N_2>. Figure 8-13 compares results for M_f=6 and M_e=1.6 (back triangles) and M_e=2 (magenta diamonds). At the jet exit, there are no significant differences. Mean values plots showed improved mixing for the lower exit Mach number in the upstream region (up to 35 mm). This is reflected in the standard deviation plots, where the regions having standard deviation above the center-line value is larger, and the peak standard deviation higher. The <T, N_2> co-variance plots show the same behavior. 100 mm from the base, the mean temperature plots are almost identical for the two cases, but the standard deviation is different, with the M_e=1.6 case having a higher standard deviation, and more negative co-variance.

Figure 8-14 compares the standard deviations and the <T, N_2> co-variance for values of M_e = 0.75, 1 and 1.6 and the higher flight Mach number, M_f= 7. Again, for higher compressibility, standard deviations peaks are lower, and the width of the region having standard deviations above the centerline value is smaller. Moving

downstream, past the location where the shear layer reaches the centerline, the standard deviation at the centerline increases, and the peak standard deviation moves toward the centerline. Past the location where the peak standard deviation occurs at the centerline, the profile flattens and the peak standard deviation starts dropping.

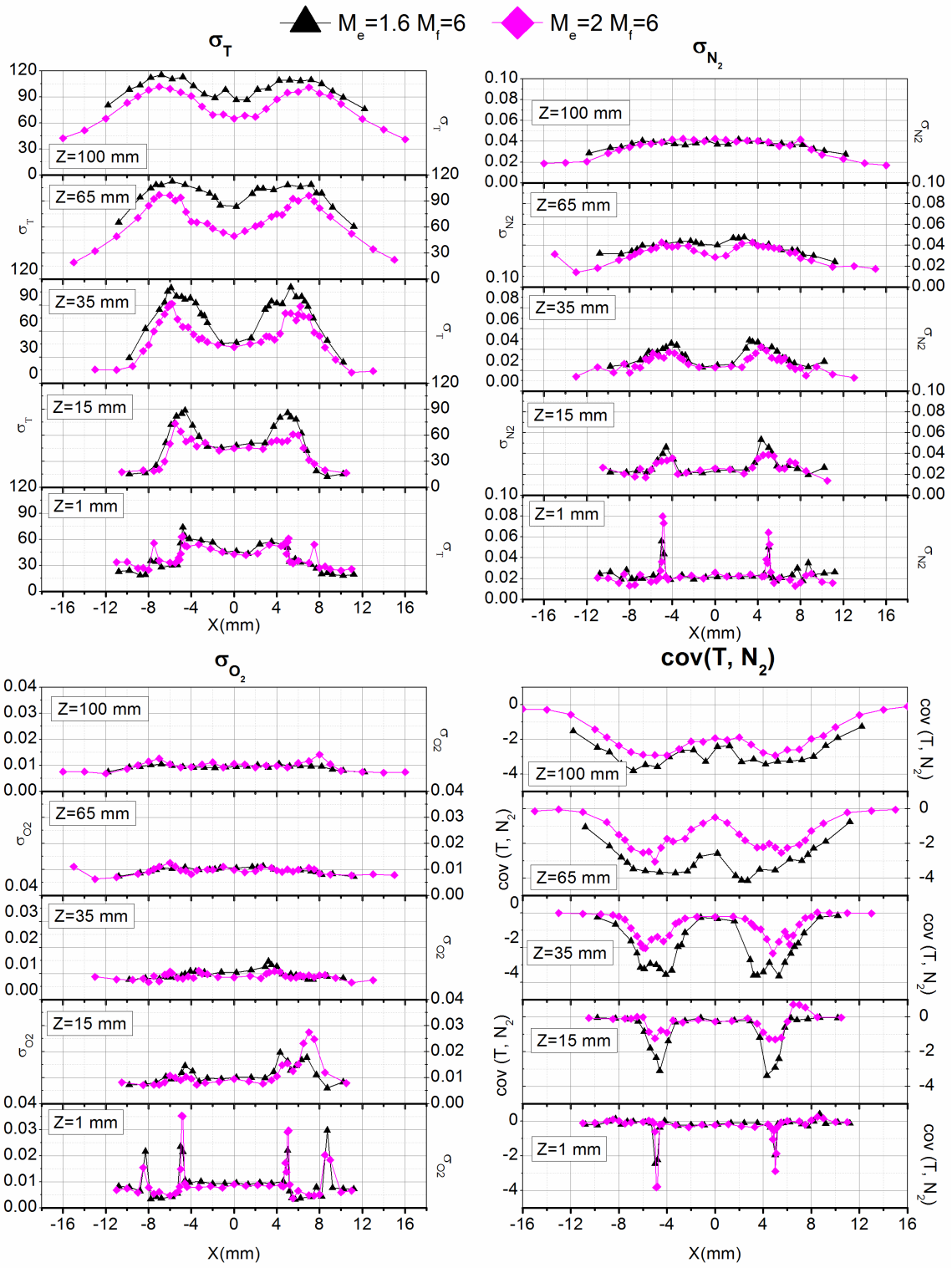

Figure 8-13: Temperature and mole fractions standard deviation, and temperature, N_2 co-variance (<T, N_2>) at different heights for M_f=6 and M_e=1.6 and 2

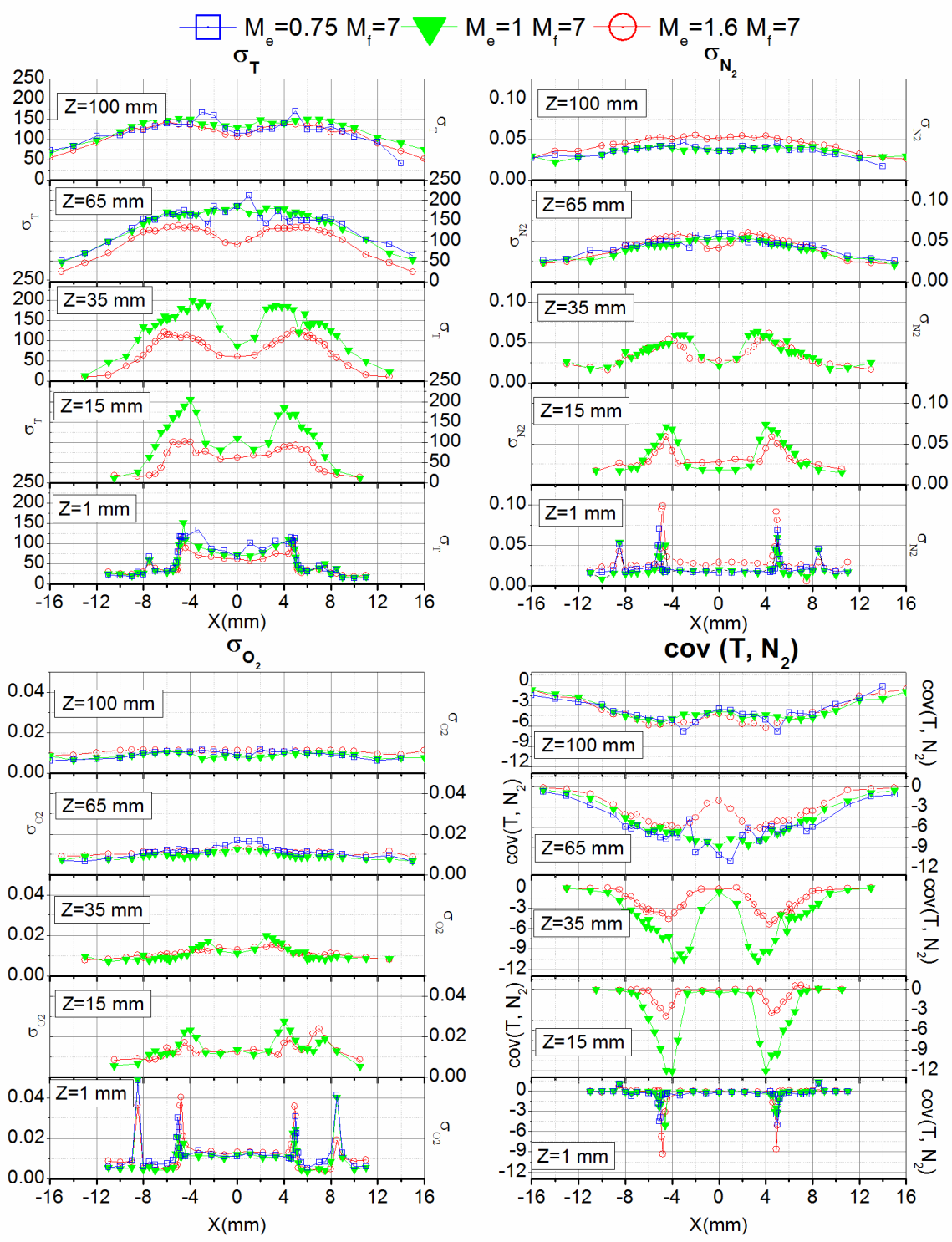

Figure 8-14: Temperature and mole fractions standard deviation, and temperature, N_2 co-variance (<T, N_2>) at different heights for M_f=7 and M_e=0.75, 1 and 1.6

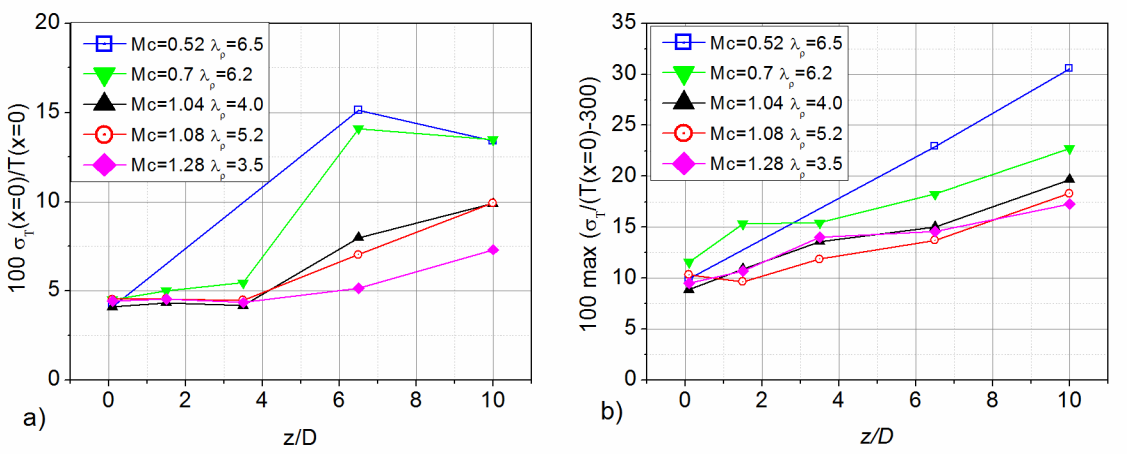

Figure 8-15: Normalized standard deviation on the centerline, and normalized peak standard deviation as function of the distance from the nozzle exit, expressed in nozzle diameters

As discussed in the background section, turbulence production is lower at higher compressibility. Figure 8-15 a) plots the temperature standard deviations at $x = 0$ normalized by the average centerline temperatures. Before the shear layer reaches the centerline, the normalized temperature standard deviation is in the 4-4.5% range for all cases. Once the shear layer reaches the centerline the normalized standard deviation increases for all cases but the slope depends on M_c. Increasing M_c, the normalized standard deviation at the centerline decreases, consistently with the reduction in turbulence production observed in other experimental and numerical studies. Once the location of the peak standard deviation has reached the centerline, its amplitude begins decreasing as observed for M_c=0.52, and M_c=0.7.

Similarly, Figure 8-15 b) shows the peak standard deviation normalized by the difference between the center jet temperature at the given z location, and the quiescent air temperature. This quantity increases moving downstream the flow, and generally decreases at higher compressibility. It differs from the normalized centerline standard deviation since it does not decrease after the location of the peak

standard deviation reaches the centerline, but keeps a roughly linear behavior up to 10 diameters from the nozzle exit. Another difference is that the behavior is not monotonic with the convective M_c number, suggesting that also the density ratio has a significant role in the evolution of this quantity. In particular increasing the density ratio appears to reduce the normalized peak standard deviation.

8.7 DP-CARS Results: Combustion Case

In this section, the results obtained for the combustion test cases are presented. Three conditions were tested, as described at the beginning of Section 8-3. Two of these have M_e=1.6 and a M_f=6 and 7 respectively for the center jet, and the third has M_e=1 and M_f= 7. For the supersonic cases the H_2 co-flow was in stoichiometric ratio with the O_2 in the center jet, although H_2 can react with the O_2 in either the quiescent air or the center jet. For the sonic case the H_2 co-flow was 120 SLPM, corresponding to an equivalence ratio of 0.5 with the O_2 in the center-jet.

8.7.1 Means, Standard Deviations and Co-Variances for the Combustion Test Cases

Figure 8-16 shows the mean temperatures, N_2, O_2 and H_2 mole fractions for the three combustion cases. Figure 8-17 shows the standard deviations for the same quantities. Figure 8-18 and Figure 8-19 shows the co-variances $\langle T, N_2 \rangle$, $\langle T, O_2 \rangle$, $\langle T, H_2 \rangle$, $\langle N_2, O_2 \rangle$, $\langle N_2, H_2 \rangle$ and $\langle O_2, H_2 \rangle$.

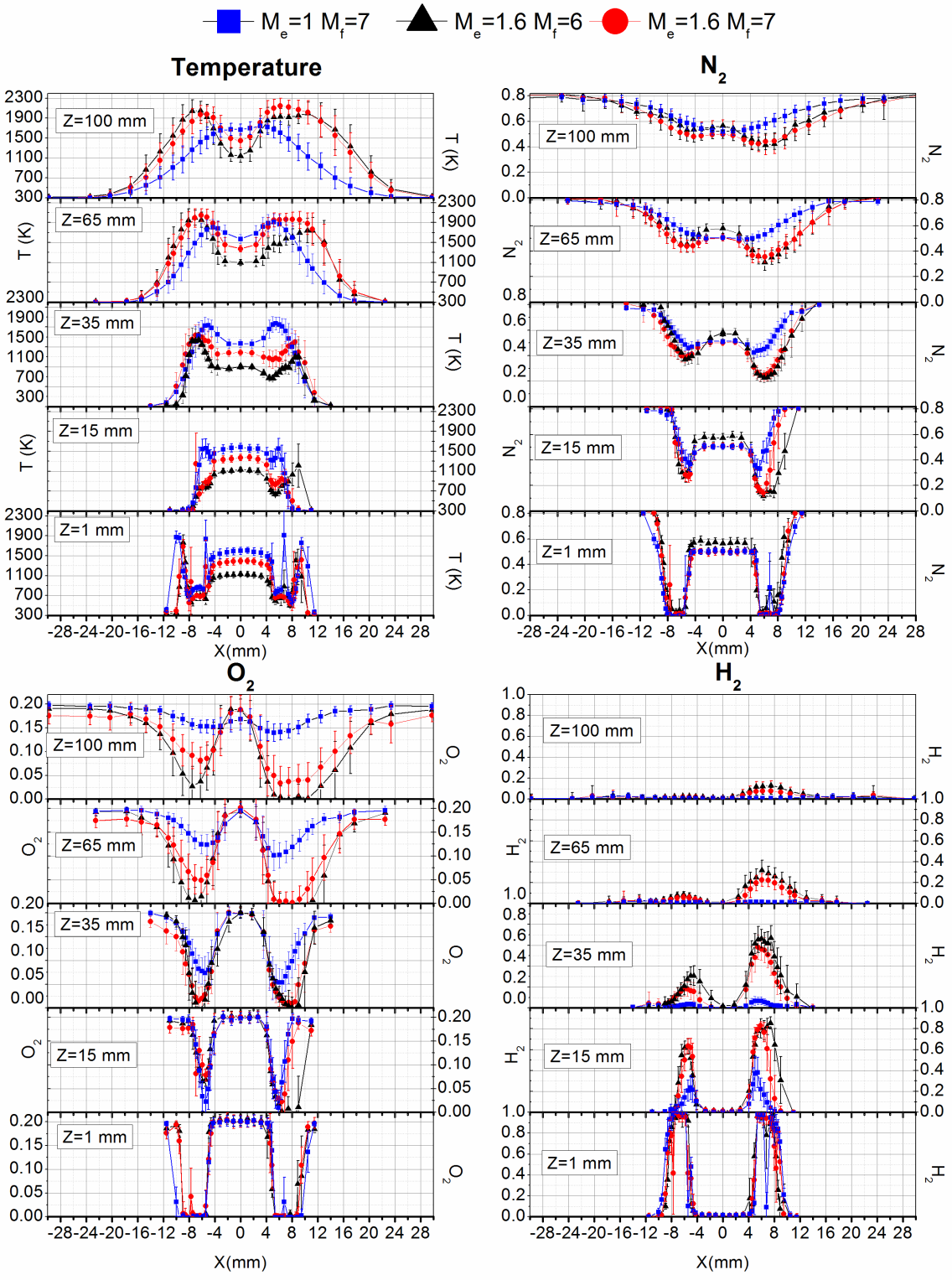

Figure 8-16: Mean temperature and mole fractions at different heights for the combustion test-cases

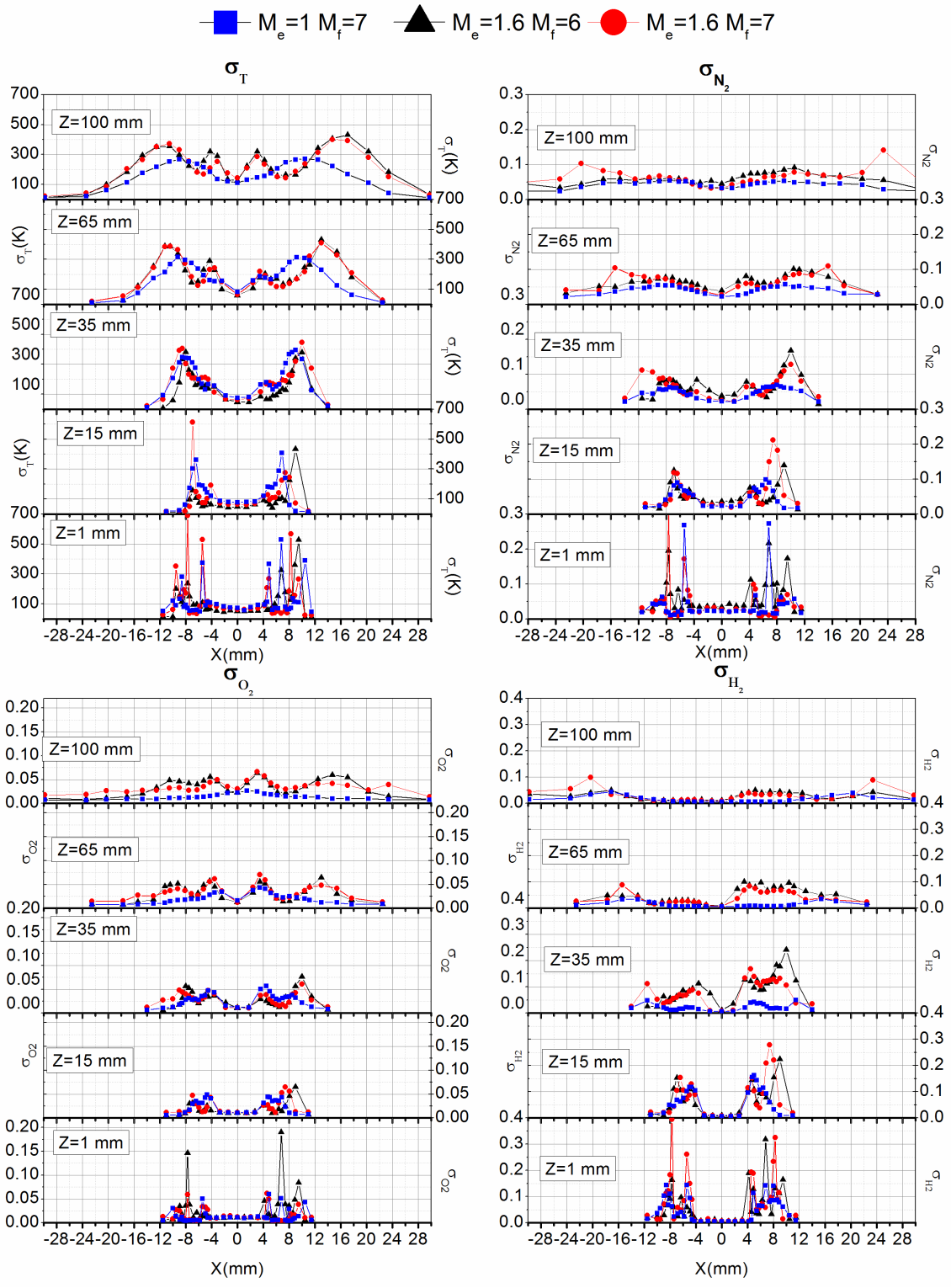

Figure 8-17: Temperature and mole fractions standard deviations at different heights for the combustion test-cases

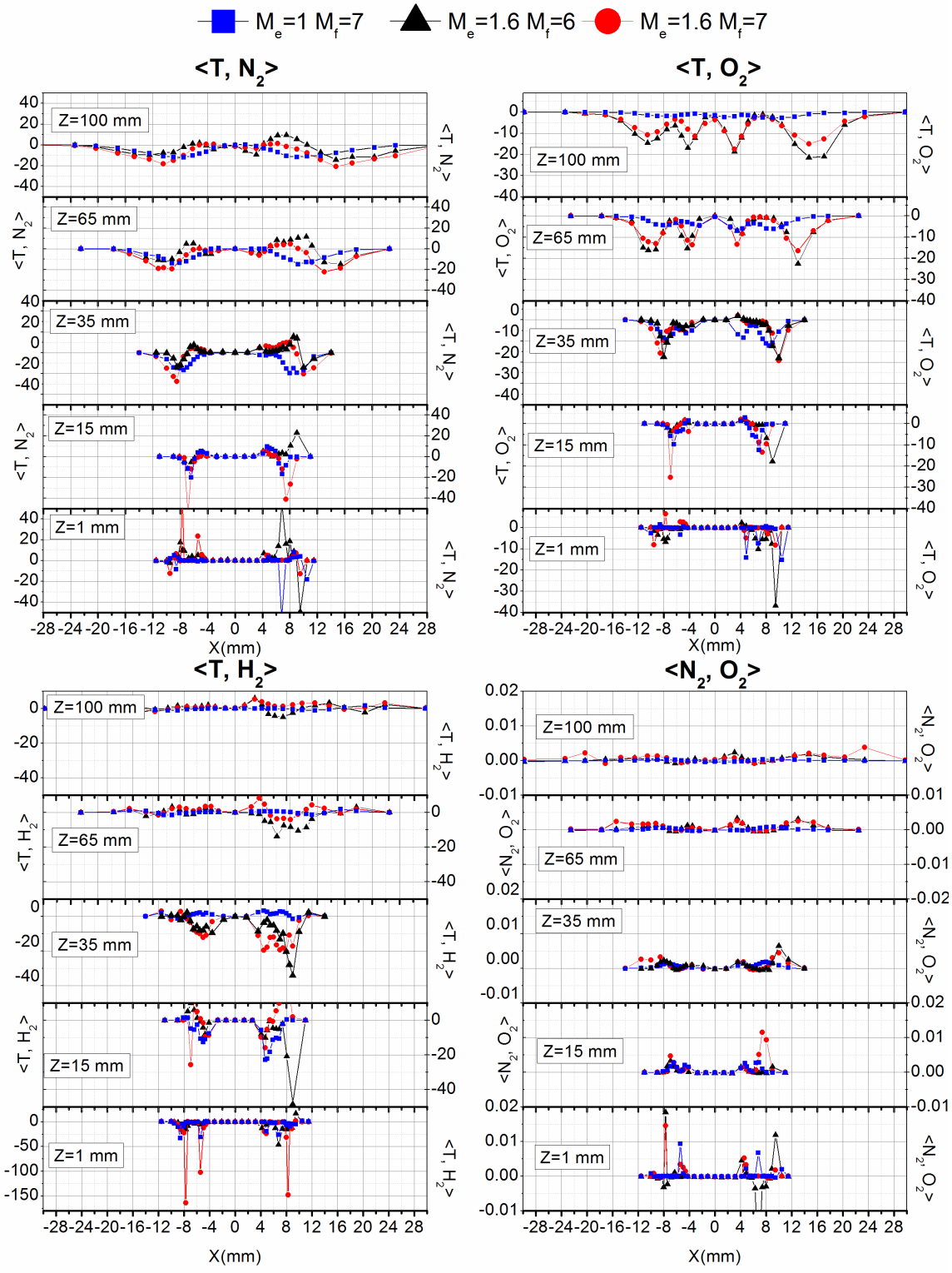

Figure 8-18: Co-variances at different heights for the combustion test-cases

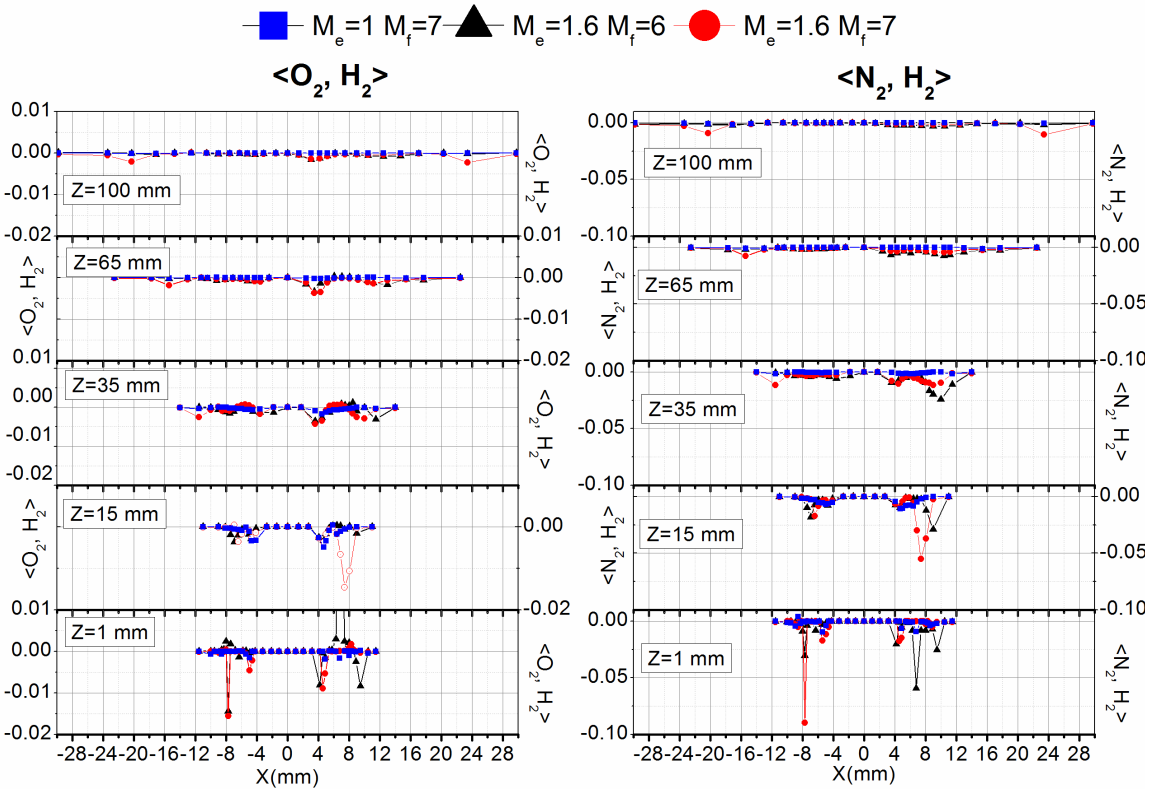

Figure 8-19: <O_2, H_2> and <N_2, H_2> at different heights for the combustion test-cases

Figure 8-20 to 8-25 re-propose some of the plots shown above, but rearranged so that each figure contains profiles for a given value of z. This arrangement of the plots is more convenient for the discussion of the results that follows

Figure 8-20 shows the mean temperature and mole fractions, the temperature and the N_2 standard deviation, and the temperature-mole fractions co-variances obtained at z = 1 mm. Profiles at the nozzle exit (z = 1 mm, and $|x|$< 5 mm) have already been compared to their mixing counterparts, and to CFD predictions in Figure 8-3 and Figure 8-4, and previously discussed. Moving further out in the radial direction, the DP-CARS probes the H_2 co-flow. Temperature was high enough so that two H_2 rotational lines, S(5) and S(6), were detected. When possible, it is preferable to

extract the temperature from the N_2 spectra, but for this region, only temperature measurements from the two H_2 lines were possible. No data are available for the accuracy and precision of these measurements. The average temperature in the co-flow is ~700 K for the supersonic cases, and ~850 K for the sonic case. The measured H_2 mole fraction in the pure H_2 co-flow is between 0.95 and 1, and the instrument correctly measures a null mole fraction of N_2 and O_2. Past 7.4 mm from the center, mixing between the co-flow and ambient air occurs. The sharp peaks in temperature and H_2O mole fraction profiles at the interface between the air and the co-flow ($x \approx \pm 8.9$ mm) indicate that combustion has occurred.

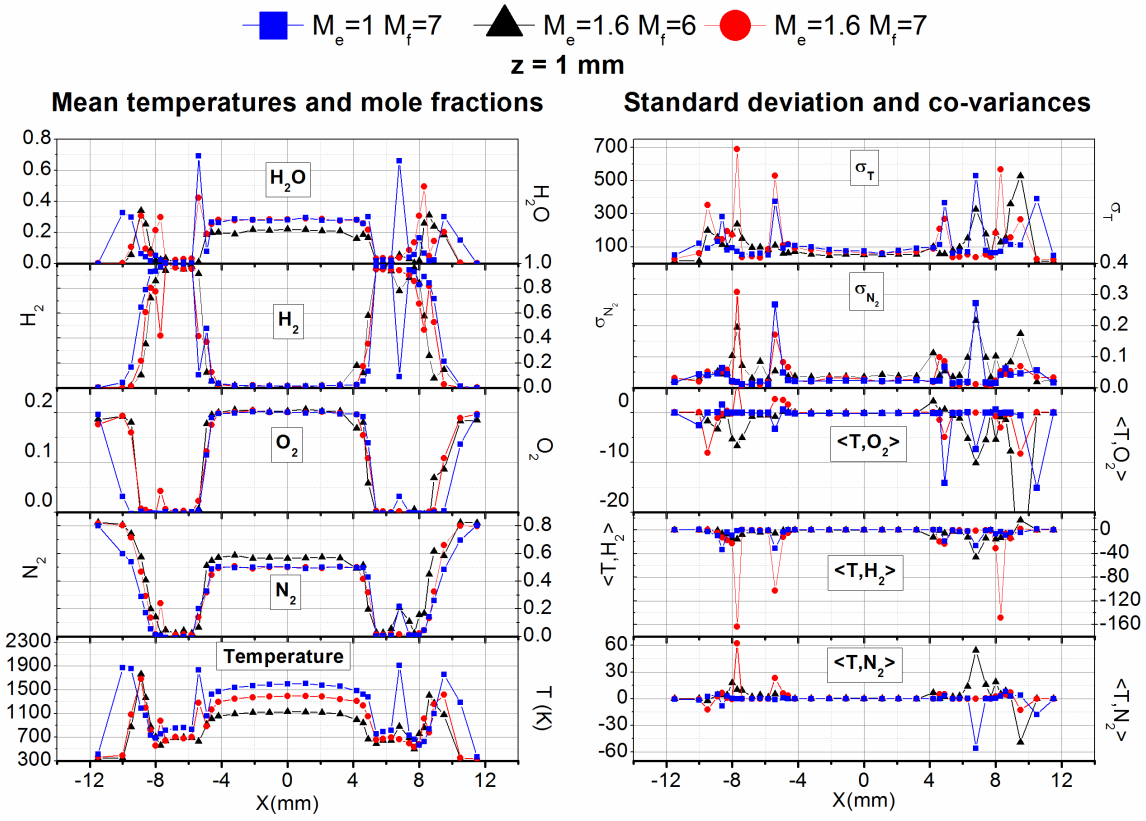

Figure 8-20: Mean, standard deviations and co-variances for z = 1 mm, combustion cases

This is consistent with the observation that the flame is flame attached to the burner in the IR image (see Figure 8-1). Notice that the flame for the sonic case is broader than what is observed for the supersonic cases. Large peaks of temperature standard deviations occur near the peak temperature ($x \approx \pm 9.5$ mm), and are likely caused by flame fluctuations.

Additional local peaks of mean temperature and H_2O are found at the interface between the co-flow and the center-jet (x = -5.4 mm) for the two higher enthalpy cases (M_f=7). Measurements at these locations present very large fluctuations, up to 690 K in temperature. Examining the evolution with time of the single shots measurements, it was found that the first shots were from high temperature fuel rich mixtures, and the rest from much colder spectra. Movement of the translation stage during the data acquisition could explain this behavior. Another possibility is that sparks produced by the focused laser beams ignites the mixture, but the flame cannot self-sustain. The behavior is consistent for all the other standard deviation peaks in Figure 8-20, except for the peaks at the interface with the quiescent air.

The inability of this instrument to resolve sharp temperature gradients must be taken into account in interpreting the CARS results near the peaks. In addition, only 250 shots are available at each location shown in Figure 8-20, limiting the accuracy of the standard deviation and co-variance estimates. For these reasons, the profiles of standard deviation and co-variances shown in Figure 8-20 are only qualitatively useful.

Figure 8-21 shows the mean temperature and mole fractions, the temperature and the N_2 standard deviation, and the temperature-mole fractions co-variances obtained

for z = 15 mm. The temperature profiles are significantly different in the three cases examined. For M_e=1 (blue squares), the flame front has moved toward the center jet, with peak temperatures at x=-5.4 and 5.9 mm. Ambient air has penetrated further in the co-flow providing the oxidizer to feed the combustion. At the peak temperature location, the N_2 mole fraction is ~ 46 %, where O_2 is completely depleted.

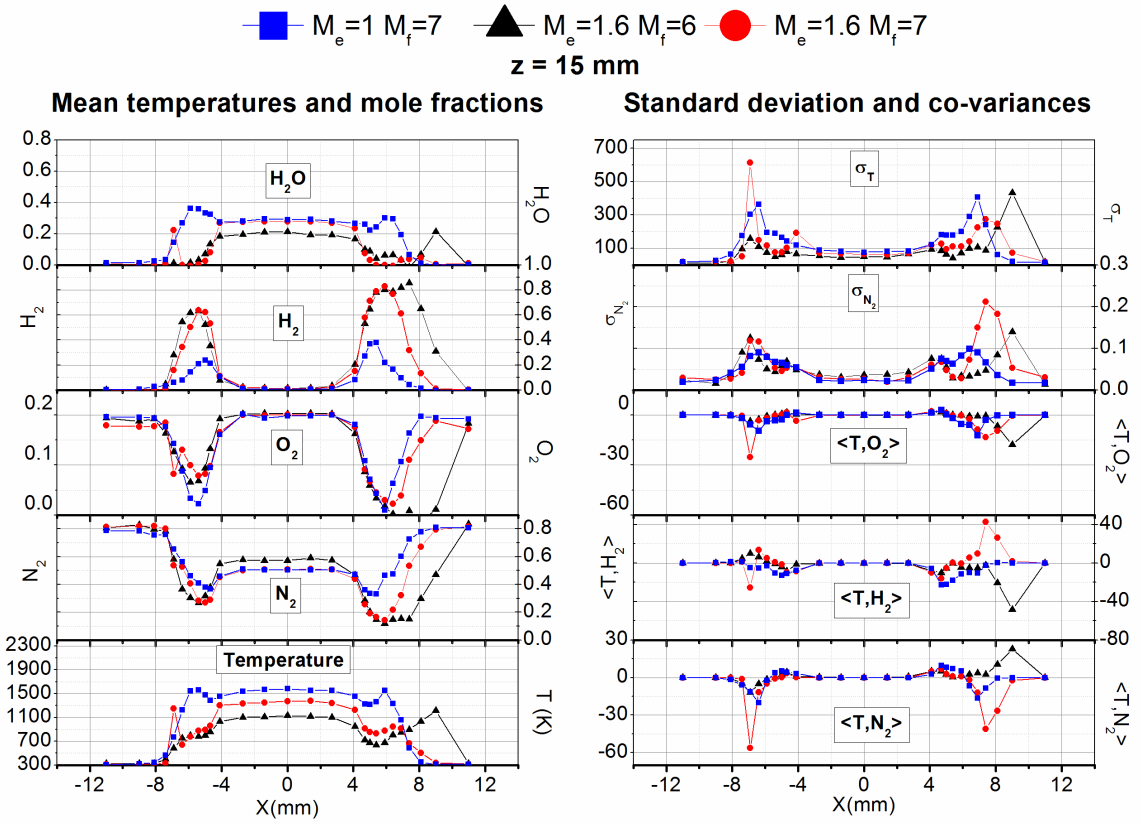

Figure 8-21: Mean, standard deviations and co-variances for z = 15 mm, combustion cases

Peak temperature gradients are much less than for z = 1 mm, therefore useful quantitative information can be obtained from the variances and co-variances. In particular, the temperature-mole fraction co-variances can be used to determine where the combustion is occurring. As already observed for z = 1 mm, near the temperature peaks the standard deviations are very high (up to 400 K for σ_T) because of flame-

front fluctuations. Between the temperature peak and the freestream the temperature-mole fraction co-variances (<T, O_2> and <T, N_2>) are negative with a peak for x = -6.4 mm and x = 6.9 mm. Negative co-variances mean that an instantaneous lower temperature typically corresponds to higher values of mole fractions. This indicates a region in which combustion products (higher temperature, lower mole fractions), mix with the colder freestream. Moving toward the centerline, <T, N_2> becomes positive, while <T, O_2> and <T, H_2> are negative. The change in the sign of <T, O_2> is an indicator of the combustion. Instantaneous high temperature are associated to high values of N_2 and low values of O_2 and H_2, that is for entrained air that has reacted with the H_2 co-flow.

Proceeding further toward the centerline, the mean temperature reaches a minimum and then rises to the center-jet plateau value. In this region <T, N_2> and <T, O_2> are positive, where <T, H_2> is negative, as consequence of the mixing between the vitiated air in the center-jet (higher T, N_2 and O_2) and the H_2 co-flow. The sign of the co-variance indicates that combustion is not occurring in this region.

For $|x| \leq 2.7$ mm the measurements are identical (within the accuracy of the instrument) to what is measured at z=1 mm. This constitutes the core of the sonic jet, that is completely unaffected by the co-flow and the entrained air.

The temperature profile for M_e=1.6 and M_f=7 (red circles), is quite different. The main features are a strong asymmetry and a local extinction of the flame for negative x, also visible in the IR images. For positive x, the mean temperature profile is similar to the one observed for the sonic case, with the only difference being a lower peak temperature. As in the previous case the location of the peak temperature moves

toward the center, from x=9.5 mm to x=6.4 mm (x=5.9 mm for M_e=1). The temperature profile between the peak temperature and the freestream appear almost overlapped to that measured in the sonic case. At the peak temperature location the mole fraction for N_2 and H_2 are 22% and 77% respectively, where for the sonic case they are 41% and 21%. The mean equivalence ratio is therefore higher in the supersonic case, lowering the peak temperature. Notice that the difference is not the consequence of the different compressibility, but of the much higher H_2 flow rate in the co-flow.

For negative x there is no peak in the temperature profile, but a smooth rise from ambient air to the center jet plateau. Single-shot spectra show simultaneous presence of O_2 and H_2, indicating that the combustion is not sustained in this region. For x = -6.9 the average temperature is 1270 K, but the time history of the single shots temperatures shows high temperatures for the first 4 seconds of acquisition and lower thereafter. A spark caused by the lasers itself could have ignited the flow, but conditions were inadequate to sustain the combustion, as suspected for those other anomalous location in the lower plane.

For the lower enthalpy case (M_f=6) the temperature profile for negative x shows local extinction similar to what is observed for M_f=7; for positive x the flame is fuel rich and it has not moved toward the centerline as for the other cases, the equivalence ratio is lower and the peak temperature higher. The reason for this difference is unclear.

For z=35 mm. shown in Figure 8-22, combustion between the H_2 co-flow and the ambient air occurs for both positive and negative values of x for all cases. The sonic case now shows a lean flame with an O_2 mole fraction of 7% and a peak temperature of 1974 K. H_2 is almost completely depleted. The valley, between the peak temperature and the center-jet plateau has disappeared. The σ_T profile shows a peak at the interface between the center-jet and the co-flow flame (x = ±4.5 mm), and another at the interface between the co-flow flame and the free stream (x = ±8.5 mm). Negative peaks of <T, O2> are present at the interface of the co-flow with the freestream and the center-jet. Although this hints to combustion between the oxidizer from the sonic jet and the H_2 in the co-flow, it is not certain because the sign of <T,

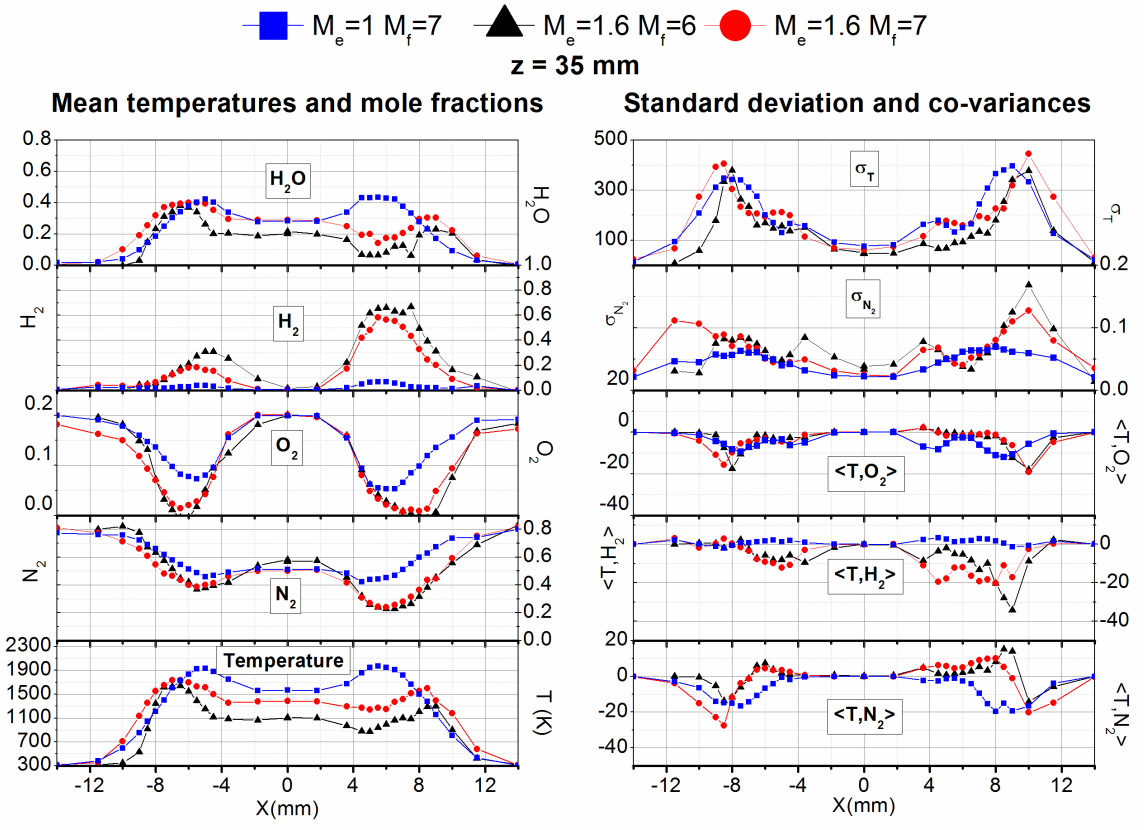

Figure 8-22: Mean, standard deviations and co-variances for z = 35 mm, combustion cases

N_2> and <T, H_2> cannot be determined (their value is lower than the measurement uncertainty).

The two supersonic test cases have profiles that are asymmetric, as consequence of the non-uniform flow rate across the co-flow nozzle. For negative values of x the profiles resemble what is observed for the sonic case, although the co-flow flame is still fuel rich, the peak temperature is lower, and it is reached further away from the centerline.

For positive values of x the profiles resemble what is observed for the sonic case at z = 15mm. In particular, the location where the temperature peaks is further away from the centerline, and there is a valley between the center-jet plateau and the peak temperature. The flame is richer (31% at the peak temperature location for M_f=6) and at lower temperature than for negative values of x.

Further downstream, 65 mm from the nozzle exit the supersonic cases differ drastically from the sonic one. In the sonic case most of the H_2 was depleted at 35 mm from the nozzle exit, (because of lower Φ), thus no further heat is released moving downstream. The high temperature co-flow entrains gas from the colder center jet, and quiescent air lowering its temperature and increasing its O_2 content. The interface between the flame and the core of the center jet moves further toward the center but does not reach the centerline, as can be observed in the σ_{N2} and <T, O_2> profiles. The temperature profile at the interface with the freestream, almost identical for all test cases in presence of heat release, is now completely different for the sonic case

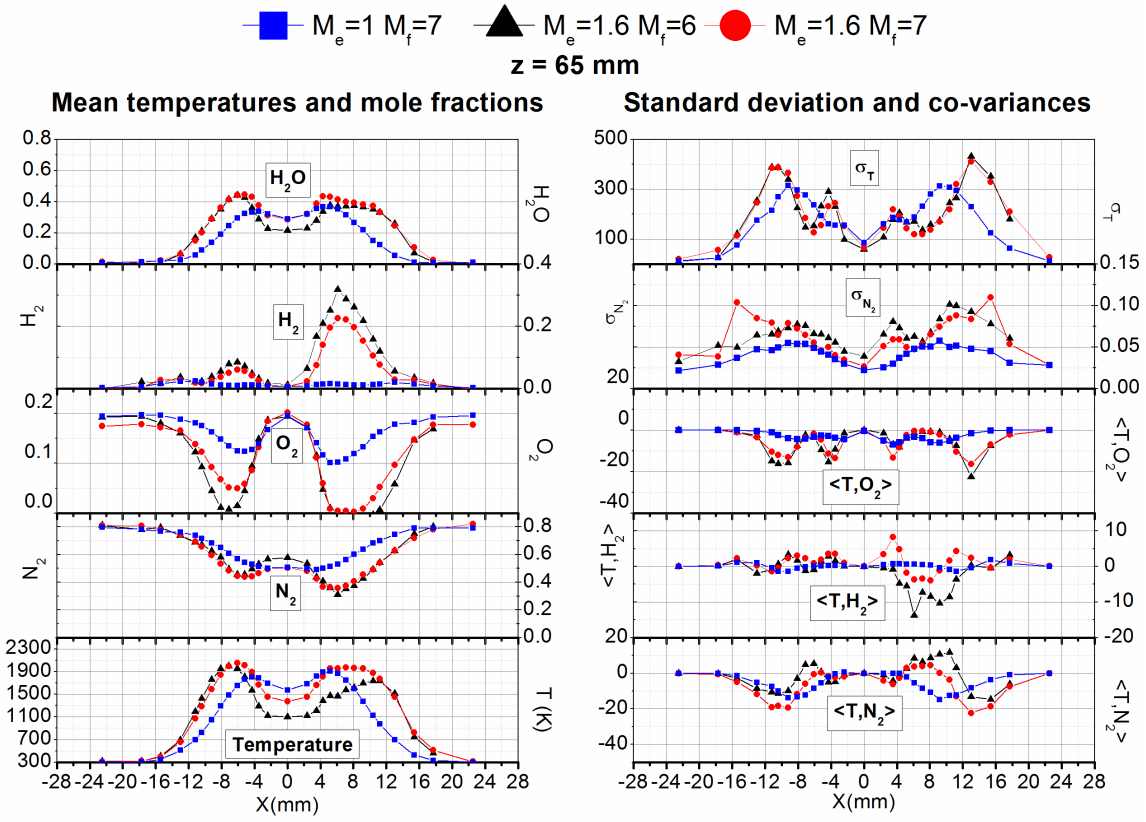

Figure 8-23: Mean, standard deviations and co-variances for z = 65 mm, combustion cases; note change in horizontal scale from Figs. 8-16 through 8-18

For the supersonic cases H_2 is still available and combustion occurred between z= 35 and z= 65 mm. The flow is still dominated by the heat release, and the same features observed for z = 35 mm appear for z = 65 mm. The asymmetry with respect to the centerline is increasingly evident, as a consequence of the increasing difference in the released heat. The shear layer between the co-flow and the supersonic jet has penetrated most of the jet core, but it has not reached the centerline. At the interface between the higher temperature, H_2 rich co-flow, and the colder center-jet rich in O_2 and N_2, <T, N2> is positive, <T, O_2> and <T, H_2> negative. This is evidence of combustion between the gases coming from the center jet, and the fuel rich co-flow.

For z=100 mm the mean profiles for the sonic nozzle show that the shear layer has

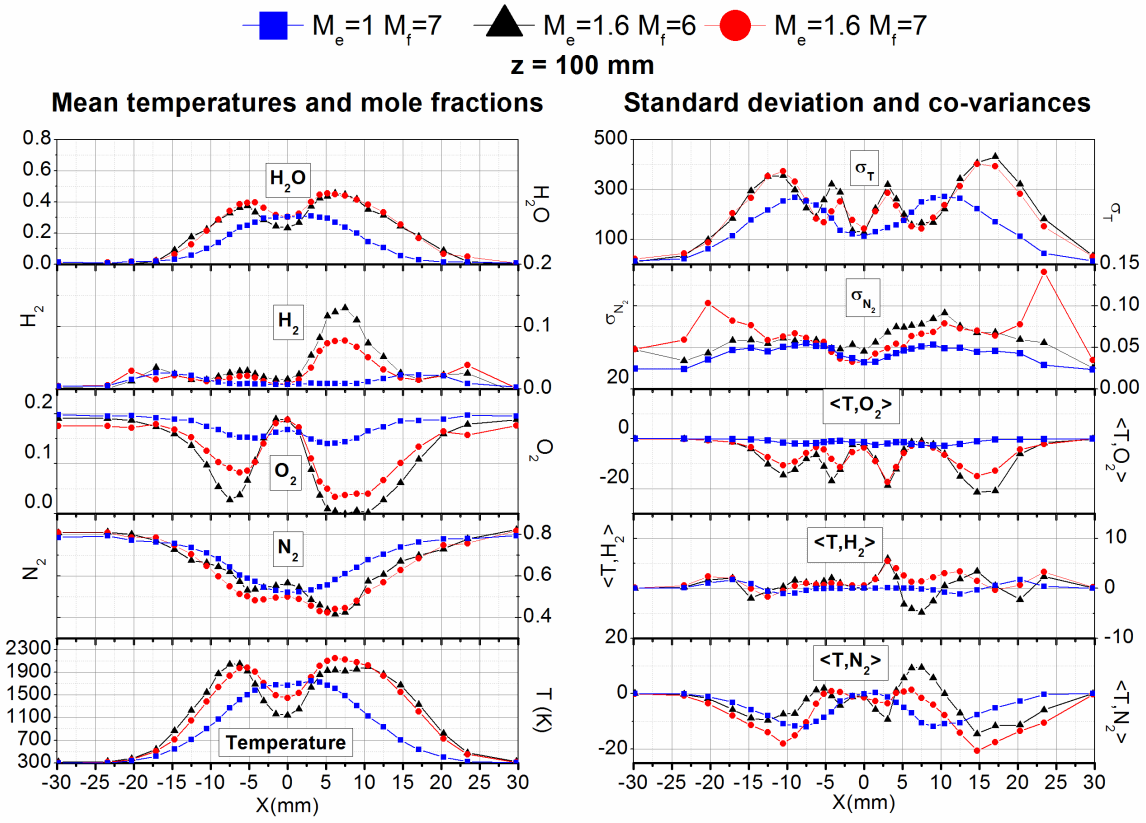

Figure 8-24: Mean, standard deviations and co-variances for z = 100 mm, combustion cases

reached the centerline, causing a temperature increase, and a decrease in the N_2 and O_2 mole fractions. For increasing distances from the centerline the temperature decreases and the N_2 mole fraction increases monotonically but the standard deviation plots shows a peak marking the interface with the ambient air. The O_2 mean profile presents a local maximum at the centerline, then it drops in the co-flow region and finally rises to its ambient air value.

For the supersonic case, since H_2 was still available for combustion, the flow profiles resemble what is observed for z=65 mm. The only difference is that the peak temperature is increased and the interface between the core of the center jet and the co-flow flame has moved further toward the center, as can be deduced from the location of the $\sigma_{T,}$ σ_{N2} and <T, O_2> peaks and valleys locations. As consequence, an increase in the centerline temperature is observed. The flame is even more asymmetric with respect to the centerline, because of the increasingly different amounts of heat is released. Further downstream the asymmetry is expected to grow since on one side the H_2 has been almost completely depleted, where on the other is still present in significant amount (up to 13%).

8.7.2 Effect of Heat Release

Comparing the results for the mixing and the combustion test cases, it is evident that the presence of reactions dramatically changes the flow field. In the mixing case the shear layer reaches the centerline 65 mm from the nozzle exit (z/D = 6.5), but this does not occur until further downstream in presence of combustion as shown in Figure 8-25 a). The figure shows, for both the mixing and the combustion cases, the

normalized temperature difference defined as the difference between the temperature and the freestream temperature, divided by the same difference computed at the nozzle exit (same of Figure 8-8 a)). Similarly the temperature standard deviation on the centerline, as a percentage of the mean temperature, stays approximately constant until 65 mm, but is significantly higher 10 diameters downstream of the nozzle exit as shown in Figure 8-25b). Heat release delays the entrainment of the co-flow in the center jet, reducing the mixing, and causing the different behavior in the mixing and combustion cases.

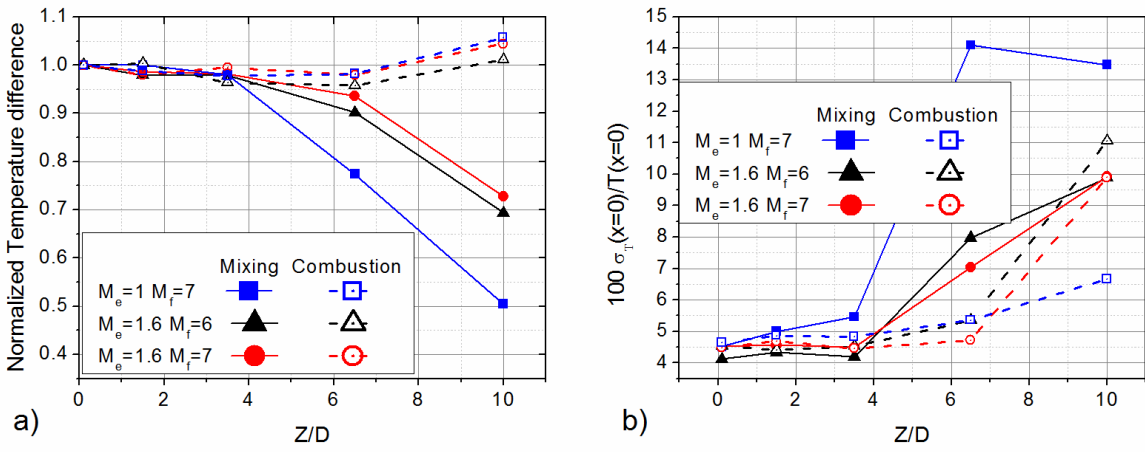

Figure 8-25: Normalized mean temperature difference (a) and normalized temperature standard deviation on the centerline (b) as function of the normalized *z* coordinate

Better understanding of the effect of the heat release on the mixing, is possible by looking at the gas composition at each location in terms of their provenance. Following the same strategy described in section 8.6.2 it is possible to determine the mole fraction of gases originated in the center-jet, the co-flow and the quiescent air. The only difference is that in this case reactions can occur and convert H_2 and O_2 into

water. This does not affect the previous strategy since it is based on a balance of atomic species. Eq. (8-6) to (8-9) modified for H_2 co-flow become:

$$\begin{aligned} V &= aN_2 + bO_2 + cH_2O \\ C &= H_2 \\ A &= dN_2 + eO_2 \end{aligned} \tag{8-14}$$

where the coefficients *a, b, c* are measured at the centerline, 1 mm from the nozzle exit, *d*=0.78, *e* =0.208. By definition

$$V + C + A = 1 \tag{8-15}$$

The atomic mole fractions of O and H in a generic mixture (*V, C, A*) can be expressed as:

$$\begin{aligned} x_O &= \frac{(2b+c)V + 2eA}{(2a+2b+3c)V + 2C + 2(d+e)A} \\ x_H &= \frac{2cV + 2C}{(2a+2b+3c)V + 2C + 2(d+e)A} \end{aligned} \tag{8-16}$$

At each location, x_O and x_H can be computed from the measured molecular mole fractions (H_2O is computed by difference).

$$\begin{aligned} x_O &= \frac{2x_{O_2} + x_{H_2O}}{2x_{N_2} + 2x_{O_2} + 2x_{H_2} + 3x_{H_2O}} \\ x_H &= \frac{2x_{H_2O} + 2x_{H_2}}{2x_{N_2} + 2x_{O_2} + 2x_{H_2} + 3x_{H_2O}} \end{aligned} \tag{8-17}$$

As shown previously the equation for x_N is linearly dependent on the other 2, so it is not necessary.

Figure 8-26 compares the results obtained for the 3 combustion cases. The different flight and exit Mach numbers do not greatly affect the profile of the mole fraction originated from the center jet, except at the most downstream location, where

the sonic case shows a lower value of the center-jet mole fraction on the centerline. The profiles for the gases that originated in the co-flow and the ambient air show larger differences; the ambient air penetrates further in the co-flow and in the center jet for the sonic case, since the H_2 co-flow is present in larger quantities for the supersonic cases. As discussed in the previous section, these differences are a consequence of the lower H_2 flow rate, rather than the different compressibility. This is a striking difference with respect to the mixing case where the compressibility significantly reduces the mixing.

Figure 8-27 compares the results for the sonic combustion case to its mixing counterpart. A direct comparison is meaningful because the co-flow rates are the same. At z = 15 mm the profiles look similar, but less air is entrained in the co-flow because of the heat release. Further downstream, the diameters of the center-jet and of the co-flow jet are increased because of the heat release. The rise in temperature reduces the density; because there is no axial pressure gradient that can accelerate the flow, the velocity is constant, and therefore the jet area must increase. Mixing is reduced as can be seen by the reduced amount of entrained air in the combustion case.

Figure 8-28 shows the locations where the mole fractions of gas coming from the center jet are 20% and 80% of their value on the centerline. The plot clearly shows for the combustion cases a higher growth rate of the center-jet (20% lines further away from the centerline), and reduced mixing (80 % lines closer to the centerline), as a consequence of the heat release.

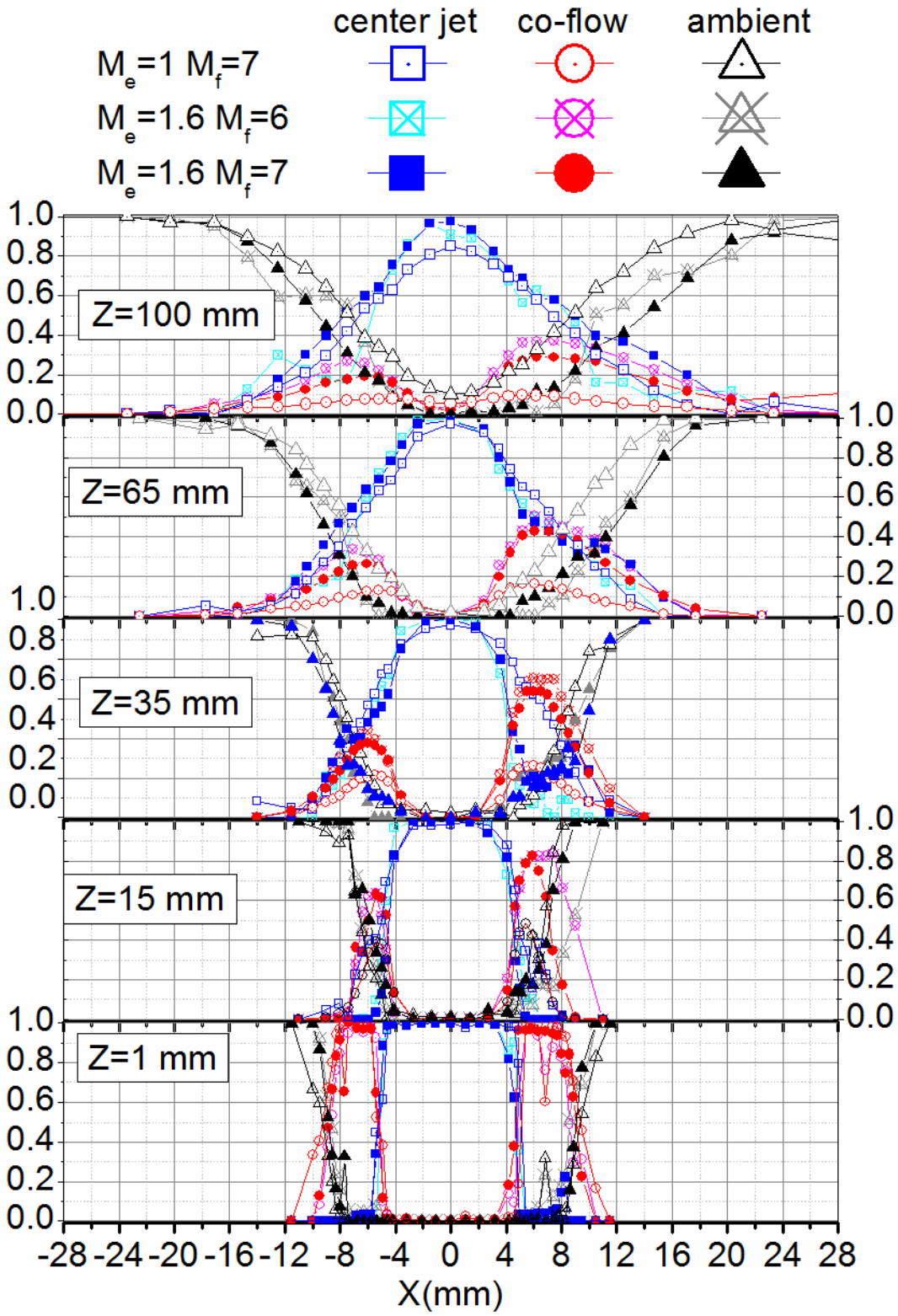

Figure 8-26: Composition by gas provenance for the combustion cases

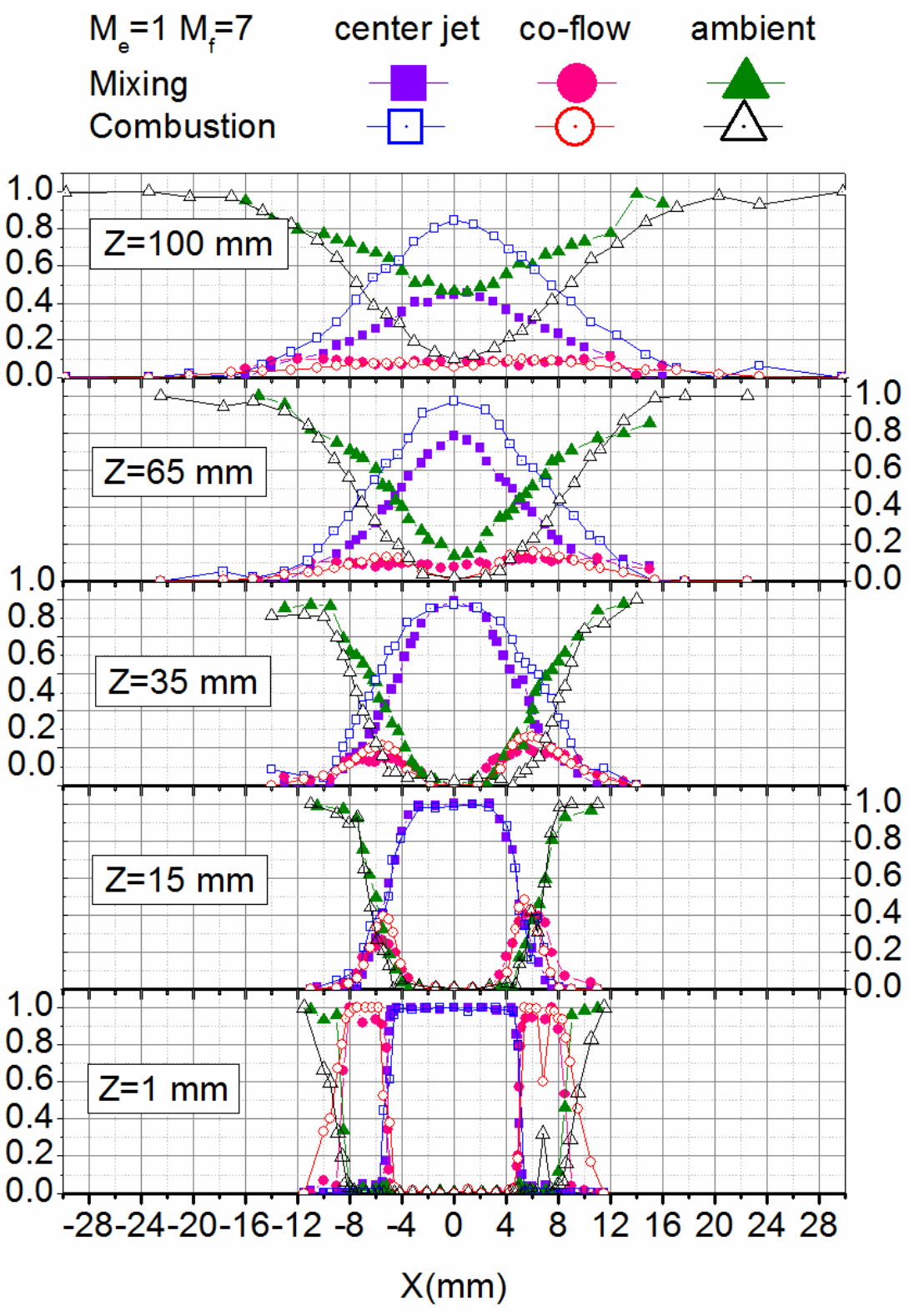

Figure 8-27: Composition by gas provenance for M_e=1 and M_f=7. Comparison between mixing and combustion

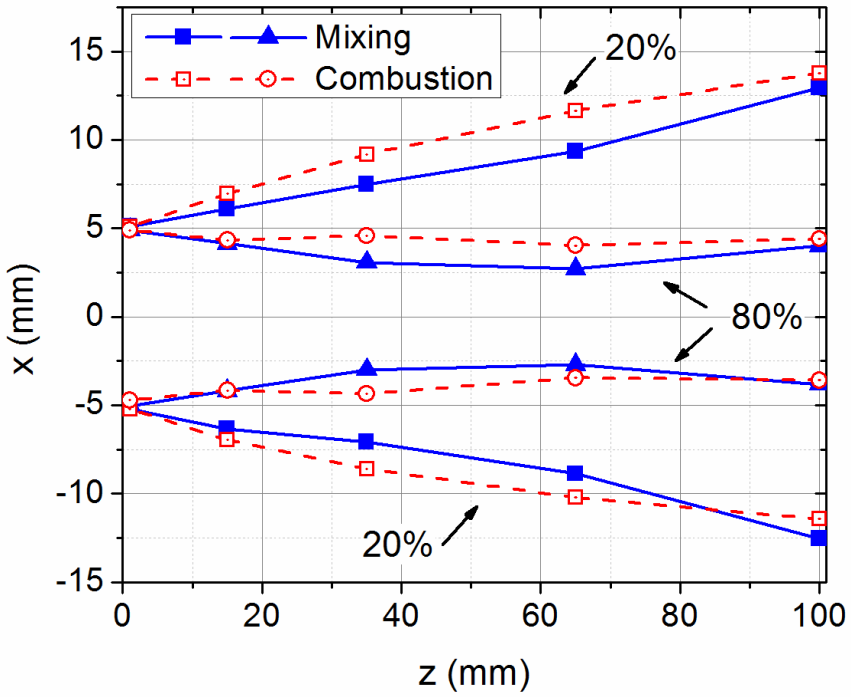

Figure 8-28: Locations where the mole fractions of gas coming from the center jet are 20% and 80% of their value on the centerline for M_e=1, and M_f=7

8.7.3 Histograms

In addition to average and standard deviations, histograms have been obtained at each location to provide additional information to the CFD modelers. Showing all the histograms would not be practical (it would require ~ 10000 plots), therefore only an example is shown here to explain how they have been obtained and to describe what additional information they provide. At each measurement location and for each variable, the post-processing code divides the measurement range in several bins, and counts the number of measurements falling in each bin. A bar-plot of these quantities

returns a histogram as shown in Figure 8-29. The choice of the bin width is based on Scott`s rule:[198]

$$w = \frac{3.5\sigma}{\sqrt[3]{n}} \tag{8-18}$$

where w is the bin-width, σ is the estimated standard deviation, and n the number of samples. This choice of the bin-width is appropriate for data that have a Gaussian distribution.

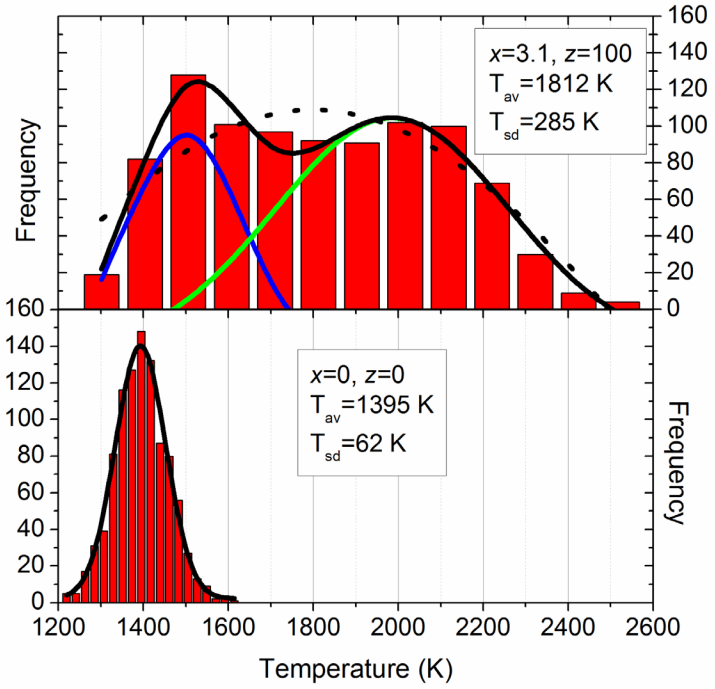

Figure 8-29: Histograms of temperature at *x*=0, *z*=1 mm (lower panel) and at *x*=14.7 mm, *z*=100 mm (upper panel). The black continuous lines are fit to a Gaussian (lower panel) and to the sum of 2 Gaussian (in blue and green)

Figure 8-29 shows histograms of temperature measurements at the nozzle exit (x = 0 and z = 1 mm, in the lower panel) and in a combustion region downstream (x = 14.7 and z = 100 mm, in the upper panel). The temperature histogram in the lower

panel has a Gaussian distribution (black curve, R^2=0.99). The temperature histogram obtained in the combustion region downstream has a much larger standard deviation (285 K) than is observed at the nozzle exit (62 K), and does not follow a Gaussian distribution (dotted curve in figure, R^2=0.77). Instead it has a bimodal distribution (black continuous line, R^2=0.97), given by the sum of a Gaussian centered at 1500 K (blue curve) and another Gaussian centered at 1986 K (green curve). The bimodal distribution indicates fluctuations of the flame front. The temperature histogram in the combustion region shows temperature ranging from 400 to 2400 K in a single location. Removing spectra that saturate the detector from the analysis, as in Ref. [66, 72], would have neglected those lower temperature shots introducing errors in the average and in the standard deviation estimates

8.8 **Discussion**

Two major drawbacks reduce the usefulness of the data set. The first is the length of the DP-CARS probe volume, and the non linear dependence of the signal amplitude with the temperature. Consequently, the accuracy of the measurements in proximity of steep temperature gradients is compromised (biased toward lower temperature) and the turbulent fluctuations are underestimated. The small size of the burner exacerbates the issue. Care must be used in interpreting the CARS measurements in proximity of steep temperature gradients.

The second major issue with the dataset is the asymmetry of the co-flow nozzle. This is a minor issue for the non reacting case, where air is rapidly entrained in the co-flow, mitigating the effects of the asymmetry. For the reacting case, the different

flow-rates directly affect the amount of heat released that is the governing factor in the flow evolution. The difference in the total amount of heat released increases proceeding downstream, and so does the flow asymmetry.

Nevertheless, there is no other data set providing statistics on temperature and mole fractions in compressible shear layers, nor in compressible reacting shear layers. The data set can be a useful tool in the development of CFD turbulence model for compressible shear layer. High fidelity, time dependent CFD simulations, for example LES simulations, could be post-processed to account for the spatial averaging inherent to the CARS technique, allowing this limitation of the dataset to be mitigated.

CHAPTER 9 -Conclusion

9.1 **Summary**

Research on CARS for supersonic combustion applications has been an ongoing effort at NASA Langley Research Center for the past 25 years.[6, 12, 66, 67, 69, 70, 72] A dual-pump (DP) CARS instrument, based on previous works from O'Byrne [6] and Tedder [66, 72], was developed to provide measurements in supersonic combustion experiments. The instrument allows instantaneous and spatially resolved, simultaneous measurements of temperature, N_2, O_2 and H_2 absolute mole fraction in H_2-air flames. The instrument was applied to measurements in a laboratory-scale supersonic combusting free jet.

The development of the instrument was focused on the resolution of several issues relevant to measurements in a H_2-air supersonic combusting free jet and more in general to supersonic combustion experiments.[6, 66, 72] Most components of the instrument hardware have been upgraded and several new features have been added. CFD validation requires large amounts of data, therefore efforts were made to increase the acquisition rate, and reduce the data processing time. The increase in the acquisition rate (compared to Ref.[66, 72]) is obtained by several changes in the Labview data acquisition software, to eliminate the need of any input from the operator once the acquisition begins. Several algorithms have been developed that provide more accurate (better background subtraction, non-resonant normalization, and improved pixel-to-frequency conversion) and faster processing of the raw CARS data. A new, faster and more precise fitting algorithm, developed by Cutler [107] was

used to fit the processed CARS spectra. Overall, the entire data analysis process is at least 10 times faster than in previous CARS experiments at NASA Langley Research Center. A faster analysis of CARS data allows identifying unforeseen issues during a test campaign and solving them before the bulk of the data is acquired. For example the need of an improved procedure for the background subtraction was found during the initial tests in the laboratory-scale supersonic combusting jet, and additional background spectra were added afterwards.

In previous experiments,[66,72] beam steering proved to be a major obstacle to the successful acquisition of CARS data in supersonic free jets. A combination of a planar BOXCARS phase matching configuration and shaping of one of the laser beams was investigated as a tool to mitigate the reduction of CARS signal caused by the refraction of the pump and Stokes beams as they pass through unsteady density gradients produced by turbulent flows. The signal loss is due both to beam wandering (relative displacement of the beams) and beam spreading (increase in the size and distortion of the shape of the beams at the focal plane). The technique results in a signal that is insensitive to displacement in the plane of the beams, and less sensitive to "out-of-plane" displacement. The spatial resolution is not affected by this technique. The approach was tested in two experiments, the first in which the beams were deflected by movements of a mirror and the second by a turbulent flow of helium and air. The beam shaping method proved to be effective in mitigating the effects of beam steering in both experiments. The amount of data rejected because of low signal-to-noise ratio was reduced by a factor 10 in the experiment involving the helium jet. The low data yield sometimes reported in turbulent measurements can be

overcome by this technique. Finally, a model of the beam interaction/signal generation process was developed and validated by comparison with the experimental results. The beam shaping approach is then applied to measurements in the laboratory-scale supersonic free jet, where beam steering is a significant issue. For CARS systems in which unused laser energy is available, the technique has no significant disadvantages while if the laser energy is limited, a compromise must be struck between the level of irradiance and the amount of ellipticity at the pump beam focus.

The typical length of the CARS probe volume (1-2 mm) affects the accuracy of measurements in presence of steep temperature gradients, and determines the size of the smallest turbulent structure that can be resolved. Options to reduce the CARS probe volume length have been investigated. Improving the spatial resolution of CARS in combustion measurements is challenging since the intensity of the CARS signal is proportional to the square of the probe volume length. So decreasing the probe volume length by increasing the beam crossing angle decreases the signal below acceptable levels. Increasing the laser irradiance also increases the CARS signal, but high irradiance effects may perturb the CARS spectra. A systematic study was conducted to determine the effect of Stark broadening and stimulated Raman pumping (SRP) on dual-pump CARS spectra of N_2, O_2 and H_2. Since these effects are not easily modeled and they are not typically included in fitting routines, they lead to errors in measurements of absolute concentration when these spectra are fitted to theory. Stark broadening alters the linewidth and amplitude of all transitions. Errors can be avoided by limiting the total irradiance at the measurement volume. SRP alters

the population difference between the lower and upper state of a transition, reducing the peak CARS signal and raising the level of the higher vibrational bands in room temperature air spectra. Errors in measured temperature and absolute and relative concentrations of resonant species can be caused by SRP. Such effects can be avoided by limiting the product of the pump and Stokes laser beam irradiances.

To explain the effects of high irradiance perturbations on CARS spectra, simple theoretical models from the literature are discussed and compared with experimental results. Experimental CARS spectra, collected in ambient air, fuel-lean and fuel-rich flames for several values of irradiance, are examined. Perturbations to the spectra are discussed and their effect on concentration and temperature measurements quantified. Both SRP and Stark broadening effects are present in the acquired spectra. Errors in O_2 concentration measurements up to 50% are observed. Other researchers, based on theoretical considerations, determined that Stark broadening may not be significant if the computed Stark shift is less than the Raman linewidth. This simple criterion is validated experimentally for O_2 and N_2, limiting the total irradiance to 250 GW/cm^2 at 1180 K and atmospheric pressure. Hydrogen spectra are particularly sensitive to Stark broadening, and small perturbations are observed even at the lowest total irradiance level tested (170 GW/cm^2). Measurements of concentration were observed to be much more sensitive to Stark broadening than are measurements of temperature. It is also shown that the characteristic SRP time has to be an order of magnitude larger than the laser pulse length to completely avoid errors in concentration measurements, but it is sufficient that it is only greater or equal to the pulse length to mole fraction of the pump-Stokes irradiance product for N_2 and O_2 concentration

measurements is 2 x 10^3 GW^2/cm^4, and for temperature it is 2 x 10^4 GW^2/cm^4. The study not only proved that the spatial resolution could not be reduced by increasing the laser irradiance, but also that high irradiance perturbation effects were present in previous experiments at NASA Langley. In particular the systematically lower H_2/N_2 reported separately by O'Byrne[6, 72] and Tedder [72] was a consequence of the Stark broadening. This finding was very important because removed a major source of systematic error in the H_2 mole fractions measurements.

In providing data for CFD validation, it is important to determine accuracy, precision and spatial resolution of the measurements. Significant improvements in the accuracy and precision of the instrument have been achieved. Results from validation measurements in a Hencken burner are discussed and the instrument accuracy and precision estimated. Calibration of the optical diffusion coefficient and the third order non-resonant susceptibility reduced systematic errors. The accuracy of the mole fractions measured for temperatures above 600 K is 0.5, 1.5 and 1% of the total composition for O_2, N_2 and H_2, respectively. Uncertainty in the non-resonant spectrum is responsible for additional errors up to 3% of the measured mole fractions, and up to 1% of the measured temperature. The precision of the temperature measurements, determined from the standard deviation of the measured temperature over 500 acquisitions, is a function of temperature and composition, and lies between 1.8 and 3.3%. Absolute mole fraction precisions are between 0.5 and 1.8% for O_2, 1.5 and 3.4% for N_2, where these percentages are given as a fraction of the total composition. The precision of H_2 mole fraction measurements is ~10% of the measured value.

Results from a numerical study show that accurate temperature and species mole fraction measurements are possible when a portion of the spectra saturates the camera. The error is within 1% for the degree of detector saturation expected in the measurements of the laboratory-scale supersonic combusting jet. This approach is highly preferable to the removal of the saturated spectra from the dataset because it does not introduce significant bias, and extends the range of temperature that the instrument is capable of measuring. The probe volume length has been measured experimentally, and 90% of the CARS signal is generated over a 1.7 mm length.

In summary the DP-CARS development efforts described in this work, have:

- Increased the data acquisition rate and the data yield
- Reduced the data processing time
- Developed a technique to mitigate the effects of beam steering without affecting the spatial resolution
- Determined thresholds for high irradiance perturbation effects (Stark broadening and SRP) , found in Stark broadening the source of systematic errors in earlier H_2 mole fraction measurements
- Provided better instrument accuracy through improvements in the theoretical modeling
- Provided better instrument precision thanks to higher spectral resolution and new fitting algorithm

The DP-CARS instrument has been used to collect data in a laboratory-scale supersonic free jet flame for several values of exit and flight Mach numbers. The flow consists of a center-jet of hot vitiated air and a co-flow of N_2 for mixing study, or H_2

for combustion studies. Approximately 800,000 CARS spectra were collected and analyzed. The signal to noise ratio was sufficiently high at all the locations tested, and data yield > 95% was achieved. Averages, variances, co-variances, and histograms have been obtained at each location probed. Measured standard deviations are consistently larger (2x or more) than what was measured in laminar flames under similar conditions. Therefore, the instrument was capable of estimating temperature fluctuations due to the turbulence in this flow.

The experimental results for the non-reacting test cases showed that increased compressibility reduces the shear layer spreading rate, and the turbulence fluctuations, in agreement with what was observed in previous experimental work. The DP-CARS measurements in the reacting test cases showed that the heat released from the combustion strongly limits the growth of the co-flow shear layer, and the mixing of the center jet. Examination of the standard deviation and of the co-variances profiles proved to be very useful in determining where significant mixing and combustion are occurring. The experimental results were in agreement with what was previously observed or predicted, but the relevance of the acquired data-set lays in providing accurate quantitative measurements of the distributions of mean and fluctuation parameters (i.e. variances covariances, pdfs).

Two major drawbacks reduce the quality of the data set. The first is the significant length of the DP-CARS probe volume, which leads to spatial averaging and to errors in the measurements in proximity of steep temperature gradients (biased toward lower temperature) and underestimated turbulent fluctuations. The small size of the burner exacerbates this issue. Care must be used in interpreting the CARS measurements in

the proximity of steep temperature gradients. Spatially resolved CFD simulations could be post-processed for direct comparison to the results.

The second major issue with the dataset is the asymmetry of the co-flow nozzle. This is a minor issue for the non-reacting case, where the co-flow rate is low and air is rapidly entrained in the co-flow, mitigating the effects of the asymmetry. For the reacting case, the different flow-rates affect directly the amount of heat released that is the governing factor in the flow evolution. The difference in the total amount of heat released increases proceeding downstream, and so does the flow asymmetry.

Nevertheless, there is no other data set providing statistics on temperature and mole fractions in compressible shear layers. The data set can be a useful tool in the development of CFD turbulence model for compressible shear layer.

9.2 **Future Work**

The DP-CARS instrument has been moved to the University of Virginia, and DP-CARS data are currently being acquired in a Dual-Mode Scramjet Combustor.[105] After this test campaign the instrument will be moved back to NASA Langley Research Center for measurements in the Durable Combustor Rig in the Direct Connect Supersonic Test Facility.

Further instrument development to improve the accuracy and the precision is recommended. The changes in the spectral shape and peak wavelength of the broadband dye laser during the data acquisition were responsible for errors in the mole fraction measurements. Improvements are possible if spectra of the broadband dye laser are collected on a separate spectrometer each time CARS data are collected.

It is then possible to determine the relationship between the broadband dye laser spectral shape, and the non-resonant spectra, and to properly account for changes in the broadband dye laser with time. This method requires a second spectrometer, and a mapping from the spectral shape of the dye laser to the corresponding non-resonant profile.

As an alternative a CARS non-resonant profile can be collected simultaneously to the resonant CARS signal.[106] Generating two CARS signals in two different probe volumes would require roughly twice the laser energy if the non-resonant medium is argon. On the other hand, a strong non-resonant CARS signal can be obtained in a solid with laser energies that are few orders of magnitude less. The low energy collected for the beam viewing system would be sufficient to generate a non-resonant signal in a 1 mm (or thicker) thick microscope slide. A strong non-resonant signal could be generated by placing the microscope slide at the image of the crossing location generated by the beam viewing system. It has the same crossing of the main probe volume, but much lower irradiance. The non-resonant signal can then be sent on the path of the main CARS signal, but slightly misplaced in the vertical direction so that it would appear on the upper or lower bin. The microscope slide could be mounted on a remotely controlled translation stage, so that the non-resonant signal level can be controlled by changing the portion of the probe volume inside the solid. This is necessary to compensate for the signal reduction when the Nd:YAG energy is reduced to avoid detector saturation. This system would allow for a shot-to-shot normalization, completely removing the uncertainty related to the changes in the broadband dye laser.

Further improvement in the modeling can help in reducing the systematic errors. The low temperature test cases may benefit from theoretical models that include the collisional narrowing effect. A furnace, providing a controlled temperature and a known composition (air) is a good validation test-case to evaluate the effect of alternative linewidth models. Additional validation measurements for H_2 at lower temperature than are used for this test are also needed to evaluate if the exponential law for the optical diffusion coefficient is appropriate at lower temperatures.

The laboratory-scale supersonic combusting jet is an interesting test case for CFD validation, and there are several additional studies that can be accomplished using variations of the CARS technique described here. The nozzle and the co-flow annulus of the laboratory scale supersonic burner have been redesigned to remove the asymmetry in the flow. This problem greatly affected the combustion cases, and I recommend repeating some of the measurements, after implementing the improvements to the CARS system discussed above. Combustion cases using ethylene as co-flow and applying Tedder`s WIDECARS [85] for simultaneous measurements of temperature, N_2, O_2, CO, CO_2, C_2H_4 and H_2 are planned. To implement the technique it is necessary to replace the oscillator of the broadband dye laser, with the version designed by Tedder [199], to replace the dye, and the spectrometer grating (from 2400 lines/mm to 1200 lines/mm).

Spatial resolution was another limitation of the data presented here. Tests in the larger scale facility alleviate the issue, and the beam shaping technique developed for this test would mitigate the beam steering effects that compromised the previous attempt.[72] Improved spatial resolution for the combustion cases is limited by the

high irradiance perturbation effects, and a probe volume length shorter than 1.5 mm is challenging with a planar BOXCARS configuration. Improvements are instead possible for the mixing cases. Lower temperature implies higher signal, therefore smaller measurement volumes are achievable. In addition, there is no H_2 in the flow, and the second hot band does not appear. This allows moving the N_2 and O_2 spectra closer to each other and to the peak of the broadband dye laser. For this test case it is recommended to reduce the width of the dye laser, so that more energy is available for the CARS process (remember that Stark broadening is determined by the total irradiance, so a narrower broadband dye laser would contribute more to the CARS and the SRP process, but not to the Stark broadening).

Also the effect of the beam steering on the length of the measurement volume should be investigated. For example, the measurement of the probe volume length described in Chapter 6.8 could be repeated in presence of the beam steering generated by the helium jet of Chapter 4.4

The use of a modeless dye lasers as Stokes beam was previously attempted but did not provide the expected precision improvements. [66] This was a consequence of the lower irradiance of the laser and of the decreased spectral bandwidth. The N_2 portion of the spectra happened to be at the edge of the modeless Stokes laser, where the mode noise is larger and the spectral energy lower. The use of a modeless dye laser should be considered for the mixing test-case. Since the N_2 and O_2 spectra can be put close to each other, the reduced bandwidth is no longer an issue. The use of the modeless dye laser combined with simultaneous acquisition of a resonant and a non-resonant CARS signal, would also allow removal of the mode noise that is a major

noise source in CARS, allowing even higher improvement in precision as discussed in Ref.[106].

References

1. W. H. Heiser and D. T. Pratt, *Hypersonic Airbreathing Propulsion*, AIAA Education Series (AIAA Inc., Washington DC, 1994).
2. C. R. McClinton, J. L. Hunt, R. H. Ricketts, P. Reukauf, and C. L. Peddie, "Airbreathing Hypersonic Technology Vision Vehicle and Development Dreams," presented at AIAA International Space Planes and Hypersonic Systems and Technologies Conference, Norfolk, VA, 1999, AIAA-99-4979.
3. E. H. Andrews and E. A. Mackley, "NASA`s Hypersonic Research Engine Project- A Review," presented at AIAA/SAE/ASM E/ASEE 29th Joint Propulsion Conference and Exhibit, Monterey, CA, 1993, AIAA-93-2323.
4. A. Kumar, J. R. Drummond, C. R. McClinton, and L. J. Hunt, "Research in Hypersonic Airbreathing Propulsion at the NASA Langley Research Center," presented at ISABE 2001,
5. R. D. Rockwell, C. P. Goyne, W. Haw, R. H. Krauss, J. C. McDaniel, and J. C. Trefny, "Experimental Study of Test-Medium Vitiation Effects on Dual-Mode Scramjet Performance," *J. Propul. Power* **27**, (5) pp.1135-1142 2011.
6. S. O'Byrne, P. M. Danehy, S. A. Tedder, and A. D. Cutler, "Dual Pump Coherent Anti-Stokes Raman Scattering Measurements in Supesonic Combustor," *AIAA J.* **45**, (4) pp.922-933 2007.
7. J. C. McDaniel, H. Chelliah, C. P. Goyne, J. R. Edwards, P. Givi, and A. D. Cutler, "US National Center for Hypersonic Combined Cycle Propulsion: an Overview," presented at 16th AIAA/DLR/DGLR International Space Planes and Hypersonic Systems and Technologies Conference Bremen, Germany, 2009, AIAA-2009-7280.
8. A. Bresson, P. Bouchardy, P. Magre, and F. Grisch, "OH/Acetone PLIF and CARS Thermometry in a Supersonic Reactive Layer," presented at AIAA/NAL-NASDA-ISAS 10th International Space Planes and Hypersonic Systems and Technologies Conference, Kyoto, 2001, AIAA-2001-1759.
9. C. P. Goyne, R. J. Stalker, and A. Paull, "Transducer for Direct Measurement of Skin Friction in Hypervelocity Impulse Facilities," *AIAA J.* **40**, (1) pp.42-49 2002.
10. M. Ryan, M. Gruber, C. Carter, and T. Mathur, "Planar laser-induced fluorescence imaging of OH in a supersonic combustor fueled with ethylene and methane," *Proceedings of the Combustion Institute* **32**, (2) pp.2429-2436 2009.
11. M. J. Robinson, D. J. Mee, C. Y. Tsai, and R. J. Balkos, "Three-Component Force Measurements on a Large Scramjet in a Shock Tunnel," *Journal of Spacecraft and Rockets* **41**, (3) pp.2004.
12. R. R. Springer, A. D. Cutler, G. S. Diskin, and M. W. Smith, "Conventional/Laser Diagnostics to Assess Flow Quality in a Combustion-Heated Facility," presented at 35th AIAA/ASME/SAE/ASEE Joint Propulsion Conference and Exhibit, Los Angeles, CA, 1999, AIAA-99-2170.
13. C. Clifton and A. D. Cutler, "A Supersonic Argon/Air Coaxial Jet Experiment for Computational Fluid Dynamics Code Validation," (The George Washington University, Washington DC, 2007).

14. A. D. Cutler, G. Diskin, J. R. Drummond, and J. White, "Supersonic Coaxial Jet Experiment for Computational Fluid Dynamics Code Validation " *AIAA J.* **44**, (3) pp.585-592 2006.
15. S. G. Goebel and J. C. Dutton, "Experimental study of compressible turbulent mixing layers " *AIAA J.* **29**, (4) pp.538-546 1991.
16. H. Ikawa and T. Kubota, "Investigation of supersonic turbulent mixing layer with zero pressure gradient. ," *AIAA J.* **13**, (5) pp.566-572 1975.
17. K. C. Schadow, E. Gutmark, and K. J. Wilson, "Compressible spreading rates of supersonic coaxial jets," *Exp. Fluids* **10**, (2) pp.161-167 1990.
18. E. Gutmark, K. C. Schadow, and K. J. Wilson, "Effect of convective Mach number on mixing of coaxial circular and rectangular jets," *Phys. Fluids A* **3**, (1) pp.29-36 1991.
19. D. Papamoschou and A. Roshko, "The compressible turbulent shear layer: an experimental study," *J. Fluid Mech.* **197**, 453-477 1988.
20. P. Magre, G. Collin, O. Pin, J. M. Badie, G. Olalde, and M. Clement, "Tempeature measurements by CARS and intrusive probe in an air-hydrogen supersonic combustion," *Int. J. Heat Mass Transfer* **44**, 4095-4105 2001.
21. A. Ratner, J. F. Driscoll, H. Huh, and R. A. Bryant, "Combustion Efficiencies of Supersonic Flames," *J. Propul. Power* **17**, (2) pp.301-307 2001.
22. K. A. Skinner and R. J. Stalker, "Species measurements in a hypersonic, hydrogen-air, combustion wake," *Combust. Flame* **106**, (4) pp.478-486 1996.
23. S. Javoy, V. Naudet, S. Abid, and C. E. Paillard, "Elementary reaction kinetics studies of interest in H2 supersonic combustion chemistry," *Exp. Therm Fluid Sci.* **27**, (4) pp.371-377 2003.
24. A. D. Cutler, G. Magnotti, R. Baurle, D. Bivolaru, S. A. Tedder, P. M. Danehy, M. Weikl, F. Beryrau, and T. Seeger, "Development of Supersonic Combustion Experiments for CFD Model development," presented at 45th AIAA Aerospace Sciences Meeting, Reno, NV, 2007, AIAA 2007-0978.
25. Y. Gong, Z. Jian-guo, Z. Jian-Rong, Y. Shi-Run, and L. Chun-Jin, "Experimental Studies on H2/Air Supersonic Combustion," presented at International Space Planes and Hypersonic Systems and Technologies Conference 1996, AIAA-96-4512-CP.
26. R. B. Whitehurst, R. H. Krauss, and J. C. McDaniel, "Parametric and Time Resolved Studies of Autoignition and Flameholding in a Clean-Air Supersonic Combustor," presented at AIAA/SAE/ASME/ASEE 28th Joint Propulsion Conference and Exhibit, Nashville, TN, 1992, AIAA PAPER 92-3424.
27. G. Magnotti and A. D. Cutler, "An Experimental and Numerical Study of a Supersonic Burner for CFD Development," presented at 44th AIAA/ASME/SAE/ASEE Joint Propulsion Conference & Exhibit, Hartford, CT, 2008, AIAA 2008-4686
28. J. Hall, P. E. Dimotakis, and H. Rosemann, "Experiments in nonreacting compressible shear layers " *AIAA J.* **31**, (12) pp.2247-2254 1993.
29. W. Waidmann, F. Alff, M. Bohm, W. Clauss, and M. Oschwald, "Supersonic Combustion of Hydrogen/Air in a Scramjet Combustor Chamber," presented at 45th IAF Congress, Jerusalem, 1994, IAF-94-S.4.429,45th.

30. A. Ben-Yakar and R. K. Hanson, "Hypervelocity Combustion Studies Using Simultaneous OH-PLIF and Schlieren imaging in an Expansion Tube " presented at 35th AIAA/ASME/SAE/ASEE Joint Propulsion Conference and Exhibit, Reston, VA, 1999, AIAA-1999-2453
31. J. D. Abbit, J. C. McDaniel, R. H. Krauss, R. B. Whitehurst, and C. Segal, "Experimental Investigation of a Supersonic Combustion Flowfield Employing Staged Transverse Injection Behind a Rearward-Facing Step," presented at 30th Aerospace Sciences Meeting & Exhibit, Reno,NV, 1992, AIAA 92-0090.
32. M. Gruber, C. Carter, M. Ryan, G. B. Rieker, J. B. Jeffries, R. K. Hanson, J. Liu, and T. Mathur, "Laser-Based Measurements of OH, Temperature, and Water Vapor Concentration in a Hydrocarbon-Fueled Scramjet," presented at 44th AIAA/ASME/SAE/ASEE Joint Propulsion Conference, Hartford, CT, 2008, AIAA 2008-5070.
33. T. Sunami, P. Magre, A. Bresson, F. Grisch, and M. Orain, "Experimental Study of Strut Injectors in a Supersonic Combustor Using OH-PLIF," presented at AIAA/CIRA 13th International Space Planes and Hypersonics Systems and Technologies, Capua, Italy, 2005, AIAA 2005-3304.
34. R. A. Bryant and J. F. Driscoll, "Structure of Supersonic Flames Imaged Using OH/Acetone Planar Laser-Induced Fluorescence," *AIAA J.* **39**, (9) pp.1735-1741 2001.
35. M. G. Allen, T. E. Parker, W. G. Reinecke, H. H. Legner, R. R. Foutter, W. T. WRawlins, and S. J. Davis, "Fluorescence Imaging of OH and NO in a Model Supersonic Combustor," *AIAA J.* **31**, (3) pp.505-512 1993.
36. G. Laufer, T. M. Quagliaroli, R. H. Krauss, R. B. Whitehurst, J. C. McDaniel, and J. H. Grinstead, "Planar OH Density and Apparent Temperature Measurements in a Supersonic Combusting Flow," *AIAA J.* **34**, (3) pp.463-469 1996.
37. G. Gauba, J. C. Klavuhn, J. C. McDaniel, K. G. Victor, R. H. Krauss, and R. B. Whitehurst, "OH Planar Laser-Induced Fluorescence Velocity Measurements in a Supersonic Combustor," *AIAA J.* **35**, (4) pp.678-686 1997.
38. T. M. Quagliaroli, G. Laufer, S. D. Hollo, R. H. Krauss, R. B. Whitehurst, and J. C. McDaniel, "Planar KrF Laser-Induced OH Fluorescence Imaging in a Supersonic Combustion Tunnel," *J. Propul. Power* **10**, (3) pp.377-381 1994.
39. G. S. Settles, D. R. Williams, B. K. Baca, and S. M. Bogdonoff, "Reattachment of a Compressible Turbulent Free Shear Layer " *AIAA J.* **20**, (1) pp.60-67 1982.
40. L. Y. Jiang and J. P. Sislian, "Velocity and Density Measurements in Supersonic High-Temperature Exhaust Plumes," *AIAA J.* **36**, (7) pp.1216-1222 1993.
41. M. Samimy, H. L. Petrie, and A. L. Addy, "A study of Compressible Turbulent Reattaching Free Shear Layer " *AIAA J.* **24**, (2) pp.261-267 1986.
42. N. Zhang, F. S. Alvi, M. B. Alkislar, and C. Shih, "Supersonic Cavity Flows and their Control," *AIAA J.* **44**, (9) pp.2118-2128 2006.
43. O. H. Unalmis, N. T. Clemens, and D. S. Dolling, "Experimental Study of Shear-Layer/Acoustics Coupling in a Mach 5 Cavity Flow," *AIAA J.* **45**, (11) pp.2770-2777 2001.
44. H. Weisgerber, R. Martinuzzi, U. Brummund, and P. Magre, "PIV Measurements in a Mach 2 Hydrogen-air Supersonic Combustion," presented at AIAA/NAL-

NASDA-ISAS 1oth International Space Planes and Hypersonic Systems and Technologies Conference, Kyoto, Japan, 2001, AIAA-2001-1757.
45. C. T. Smith and C. P. Goyne, "Three-component Velocimetry in a Scramjet Combustor," presented at 44th AIAA/ASME/SAE/ASEE Joint Propulsion Conference & Exhibit, Hartford, CT, 2008, AIAA 2008-5073.
46. S. Koike, H. Takahashi, K. Hirota, K. Takita, and G. Masuya, "Correction Method for Particle Imaging Data Based on the Stokes Drag Law," *AIAA J.* **45**, (11) pp.2770-2777 2007.
47. J. C. Klavuhn, G. Gauba, and J. C. McDaniel, "OH Laser-Induced Fluorescence Velocimetry Technique for steady, High Speed Reacting Flows," *J. Propul. Power* **10**, (6) pp.787-797 1994.
48. M. Allen, S. Davis, W. Kessler, H. Legner, K. McManus, P. Mulhall, T. Parker, and D. Sonnenfroh, "Velocity Field Imaging in Supersonic Reacting Flows Near Atmospheric Pressure," *AIAA J.* **32**, (8) pp.1676-1682 1994.
49. P. H. Paul, M. P. Lee, and R. K. Hanson, "Molecular velocity imaging of supersonic flows using pulsed planar laser-induced fluorescence of NO," *Opt. Lett.* **14**, (9) pp.417-419 1989.
50. J. C. McDaniel, B. Hiller, and R. K. Hanson, "Simultaneous multiple-point velocity measurements using laser-induced iodine fluorescence," *Opt. Lett.* **8**, (1) pp.51-53 1983.
51. D. Bivolaru, A. D. Cutler, P. M. Danehy, R. L. J. Gaffney, and R. Baurle, "Spatialy and Temporally Resolved Measurements of Velocity in a H2-Air Combustion-Heated-Supersonic Jet," presented at 47th Aerospace Science Meeting and Exhibit, Reno, NV, 2009, AIAA-2009-0027.
52. M. D. Lahr, R. W. Pitz, Z. W. Douglas, and C. D. Carter, "Hydroxil-Tagging-Velocimetry Measurements of a Supersonic Flow over a Cavity," *J. Propul. Power* **26**, (4) pp.790-797 2010.
53. M. Samimy and M. P. Wernet, "Review of Planar Multiple-Component Velocimetry in High-Speed Flows," *AIAA J.* **38**, (4) pp.553-574 2000.
54. C. L. Strand and R. K. Hanson, "Thermometry and Velocimetry in Supersonic Flow via Scanned Wavelength-Modulation Absorption Spectroscopy," presented at 47th AIAA/ASME/SAE/ASEE Joint Propulsion Conference, San Diego, 2011, AIAA-2011-5600.
55. L. S. Chang, J. B. Jeffries, and R. K. Hanson, "Mass Flux Sensing via Tunable Diode Laser Absorption of Water Vapor," *AIAA J.* **48**, (11) pp.2687-2693 2010.
56. L. S. Chang, C. L. Strand, J. B. Jeffries, R. K. Hanson, G. S. Diskin, R. L. J. Gaffney, and D. P. Capriotti, "Supersonic Mass-Flux Measurements via Tunable Diode Laser Absorption and Nonuniform Flow Modeling," *AIAA J.* **49**, (12) pp.2783-2790 2011.
57. C. Lindstrom, C. J. Tam, D. Davis, D. Eklund, and S. Williams, "Diode Laser Absorption Tomography of 2D Supersonic Flow," presented at 43rd AIAA/ASME/SAE/ASEE Joint Propulsion Conference Cincinnati, OH, 2007, AIAA 2007-5014.
58. K. Busa, E. Bryner, J. C. McDaniel, C. P. Goyne, and C. T. Smith, "Demonstration of Capability of Water Flux Measurements in a Scramjet Combustor Using Tunable Diode Laser Absorption Tomographyand Stereoscopic

PIV," presented at 49th AIAA Aerospace Sciences Meeting Orlando, FL, 2011, AIAA 2011-1294.
59. R. W. Pitz, N. R. Grady, S. W. Shopoff, S. Hu, and C. D. Carter, "UV Raman Scattering Measurements of a Mach 2 Reacting Flow over a Piloted Cavity," presented at 46th AIAA Aerospace Sciences Meeting and Exhibit, Reno, NV, 2008, AIAA 2008-244.
60. N. R. Grady, J. H. Frankland, R. W. Pitz, C. D. Carter, and K. Y. Hsu, "UV Raman Scattering Measuremetns of Supersonic Reacting Flow over a Piloted, Ramped Cavity," presented at 50th AIAA Aerospace Science Meeting Nashville, TN, 2012, AIAA 2012-0614.
61. T. J. Anderson, L. W. Kay, and Peschke, "CARS Feasibility Demonstration in Supersonic Combusting Flows," in *22nd JANNAF Combustion meeting*, 1986, 417-428.
62. T. J. Anderson and A. C. Eckbreth, "Simultaneous Coherent Anti-Stokes Raman Spectroscopy Measurements in Hydrogen Fueled Supersonic Combustion," *J. Propul. Power* **8**, (1) pp.7-15 1992.
63. J. R. Zhao, S. R. Yang, J. G. Li, G. Yu, and C. J. Li, "CARS measurements in a hydrogen/air supersonic combustor," presented at 35th AIAA Aerospace Sciences Meeting & Exhibit, Reno, NV, 1997, AIAA-1997-122
64. S. R. Yang, J. R. Zhao, C. J. Sung, and G. Yu, "Multiplex CARS measurements in supersonic H2/air combustion," *Appl. Phys. B: Lasers Opt.* **68**, (2) pp.257-265 1999.
65. P. Magre and P. Bouchardy, "Nitrogen and hydrogen coherent anti-stokes raman scattering thermometry in a supersonic reactive mixing layer," *Proceedings of the Combustion Institute* **28**, (1) pp.697-703 2000.
66. S. A. Tedder, D. Bivolaru, and P. M. Danehy, "Characterization of a Combined CARS and Interferometric Rayleigh Scattering System," presented at 45th AIAA Aerospace Science Meeting, Reno, 2007, AIAA 2007-871
67. O. Jarrett Jr, R. R. Antcliff, T. Chitsomboon, G. Diskin, and A. D. Cutler, "Dual Stokes CARS measurements in supersonic combusting flow," in *The 24th JANNAF Combustion Meeting*, 1987, 171-178.
68. A. D. Cutler, G. Diskin, P. M. Danehy, and J. R. Drummond, "Fundamental Mixing and Combustion Experiments for Propelled Hypersonic Flight," presented at 38th AIAA/ASME/SAE/ASEE Joint Propulsion Conference and Exhibit, Indianapolis, 2002, AIAA-2002-3879.
69. M. W. Smith, O. Jarrett Jr, R. R. Antcliff, G. B. Northam, and A. D. Cutler, "Coherent Anti-Stokes Raman Spectroscopy Temperature Measurements in a Hydrogen-Fueled Supersonic Combustor," *J. Propul. Power* **1993**, (2) pp.163-168 1993.
70. A. D. Cutler, P. M. Danehy, R. R. Springer, S. O'Byrne, D. P. Capriotti, and R. DeLoach, "Coherent Anti-Stokes Raman Spectroscopic Termomethry in a Supersonic Combustor," *AIAA J.* **41**, (12) pp.2003.
71. C. G. Rodriguez and A. D. Cutler, "Computational Simulation of a Supersonic - Combustion Benchmark Experiment," presented at 41st AIAA/ASME/SAE/ASEE Joint Propulsion Meeting and Exhibit, Tucson, AZ, 2005, AIAA-2005-4424

72. S. A. Tedder, P. M. Danehy, G. Magnotti, and A. D. Cutler, "CARS Temperature Measurements in a Combustor-Heated Mach 1.6 Jet," presented at 47th Aerospace Sciences Meeting, Orlando, FL, 2009, AIAA-2009-0524
73. D. Bivolaru, P. M. Danehy, K. D. Grinstead, S. A. Tedder, and A. D. Cutler, "Simultaneous CARS and Interferometric Rayleigh Scattering " presented at AIAA Aeroynamic Measurement Technology and Ground Testing Conference San Francisco, 2006, AIAA-2006-2968.
74. P. M. Danehy, G. Magnotti, D. Bivolaru, S. A. Tedder, and A. D. Cutler, "Simultaneous Temperature and Velocity Measurements in a Large Scale Supersonic Heated Jet," presented at 55th JANNAF Propulsion Meeting, Boston, MA, 2008, paper-1193.
75. S. A. Tedder, "Advancements in Dual-Pump Broadband CARS for Supersonic Combustion Measurements," (College of William and Mary, Williamsburg, 2010).
76. P. D. Maker and R. W. Terhune, "Study of Optical Effects Due to an Induced Polarization Third Order in the Electric Field Strength," *Physical Review* **137**, (3A) pp.A801-A818 1965.
77. P. R. Régnier, F. Moya, and J. P. E. Taran, "Gae Concentration Measurements by Coherent Raman Anti-Stokes Scattering," *AIAA J.* **12**, (6) pp.826-831 1974.
78. P. R. Regnier and J. P. E. Taran, "On the possibility of measuring gas concentrations by stimulated anti-Stokes scattering," *Appl. Phys. Lett.* **23**, (5) pp.240-242 1973.
79. S. Roy, J. R. Gord, and A. K. Patnaik, "Recent advances in coherent anti-Stokes Raman scattering spectroscopy: Fundamental developments and applications in reacting flows," *Progr. Energy Combust. Sci.* **36**, (2) pp.280-306 2010.
80. R. E. Teets, "Laser mode effects on coherent anti-Stokes Raman spectroscopy," presented at First International Laser Science Conference, Dallas, TX, 1985,
81. R. P. Lucht, "Three-laser coherent anti-Stokes Raman scattering measurements of two species," *Opt. Lett.* **12**, (2) pp.78-80 1987.
82. S. Roy, T. R. Meyer, M. S. Brown, V. N. Velur, R. P. Lucht, and J. R. Gord, "Triple-pump coherent anti-Stokes Raman scattering (CARS): temperature and multiple-species concentration measurements in reacting flows," *Opt. Commun.* **224**, (1–3) pp.131-137 2003.
83. T. R. Meyer, S. Roy, R. P. Lucht, and J. R. Gord, "Dual-pump dual-broadband CARS for exhaust-gas temperature and CO2–O2–N2 mole-fraction measurements in model gas-turbine combustors," *Combust. Flame* **142**, (1–2) pp.52-61 2005.
84. S. Roy, T. R. Meyer, R. P. Lucht, M. Afzelius, P.-E. Bengtsson, and J. R. Gord, "Dual-pump dual-broadband coherent anti-Stokes Raman scattering in reacting flows," *Opt. Lett.* **29**, (16) pp.1843-1845 2004.
85. S. A. Tedder, J. L. Wheeler, A. D. Cutler, and P. M. Danehy, "Width-increased dual-pump enhanced coherent anti-Stokes Raman spectroscopy," *Appl. Opt.* **49**, (8) pp.1305-1313 2010.
86. S. F. Hanna, W. D. Kulatilaka, Z. Arp, T. Opatrny, M. O. Scully, J. P. Kuehner, and R. P. Lucht, "Electronic-resonance-enhanced coherent anti-Stokes Raman spectroscopy of nitric oxide," *Appl. Phys. Lett.* **83**, (9) pp.1887-1889 2003.

87. A. C. Eckbreth, *Laser Diagnostics for Combustion Temperature and Species,* Second ed., Combustion Science and Technology Book Series (Taylor and Francis, New York, 1996).
88. G. Herzberg, *Molecular Spectra and Molecular Structure* (D. Van Nostrand Company, Inc., 1939).
89. R. H. Dicke, "The Effect of Collisions upon the Doppler Width of Spectral Lines," *Physical Review* **89**, (2) pp.472-473 1953.
90. P. L. Varghese and R. K. Hanson, "Collisional narrowing effects on spectral line shapes measured at high resolution," *Appl. Opt.* **23**, (14) pp.2376-2385 1984.
91. A. S. Pine, "Collisional narrowing of HF fundamental band spectral lines by neon and argon," *Journal of Molecular Spectroscopy* **82**, (2) pp.435-448 1980.
92. L. Galatry, "Simultaneous Effect of Doppler and Foreign Gas Broadening on Spectral Lines," *Physical Review* **122**, (4) pp.1218-1223 1961.
93. F. Herbert, "Spectrum line profiles: A generalized Voigt function including collisional narrowing," *Journal of Quantitative Spectroscopy and Radiative Transfer* **14**, (9) pp.943-951 1974.
94. W. K. Bischel and M. J. Dyer, "Temperature dependence of the Raman linewidth and line shift for the Q(1) and Q(0) transitions in normal and para-H_{2}," *Phys. Rev. A* **33**, (5) pp.3113 1986.
95. P. Duggan, P. M. Sinclair, M. P. Le Flohic, J. W. Forsman, R. Berman, A. D. May, and J. R. Drummond, "Testing the validity of the optical diffusion coefficient: Line-shape measurements of CO perturbed by N_{2}," *Phys. Rev. A* **48**, (3) pp.2077 1993.
96. J. Kojima and Q.-V. Nguyen, "Quantitative analysis of spectral interference of spontaneous Raman scattering in high-pressure fuel-rich H2–air combustion," *Journal of Quantitative Spectroscopy and Radiative Transfer* **94**, (3-4) pp.439-466 2005.
97. R. J. Hall and D. A. Greenhalgh, "Application of the rotational diffusion model to gaseous N2 CARS spectra," *Opt. Commun.* **40**, (6) pp.417-420 1982.
98. W. B. Roh, P. W. Schreiber, and J. P. E. Taran, "Single-pulse coherent anti-Stokes Raman scattering," *Appl. Phys. Lett.* **29**, (3) pp.174-176 1976.
99. R. P. Lucht, P. Velur-Natarajan, C. D. Carter, K. D. Grinstead, J. R. Gord, and P. M. Danehy, "Dual-pump coherent anti-Stokes Raman scattering temperature and CO_2 concentration measurements " *AIAA J.* **41**, 679-686 2003.
100. S. M. Green, P. J. Rubas, M. A. Paul, J. E. Peters, and R. P. Lucht, "Annular Phase-Matched Dual-Pump Coherent Anti-Stokes Raman Spectroscopy System for the Simultaneous Detection of Nitrogen and Methane," *Appl. Opt.* **37**, (9) pp.1690-1701 1998.
101. Y. Gao, M. C. Weikl, T. Seeger, A. Leipertz, P. Joubert, and J. Bonamy, "Evaluation of temperature and concentration in H2 [illegible] N2 pure CARS spectra using the Keilson and Storer three-dimensional model for H2 Q-branch," *J. Raman Spectrosc.* **40**, (7) pp.781-787 2009.
102. T. Seeger, J. Kiefer, A. Leipertz, B. D. Patterson, C. J. Kliewer, and T. B. Settersten, "Picosecond time-resolved pure-rotational coherent anti-Stokes Raman spectroscopy for N2 thermometry," *Opt. Lett.* **34**, (23) pp.3755-3757 2009.

103. P. Hsu, A. Patnaik, J. Gord, T. Meyer, W. Kulatilaka, and S. Roy, "Investigation of optical fibers for coherent anti-Stokes Raman scattering (CARS) spectroscopy in reacting flows," *Exp. Fluids* **49**, (4) pp.969-984 2010.
104. D. Bivolaru and G. C. Herring, "Focal Plane Imaging of Crossed Beams in Non-linearOptics Experiments," *Rev. Sci. Instrum.* **78**, (5) pp.2007.
105. A. D. Cutler, G. Magnotti, L. Cantu, E. Gallo, and P. M. Danehy, "Dual-Pump CARS Measurements in the University of Virginia`s Dual-Mode Scramjet: Configuration "A"," presented at 50th AIAA Aerospace Sciences Meeting, Nashville TN, 2012, AIAA-2012-114
106. E. H. van Veen and D. Roekaerts, "Thermometry for turbulent flames by coherent anti-Stokes Raman spectroscopy with simultaneous referencing to the modeless excitation profile," *Appl. Opt.* **44**, (32) pp.6995-7004 2005.
107. A. D. Cutler and G. Magnotti, "CARS Spectral Fitting with Multiple Resonant Species Using Sparse Libraries," *J. Raman Spectrosc.* **42**, (11) pp.1949-1957 2011.
108. R. E. Palmer, "The CARSFT Computer Code for Calculating Coherent Anti-Stokes Raman Spectra: User and Programmer Information," (SANDIA National Labs, Livermore, CA, 1989).
109. R. D. Hancock, F. R. Schauer, R. P. Lucht, and R. L. Farrow, "Dual-pump coherent anti-Stokes Raman scattering measurements of nitrogen and oxygen in a laminar jet diffusion flame," *Appl. Opt.* **36**, (15) pp.3217-3226 1997.
110. P. M. Danehy, S. O'Byrne, and A. D. Cutler, "Coherent Anti-Stokes Raman Scattering (CARS) as a probe for Supersonic Hydrogen-Fuel/Air Mixing," in *Proceedings of the JANNAF APS/CS/PSHS/MSS Joint Meeting,* (2003).
111. R. Herman, "Influence of Vibration/Rotation Interaction on Line Intensities in Vibration/Rotation Bands of Diatomic Molecules," *J. Chem. Phys.* **23**, (4) pp.637 1955.
112. T. James, "Line Intensities in the Raman Effect of $^{1}\Sigma$ Diatomic Molecules," *J. Chem. Phys.* **31**, (1) pp.130 1959.
113. M. Marrocco, "Comparative analysis of Herman-Wallis factors for uses in coherent anti-Stokes Raman spectra of light molecules," *J. Raman Spectrosc.* **40**, (7) pp.741-747 2009.
114. M. Marrocco, G. Magnotti, and A. D. Cutler, "Herman-Wallis corrections in dual-pump CARS intensities for combustion temperature and species," *J. Raman Spectrosc.* **in press**, 2012.
115. R. H. Tipping and J. P. Bouanich, "On the use of Herman–Wallis factors for diatomic molecules," *Journal of Quantitative Spectroscopy and Radiative Transfer* **71**, (1) pp.99-103 2001.
116. D. R. Snelling, G. J. Smallwood, R. A. Sawchuk, and T. Parameswaran, "Precision of multiplex CARS temperatures using both single-mode and multimode pump lasers," *Appl. Opt.* **26**, (1) pp.99-110 1987.
117. E. J. Jumper and R. J. Hugo, "Quantification of Aero-Optical Phase Distortion Using the Small-Aperture Beam Technique," *AIAA J.* **33**, (11) pp.1995.
118. R. Barille and P. LaPenna, "Multifractality of laser beam spatial intensity in a turbulent medium," *Appl. Opt.* **45**, (14) pp.3331-3339 2006.

119. B. Hemmerling, "Beam-steering effects in turbulent high-pressure flames," *Proc. SPIE* **3108**, 32-36 1997.
120. B. Attal-Trétout, P. Bouchardy, P. Magre, M. Péalat, and J. P. Taran, "CARS in combustion: Prospects and problems," *Appl. Phys. B: Lasers Opt.* **51**, (1) pp.17-24 1990.
121. D. N. Klimenko, W. Clauss, M. Oschwald, J. Smith, and W. Mayer, "CARS temperature mapping in a cryogenic LOX–H2 rocket combustion chamber under supercritical conditions," *J. Raman Spectrosc.* **33**, (11-12) pp.900-905 2002.
122. B. Hemmerling, R. Bombach, and W. Kreutner, "Measurements of temperature fluctuations in a large-scale turbulent high-pressure flame using CARS," *Proc. SPIE* **2506**, (1) pp.94 1995.
123. G. C. Herring, R. C. Hart, F. M. T., B. J., and H. B., "Prospects for Nonlinear Laser Diagnostics in the Jet Noise Laboratory," TM-2007-214893 (NASA, 2007).
124. K. A. Marko and L. Rimai, "Space- and time-resolved coherent anti-Stokes Raman spectroscopy for combustion diagnostics," *Opt. Lett.* **4**, (7) pp.211-213 1979.
125. A. C. Eckbreth, G. M. Dobbs, J. H. Stufflebeam, and P. A. Tellex, "CARS temperature and species measurements in augmented jet engine exhausts," *Appl. Opt.* **23**, (9) pp.1328-1339 1984.
126. J. A. Shirley, R. J. Hall, and A. C. Eckbreth, "Folded BOXCARS for rotational Raman studies," *Opt. Lett.* **5**, (9) pp.380-382 1980.
127. D. A. Greenhalgh, "Comments on the use of BOXCARS for gas-phase CARS spectroscopy," *J. Raman Spectrosc.* **14**, (3) pp.150-153 1983.
128. G. Singh and F. Yueh, "An Evaluation of CARS Phase Matching Techniques for Field Application," presented at 22nd Fluid Dynamics, PlasmaDynamics & Laser Conference, Honolulu, HI, 1991, AIAA-91-1520.
129. R. E. Teets, "CARS signals: phase matching, transverse modes, and optical damage effects," *Appl. Opt.* **25**, (6) pp.855-862 1986.
130. E. Hecht, *Optics,* 3rd ed. (Addison Wesley Longman Publishers, 2001).
131. V. S. Sirazetdinov, "Experimental study and numerical simulation of laser beams propagation through the turbulent aerojet," *Appl. Opt.* **47**, (7) pp.975-985 2008.
132. M. A. Woodmansee, R. P. Lucht, and J. C. Dutton, "Stark Broadening and Stimulated Raman Pumping in High Resolution N_2 Coherent Anti-Stokes Raman Scattering Spectra," *AIAA J.* **40**, (6) pp.1078-1086 2002.
133. S. Kröll, M. Aldén, P. E. Bengtsson, and C. Löfström, "An evaluation of precision and systematic errors in vibrational CARS thermometry," *Appl. Phys. B: Lasers Opt.* **49**, (5) pp.445-453 1989.
134. A. Gierulski, M. Noda, T. Yamamoto, G. Marowsky, and A. Slenczka, "Pump-induced population changes in broadband coherent anti-Stokes Raman scattering," *Opt. Lett.* **12**, (8) pp.608-610 1987.
135. M. Péalat, P. Magre, P. Bouchardy, and G. Collin, "Simultaneous temperature and sensitive two-species concentration measurements by single-shot CARS," *Appl. Opt.* **30**, (10) pp.1263-1273 1991.
136. P. Chýlek, M. A. Jarzembski, V. Srivastava, R. G. Pinnick, J. D. Pendleton, and J. P. Cruncleton, "Effect of spherical particles on laser-induced breakdown of gases," *Appl. Opt.* **26**, (5) pp.760-762 1987.

137. G. L. Switzer, C. G. Meyers, and W. B. Roh, "Gas Breakdown Thresholds in Flame Induced by Ruby Laser," *AIAA J.* **16**, 766-768 1978.
138. H. Moosmuller, C. Y. She, and W. M. Huo, "Optical Stark effect in the four-wave mixing and stimulated Raman spectra of N2," *Phys. Rev. A* **40**, (12) pp.6983 1989.
139. R. L. Farrow and L. A. Rahn, "Optical Stark Splitting of Rotational Raman Transitions," *Phys. Rev. Lett.* **48**, (6) pp.395 1982.
140. L. A. Rahn, R. L. Farrow, M. L. Koszykowski, and P. L. Mattern, "Observation of an Optical Stark Effect on Vibrational and Rotational Transitions," *Phys. Rev. Lett.* **45**, (8) pp.620 1980.
141. M. J. Dyer and W. K. Bischel, "Optical Stark shift spectroscopy: Measurement of the v=1 polarizability in H2," *Phys. Rev. A* **44**, (5) pp.3138 1991.
142. A. Owyoung, R. A. Hill, and P. Esherick, "Optical Stark effects on pure-spin Raman transitions in molecular oxygen," *Opt. Lett.* **8**, (8) pp.425-427 1983.
143. G. C. Herring and M. E. Hillard, "Stark broadening using crossed Gaussian beams in stimulated Raman spectroscopy of N2," *J. Quant. Spectrosc. Radiat. Transfer* **57**, (6) pp.739-744 1997.
144. M. Péalat, M. Lefebvre, J. P. E. Taran, and P. L. Kelley, "Sensitivity of quantitative vibrational coherent anti-Stokes Raman spectroscopy to saturation and Stark shifts," *Phys. Rev. A* **38**, (4) pp.1948 1988.
145. M. Péalat and M. Lefebvre, "Temperature measurement by single-shot dual-line CARS in low-pressure flows," *Appl. Phys. B: Lasers Opt.* **53**, (1) pp.23-29 1991.
146. F. Grisch, P. Bouchardy, M. Péalat, B. Chanetz, T. Pot, and M. C. Coët, "Rotational temperature and density measurements in a hypersonic flow by dual-line CARS," *Appl. Phys. B: Lasers Opt.* **56**, (1) pp.14-20 1993.
147. N. J. Bridge and A. D. Buckingham, "The Polarization of Laser Light Scattered by Gases," *Proc. R. Soc. London, A* **295**, (1442) pp.334-349 1966.
148. M. D. Duncan, P. Oesterun, F. König, and R. L. Byer, "Observation of saturation broadening of the coherent anti-stokes raman spectrum (cars) of acetylene in a pulsed molecular beam," *Chem. Phys. Lett.* **80**, (2) pp.253-256 1981.
149. R. L. Farrow and R. P. Lucht, "High-resolution measurements of saturated coherent anti-Stokes Raman spectroscopy line shapes," *Opt. Lett.* **11**, (6) pp.374-376 1986.
150. I. L. Shumay, V. N. Zadkov, D. J. Heinzen, M. M. Kash, and M. S. Feld, "Observation of the saturation effect in continuous-wave coherent anti-Stokes Raman spectroscopy of liquid nitrogen," *Opt. Lett.* **11**, (4) pp.233-235 1986.
151. R. Bombach, B. Hemmerling, and W. Hubschmid, "Saturation effects and stark shift in hydrogen Q-branch CARS spectra," *Chem. Phys.* **144**, (2) pp.265-271 1990.
152. R. P. Lucht and R. L. Farrow, "Saturation effects in coherent anti-Stokes Raman scattering spectroscopy of hydrogen," *J. Opt. Soc. Am. B: Opt. Phys.* **6**, (12) pp.2313-2326 1989.
153. A. D. Wilson-Gordon and H. Friedmann, "Comment : Comment on saturation effects in high-resolution coherent anti-stokes Raman spectroscopy of a pulsed molecular beam," *Chem. Phys. Lett.* **89**, (3) pp.273-278 1982.

154. V. N. Zadkov and N. I. Koroteev, "Saturation effects in cars: Collisionally narrowed raman spectra of diatomic gases," *Chem. Phys. Lett.* **105**, (1) pp.108-113 1984.
155. R. P. Lucht and R. L. Farrow, "Calculation of saturation line shapes and intensities in coherent anti-Stokes Raman scattering spectra of nitrogen," *J. Opt. Soc. Am. B: Opt. Phys.* **5**, (6) pp.1243-1252 1988.
156. R. D. Hancock, K. E. Bertagnolli, and R. P. Lucht, "Nitrogen and hydrogen CARS temperature measurements in a hydrogen/air flame using a near-adiabatic flat-flame burner," *Combust. Flame* **109**, (3) pp.323-331 1997.
157. T. Lundeen, S.-Y. Hou, and J. W. Nibler, "Nonresonant third order susceptibilities for various gases," *J. Chem. Phys.* **79**, (12) pp.6301 1983.
158. M. Marrocco, "Reliability of Herman–Wallis factors for Raman spectroscopy of Q-branch molecular transitions," *Chem. Phys. Lett.* **442**, (4-6) pp.224-227 2007.
159. M. Marrocco, "Herman–Wallis factor to improve thermometric accuracy of vibrational coherent anti-Stokes Raman spectra of H2," *Proceedings of the Combustion Institute* **32**, (1) pp.863-870 2009.
160. M. Marrocco, "CARS thermometry revisited in lightof the intramolecular perturbation," *J. Raman Spectrosc.* **41**, (8) pp.870-874 2010.
161. L. A. Rahn and R. E. Palmer, "Studies of nitrogen self-broadening at high temperature with inverse Raman spectroscopy," *J. Opt. Soc. Am. B* **3**, (9) pp.1164-1169 1986.
162. W. D. Kulatilaka, "Direct measurement of rotationally resolved H2 Q-branch Raman coherence lifetimes using time-resolved picosecond coherent anti-Stokes Raman scattering," *Appl. Phys. Lett.* **97**, (8) pp.081112 2010.
163. G. Magnotti, A. D. Cutler, G. C. Herring, S. A. Tedder, and P. M. Danehy, "Saturation and Stark Broadening Effects in Dual-Pump CARS of N2, O2 and H2," *J. Raman Spectrosc.*, 2012.
164. S. La and L. E. Harris, "Relative value of the third-order nonresonant susceptibility ofwater," *Appl. Opt.* **25**, (23) pp.4501-4503 1986.
165. G. J. Rosasco and W. S. Hurst, "Dispersion of the electronic contribution to the third-order nonlinear susceptibility of H2," *J. Opt. Soc. Am. B* **3**, (10) pp.1251-1256 1986.
166. R. L. Farrow, R. P. Lucht, and L. A. Rahn, "Measurements of the nonresonant third-order susceptibilities of gases using coherent anti-Stokes Raman spectroscopy," *J. Opt. Soc. Am. B* **4**, (8) pp.1241-1246 1987.
167. D. P. Shelton and J. E. Rice, "Measurements and calculations of the hyperpolarizabilities of atoms and small molecules in the gas phase," *Chem. Rev.* **94**, (1) pp.3-29 1994.
168. J. W. Hahn and E. S. Lee, "Measurement of nonresonant third-order susceptibilities of various gases by the nonlinear interferometric technique," *J. Opt. Soc. Am. B* **12**, (6) pp.1021-1027 1995.
169. G. Hauchecorne, F. Kerherve, and G. Mayer, "Mesure des interactions entre ondes lumineuses dans diverses substances," *Journal de Physique* **32**, 47 1971.
170. M. Pealat, P. Bouchardy, M. Lefebvre, and J. P. Taran, "Precision of multiplex CARS temperature measurements," *Appl. Opt.* **24**, (7) pp.1012-1022 1985.

171. S. Prucker, W. Meier, and W. Stricker, "A flat flame burner as calibration source for combustion research: Temperatures and species concentrations of premixed H2/air flames," *Rev. Sci. Instrum.* **65**, (9) pp.2908 1994.
172. T. Seeger and A. Leipertz, "Experimental comparison ofsingle-shot broadband vibrationaland dual-broadband pure rotationalcoherent anti-Stokes Raman scattering in hot air," *Appl. Opt.* **35**, (15) pp.2665-2671 1996.
173. J. P. Kuehner, M. A. Woodmansee, R. P. Lucht, and J. C. Dutton, "High-Resolution Broadband N2 Coherent Anti-Stokes Raman Spectroscopy: Comparison of Measurements for Conventional And Modeless Broadband Dye Lasers," *Appl. Opt.* **42**, (33) pp.6757-6767 2003.
174. G. Hartung, J. W. Walewski, J. F. Hult, and C. F. Kaminski, "A flat flame burner for the calibration of laser thermometry techniques," *Meas. Sci. Technol.* **17**, 2485 2005.
175. J. W. Hahn, C. W. Park, and S. N. Park, "Broadband coherent anti-Stokes Raman spectroscopy with a modeless dye laser," *Appl. Opt.* **36**, (27) pp.6722-6728 1997.
176. K. M. Bultitude, P. M. Danehy, E. Fraval, J. S. Fox, and A. F. P. Houwing, "Broadband coherent anti-Stokes Raman spectroscopy (BB-CARS) in flames and hypersonic flows," presented at 2nd Australian Conference on Laser Diagnostics in Fluid Mechanics and Combustion, Monash University, Melbourne Australia 1999,
177. R. L. J. Gaffney and A. D. Cutler, "CFD modeling needs and what makes a good supersonic combustion validation experiment," presented at 53rd JANNAF Propulsion Meeting, 2005,
178. R. Baurle and J. R. Edwards, "Hybrid Reynolds-Average/ Large Edddy Simulationsnof a Coaxial Supersonic Free Jet Experiment," presented at 47th AIAA Aerospace Sciences Meeting, Orlando, FL., 2009, AIAA-2009-0524.
179. R. Baurle, (11/15/2010), retrieved http://vulcan-cfd.larc.nasa.gov/.
180. D. C. Wilcox, *Turbulence modeling for cFD,* 2nd ed. (DCW Industries, 1998).
181. M. Samimy and G. S. Elliot, "Effects of compressibility on the characteristics of free shear layers," *AIAA J.* **28**, (3) pp.439-445 1990.
182. N. T. Clemens and M. G. Mungal, "Large-scale structure and entrainment in the supersonic mixing layer," *J. Fluid Mech.* **284**, 171-216 1995.
183. S. K. Lele, "Compressibility effects on turbulence," *Annu. Rev. Fluid Mech.* **26**, 211-254 1994.
184. D. A. Yoder and N. J. Georgiadis, "Fundamentals of Compressible Turbulent Mixing," in *Encyclopedia of Aerospace Engineering* (John Wiley & Sons, Ltd, 2010).
185. S. L. Birch and J. M. Eggers, "A critical review of the experimental data on turbulent shear layers," NASA SP 321 (NASA, 1972).
186. G. L. Brown and A. Roshko, "On density effects and large structure in turbulent mixing layers," *J. Fluid Mech.* **64**, (04) pp.775-816 1974.
187. P. J. Ortwerth and A. J. Shine, "On the scaling of plane turbulent shear layer.," AFWL-TR-77-118 (1977).
188. H. Oertel, "Mach wave radiation of hot supersonic jets investigated by means of the shock tube and new optical techniques. ," in *12th Intl Symp. of Shock Tubes and Waves.*, 1979, 266-275.

189. D. W. Bogdanoff, "Compressibility Effects in Turbulent Shear Layers," *AIAA J.* **21**, (6) pp.926-927 1983.
190. M. D. Slessor, M. Zhuang, and P. E. Dimotakis, "Turbulent shear-layer mixing: growth-rate compressibility scaling," *J. Fluid Mech.* **414**, 35-45 2000.
191. C. Pantano and S. Sarkar, "A study of compressibility effects in the high-speed turbulent shear layer using direct simulation," *J. Fluid Mech.* **451**, 329-371 2002.
192. J. C. Hermanson and P. E. Dimotakis, "Effects of heat release in a turbulent, reacting shear layer," *J. Fluid Mech.* **199**, 333-375 1989.
193. P. A. Mcmurtry, J. J. Riley, and R. W. Metcalfe, "Effects of heat release on the large-scale structure in turbulent mixing layers," *J. Fluid Mech.* **199**, 297-332 1989.
194. C. Pantano, S. Sarkar, and F. A. Williams, "Mixing of a conserved scalar in a turbulent reacting shear layer," *J. Fluid Mech.* **481**, 291-328 2003.
195. C. H. Hicks and K. V. J. Turner, *Fundamental Concepts in the Design of Experiments,* 5th ed. (Oxford University Press, Oxford NY, 1999).
196. J. P. Boquillon, M. Péalat, P. Bouchardy, G. Collin, P. Magre, and J. P. Taran, "Spatial averaging and multiplex coherent anti-Stokes Raman scattering temperature-measurement error," *Opt. Lett.* **13**, (9) pp.722-724 1988.
197. P. E. Dimotakis, "Two-dimensional shear layer entrainment," *AIAA J.* **24**, (1791-1796) pp.1986.
198. D. W. Scott, "Scott's rule," *Wiley Interdisciplinary Reviews: Computational Statistics* **2**, (4) pp.497-502 2010.
199. S. A. Tedder, J. L. Wheeler, and P. M. Danehy, "Characteristics of a broadband dye laser using Pyrromethene and Rhodamine dyes," *Appl. Opt.* **50**, (6) pp.901-914 2011.

REPORT DOCUMENTATION PAGE

Form Approved
OMB No. 0704-0188

1. REPORT DATE *(DD-MM-YYYY)*	2. REPORT TYPE	3. DATES COVERED *(From - To)*
01- 05 - 2012	Contractor Report	

4. TITLE AND SUBTITLE

Dual-Pump CARS Development and Application to Supersonic Combustion

5a. CONTRACT NUMBER

NNX08AB31A, NNX07AC32A

5b. GRANT NUMBER

5c. PROGRAM ELEMENT NUMBER

6. AUTHOR(S)

Magnotti, Gaetano; Cutler, Andrew D.

5d. PROJECT NUMBER

5e. TASK NUMBER

5f. WORK UNIT NUMBER

599489.02.07.07.02.21.22

7. PERFORMING ORGANIZATION NAME(S) AND ADDRESS(ES)

NASA Langley Research Center
Hampton, Virginia 23681-2199

The George Washington University
1 Old Oyster Point
Newport News, Virginia 23602

8. PERFORMING ORGANIZATION REPORT NUMBER

9. SPONSORING/MONITORING AGENCY NAME(S) AND ADDRESS(ES)

National Aeronautics and Space Administration
Washington, DC 20546-0001

10. SPONSOR/MONITOR'S ACRONYM(S)

NASA

11. SPONSOR/MONITOR'S REPORT NUMBER(S)

NASA/CR-2012-217569

12. DISTRIBUTION/AVAILABILITY STATEMENT

Unclassified - Unlimited
Subject Category 34
Availability: NASA CASI (443) 757-5802

13. SUPPLEMENTARY NOTES

Langley Technical Monitor: Paul M. Danehy

14. ABSTRACT

A dual-pump Coherent Anti-Stokes Raman Spectroscopy (CARS) instrument has been developed to obtain simultaneous measurements of temperature and absolute mole fractions of N2, O2 and H2 in supersonic combustion and generate databases for validation and development of CFD codes. Issues that compromised previous attempts, such as beam steering and high irradiance perturbation effects, have been alleviated or avoided. Improvements in instrument precision and accuracy have been achieved. An axis-symmetric supersonic combusting coaxial jet facility has been developed to provide a simple, yet suitable flow to CFD modelers.Approximately one million dual-pump CARS single shots have been collected in the supersonic jet for varying values of flight and exit Mach numbers at several locations. Data have been acquired with a H2 co-flow (combustion case) or a N2 co-flow (mixing case). Results are presented and the effects of the compressibility and of the heat release are discussed.

15. SUBJECT TERMS

CARS; CFD validation; Experiments; Fluid mechanics; Gas dynamics; Laser Diagnostics; Scramjets; Supersonic jets; Supersonic mixing; Supersonic shear layers

16. SECURITY CLASSIFICATION OF:			17. LIMITATION OF ABSTRACT	18. NUMBER OF PAGES	19a. NAME OF RESPONSIBLE PERSON
a. REPORT	b. ABSTRACT	c. THIS PAGE			STI Help Desk (email: help@sti.nasa.gov)
					19b. TELEPHONE NUMBER *(Include area code)*
U	U	U	UU	301	(443) 757-5802